



THÈSE / UNIVERSITÉ DE RENNES 1

sous le sceau de l'Université Européenne de Bretagne

pour le grade de

DOCTEUR DE L'UNIVERSITÉ DE RENNES 1

Mention : Traitement du Signal et Télécommunications

École doctorale Matisse

présentée par

Juan José Mantilla Jauregui

Préparée à l'unité de recherche INSERM, U1099

Laboratoire de Traitement du Signal et de l'Image

UFR ISTIC: Informatique et Électronique

**Caractérisation
de pathologies
cardiaques en
Imagerie par
Résonance
Magnétique par
approches
parcimonieuses**

Thèse à soutenir à Rennes

le 24 Novembre 2015

devant le jury composé de :

Nicole VINCENT

PU, Université Paris Descartes / *Rapporteur*

Alain LALANDE

MCU-PH, HDR, Université de Bourgogne / *Rapporteur*

Denis KOUAME

PU, Université Paul Sabatier Toulouse 3 / *Examineur*

Mathieu LEDERLIN

PH, Université de Rennes 1, CHU de Rennes / *Examineur*

Mireille GARREAU

PU à l'Université de Rennes 1 / *Directrice de thèse*

José Luis PAREDES

PU, Université des Andes, Venezuela / *Co-directeur de thèse*

À la memoire de mon père

Remerciements

Je tiens à exprimer mes remerciements au Professeur Lotfi SENHADJI, directeur du LTSI, pour m'avoir accueilli chaleureusement au sein de son laboratoire.

Je remercie mes directeurs de thèse, Mme. Mireille GARREAU et M. José Luis PAREDES, pour leur soutien et tous leurs conseils tout au long de cette thèse, ainsi que pour les remarques constructives qu'ils ont su me donner lors de la rédaction de ce manuscrit et des articles scientifiques.

Je remercie également M. Jean-Jacques Bellanger qui a co-encadré ma thèse et qui a apporté des remarques techniques tout au long de la rédaction et pour la présentation de travaux dans des conférences internationales.

Je remercie vivement M. Alain LALANDE et Mme. Nicole VINCENT de l'intérêt qu'ils ont porté à ce travail, d'avoir accepté de participer à mon jury de thèse comme rapporteurs et pour la qualité de leur rapport. Je remercie aussi M. Denis KOUAME, président du jury et M. Mathieu LEDERLIN pour leurs commentaires constructifs et suggestions apportées à mes travaux de recherche.

Je remercie l'Université de Tachira pour le financement de la thèse et aussi M. Antonio BRAVO responsable du côté Vénézuélien du projet ECOS-NORD FONACIT, qui ont permis le développement de cette thèse en France.

Je remercie aussi le personnel administratif du LTSI, Mesdames Patricia BERNABE, Soizic CHARPENTIER et Muriel DIOP qui m'ont aidé à résoudre de nombreux problèmes administratifs et m'ont aussi encouragé à la fin de ma thèse.

Je remercie ma famille, tout spécialement ma mère Isabel, mes frères Adolfo et Nixon, et ma sœur Eilyn, pour leur présence, amour et leur soutien inconditionnel à tout moment, malgré la distance. Je remercie aussi mes trois nièces Liah, Mariel et Karlin, et mes quatre neveux Éros, Sebas, Matias et Anthony pour leurs messages d'encouragement et d'affection pendant ces trois années de thèse. Merci aussi à mes belles-soeurs Lisbeth et Adriana et à mon beau-frère Mario.

Je remercie mes amis Vénézuéliens qui m'ont accompagné malgré la distance avec leurs messages d'encouragement, particulièrement Maria VALERO, José CLEMENTE, Marcel MOLINA, Giancarlo COLMENARES, Marlond LIZCANO et Gabriela CABRERA, et plus proche de Rennes, mes amis Rémy GOURDIN et Nadia GOURDIN.

Pendant ces trois années au LTSI j'ai fait la connaissance de gens exceptionnels, des doctorants et postdoctorants avec qui j'ai passé de bons moments scientifiques et non-scientifiques. Je tiens à remercier plus particulièrement Héctor ROMERO, Daniel ROMERO, Mireia CALVO, David OJEDA, Richard RIOS, Julian BETANCUR, Zulma SANDOVAL, Sophie BRUGE, Diego PEREZ, Gustavo GUERRERO, Frédéric COMMANDEUR, Sophie COLLIN, Hélène FEUILLATRE et Aureline FARGEAS.

À vous tous, merci beaucoup!

Abstract

This work concerns the use of sparse representation and Dictionary Learning (DL) in order to get insights about the diseased heart in the context of Cardiovascular Diseases (CVDs). Specifically, this work focuses on 1) assessment of Left Ventricle (LV) wall motion in patients with heart failure and 2) fibrosis detection in patients with hypertrophic cardiomyopathy (HCM).

In the context of heart failure (HF) patients, the work focuses on LV wall motion analysis in cardiac cine-MRI. The first contribution in this topic is a feature extraction method that exploits the partial information obtained from all temporal cardiac phases and anatomical segments in a spatio-temporal representation from sequences cine-MRI in short-axis view. These features correspond to spatio-temporal profiles in different anatomical segments of the LV. The proposed representations exploit information of the LV wall motion without segmentation needs. Three representations are proposed : 1) diametrical spatio-temporal profiles where radial motions of LV's walls are observed at the same time in opposite anatomical segments 2) radial spatio-temporal profiles where motion of LV's walls is observed for each segment of the LV cavity and 3) quantitative parameters extracted from the radial spatio-temporal profiles. A second contribution involves the use of these features as input atoms in the training of discriminative dictionaries to classify normal or abnormal regional LV motion. We propose two levels of evaluation, a first one where the global status of the subject (normal/pathologic) is used as ground truth to label the proposed spatio-temporal representations, and a second one where local strain information obtained from 2D Speckle Tracking Echocardiography (STE), is taken as ground truth to label the proposed features, where a profile is classified as normal or abnormal (akinetic or hypokinetic cases).

In the context of Hypertrophic cardiomyopathy (HCM), we address the problem of fibrosis detection in Late Gadolinium Enhanced LGE-Short axis (SAX) images by using a sparse-based clustering approach and DL. In this framework, random image patches are taken as input atoms in order to train a classifier based on the sparse coefficients obtained with a DL approach based on kernels. For a new test LG-SAX image, the label of each pixel is predicted by using the trained classifier allowing the detection of fibrosis. A subsequent postprocessing step allows the spatial localization of fibrosis that is represented according to the American Heart Association (AHA) 17-segment model and a quantification of fibrosis in the LV myocardium.

Résumé en français

Dans le domaine du traitement du signal, il est souvent utile de pouvoir représenter des informations contenues dans des signaux de grande dimension dans un autre espace plus approprié à l'analyse ou à un traitement. Traditionnellement, les signaux sont représentés dans un domaine spatial où la représentation du signal est unique. La représentation parcimonieuse de signaux a démontré être un outil extrêmement puissant pour l'acquisition, la représentation, la compression et la classification des signaux de grande dimension (AHARON et al., 2006 ; ELAD et al., 2006 ; LI et al., 2013 ; RUBINSTEIN et al., 2010 ; WRIGHT et al., 2010).

L'apprentissage de dictionnaires parcimonieux est une approche récente qui vise à utiliser des techniques d'apprentissage automatique pour déduire un dictionnaire d'un ensemble de signaux d'entrée. Un signal donné peut être alors bien estimé simplement comme une combinaison linéaire de quelques atomes du dictionnaire. Les méthodes d'apprentissage de dictionnaires parcimonieuses sont à l'origine conçues pour apprendre un dictionnaire qui peut fidèlement représenter des signaux. Dans le contexte du traitement d'images, la représentation d'images et la reconstruction sont considérées comme les problématiques les plus étudiées à l'aide de ces techniques. Par ailleurs, des tâches de classification ont commencé à être abordées dans le cadre d'apprentissage de dictionnaires. En confirmant ce qui a été observé en classification sur des images naturelles, nous cherchons à étudier les avantages à utiliser des dictionnaires, directement appris d'un ensemble d'images médicales qui permettent de capturer la distribution des données et qui puissent être utiles ensuite dans des tâches telles que la classification et la détection.

Dans cette étude, nous abordons l'utilisation de la représentation parcimonieuse et l'apprentissage de dictionnaires pour l'aide au diagnostic dans le contexte de Maladies Cardiovasculaires (CVDs). Spécifiquement, notre travail se concentre : 1) sur l'évaluation du mouvement des parois du Ventricule Gauche (VG) chez des patients souffrant d'Insuffisance Cardiaque (IC) ; 2) la détection de fibrose chez des patients présentant une Cardiomyopathie Hypertrophique (CMH). Ces types de pathologies sont étudiées par ailleurs en Imagerie par Résonance Magnétique Cardiaque (IRMC). Ces travaux ont été exécutés en collaboration avec le CIC-IT (Centre d'Investigation Clinique Innovation Technologique) du CHU de Rennes.

En 2010, les CVDs ont causé 223 morts pour 100000 individus en France (environ 27% de décès totaux), étant la première cause de maladies chez les femmes et la deuxième chez les hommes. La mortalité par CVDs au niveau mondial est très semblable. 17.3 millions de personnes sont décédées de CVDs en 2008, représentant 30% de tous les décès, selon l'Organisation Mondiale de la Santé (WHO, 2014). Les CVDs affectent le cœur, les vaisseaux sanguins ou les deux à

la fois. Les pathologies les plus fréquentes sont : l'Ischémie, la Maladie d'artère Coronaire, la Cardiomyopathie et l'Insuffisance Cardiaque.

La première pathologie abordée dans cette étude est l'**Insuffisance Cardiaque (IC)** qui est un syndrome clinique complexe qui résulte d'une diminution structurelle ou fonctionnelle du remplissage ventriculaire ou de l'éjection de sang (YANCY et al., 2013). Le syndrome clinique d'IC peut résulter de troubles du péricarde, du myocarde, de l'endocarde, des valves du cœur ou de grands vaisseaux, ou de certaines anomalies métaboliques, mais la plupart des patients souffrant d'IC ont plusieurs symptômes, en raison d'une fonction myocardique ventriculaire gauche détériorée.

Cliniquement, l'IC a un pronostic pauvre et son diagnostic de stade précoce peut jouer un rôle essentiel dans la planification du traitement. Un changement courant de la fonction ventriculaire gauche normale chez des patients avec IC est l'asynchronisme intra-ventriculaire quand les segments anatomiques des ventricules se contractent de façon non synchronisée. Les anomalies du mouvement ventriculaire gauche segmentaire sont en particulier significatives dans de multiples pathologies cardiaques et leur diagnostic est d'une importance capitale (GARCIA-FERNANDEZ et al., 2003).

L'**imagerie par résonance magnétique Cardiaque (IRMC)** est actuellement utilisée en imagerie médicale pour l'évaluation de la fonction ventriculaire gauche (KIRSCHBAUM et al., 2011). Cette modalité permet d'obtenir des paramètres différents, qui caractérisent la fonction ventriculaire et qui peuvent être regroupés en deux catégories : les indicateurs globaux et les indicateurs locaux. Les indicateurs globaux peuvent inclure : des volumes ventriculaires, la masse ventriculaire, la fraction d'éjection ou le débit cardiaque. Les indicateurs locaux sont extraits par segment anatomique du ventricule gauche selon le modèle à 17 segments proposé par l'American Heart Association (AHA)(CERQUEIRA et al., 2002) et peuvent inclure : la fraction d'éjection régionale, l'épaississement myocardique, des informations de déplacement, de vitesse et de déformation locale de mouvement. L'analyse globale de la dynamique cardiaque en cine-IRMC est concentrée au niveau temporel sur deux phases particulières du cycle cardiaque : la fin de diastole et la fin de systole.

Un autre type de modalité d'imagerie cardiaque considérée comme la référence pour l'analyse de la mécanique cardiaque est l'Échocardiographie. L'évaluation de la fonction ventriculaire gauche peut-être effectuée en utilisant l'analyse des déformations de la paroi ventriculaire gauche en échocardiographie (GORCSAN et al., 2011). Des méthodes actuellement appliquées pour l'analyse de la fonction régionale du VG intègrent des mesures d'échographie 2D (BECKER et al., 2006). Notamment l'**échographie de speckle tracking (STE)** est utilisée comme une technique d'imagerie pour la quantification de la déformation myocardique dans l'évaluation globale et segmentaire de la fonction cardiaque et pour l'évaluation de l'asynchronisme ventriculaire (TANABE et al., 2008). Des avancées récentes dans le développement d'imagerie en échocardiographie permettent l'acquisition des images 3D qui surmontent quelques limitations de l'imagerie 2D conventionnelle. L'imagerie en échocardiographie 3D (FENSTER et al., 2001 ; MAFFESENTI et al., 2009) a le potentiel de fournir les visualisations temps réel 3D du cœur.

Cependant, la résolution temporelle est inférieure à celle de l'imagerie en échocardiographie 2D.

Pour ce qui concerne les travaux de la littérature sur le domaine, les techniques actuelles pour l'évaluation du mouvement des parois du VG sont le plus souvent composées d'une étape de prétraitement, suivie de la segmentation des frontières, puis de l'extraction des caractéristiques et de leur classification. La plupart des approches ont besoin de la segmentation de la cavité du VG et exigent une interaction importante de l'utilisateur ou une semi / totale délimitation automatique des frontières du myocarde.

Les enjeux recherchés sont ici de pouvoir trouver une méthode d'extraction de caractéristiques qui à la fois, ne nécessite pas la segmentation de la cavité du VG, exploite toutes les informations du cycle cardiaque et qui permettent d'extraire des informations discriminatoires pour la caractérisation du mouvement. Il est aussi exigé d'employer ou de développer un classifieur ayant une haute capacité de généralisation.

Une technique de classification récente qui est largement exploitée dans les images naturelles est la Classification basée sur la représentation parcimonieuse (SRC) (WRIGHT et al., 2009) qui implique l'utilisation d'algorithmes différents pour, dans un premier temps, apprendre des dictionnaires à partir de l'ensemble étiqueté de données d'apprentissage, et dans un second temps, exploiter la décomposition parcimonieuse du signal de test pour sa classification.

Quelques applications ont été proposées en imagerie médicale (IRM, tomographie, échocardiographie et microscopie) et ont été explorées dans les domaines de la représentation parcimonieuse et de l'apprentissage de dictionnaires. On retrouve dans ces travaux par exemple, les problèmes de reconstruction d'image, de débruitage, de fusion, de segmentation, de rehaussement par approches multimodales et de classification. À notre connaissance, la classification du mouvement des parois du VG par apprentissage de dictionnaires en IRM cardiaque n'a pas été précédemment rapportée.

Dans le contexte de l'IC notre contribution porte sur l'évaluation de mouvement du VG dans des séquences cine-IRMC. Nous proposons dans un premier temps, une méthode d'extraction de caractéristiques qui exploite les informations partielles obtenues à partir de toutes les phases cardiaques temporelles et des segments anatomiques, dans une représentation spatio-temporelle en cine-IRM petit axe. Les représentations proposées exploitent les informations du mouvement des parois du VG sans avoir recours à la segmentation et disposent des informations discriminatoires qui pourraient contribuer à la détection et à la caractérisation du mouvement. Deuxièmement, nous proposons l'utilisation de ces caractéristiques comme des atomes d'entrée dans l'apprentissage de dictionnaires discriminatoires pour classifier le mouvement régional du VG dans les cas normaux ou anormaux.

La méthode développée est la suivante :

Des séquences cine-IRM cardiaques en vue petit axe sont regroupés en deux populations : les séquences pathologiques et les séquences de contrôle. Le processus se déroule en trois étapes principales : Dans une étape de prétraitement, une région d'intérêt (ROI) est définie dans le premier cadre de chaque séquence pour analyser seulement la structure du VG. La ROI est projetée dans toute la séquence et est normalisée selon la représentation AHA pour identifier les segments anatomiques, où les plans basal et médial sont divisés en 6 segments : Antérieur,

Antéro-Septal, Inféro-Septal, Inférieur, Inféro-Latéral, Antéro-latéral. Le plan apical est divisé en 4 segments : Antérieur, Septal, Inférieur et Latéral. L'extraction d'images spatio-temporelles a été proposée, permettant la construction de trois nouveaux types de représentations :

Profils spatio-temporels diamétraux Un premier type de représentation a été proposée par l'extraction de profils spatio-temporels diamétraux qui montrent l'évolution temporelle de l'épicarde et de l'endocarde, de façon conjointe, dans deux segments anatomiques opposés du VG, exploitant ainsi, leur comportement à partir des profils radiaux de même orientation.

Profils spatio-temporels radiaux Un deuxième type de représentation a été proposée par l'extraction de profils spatio-temporels radiaux où le mouvement pariétal est observé pour chaque segment de la cavité du VG.

Paramètres extraits à partir des courbes de temps-intensité dans des profils radiaux

Une troisième type de représentation a été proposée par l'extraction de courbes de signal temps-intensité (TSICs) directement des profils spatio-temporels radiaux dans chaque segment anatomique. Des paramètres différents sont alors définis de ces courbes qui reflètent les informations dynamiques de la contraction du VG. Pour chaque TSIC obtenu dans un profil d'image radiale, nous avons réalisé l'interprétation d'images paramétriques proposée dans (KACHENOURA et al., 2007). Nous nous intéressons aux courbes qui reflètent la contraction de la cavité ventriculaire et quatre paramètres sont extraits de ces courbes : un paramètre de partitionnement de courbe (Cl), un paramètre de dissymétrie (Sk) et un paramètre de corrélation croisée (Co). Nous proposons également d'utiliser le paramètre de temps de transition moyen (Mt) proposé par (KACHENOURA et al., 2007), calculé sur le partitionnement de courbe.

Chaque profil spatio-temporel est identifié avec son étiquette de classe respective $y_i \in (1, 0)$, où 1 correspond aux profils anormaux et 0 correspond aux profils normaux. La discrimination de mouvement pariétal normal et anormal est réalisée par l'utilisation des caractéristiques proposées comme des atomes d'entrée dans **l'apprentissage de dictionnaires**. Pour cela, des signaux d'entrée $\mathbf{Y} \in \mathbb{R}^{n \times N}$ sont représentés comme une matrice de données où chaque colonne est un signal n -dimensionnel d'entrée (des représentations spatio-temporelles vectorisées). Les coefficients parcimonieux $\mathbf{X} \in \mathbb{R}^{K \times N}$ des signaux d'entrée \mathbf{Y} et le dictionnaire $\mathbf{D} \in \mathbb{R}^{n \times K}$, avec K atomes sont appris en adaptant trois algorithmes de classification pour la classification de mouvement pariétal du VG basés sur l'apprentissage de dictionnaire :

Un premier algorithme d'apprentissage de dictionnaire est retenu, où la discrimination du dictionnaire appris est respectée en imposant des contraintes structurelles du dictionnaire : "The Label Consistent K-SVD algorithme (LC-KSVD)" (JIANG et al., 2013). Un deuxième algorithme est également retenu, où la discrimination est respectée en imposant un terme discriminatoire sur les vecteurs de décomposition parcimonieuse : "The Fisher discriminant Dictionary learning (DL) algorithme" (YANG et al., 2014). Ces deux algorithmes prennent comme atomes d'entrée les profils diamétraux ou les profils radiaux.

Un autre type d'algorithme d'apprentissage de dictionnaire basé sur des noyaux est adapté à la classification de mouvement pariétal du VG en utilisant des paramètres extraits des profils spatio-temporels radiaux : l'algorithme KSRDL (LI et al., 2013). Dans l'approche paramétrique, \mathbf{Y} représente une matrice de données de paramètres où chaque colonne est un vecteur de paramètres extraits des profils spatiaux-temporels radiaux.

La sparsité de ces techniques est mesurée par des normes différentes. L'algorithme LC-KSVD utilise une norme ℓ_0 qui compte le nombre d'éléments non-zéro de \mathbf{X} , tandis que l'algorithme FD-DL et l'algorithme KSRDL utilise une norme ℓ_1 - avec un paramètre de régularisation λ_1 dont la valeur dirige la sparsité de la solution. On considère la sparsité comme une mesure de robustesse des techniques de classification d'apprentissage de dictionnaire.

Pour évaluer la capacité de généralisation des techniques d'apprentissage automatique en ce qui concerne la précision, la sensibilité et la spécificité, et pour leur comparaison postérieure, nous avons exécuté une validation croisée par sous-échantillonnage aléatoire de la base de données. Cette méthode divise aléatoirement l'ensemble de données dans des données de validation et des données d'apprentissage. En outre, en raison du petit nombre de patients actuellement disponibles pour chaque classe, nos classifieurs sont évalués en utilisant le critère "leave-one-out cross-validation" (CHAPELLE et al., 2002).

Pour cette étude, des séquences cine-IRM en vue petit axe sont issues de quatre bases de données : deux groupes de données de patients qui ont été acquises suivant des protocoles cliniques dans des projets de recherche nationaux et internationaux : i) le projet ANR «Utility of medical imaging for the optimization of the implantation of implantable cardiac devices» (IMOP)¹ et ii) le projet européen «European Community's Seventh Framework Programme» (euHeart)²; et deux groupes de sujets sains obtenus de deux défis de MICCAI³ : iii) "the Cardiac MR Left Ventricle Segmentation Challenge MICCAI 2009" (RADAU et al., 2009) et iv) "the first Cardiac Motion Analysis Challenge MICCAI 2011" (TOBON-GOMEZ et al., 2013).

Nous avons proposé un protocole d'évaluation basé sur les informations disponibles sur la population décrite et le type de caractéristique utilisé pour former les classifieurs qui se décompose comme suit :

L'évaluation globale multi-coupe non-paramétrique : L'évaluation globale multi-coupe non-paramétrique a été exécutée en utilisant le statut global du sujet : Normal/Pathologique, comme l'étiquette de référence des profils spatio-temporels diamétraux extraits dans une coupe apicale, médiale ou basale en petite axe. Les séquences cine-IRM en petit axe utilisées dans cette expérience comprennent 20 études regroupées en deux classes : 1) échantillons de mouvement anormaux du VG correspondant à 14 patients avec asynchronisme cardiaque et 2) échantillons de mouvement normaux du VG correspondant à 6 sujets sains. Pour chaque sujet, 18 profils spatio-temporels diamétraux ont été extraits, ce qui fait un total

1. ANR CIC-IT n^o 04 187-188-189-190. Acronym from the French "utilité de l'Imagerie Médicale dans l'Optimisation de la Pose de prothèses cardiaques implantables", utility of medical imaging in the optimization of the implantation of implantable cardiac prosthesis.

2. euHeart : Personalised and Integrated Cardiac Care, FP7/2008-2012

3. MICCAI - Medical image computing and computer-assisted intervention

de 360 profils : 252 considérés comme anormaux (14 patients, 18 profils par patient) et 108 considérés comme normaux (6 sujets de contrôle, 18 profils par sujet). Les expériences ont été exécutées en utilisant les profils spatio-temporels diamétraux dans le domaine original (des niveaux de Gris), mais aussi dans le domaine de Fourier, le domaine des Ondelettes et le domaine des Curvelets.

Après expérimentation, les résultats obtenus montrent que le domaine des Ondelettes résulte être le meilleur espace où la représentation originale (profils spatio-temporels diamétraux) rapporte la meilleure précision et la meilleure sensibilité de toutes les techniques de classification (SVM et techniques d'apprentissage de dictionnaire). Ceci peut être dû au débruitage implicite qui est impliqué dans la transformée d'ondelette qui rend la classification plus précise. La représentation en niveaux de Gris et la représentation de Fourier sont classés deuxième et troisième respectivement. En matière de spécificité, le domaine des niveaux de Gris fournit de meilleurs résultats que le domaine des Ondelettes dans les coupes médiale et apicale. La meilleure performance pour la classification de mouvement pariétal anormal et normal du VG, en utilisant des profils spatio-temporels diamétraux, est réalisée dans le domaine des Ondelettes avec un classificateur FD-DL qui atteint 96.51% de précision, 96.48 % de sensibilité et 96.67% de spécificité, obtenues dans la coupe ventriculaire médiale (MANTILLA et al., 2013a,b). Ces résultats sont en accord avec ceux trouvés dans (SUINESIAPUTRA et al., 2009) et (PUNITHAKUMAR et al., 2010) en raison du fait que le mouvement pariétal au niveau médial est bien défini et plus stable comparé aux coupes basales et apicales.

L'évaluation globale en coupe médiale non-paramétrique : L'évaluation globale en coupe médiale non-paramétrique a été exécutée en utilisant le statut global du sujet : Normal/Pathologique, comme l'étiquette de profils spatio-temporels diamétraux ou radiaux extraits dans une coupe médiale en petit axe. Les séquences cine-IRM en petit axe utilisées dans cette expérience comprennent 18 cas regroupés en deux classes : 1) des patients avec un mouvement anormal du VG correspondant à 9 patients avec asynchronisme cardiaque et pour lesquels nous avons les déformations radiales aux coupes médiales ventriculaires obtenues par la modalité échographique (2D-STE) et 2) des patients avec mouvements normaux du VG qui correspondent à 9 sujets sains. Pour chaque sujet, 36 profils spatio-temporels radiaux et 18 profils spatio-temporels diamétraux ont été extraits, ainsi, nous avons : i) un total de 324 profils diamétraux, 162 considérés comme anormaux (9 patients, 18 profils par patient) et 162 considérés comme normaux (9 contrôles, 18 profils par sujet) et ii) un total de 648 profils radiaux, 324 considérés comme anormaux (9 patients, 36 profils par patient) et 324 considérés comme normaux (9 contrôles, 36 profils par sujet). Les expériences ont été réalisées en utilisant les profils spatio-temporels diamétraux ou radiaux dans le domaine original (des niveaux de Gris), mais aussi dans le domaine des Ondelettes.

Le domaine des niveaux de Gris est le domaine où la précision de classification est la plus haute, en utilisant des profils diamétraux et par l'algorithme LC-KSVD. De même, le domaine des niveaux de Gris est le domaine spatial où des profils radiaux réalisent la

meilleure précision de classification, dans ce cas par l'algorithme FD-DL. En utilisant des profils radiaux et une évaluation globale, la précision obtenue est plus haute que celle obtenue en utilisant des profils diamétraux.

L'évaluation locale en coupe médiale non-paramétrique : L'évaluation locale en coupe médiale non-paramétrique a été réalisée en utilisant les informations de déformation locales fournies par l'analyse des images échographiques de référence en clinique (2D-STE) (MANTILLA et al., 2015c). Les séquences cine-IRM en petit axe, utilisées dans cette expérience comprennent la même population que dans le cas d'évaluation globale au niveau médial : 18 cas regroupés en deux classes : 1) des patients avec des mouvements anormaux du VG correspondant à 9 patients avec asynchronisme cardiaque et pour lesquels nous avons l'information de déformation radiale au niveau de la coupe médiale ventriculaire mesurée à partir de la 2D-STE et 2) des patients avec des mouvements normaux du VG correspondant à 9 sujets sains.

Pour chaque sujet, 36 profils radiaux et 18 profils diamétraux ont été extraits. Sur 324 profils diamétraux des 18 sujets dans l'étude : 162 sont considérés comme anormaux (9 patients, 18 profils par patient) et 162 sont considérés comme normaux (9 contrôles, 18 profils par sujet). Nous basons notre analyse après le groupement de deux segments opposés en considérant un profil normal si tous les deux sont normaux. Sur un total de 648 profils radiaux, 276 sont considérés anormaux et 372 sont considérés normaux dans la population. Les résultats montrent que le meilleur taux de classification est obtenu par la technique de FD-DL dans le domaine original (le domaine des niveaux de Gris) avec une moyenne de 92.81% de précision. Cette technique offre la spécificité la plus élevée dans le domaine original et aussi dans le domaine des Ondelettes. En outre, le classifieur obtenu dans la technique LC-KSVD trouve les codes parcimonieux dans le domaine des Ondelettes le plus discriminant pour la classification de profils spatio-temporels. En matière de sensibilité, les résultats le plus élevés sont obtenus avec l'algorithme LC-KSVD et sont meilleurs que ceux obtenus avec l'algorithme SVM en utilisant un noyau RBF dans le domaine des Ondelettes. Sur ces résultats, on observe que les techniques d'apprentissage de dictionnaires discriminatoires surpassent légèrement la technique de SVM, mais avec un coût informatique plus élevé. Les techniques d'apprentissage de dictionnaires exigent plus de temps dans les étapes d'apprentissage et de test que la technique SVM, et plus particulièrement la technique de FD-DL. En outre, la différence de temps dans l'apprentissage et le test entre les techniques SVM et les techniques LC-KSVD est très basse (environ 6 secondes pour l'apprentissage et 0.02 secondes pour le test). L'utilisation de profils radiaux améliore les résultats de classification donnés par des profils diamétraux dans le plan médial de la cavité. En outre, avec une évaluation globale, les profils radiaux donnent de meilleurs résultats de classification que les profils diamétraux. Les résultats montrent que la technique LC-KSVD représente le meilleur compromis entre la précision, la sensibilité, la spécificité et la complexité en matière de temps de calcul et de sparsité, dans le domaine des Ondelettes.

L'évaluation locale en coupe médiale paramétrique : L'évaluation locale en coupe mé-

diale paramétrique a été exécutée en utilisant les paramètres descriptifs extraits des profils spatio-temporels radiaux et en exploitant les informations de déformation locale fournies par l'étude 2D-STE. Les séquences cine IRM en petite axe utilisées dans cette expérience correspondent à la même population que celle utilisée dans l'évaluation locale non paramétrique de la cavité. A partir des profils radiaux, différents paramètres ont été proposés ou repris de la littérature et ont été combinés. Ils sont décrits ci-dessous.

Paramètre de partitionnement de courbe (Cl) : Chaque segment anatomique du VG est divisé en 6 sous-régions angulaires comprenant dix profils consécutifs. Un processus de partitionnement basé sur des ondelettes (MISITI et al., 2007) divise l'ensemble de signaux de profils radiaux dans chaque sous-région angulaire en deux groupes. La moyenne des signaux dans le plus grand groupe est alors calculée, représentant le plus grand groupe de signaux avec un modèle de contraction similaire.

Paramètre de dissymétrie (Sk) : Nous calculons le skewness de courbes moyennes (Cl) comme une mesure de symétrie. Un skewness négatif indique que la distribution de données est "gauche-biaisée" reflétant une contraction régionale du VG retardée. Un skewness positif indique que la distribution de données est "droite-biaisée" reflétant une contraction régionale du VG normale.

Paramètre de corrélation croisée (Co) : Un paramètre basé sur l'analyse de corrélation croisée est calculé entre chaque courbe moyenne (Cl) et une référence spécifique de la population saine. Pour définir cette référence, nous exécutons un processus de partitionnement basé sur des ondelettes (MISITI et al., 2007) appliqué sur l'ensemble de signaux des profils qui appartiennent aux sujets de contrôle. La moyenne du groupe avec la taille maximale est une référence spécifique de la population saine. La corrélation croisée est alors calculée entre chaque courbe moyenne (Cl) et la référence dite normale.

Paramètre de temps de transition moyen (Mt) : Le paramètre de temps de transition moyen $Mt = (TON + TOFF)/2$ est calculé à partir du paramètre $TON(c)$, qui représente le temps où la contraction commence et $TOFF(c)$, qui représente le temps de la fin du mouvement endo-cardiaque sur le pixel c .

La procédure d'extraction de paramètres est appliquée sur tous les profils spatio-temporels radiaux. Nous construisons des vecteurs différents pour initialiser un dictionnaire basé sur l'algorithme KSRDL (LI et al., 2013) afin d'obtenir les représentations parcimonieuses du signal d'entrée et d'utiliser ces représentations pour former un classifieur de type "K plus proches voisins" (K -NN). Les résultats montrent que le meilleur taux de classification est réalisé avec l'algorithme KSRDL en utilisant des vecteurs construits avec le paramètre de skewness (Sk) et le paramètre de partitionnement de courbe (Cl) avec une précision de 94.49%. La meilleure performance pour l'algorithme SVM en utilisant un noyau RBF et l'algorithme LC-KSVD est réalisée quand tous les paramètres sont utilisés comme entrées (MANTILLA et al., 2015a,b,e). La précision des classifieurs est significativement réduite

quand les vecteurs sont construits seulement avec le paramètre de partitionnement de courbe (Cl) et le paramètre de corrélation-croisée (Co), mettant en évidence l'importance du paramètre de skewness dans la caractérisation de l'asynchronisme ventriculaire.

Notre méthode est limitée par le nombre de patients et la disponibilité des informations de déformation, mais les résultats obtenus avec l'évaluation locale peuvent être analysés en prenant des résultats de référence obtenus par des méthodes de la littérature. Notre méthode possède deux caractéristiques principales qui peuvent être synthétisées comme : i) en exécutant une évaluation locale par segments à l'aide des informations de déformation et des informations issues de toutes les phases temporelles, nous avons pu déterminer une évaluation de mouvement pariétal comparable avec le mouvement pariétal manuel standard réalisé par un spécialiste, ii) nous avons montré que l'analyse des profils spatio-temporels radiaux dans des séquences cine-IRM cardiaques au niveau médial en petit axe, suffisent pour détecter des anomalies de mouvement pariétal dans l'ensemble des données analysé. Du point de vue méthodologique, l'adaptation de méthodes d'apprentissage de dictionnaire à la tâche de classification a abouti à une technique prometteuse pour l'analyse de mouvement du VG, en réalisant un compromis entre précision de résultats, complexité et simplicité des algorithmes.

La deuxième pathologie considérée dans cette étude est la **Cardiomyopathie Hypertrophique (CMH)**, qui appartient à la large classe des Cardiomyopathies qui représentent un groupe hétérogène de maladies myocardiques. La CMH survient lorsque des cellules du muscle du cœur grandissent et provoquent l'épaississement des parois des ventricules (généralement le ventricule gauche). Malgré cet épaississement, la taille du ventricule reste souvent normale. Cependant, l'épaississement peut bloquer le flux sanguin du ventricule. L'imagerie de résonance magnétique cardiaque est utilisée pour mesurer l'épaisseur pariétale myocardique et diagnostiquer la CMH (MEMBERS et al., 2011). Aussi, elle est utilisée pour caractériser le tissu myocardique, permettant de qualifier également la présence de fibrose (MOON et al., 2004) souvent présente dans ces pathologies. Il est documenté qu'approximativement la moitié de patients avec CMH ont des séquences IRM de rehaussement tardif (LGE-IRM) avec des zones suggestives de fibrose (MARON et al., 2008).

Plusieurs études ont montré la pertinence de l'image en rehaussement tardif (LGE)-IRM cardiaque pour la localisation et l'évaluation de la fibrose myocardique (ORDOVAS et al., 2011). L'évaluation précise de ces régions de fibrose est cruciale, la présence de fibrose étant directement liée au risque de mort subite et à la présence d'arythmies. Elle est également importante afin d'évaluer le rétablissement myocardique fonctionnel après thérapie de reperfusion, mais aussi pour mieux stratifier les cas de CMH et leur pronostic. Aussi, le degré d'amélioration du mouvement pariétal global et de la fraction d'éjection est significativement lié à la mesure transmurale de fibrose en LGE (ADABAG et al., 2008). Au niveau clinique, la taille d'infarctus est un facteur pronostique indépendant pour l'insuffisance cardiaque, les arythmies et mortalité à cause d'événements cardiaque (MEWTON et al., 2011).

En routine clinique, l'évaluation de la mesure transmurale des régions hyper-rehaussées est exécutée de façon visuelle souvent en utilisant les échelles semi-quantitatives de Likert (KIM et al.,

2000). Dans la littérature, plusieurs méthodes basées sur le réglage de seuils avec interaction manuelle de l'utilisateur (AMADO et al., 2004; GERBER et al., 2002; KIM et al., 2000; SCHUIJF et al., 2004) ou avec la définition automatisée des zones infarctées en utilisant des opérateurs morphologiques (HSU et al., 2006; KOLIPAKA et al., 2005) ont été développées à cette fin. À notre connaissance, la détection de zones de fibrose basée sur l'apprentissage de dictionnaires en imagerie LGE-IRM n'a pas été précédemment rapportée.

Dans le contexte de la CMH, nous abordons le problème de détection de la fibrose en LGE-IRM en vue petit axe (SAX) en utilisant une approche de partitionnement de données et d'apprentissage de dictionnaires. Dans ce cadre, les caractéristiques extraites d'images de LGE-SAX sont prises comme des atomes d'entrée pour former un classifieur basé sur les codes parcimonieux obtenus avec une approche d'apprentissage de dictionnaires. Une étape de post-traitement permet la délimitation du myocarde (zone d'Intérêt pour l'analyse de la fibrose) et la localisation spatiale de la fibrose par segment anatomique.

Une première étape de traitement consiste en : 1) l'extraction aléatoire de patches non-chevauchés à partir des images LGE-SAX et le calcul d'une matrice de similarité entre les patches. 2) le partitionnement des données en deux groupes, patches labellisés "rehaussés" (LGE) ou "non-rehaussés" (Non-LGE) à partir de la matrice de similarité et par l'exécution d'un algorithme de partitionnement hiérarchique (MISITI et al., 2007) basé sur une représentation en Ondelettes de Haar.

Dans une deuxième étape de traitement, nous construisons un dictionnaire initial avec les patches extraits et classés en deux catégories (avec rehaussement tardif et sans rehaussement tardif). Nous appliquons ensuite l'algorithme KSRDL (LI et al., 2013) pour obtenir les codes parcimonieux des patches d'entrée qui sont ensuite utilisés pour former un classifieur *K- plus proches voisins*. Notre méthode est testée pour la détection de la fibrose et est appliquée indépendamment sur chaque coupe de la base d'images LGE-IRM.

Plusieurs expériences ont été menées en modifiant la taille des patches de caractéristiques. Ainsi, la meilleure précision de détection de pixels hyper-rehaussés est obtenue avec des patches ayant une dimension de $[3 \times 3]$.

L'approche de détection a été appliquée sur une population de 11 patients avec CMH sur des séquences LGE-IRM en inversion-récupération (IR) en vue petit axe. Pour chaque patient, les images traitées comprennent 16 images de coupes couvrant les plans apical, médial et basal. La méthode proposée a permis la détection de fibrose à l'intérieur du myocarde en utilisant les frontières endo- et épicaudiques tracées manuellement par un expert.

Notre méthode a été évaluée dans un premier temps par une évaluation visuelle confrontée à l'avis de l'expert, puis en comparant les résultats de la méthode proposée avec une méthode de la littérature : la méthode de classification du type C-moyenne floue proposée par (KACHENOURA et al., 2008). Les zones de fibrose ont été identifiées dans les deux méthodes, pour ces régions présentant une haute concentration de pixels avec rehaussement tardif. Notre méthode détecte la fibrose avec succès dans 9 des 11 patients. En revanche, des zones LGE sont mal classées chez deux patients en raison du contraste parfois faible entre le myocarde et l'intérieur de la cavité du

VG (MANTILLA et al., 2015d).

Nous proposons la localisation spatiale du myocarde fibrosé selon la représentation à 17 segments proposée par l'AHA. Pour réaliser cette représentation, le centroïde du VG est automatiquement calculé en utilisant le contour de l'endocarde et l'intersection antérieure entre les ventricules droit et gauche est manuellement placée par l'utilisateur pour une normalisation spatiale segmentaire selon la représentation AHA. Cette procédure permet l'identification de la fibrose par segment anatomique.

Les résultats obtenus sont en accord avec les observations dans (HOEY et al., 2014) dans lesquelles les zones LGE sont souvent identifiées dans le septum inter ventriculaire, et plus particulièrement dans les segments antéro-septal au niveau des coupes médiale et basale et dans les points d'intersection entre les ventricules droit et gauche.

Les perspectives de cette étude incluent les aspects suivants :

La performance de classification de mouvement pariétal du VG pourrait être améliorée par un placement manuel du point de repère anatomique entre le VG et le ventricule droit (VD). En outre, la précision dans la quantification de la mesure transmurale de fibrose associée à des segments anatomiques du VG pourrait être améliorée, puisqu'elle dépend de la décomposition AHA et ainsi de la localisation de l'intersection antérieure du VD et du VG.

Nous avons exécuté une classification binaire entre le mouvement normal/anormal du VG basé sur les représentations spatio-temporelles extraites des segments anatomiques. Cette classification pourrait être étendue à une classification plus précise du mouvement dans une des quatre classes de mouvement pariétal du VG : normale, hypokinétique, akinétique et dyskinétique.

D'autres paramètres discriminants pour l'asynchronisme cardiaque pourraient être également incorporés comme des atomes d'entrée dans les méthodes de classification basées sur l'apprentissage de dictionnaires. Ces paramètres peuvent inclure des informations d'indices fonctionnels globaux comme des courbes de temps-volume, la fraction d'éjection, le débit cardiaque, le volume d'éjection systolique ainsi que des paramètres fonctionnels régionaux, comme l'épaississement du myocarde et des délais mécaniques.

Les perspectives de ce travail concernent également une validation étendue en utilisant plus de patients, que ce soit dans le cadre de la caractérisation du mouvement en IC ou de la détection de fibrose en CMH. Elle pourrait être également étendue pour une classification plus précise selon des sous-groupes dans les pathologies étudiées, comme la classification de patients répondeurs ou non-répondeurs dans le contexte de la CRT. Elle pourrait être enfin appliquée à la caractérisation d'autres pathologies cardiaques et analysées à partir de différentes modalités d'imagerie.

Références

- ADABAG, A. S., B. J. MARON, E. APPELBAUM, C. J. HARRIGAN, J. L. BUROS, C. M. GIBSON, J. R. LESSER, C. A. HANNA, J. E. UDELSON, W. J. MANNING et M. S. MARON (2008). « Occurrence and frequency of arrhythmias in hypertrophic cardiomyopathy in relation to

- delayed enhancement on cardiovascular magnetic resonance ». In : *Journal of the American College of Cardiology* 51.14, p. 1369–1374.
- AHARON, M., M. ELAD et A. BRUCKSTEIN (2006). « K-SVD: An Algorithm for Designing Overcomplete Dictionaries for Sparse Representation ». In : *IEEE Transactions on Signal Processing* 54.11, p. 4311–4322.
- AMADO, L. C., B. L. GERBER, S. N. GUPTA, D. W. RETTMANN, G. SZARF, R. SCHOCK, K. NASIR, D. L. KRAITCHMAN et J. A. C. LIMA (2004). « Accurate and objective infarct sizing by contrast-enhanced magnetic resonance imaging in a canine myocardial infarction model ». In : *Journal of the American College of Cardiology* 44.12, p. 2383–2389.
- BECKER, M., E. BILKE, H. KUHL, M. KATOH, R. KRAMANN, A. FRANKE, A. BUCKER, P. HANRATH et R. HOFFMANN (2006). « Analysis of myocardial deformation based on pixel tracking in two dimensional echocardiographic images enables quantitative assessment of regional left ventricular function ». In : *Heart* 92.8, p. 1102–1108.
- CERQUEIRA, M. D., N. J. WEISSMAN, V. DILSIZIAN, A. K. JACOBS, S. KAUL, W. K. LASKEY, D. J. PENNELL, J. A. RUMBERGER, T. RYAN, M. S. VERANI et AMERICAN HEART ASSOCIATION WRITING GROUP ON MYOCARDIAL SEGMENTATION AND REGISTRATION FOR CARDIAC IMAGING (2002). « Standardized Myocardial Segmentation and Nomenclature for Tomographic Imaging of the Heart: A Statement for Healthcare Professionals from the Cardiac Imaging Committee of the Council on Clinical Cardiology of the American Heart Association ». In : *Circulation* 105.4, p. 539–542.
- CHAPELLE, O., V. VAPNIK, O. BOUSQUET et S. MUKHERJEE (2002). « Choosing Multiple Parameters for Support Vector Machines ». In : *Machine Learning* 46.1-3, p. 131–159.
- ELAD, M. et M. AHARON (2006). « Image Denoising Via Sparse and Redundant Representations Over Learned Dictionaries ». In : *IEEE Transactions on Image Processing* 15.12, p. 3736–3745.
- FENSTER, A., D. B. DOWNEY et H. N. CARDINAL (2001). « Three-dimensional ultrasound imaging ». In : *Physics in Medicine and Biology* 46.5, R67–99.
- GARCIA-FERNANDEZ, M. A., J. BERMEJO, E. PEREZ-DAVID, T. LOPEZ-FERNANDEZ, M. J. LEDESMA, P. CASO, N. MALPICA, A. SANTOS, M. MORENO et M. DESCO (2003). « New techniques for the assessment of regional left ventricular wall motion ». In : *Echocardiography (Mount Kisco, N.Y.)* 20.7, p. 659–672.
- GERBER, B. L., J. GAROT, D. A. BLUEMKE, K. C. WU et J. A. C. LIMA (2002). « Accuracy of Contrast-Enhanced Magnetic Resonance Imaging in Predicting Improvement of Regional Myocardial Function in Patients After Acute Myocardial Infarction ». In : *Circulation* 106.9, p. 1083–1089.
- GORCSAN, J. et H. TANAKA (2011). « Echocardiographic assessment of myocardial strain ». In : *Journal of the American College of Cardiology* 58.14, p. 1401–1413.
- HOEY, E. T., M. ELASSALY, A. GANESHAN, R. W. WATKIN et H. SIMPSON (2014). « The role of magnetic resonance imaging in hypertrophic cardiomyopathy ». In : *Quantitative Imaging in Medicine and Surgery* 4.5, p. 397–406.

- HSU, L.-Y., A. NATANZON, P. KELLMAN, G. A. HIRSCH, A. H. ALETRAS et A. E. ARAI (2006). « Quantitative myocardial infarction on delayed enhancement MRI. Part I: Animal validation of an automated feature analysis and combined thresholding infarct sizing algorithm ». In : *Journal of magnetic resonance imaging: JMRI* 23.3, p. 298–308.
- JIANG, Z., Z. LIN et L. S. DAVIS (2013). « Label Consistent K-SVD: Learning a Discriminative Dictionary for Recognition ». In : *IEEE Transactions on Pattern Analysis and Machine Intelligence* 35.11, p. 2651–2664.
- KACHENOURA, N., A. REDHEUIL, D. BALVAY, C. RUIZ-DOMINGUEZ, A. HERMENT, E. MOUSSEAUX et F. FROUIN (2007). « Evaluation of regional myocardial function using automated wall motion analysis of cine MR images: Contribution of parametric images, contraction times, and radial velocities. » In : *J Magn Reson Imaging* 26.4, p. 1127–1132.
- KACHENOURA, N., A. REDHEUIL, A. HERMENT, E. MOUSSEAUX et F. FROUIN (2008). « Robust assessment of the transmural extent of myocardial infarction in late gadolinium-enhanced MRI studies using appropriate angular and circumferential subdivision of the myocardium ». In : *European Radiology* 18.10, p. 2140–2147.
- KIM, R., E. WU, A. RAFAEL, E. CHEN, M. PARKER, O. SIMONETTI, F. KLOCKE, R. BONOW et R. JUDD (2000). « The Use of Contrast-Enhanced Magnetic Resonance Imaging to Identify Reversible Myocardial Dysfunction ». In : *New England Journal of Medicine* 343.20, p. 1445–1453.
- KIRSCHBAUM, S., P. DE FEYTER et R. VAN GEUNS (2011). « Cardiac magnetic resonance imaging in stable ischaemic heart disease. » In : *Neth Heart J* 19.5, p. 229–35.
- KOLIPAKA, A., G. P. CHATZIMAVROUDIS, R. D. WHITE, T. P. O'DONNELL et R. M. SETSER (2005). « Segmentation of non-viable myocardium in delayed enhancement magnetic resonance images ». In : *The International Journal of Cardiovascular Imaging* 21.2-3, p. 303–311.
- LI, Y. et A. NGOM (2013). « Sparse representation approaches for the classification of high-dimensional biological data ». In : *BMC Systems Biology* 7.Suppl 4, S6.
- MAFFESENTI, F., H.-J. NESSER, L. WEINERT, R. STERINGER-MASCHERBAUER, J. NIEL, W. GORISSEN, L. SUGENG, R. M. LANG et V. MOR-AVI (2009). « Quantitative evaluation of regional left ventricular function using three-dimensional speckle tracking echocardiography in patients with and without heart disease ». In : *The American Journal of Cardiology* 104.12, p. 1755–1762.
- MANTILLA, J., M. GARREAU, J.-J. BELLANGER, C. LECLERCQ et J. PAREDES (2015a). « DL-based classification of LV wall motion in cardiac MRI with a parametric approach ». In : *Recherche en Imagerie et Technologies pour la Santé (RITS)*. (in press).
- MANTILLA, J., M. GARREAU, J.-J. BELLANGER et J. L. PAREDES (2015b). « Valoración del movimiento del ventriculo izquierdo en MRI cardiaca usando un enfoque parametrico y aprendizaje de diccionarios ». In : *V Congreso Venezolano de Bioingenieria*. (in press).
- MANTILLA, J., M. GARREAU, J.-J. BELLANGER et J. L. PAREDES (2013a). « Automated classification of LV regional wall motion based on spatio-temporal profiles from cardiac cine magnetic resonance imaging ». In : *Proc. SPIE*. T. 8922, pages.

- MANTILLA, J., M. GARREAU, J.-J. BELLANGER et J. L. PAREDES (2013b). « Machine Learning Techniques for LV Wall Motion Classification Based on Spatio-temporal Profiles from Cardiac Cine MRI ». In : *IEEE Machine Learning and Applications (ICMLA), 2013 12th International Conference on*. T. 1, p. 167–172.
- (2015c). « SVM-based classification of LV wall motion in cardiac MRI with the assessment of STE ». In : *Proc. SPIE 9287, 10th International Symposium on Medical Information Processing and Analysis*. T. 9287, pages.
- MANTILLA, J., J. L. PAREDES, J.-J. BELLANGER, J. BETANCUR, F. SCHNELL, C. LECLERCQ et M. GARREAU (2015d). « Detection of fibrosis in LGE-cardiac MRI using Kernel DL-based clustering ». In : *Computing in Cardiology*. (in press).
- MANTILLA, J., J. PAREDES, J.-J. BELLANGER, E. DONAL, C. LECLERCQ, R. MEDINA et M. GARREAU (2015e). « Classification of LV wall motion in cardiac MRI using kernel Dictionary Learning with a parametric approach ». In : *37th Annual International Conference of the IEEE Engineering in Medicine and Biology Society (EMBS)*. (in press), p. 7292–7295.
- MARON, M., E. APPELBAUM, C. HARRIGAN, J. BUROS, C. GIBSON, C. HANNA, J. LESSER, J. UDELSON, W. MANNING et B. MARON (2008). « Clinical profile and significance of delayed enhancement in hypertrophic cardiomyopathy ». In : *Circulation. Heart Failure* 1.3, p. 184–191.
- MEMBERS, W. C., B. J. GERSH, B. MARON, R. O. BONOW, J. A. DEARANI, M. A. FIFER, M. S. LINK, S. S. NAIDU, R. A. NISHIMURA, S. R. OMMEN, H. RAKOWSKI, C. E. SEIDMAN, J. A. TOWBIN, J. E. UDELSON et C. W. YANCY (2011). « 2011 ACCF/AHA Guideline for the Diagnosis and Treatment of Hypertrophic Cardiomyopathy A Report of the American College of Cardiology Foundation/American Heart Association Task Force on Practice Guidelines ». In : *Circulation* 124.24, e783–e831.
- MEWTON, N., C. Y. LIU, P. CROISILLE, D. BLUEMKE et J. A. C. LIMA (2011). « Assessment of myocardial fibrosis with cardiovascular magnetic resonance ». In : *Journal of the American College of Cardiology* 57.8, p. 891–903.
- MISITI, M., Y. MISITI, G. OPPENHEIM et J.-M. POGGI (2007). « Clustering Signals Using Wavelets ». In : *Computational and Ambient Intelligence*. Sous la dir. de F. SANDOVAL, A. PRIETO, J. CABESTANY et M. GRAÑA. Lecture Notes in Computer Science 4507. Springer Berlin Heidelberg, p. 514–521.
- MOON, J. C. C., E. REED, M. N. SHEPPARD, A. G. ELKINGTON, S. Y. HO, M. BURKE, M. PETROU et D. J. PENNELL (2004). « The histologic basis of late gadolinium enhancement cardiovascular magnetic resonance in hypertrophic cardiomyopathy ». In : *Journal of the American College of Cardiology* 43.12, p. 2260–2264.
- ORDOVAS, K. G. et C. B. HIGGINS (2011). « Delayed Contrast Enhancement on MR Images of Myocardium: Past, Present, Future ». In : *Radiology* 261.2, p. 358–374.
- PUNITHAKUMAR, K., I. AYED, A. ISLAM, I. ROSS et S. LI (2010). « Regional Heart Motion Abnormality Detection via Information Measures and Unscented Kalman Filtering ». In : *Medical Image Computing and Computer-Assisted Intervention – MICCAI 2010*. Sous la dir.

- de T. JIANG, N. NAVAB, J. PLUIM et M. VIERGEVER. T. 6361. Lecture Notes in Computer Science. Springer Berlin Heidelberg, p. 409–417.
- RADAU, P., Y. LU, K. CONNELLY, G. PAUL, A. DICK et G. WRIGHT (2009). « Evaluation Framework for Algorithms Segmenting Short Axis Cardiac MRI. » In : *The MIDAS Journal - Cardiac MR Left Ventricle Segmentation Challenge*.
- RUBINSTEIN, R., M. ZIBULEVSKY et M. ELAD (2010). « Double Sparsity: Learning Sparse Dictionaries for Sparse Signal Approximation ». In : *Signal Processing, IEEE Transactions on* 58.3, p. 1553–1564.
- SCHUIJF, J. D., T. A. M. KAANDORP, H. J. LAMB, R. J. v. D. GEEST, E. P. VIERGEVER, E. E. v. D. WALL, A. DE ROOS et J. J. BAX (2004). « Quantification of myocardial infarct size and transmuralty by contrast-enhanced magnetic resonance imaging in men ». In : *The American Journal of Cardiology* 94.3, p. 284–288.
- SUINESIAPUTRA, A., A. F. FRANGI, T. A. M. KAANDORP, H. J. LAMB, J. J. BAX, J. H. C. REIBER et B. P. F. LELIEVELDT (2009). « Automated Detection of Regional Wall Motion Abnormalities Based on a Statistical Model Applied to Multi-Slice Short-Axis Cardiac MR Images. » In : *IEEE Transactions on Medical Imaging* 4.28, p. 595–607.
- TANABE, M., B. LAMIA, H. TANAKA, D. SCHWARTZMAN, M. R. PINSKY et J. GORCSAN III (2008). « Echocardiographic Speckle Tracking Radial Strain Imaging to Assess Ventricular Dyssynchrony in a Pacing Model of Resynchronization Therapy ». In : *Journal of the American Society of Echocardiography* 21.12, p. 1382–1388.
- TOBON-GOMEZ, C., M. DE CRAENE, K. MCLEOD, L. TAUTZ, W. SHI, A. HENNEMUTH, A. PRAKOSA, H. WANG, G. CARR-WHITE, S. KAPETANAKIS, A. LUTZ, V. RASCHE, T. SCHAEFFTER, C. BUTAKOFF, O. FRIMAN, T. MANSI, M. SERMESANT, X. ZHUANG, S. OURSELIN, H.-O. PEITGEN, X. PENNEC, R. RAZAVI, D. RUECKERT, A. F. FRANGI et K. S. RHODE (2013). « Benchmarking framework for myocardial tracking and deformation algorithms: An open access database ». In : *Medical Image Analysis* 17.6, p. 632–648.
- WHO (2014). *Global status report on noncommunicable diseases 2014*. World Health Organization.
- WRIGHT, J., Y. MA, J. MAIRAL, G. SAPIRO, T. HUANG et S. YAN (2010). « Sparse Representation for Computer Vision and Pattern Recognition ». In : *Proceedings of the IEEE* 98.6, p. 1031–1044.
- WRIGHT, J., A. YANG, A. GANESH, S. SASTRY et Y. MA (2009). « Robust Face Recognition via Sparse Representation ». In : *IEEE Transactions on Pattern Analysis and Machine Intelligence* 31.2, p. 210–227.
- YANCY, C. W., M. JESSUP, B. BOZKURT, J. BUTLER, D. E. CASEY, M. H. DRAZNER, G. C. FONAROW, S. A. GERACI, T. HORWICH, J. L. JANUZZI, M. R. JOHNSON, E. K. KASPER, W. C. LEVY, F. A. MASOUDI, P. E. MCBRIDE, J. J. V. MCMURRAY, J. E. MITCHELL, P. N. PETERSON, B. RIEGEL, F. SAM, L. W. STEVENSON, W. H. W. TANG, E. J. TSAI et B. L. WILKOFF (2013). « 2013 ACCF/AHA Guideline for the Management of Heart Failure A Report of the American College of Cardiology Foundation/American Heart Association Task Force on Practice Guidelines ». In : *Circulation* 128.16, e240–e327.

YANG, M., L. ZHANG, X. FENG et D. ZHANG (2014). « Sparse Representation Based Fisher Discrimination Dictionary Learning for Image Classification ». In : *International Journal of Computer Vision* 109.3, p. 209–232.

Contents

Abstract	v
Références	xvii
Contents	xxiii
1 Introduction	1
References	4
2 Sparse representation of signals in overcomplete dictionaries	7
2.1 Introduction	7
2.2 The sparse representation problem	8
2.3 Optimization techniques for solving sparse approximation problems	10
2.3.1 Greedy pursuit methods	10
2.3.1.1 Orthogonal Matching Pursuit (OMP) algorithm	11
2.3.2 Convex relaxation methods	13
2.3.3 Bayesian methods	13
2.3.4 Non-convex optimization methods	14
2.3.5 Other methods	15
2.4 Design of the dictionary	15
2.4.1 Standard overcomplete basis	16
2.4.1.1 The Fast Fourier Transform (FFT)	16
2.4.1.2 Wavelets	17
2.4.1.3 Curvelets	19
2.4.2 Dictionary Learning (DL)	19
2.4.2.1 Probabilistic methods	20
2.4.2.2 Clustering-based methods	22
2.4.2.3 Parametric training methods	23
2.5 Applications of the sparse representation	24
2.5.1 Image super-resolution	24
2.5.2 Image inpainting	26
2.5.3 Image Denoising	26
2.5.4 Signal Separation	27

2.5.5	Clustering and Image classification	27
2.6	DL-based classification methods	28
2.6.1	Discriminative DL	30
2.6.1.1	Label consistent K-SVD (LC-KSVD)	32
2.6.1.2	Fisher Discriminant DL (FD-DL)	33
2.6.2	Kernel-based DL for classification	35
2.7	Support Vector Machines (SVM)-based classification	36
2.8	Conclusion	38
	References	39
3	Sparse representation in Medical Imaging: State-of-the-art	45
3.1	Introduction	45
3.2	Related work	45
3.2.1	Image reconstruction	45
3.2.2	Image denoising	46
3.2.3	Image Fusion	47
3.2.4	Image Segmentation	48
3.2.5	Multimodal images analysis	50
3.2.6	Classification	51
3.2.7	Other applications	53
3.3	Conclusions	53
	References	54
4	Feature extraction and Dictionary Learning for the Assessment of LV wall motion in cardiac MRI	59
4.1	Introduction	59
4.2	The Cardiovascular system	60
4.2.1	Heart anatomy	60
4.2.2	Electrical function	62
4.2.3	Mechanical function	63
4.3	Cardiac Pathologies: Heart Failure	67
4.4	Imaging of the Cardiovascular System	70
4.4.1	Cardiac Magnetic Resonance Imaging (cMRI)	71
4.4.2	Echocardiography (US)	72
4.5	The assessment of cardiac Left Ventricular (LV) function in cardiac cine-MRI: a brief state-of-the-art	76
4.5.1	Methods based on shape statistics	77
4.5.2	Methods based on image features extraction	79
4.5.3	Methods based on parametric imaging-based quantification	80
4.6	The proposed method	81
4.6.1	Overall scheme	82

4.6.2	Pre-processing stage	85
4.6.2.1	ROI extraction	85
4.6.2.2	Spatial normalization according to American Heart Association 17-Segment Model (AHA)	86
4.6.3	Feature extraction stage	86
4.6.3.1	Extraction of Diametral Spatio-temporal profiles	87
4.6.3.2	Extraction of Radial Spatio-temporal profiles	91
4.6.3.3	Extraction of parameters from radial Spatio-temporal profiles	93
4.6.4	Dictionary Learning-based classification	98
4.7	Conclusion	102
	References	103

5	Dictionary Learning for LV wall motion classification based on Spatio-temporal profiles: Experiments and Results	109
5.1	Introduction	109
5.2	Study population	109
5.2.1	Patient data	110
5.2.1.1	Image Data	111
5.2.2	Control Subjects	111
5.3	Evaluation protocol	112
5.3.1	2D-STE Radial strain assessment for local evaluation	115
5.3.2	Selection of correct number of profiles	120
5.3.3	Performance measures	120
5.3.4	Parameter selection of the machine learning techniques	122
5.4	Global non-parametric multi-slice evaluation	122
5.4.1	Experiments with SVM	123
5.4.2	Experiments with discriminative Dictionary Learning methods	128
5.4.2.1	Results with LC-KSVD algorithms	128
5.4.2.2	Results with the FD-DL algorithm	131
5.4.3	Comparison of algorithms	132
5.5	Global non-parametric LV mid-cavity evaluation	133
5.5.1	Results using diametral Spatio-temporal profiles	135
5.5.1.1	Experiments with SVM: Leave-one-out LOO cross validation	135
5.5.1.2	Experiments with SVM and DL: Random sub-sampling cross validation	136
5.5.2	Results using radial spatio-temporal profiles	137
5.5.2.1	Experiments with SVM: Leave-one-out LOO cross validation	137
5.5.2.2	Experiments with SVM and DL: Random sub-sampling cross validation	138
5.5.3	Comparison of algorithms	139

5.6	Local non-parametric LV mid-cavity evaluation	139
5.6.1	Experiments with SVM: Leave One Out LOO cross validation	141
5.6.2	Experiments with SVM and DL: Random sub-sampling cross validation	142
5.6.3	Comparison of algorithms	145
5.7	Local parametric LV mid-cavity evaluation	148
5.7.1	Parameter analysis	149
5.7.1.1	Average clustered curve (Cl)	149
5.7.1.2	Mean transition time (Mt)	149
5.7.1.3	Skewness parameter (Sk)	150
5.7.1.4	Cross Correlation parameter (Co)	151
5.7.2	Experiments with SVM, LC-KSVD and KSRDL	151
5.8	Discussion	154
5.9	Limitations	157
5.10	Conclusion	159
	References	160
6	Dictionary Learning-based Classification for Fibrosis detection in cardiac MRI	165
6.1	Introduction	165
6.2	Hypertrophic cardiomyopathy and Fibrosis	165
6.2.1	Myocardial Fibrosis in HCM	167
6.3	Cardiac magnetic resonance imaging with Late gadolinium enhancement (LGE)-MRI	169
6.4	The assessment of cardiac fibrosis detection in LGE-MRI: A brief state-of-the-art	170
6.5	The proposed method	173
6.5.1	Feature extraction	173
6.5.2	Clustering	175
6.5.3	DL-based classification: training stage	176
6.5.4	DL-based classification: testing stage	176
6.6	First experiments and results	177
6.6.1	Study population	177
6.6.1.1	Patient selection	177
6.6.1.2	Cardiac magnetic resonance imaging	177
6.6.2	Results	178
6.6.3	Evaluation	179
6.7	Qualification and Quantification of myocardial Fibrosis: A first proposal	181
6.8	Conclusion	185
	References	186
7	Conclusion and Perspectives	191
	References	196

A List of associated publications	197
A.1 International journals	197
A.2 International conferences	197
A.3 National conferences	198
List of Figures	199
List of Tables	203

List of Symbols or abbreviations

AHA	American Heart Association
ARVCM	Arrhythmogenic right ventricular cardiomyopathy
AV	Atrio-ventricular
BP	Basis Pursuit
CAP	Cardiac Atlas Project
CHF	Congestive Heart Failure
CIC-IT	Centre d'Investigation Clinique Innovation Technologique
Cl	Average clustered curve
CM	Cardiomyopathies
CMRI	Cardiac magnetic resonance imaging
Co	Cross Correlation parameter
CoSaMP	Compressive Sampling Matched Pursuit
CRT	Cardiac resynchronization therapy
CS	Compressive Sensing
CT	Computed Tomography
CVDs	Cardiovascular Diseases
D-KSVD	Discriminative K-SVD algorithm
DL	Dictionary Learning
DCM	Dilated cardiomyopathy DCM
DCT	Discrete Cosine Transform
DE-CMRI	Delayed enhanced CMRI
DFT	Discrete version of the Fourier transform
DLSI	Dictionary learning with structure incoherence
DTI	Diffusion tensor imaging
DWT	Discrete Wavelet transform
ECG	Electrocardiogram
EF	Ejection Fraction
EM	Expectation-maximisation
euHeart	Personalised and Integrated Cardiac Care, FP7/2008-2012 project
FDDL	Fisher Discriminant DL algorithm
FFT	Fast Fourier Transform

FOCUSS	Focal Underdetermined System Solver
FTSICs	Fitted Time-Signal Intensity curves
FWHM	Full-width-at-half-maximum
HCM	Hypertrophic cardiomyopathy
HF	Heart failure
ICA	Independent Component Analysis
IHT	Iterative hard thresholding
IMOP	French project "Utility of medical imaging for the optimization of the implantation of implantable cardiac devices"
IR-CMR	Inversion recovery CMR
K-NN	K -Nearest Neighbor
KSR	Sparse representation with kernels
KSRC	Kernel Sparse representation based classification
KSRDL	Kernel Sparse Representation DL
LA	Left atrium
LAX	Long-axis-view
LBBB	Left bundle branch block
LC-KSVD	Label Consistent K-SVD algorithm
LDA	Linear Discriminant Analysis
LDCT	Low-dose CT
LGE	Late gadolinium enhancement
LV	Left Ventricle
LVEDV	LV End Diastolic Volume
LVEF	LV Ejection Fraction
LVESV	LV End Systolic Volume
MAP	Maximum a posteriori probability
MCA	Morphological Component Analysis
MCP	Multiple clusters pursuit
ML	Maximum likelihood
MOD	Method of optimal directions
MP	Matching Pursuit
MRI	Magnetic resonance imaging
mSRC	Multimodal sparse representation-based classification
Mt	Mean transition time parameter
NNQP	Non negative Quadratic Problem
NP-hard	Non-deterministic Polynomial-time hard
NYHA	New York Heart Association
ODL.	Online Dictionary Learning
OMP	Orthogonal Matching Pursuit
PCA	Principal Component Analysis

PD	Proton Density
PET	Positron emission tomography
PSIR-CMR	Phase sensitive inversion recovery CMR
RA	Right atrium
RBF	Radial basis function
RCM	Restrictive cardiomyopathy
RDCs	Radial displacement curves
RIP	Restricted Isometry Property
ROI	Region of interest
ROMP	Regularized Orthogonal Matching Pursuit
RV	Right ventricle
SA	Sinoatrial node
SAX	Short-axis-view
SBL	Sparse Bayesian Learning Model
SD	Standard deviation
SDCT	Standard-dose CT
SDE	Shannon's differential entropy
Sk	Skewness parameter
SOMP	Simultaneous orthogonal matching pursuit
SP	Subspace pursuit
SPM	Spatial pyramid matching
SR	Super-resolution
SRC	Sparse Representation Classification
SSFP	Steady-State Free Precession
STE	Speckle Tracking Echocardiography
StOMP	Stagewise Orthogonal Matching Pursuit
SV	Stroke volume
SVD	Singular-Value-Decomposition
SVM	Support Vector Machines
T1	Longitudinal relaxation time
T2	Transverse relaxation time
TDI	Tissue Doppler imaging
TI	Time of inversion
TSICs	Time-signal intensity curves
TTE-US	Transthoracic echocardiographic
TV	Total Variation
US	Ultrasound
VWMS	Visual wall motion scores
WT	Wall thickening



Introduction

Dictionary Learning (DL) is a recent approach that aims at using machine learning techniques to infer a dictionary from a set of input signals. A given signal can be well approximated only with a linear combination of a few atoms in the dictionary. DL methods are originally designed to learn a dictionary which can faithfully represent signals. In the context of image processing, image representation, denoising and reconstruction are considered as the most popular goals by this discipline besides classification tasks that are starting to be addressed under the DL framework. We search the benefits of using dictionaries, directly learned from a set of training medical images, that better capture the distribution of the data and later, can be useful in tasks such as classification and detection. In this study, we address the use of sparse representation and DL in order to get insights about the diseased heart in the context of Cardiovascular Diseases (CVDs). Specifically, our work focuses on 1) assessment of LV wall motion in patients with heart failure (HF) and 2) fibrosis detection in patients with hypertrophic cardiomyopathy (HCM); both pathologies are studied in cardiac magnetic resonance imaging (MRI).

By 2010, CVDs caused 223 deaths per 100 thousand individuals in France (about 27% of total deceases), being the first cause of decease in the country for women and the second for men. CVDs mortality in the world is very similar: 17.3 million people died from CVDs in 2008, representing 30% of all global deaths that year, according to the World Health Organization (WHO, 2014). CVDs affects the heart, the blood vessels or both. Most frequent pathologies are: Ischemia, Coronary Artery Disease, Cardiomyopathy and Heart Failure (HF).

The first pathology addressed in this study is HF which is a complex clinical syndrome that results from any structural or functional impairment of ventricular filling or ejection of blood (YANCY et al., 2013). The clinical syndrome of HF may result from disorders of the pericardium, myocardium, endocardium, heart valves, or great vessels or from certain metabolic abnormalities, but most patients with HF have symptoms due to impaired left ventricular (LV) myocardial function. Clinically, HF has a poor prognosis and its early stage diagnosis can play an essential role for physicians in planning the therapy or interventional gesture and the stages of the treatment. A common alteration of the normal LV function in patients with HF is the

intra-ventricular dyssynchrony which occurs when regions of the ventricle contract at different times. Abnormal local LV wall motion is an early finding in a lot of cardiac pathologies and its diagnosis is of critical importance (GARCIA-FERNANDEZ et al., 2003).

Cardiac Magnetic Resonance Imaging (MRI) is currently used in medical imaging for the assessment of LV function (KIRSCHBAUM et al., 2011). This modality allows obtaining different parameters, that characterize the ventricular function and can be classified in global parameters and local parameters associated to anatomical segments of the LV, following the American Heart Association (AHA) 17 model representation (CERQUEIRA et al., 2002). Global analysis of the cardiac dynamic in cine-MRI is also most often focused on two particular phases of the cardiac cycle: end-diastole and end-systole.

Current techniques for the LV wall motion assessment typically include a preprocessing step, followed by a segmentation of the LV endocardial and epicardial boundaries, a feature extraction and classification or motion estimation. In the context of classification, some of the approaches in the literature need the segmentation of the LV cavity and require important user interaction or semi-/fully automatic delineation to define myocardial boundaries and then extract features in order to train the respective classifier.

Some successful applications in medical imaging (MRI, Computed Tomography, Echocardiography and microscopy images) have been explored for image reconstruction, image denoising, image fusion, image segmentation, multimodal images enhancement and classification based on sparse representation and DL approaches. To the best of our knowledge, classification of LV wall motion based on discriminative DL in cardiac MRI has not been previously reported.

Our contribution in the context of patients with HF is related to the assessment of LV motion in cardiac cine MRI in short-axis view. Firstly, we propose a feature extraction method that exploits the partial information obtained from all temporal cardiac phases and anatomical segments in a spatio-temporal representation which we call spatio-temporal profiles from cine-MRI sequences. Three novel representations are proposed: i) diametral spatio-temporal profiles, ii) radial spatio-temporal profiles, and iii) time signal intensity curve parameters extracted from the radial profiles. The proposed representations exploit information of the LV wall motion without segmentation needs and inherently dispose discriminatory information that could help in the detection and characterization of LV cardiac function abnormalities. Secondly, based on these three new types of representation, three respective approaches based on Dictionary Learning are proposed for LV wall motion classification. In each case, the proposed representations are taken as input atoms for the training of DL approaches to provide a classification of local normal/abnormal LV wall motion. We propose two levels of evaluation, a first one where the global status of the subject (normal/pathologic) is used as ground truth to label the proposed spatio-temporal representations, and a second one where local strain information obtained from 2D Speckle Tracking Echocardiography (STE), is taken as ground truth to label the proposed features, where a profile is classified as normal or abnormal (akinetic or hypokinetic cases) allowing thus to identify a particular segment of the LV that has a local normal or abnormal wall motion.

The second pathology addressed in this study is Hypertrophic Cardiomyopathy (HCM) that belongs to the broad class of Cardiomyopathies (CM), meaning literally the diseases of cardiac muscle, which are an heterogeneous group of myocardial diseases. HCM occurs if heart muscle cells enlarge and cause the walls of the ventricles (usually the left ventricle) to thicken. Despite this thickening, the ventricle size often remains normal but the thickening may block blood flow out of the ventricle. Cardiac magnetic resonance is the new gold standard to measure myocardial wall thickness and to diagnose HCM (MEMBERS et al., 2011). Also, it is used to characterize myocardial tissue enabling to quantify the fibrosis/scar extension (MOON et al., 2004) that is often present in HCM. It is now documented that approximately half of patients with HCM have late gadolinium enhancement (LGE) suggestive of areas of fibrosis (MARON et al., 2008).

Several studies have shown the relevance of LGE in cardiac MRI in the location and the assessment of myocardial fibrosis (ORDOVAS et al., 2011). The accurate estimation of the transmural extent of the hyper-enhanced regions is crucial to estimate for example functional myocardial recovery after reperfusion therapy. Also, the degree of improvement in global wall-motion and ejection fraction is significantly related to the transmural extent of LGE. At the clinical level, infarct size is an independent prognostic factor for heart failure, arrhythmic events and cardiac mortality (MEWTON et al., 2011). Patterns of fibrosis may be also used to differentiate HCM from secondary causes of LV hypertrophy such as aortic stenosis or severe hypertension (RUDOLPH et al., 2009).

An automated scoring of infarct extent begins with the detection of the infarct on the images. Several methods based on the tuning of thresholds with manual interaction of the user (AMADO et al., 2004; GERBER et al., 2002; KIM et al., 2000; SCHUIJF et al., 2004) or automated definition of the infarcted zones using morphological operators (HSU et al., 2006; KOLIPAKA et al., 2005) have been developed to this end. To the best of our knowledge, fibrosis detection based on DL in LGE cardiac MRI has not been previously reported.

In the context of Hypertrophic cardiomyopathy (HCM), we address the problem of fibrosis detection in Late Gadolinium Enhanced LGE-Short axis (SAX) images by using a sparse-based clustering approach and DL. In this framework, features extracted from LGE-SAX images are taken as input atoms in order to train a classifier based on the sparse codes obtained with a DL approach. Firstly, an initial dictionary is constructed with learning samples from 2 clusters (LGE and Non-LGE regions). Secondly, the sparse coefficients of the learning data are computed and then used to train a K -Nearest Neighbor (K -NN) classifier. Finally, the label (LGE/Non-LGE) of a test patch is obtained with its respective sparse coefficients obtained over the learned dictionary and using the trained K -NN classifier. A subsequent post-processing step allows the spatial localization of fibrosis that is represented according to the American Heart Association (AHA) 17-segment model.

This work was conducted as part of two existing clinical protocols in national and international research projects where LTSI was either responsible: the French project «Utility of medical imaging for the optimization of the implantation of implantable cardiac devices» (IMOP) or participated: the European project « European Community's Seventh Framework Programme »

(euHeart). This study was also performed in collaboration with the CIC-IT (Centre d'Investigation Clinique Innovation Technologique) 804 and approved by the ethics committee of the CHU-Pontchaillou in Rennes.

This document is composed of three main parts: The first part provides a background for this study. It is composed on two chapters presenting: a brief state-of-art of different aspects in Sparse representation of signals in overcomplete dictionaries (Chapter 2) and Sparse representation in Medical Images (Chapter 3), respectively. The second part represents the main contribution of this thesis. It covers the assessment of LV wall motion in cardiac cine-Magnetic Resonance Imaging (MRI) by using DL-based classification approaches and is divided in two Chapters presenting: 1) the novel feature representation approach for LV wall motion classification based on dynamic images and the DL-based proposed approaches; (Chapter 4) and 2) the experimental part and the evaluation by combining the proposed representations with dictionary learning (DL) techniques to classify local normal/abnormal left ventricle wall motion (Chapter 5). Last part presents a second contribution of this thesis. It involves the detection of fibrosis in LGE-SAX MRI using a sparse-based clustering approach and DL (Chapter 6). Finally, Chapter 7 presents concluding remarks and perspectives.

References

- AMADO, L. C., B. L. GERBER, S. N. GUPTA, D. W. RETTMANN, G. SZARF, R. SCHOCK, K. NASIR, D. L. KRAITCHMAN, and J. A. C. LIMA (2004). "Accurate and objective infarct sizing by contrast-enhanced magnetic resonance imaging in a canine myocardial infarction model". In: *Journal of the American College of Cardiology* 44.12, pp. 2383–2389.
- CERQUEIRA, M. D., N. J. WEISSMAN, V. DILSIZIAN, A. K. JACOBS, S. KAUL, W. K. LASKEY, D. J. PENNELL, J. A. RUMBERGER, T. RYAN, M. S. VERANI, and AMERICAN HEART ASSOCIATION WRITING GROUP ON MYOCARDIAL SEGMENTATION AND REGISTRATION FOR CARDIAC IMAGING (2002). "Standardized Myocardial Segmentation and Nomenclature for Tomographic Imaging of the Heart: A Statement for Healthcare Professionals from the Cardiac Imaging Committee of the Council on Clinical Cardiology of the American Heart Association". In: *Circulation* 105.4, pp. 539–542.
- GARCIA-FERNANDEZ, M. A., J. BERMEJO, E. PEREZ-DAVID, T. LOPEZ-FERNANDEZ, M. J. LEDESMA, P. CASO, N. MALPICA, A. SANTOS, M. MORENO, and M. DESCO (2003). "New techniques for the assessment of regional left ventricular wall motion". In: *Echocardiography (Mount Kisco, N.Y.)* 20.7, pp. 659–672.
- GERBER, B. L., J. GAROT, D. A. BLUEMKE, K. C. WU, and J. A. C. LIMA (2002). "Accuracy of Contrast-Enhanced Magnetic Resonance Imaging in Predicting Improvement of Regional Myocardial Function in Patients After Acute Myocardial Infarction". In: *Circulation* 106.9, pp. 1083–1089.
- HSU, L.-Y., A. NATANZON, P. KELLMAN, G. A. HIRSCH, A. H. ALETRAS, and A. E. ARAI (2006). "Quantitative myocardial infarction on delayed enhancement MRI. Part I: Animal validation

- of an automated feature analysis and combined thresholding infarct sizing algorithm". In: *Journal of magnetic resonance imaging: JMRI* 23.3, pp. 298–308.
- KIM, R., E. WU, A. RAFAEL, E. CHEN, M. PARKER, O. SIMONETTI, F. KLOCKE, R. BONOW, and R. JUDD (2000). "The Use of Contrast-Enhanced Magnetic Resonance Imaging to Identify Reversible Myocardial Dysfunction". In: *New England Journal of Medicine* 343.20, pp. 1445–1453.
- KIRSCHBAUM, S., P. DE FEYTER, and R. VAN GEUNS (2011). "Cardiac magnetic resonance imaging in stable ischaemic heart disease." In: *Neth Heart J* 19.5, pp. 229–35.
- KOLIPAKA, A., G. P. CHATZIMAVROUDIS, R. D. WHITE, T. P. O'DONNELL, and R. M. SETSER (2005). "Segmentation of non-viable myocardium in delayed enhancement magnetic resonance images". In: *The International Journal of Cardiovascular Imaging* 21.2-3, pp. 303–311.
- MARON, M., E. APPELBAUM, C. HARRIGAN, J. BUROS, C. GIBSON, C. HANNA, J. LESSER, J. UDELSON, W. MANNING, and B. MARON (2008). "Clinical profile and significance of delayed enhancement in hypertrophic cardiomyopathy". In: *Circulation. Heart Failure* 1.3, pp. 184–191.
- MEMBERS, W. C., B. J. GERSH, B. MARON, R. O. BONOW, J. A. DEARANI, M. A. FIFER, M. S. LINK, S. S. NAIDU, R. A. NISHIMURA, S. R. OMMEN, H. RAKOWSKI, C. E. SEIDMAN, J. A. TOWBIN, J. E. UDELSON, and C. W. YANCY (2011). "2011 ACCF/AHA Guideline for the Diagnosis and Treatment of Hypertrophic Cardiomyopathy A Report of the American College of Cardiology Foundation/American Heart Association Task Force on Practice Guidelines". In: *Circulation* 124.24, e783–e831.
- MEWTON, N., C. Y. LIU, P. CROISILLE, D. BLUEMKE, and J. A. C. LIMA (2011). "Assessment of myocardial fibrosis with cardiovascular magnetic resonance". In: *Journal of the American College of Cardiology* 57.8, pp. 891–903.
- MOON, J. C. C., E. REED, M. N. SHEPPARD, A. G. ELKINGTON, S. Y. HO, M. BURKE, M. PETROU, and D. J. PENNELL (2004). "The histologic basis of late gadolinium enhancement cardiovascular magnetic resonance in hypertrophic cardiomyopathy". In: *Journal of the American College of Cardiology* 43.12, pp. 2260–2264.
- ORDOVAS, K. G. and C. B. HIGGINS (2011). "Delayed Contrast Enhancement on MR Images of Myocardium: Past, Present, Future". In: *Radiology* 261.2, pp. 358–374.
- RUDOLPH, A., H. ABDEL-ATY, S. BOHL, P. BOYÉ, A. ZAGROSEK, R. DIETZ, and J. SCHULZ-MENGER (2009). "Noninvasive detection of fibrosis applying contrast-enhanced cardiac magnetic resonance in different forms of left ventricular hypertrophy relation to remodeling". In: *Journal of the American College of Cardiology* 53.3, pp. 284–291.
- SCHULJF, J. D., T. A. M. KAANDORP, H. J. LAMB, R. J. V. D. GEEST, E. P. VIERGEVER, E. E. V. D. WALL, A. DE ROOS, and J. J. BAX (2004). "Quantification of myocardial infarct size and transmuralty by contrast-enhanced magnetic resonance imaging in men". In: *The American Journal of Cardiology* 94.3, pp. 284–288.
- WHO (2014). *Global status report on noncommunicable diseases 2014*. World Health Organization.

YANCY, C. W., M. JESSUP, B. BOZKURT, J. BUTLER, D. E. CASEY, M. H. DRAZNER, G. C. FONAROW, S. A. GERACI, T. HORWICH, J. L. JANUZZI, M. R. JOHNSON, E. K. KASPER, W. C. LEVY, F. A. MASOUDI, P. E. MCBRIDE, J. J. V. McMURRAY, J. E. MITCHELL, P. N. PETERSON, B. RIEGEL, F. SAM, L. W. STEVENSON, W. H. W. TANG, E. J. TSAI, and B. L. WILKOFF (2013). “2013 ACCF/AHA Guideline for the Management of Heart Failure A Report of the American College of Cardiology Foundation/American Heart Association Task Force on Practice Guidelines”. In: *Circulation* 128.16, e240–e327.

Sparse representation of signals in overcomplete dictionaries

2.1 Introduction

It is often useful in the field of signal processing to represent information contained in high-dimensional signals in another space more suitable to analysis or further manipulations. Traditionally, signals are mapped to a space domain where the signal representation is unique. Sparse signal representation has proven to be an extremely powerful tool for acquiring, representing, compressing and classifying high-dimensional signals (AHARON et al., 2006; ELAD et al., 2006; LI et al., 2013; RUBINSTEIN et al., 2010b; WRIGHT et al., 2010). There are many areas of science and technology which have greatly benefited from advances involving sparse representation. For example, image and signal processing have been influenced in numerous ways such as denoising, image compression, feature extraction and many more. In this chapter, we present the sparse representation problem which is a parsimonious principle that a sample can be approximated by a sparse linear combination of basis vectors over a redundant dictionary. We describe three main aspects dealing with this problem: optimization techniques for solving sparse approximation problems (an inverse problem that arises in the representation), the choice of a dictionary and the applications of sparse representations. We further show that sparse representation and Dictionary Learning can be extended to address specific tasks such as classification when the learning includes a discrimination criteria in the objective function. We take one step further towards classification by taking advantage of sparse representation and dictionary learning; dealing with two specific problems we are interested in this work: classification of LV wall motion and detection of cardiac fibrosis in cardiac medical images.

2.2 The sparse representation problem

In linear algebra the term sparse refers to a measurable property of vectors. Sparsity is not an indicator of the size of the vector, but it concerns the number of non-zero coefficients in the vector that is measured by the ℓ^0 norm denoted as $\|\cdot\|_0$. One of the main advantages of sparsity is the simplicity of calculation that this property brings in vector calculations, for example a multiplication of a matrix by a sparse vector takes less computational time compared to a dense matrix-vector multiplication.

Sparse representations are representations that account for most or all information of a signal with a linear combination of a small number of elementary signals called basis vectors or atoms. These basis vectors capture high-level patterns in the input data. The problem solved by the sparse representation is to search for the most compact representation of a signal in terms of linear combination of a few atoms in an overcomplete dictionary.

Using an overcomplete dictionary $\mathbf{D} = [\mathbf{d}_1, \mathbf{d}_2, \mathbf{d}_3, \dots, \mathbf{d}_K] \in \mathbb{R}^{N \times K}$ that contains K elementary N -dimensional signals called atoms of the dictionary, with $K > N$ and usually $K \gg N$, a signal $\mathbf{y} \in \mathbb{R}^N$ can be represented as a linear combination of these atoms. An illustrative example can be seen in Figure 2.1. The problem of sparse representation is to find a coefficient (sparse) vector $\mathbf{x} \in \mathbb{R}^{K \times 1}$, such that:

$$\mathbf{y} = \mathbf{D}\mathbf{x} \quad (2.1)$$

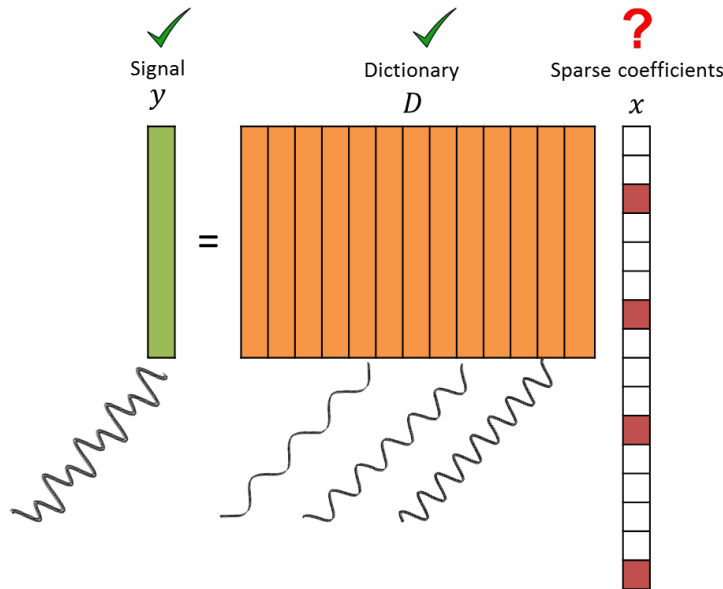


FIGURE 2.1— Example of a sparse signal \mathbf{y} represented by a linear combination of basis (atoms) of an orthogonal representation matrix (Dictionary). The ℓ^0 norm of the sparse coefficients vector \mathbf{x} is 4.

In this problem, if a sparse vector \mathbf{x} can be found, it is called the sparse representation of \mathbf{y} . This is due to the fact that \mathbf{x} is the vector that can be used to reproduce or better to say, “represent” \mathbf{y} . The representation of \mathbf{y} may either be exact (Equation 2.1), or approximate

$\mathbf{y} \cong \mathbf{D}\mathbf{x}$ with a prescribed error tolerance ε , satisfying:

$$\|\mathbf{y} - \mathbf{D}\mathbf{x}\|_p \leq \varepsilon \quad (2.2)$$

In approximation methods, typical norms used for measuring the deviation are the ℓ^p -norms for $p = 1, 2$ and ∞ . The ℓ^1 and ℓ^2 norms denoted as $\|\cdot\|_1$ and $\|\cdot\|_2$ respectively, are also indicators of sparsity. The ℓ^1 norm is the sum of the absolute value of the coefficients in a vector defined as:

$$\sum_{i=1}^n |\mathbf{x}_i| \quad (2.3)$$

and the ℓ^2 norm is the Euclidean length of a vector defined as:

$$\sqrt{\sum_{i=1}^n |\mathbf{x}_i|^2} \quad (2.4)$$

In a more general context, the ℓ^p norm is defined as $\left[\sum_{i=1}^n |\mathbf{x}_i|^p \right]^{\frac{1}{p}}$.

(TROPP et al., 2010) present four basic sparse representation problems, which manage different compromises between the error ε in approximation and the cost of representing the approximation:

- The Sparsest Representation of a Signal \mathbf{y} : The solution with the fewest number of non-zero coefficients is the most basic problem:

$$\arg \min_{\mathbf{x}} \|\mathbf{x}\|_0 \quad s.t. \quad \mathbf{y} = \mathbf{D}\mathbf{x} \quad (2.5)$$

- Error-Constrained Approximation: Given a target signal \mathbf{y} , find the sparsest coefficient vector \mathbf{x} that represents an approximation with a prescribed error tolerance:

$$\arg \min_{\mathbf{x}} \|\mathbf{x}\|_0 \quad s.t. \quad \|\mathbf{y} - \mathbf{D}\mathbf{x}\|_2 \leq \varepsilon \quad (2.6)$$

It is most common to measure the prediction–observation discrepancy with the Euclidean norm ($\|\cdot\|_2$), but other metrics may also be appropriate.

- Sparsity-Constrained Approximation: From all coefficient vectors with a predefined level of sparsity $T \geq 1$, find the one that yields the best approximation to the target signal \mathbf{y} :

$$\arg \min_{\mathbf{x}} \|\mathbf{y} - \mathbf{D}\mathbf{x}\|_2 \quad s.t. \quad \|\mathbf{x}\|_0 \leq T \quad (2.7)$$

- Subset selection problem: Given a target signal \mathbf{y} , find a coefficient vector that balances the sparsity and approximation error by solving an ℓ^0 -regularized least square optimization problem, where $\lambda > 0$ is the regularization parameter whose value governs the sparsity of the solution.

$$\arg \min_{\mathbf{x}} \frac{1}{2} \|\mathbf{y} - \mathbf{D}\mathbf{x}\|_2^2 + \lambda \|\mathbf{x}\|_0 \quad (2.8)$$

If the dictionary \mathbf{D} is orthonormal, it is possible to solve the sparsest representation of a signal \mathbf{y} by choosing the atoms whose absolute inner products with the target signal take the largest values. Otherwise, the extraction of the sparsest representation is a Non-deterministic Polynomial-time hard (NP-hard) problem (DONOHO et al., 2012). Algorithms for finding approximating solutions have been extensively investigated and, indeed, several effective decomposition algorithms are available.

In the next sections we address two main concepts in the Sparse signal representation problem:

- Given a new signal \mathbf{y} and a dictionary \mathbf{D} , finding the sparse coefficient \mathbf{x} is called **Sparse Coding**.
- Given training data \mathbf{Y} , learning the dictionary \mathbf{D} , the coefficient vectors \mathbf{X} , and the number of dictionary atoms K is called **Dictionary Learning (DL)**.

First, we address three main aspects dealing with the sparse coding problem: optimization techniques for solving sparse approximation problems, the choice of Dictionary and the applications of the sparse representation. Then, we address the problem of dictionary learning adapted for classification.

2.3 Optimization techniques for solving sparse approximation problems

The goal in solving sparse approximation problems is to achieve some compromise between the error in approximation and the computational cost in doing such approximation, which is measured as the number of elementary signals that participate in the approximation. In this section, numerical algorithms and approaches for solving the problem of sparse approximation will be presented in details. A classification of these techniques is presented by (TROPP et al., 2010) based on a computational point of view:

2.3.1 Greedy pursuit methods

A pursuit method for sparse approximation is a greedy based approach that iteratively refines the current estimate for the coefficient vector \mathbf{x} by modifying one or several coefficients chosen to yield a substantial improvement in approximating the signal (TROPP et al., 2010). Matching Pursuit (MP), the clearest example of such algorithm, was introduced by (MALLAT et al., 1993) where a signal is decomposed into a linear expansion of waveforms that belong to a redundant dictionary of functions. It is presented in Algorithm 1. Each iteration of the algorithm consists of two steps: an atom selection step and a residual update step. The atom selection step finds the atom in the dictionary which has the highest absolute correlation $|\langle \mathbf{d}_j, \mathbf{r}^{(k)} \rangle|$ (where $\langle \cdot \rangle$ denotes the inner-product operation defined as $\langle \mathbf{u}, \mathbf{v} \rangle = \mathbf{u}^T \mathbf{v}$) with the current residual error, where the correlation is measured as the length of the orthogonal projection. The update step, updates the residual error by subtracting a scaled version of the atom just found in the previous step.

The algorithm terminates if the norm of the residual falls below the desired approximation error bound, or if the number of distinct atoms found in the approximation equals the desired limit.

Algorithm 1 Matching Pursuit (MP)

- 1: **Input:** Signal: \mathbf{y} , dictionary \mathbf{D} , stopping rule: threshold value or number of different atoms
 - 2: Let \mathbf{d}_j , $1 \leq j \leq N$, denote the j -th column (atom) of the dictionary matrix \mathbf{D}
 - 3: **Initialization:** Set $k=0$, the number of iterations
 - 4: Initial solution: $\hat{\mathbf{x}}^{(0)} = 0$
 - 5: Initial residual: $\mathbf{r}^{(0)} = \mathbf{y}$
 - 6: **Repeat** ($k = k + 1$) and perform:
 - 7: Atom selection:
 - 8: Compute the current correlation: $\mathbf{c}_j^{(k)} = \langle \mathbf{d}_j, \mathbf{r}^{(k)} \rangle$;
 - 9: Identify the index \hat{j} such that: $\hat{j} = \max_j |\mathbf{c}_j^{(k)}|$;
 - 10: Residual update step:
 - 11: Update $\hat{\mathbf{x}}_{\hat{j}}^{(k)} = \hat{\mathbf{x}}_{\hat{j}}^{(k-1)} + \mathbf{c}_{\hat{j}}^{(k)}$;
 - 12: Update $\mathbf{r}^{(k)} = \mathbf{r}^{(k-1)} - \mathbf{c}_{\hat{j}}^{(k)} \mathbf{d}_{\hat{j}}$;
 - 13: **Stopping rule** ($|\mathbf{r}_j| < \text{thresholdvalue}$)
-

Note that MP may select the same index many times over when the dictionary is not orthogonal. In non-orthogonal (or basic) MP, the dictionary atoms are not mutually orthogonal vectors. Therefore, subtracting subsequent residuals from the previous one can introduce components that are not orthogonal to the span of previously included atoms. The Orthogonal Matching Pursuit (OMP) algorithm (Tropp et al., 2007) was developed to remove this drawback as will be seen it shortly. The greedy selection in the MP algorithm nominally involves computing all the inner products between the residual and the dictionary, which generally requires a complexity of $\mathcal{O}(NK)$ (Tropp, 2004b). If the loop is executed T times, then the cost of the algorithm is at most $\mathcal{O}(NTK)$.

2.3.1.1 Orthogonal Matching Pursuit (OMP) algorithm

The Orthogonal Matching pursuit algorithm (OMP) (Pati et al., 1993; Tropp et al., 2007) is based on a variation of Matching Pursuit. MP simply removes the selected column vector (atom) from the residual vector at each iteration. OMP uses a least-squares step at each iteration to update the residual vector in order to improve the approximation. It is presented in Algorithm 2. Similar to MP, in OMP each iteration of the algorithm consists of two steps: an atom selection step and a residual update step. At each step, the OMP algorithm picks the dictionary atom that has the maximal projection onto the residual signal; it should be note that the dictionary elements are normalized in this process. Following the selection of atoms, the sparse representation coefficients are found by means of least-squares with respect to the atoms that are chosen so far.

In the OMP algorithm, $\mathcal{S}^{(k)}$ is the support¹ of $\hat{\mathbf{x}}$ at the iteration k and $\mathbf{D}_{\mathcal{S}^{(k)}}$ is the matrix

1. The support of a vector \mathbf{a} is the set of indices containing non-zero entries.

Algorithm 2 Orthogonal Matching Pursuit (OMP)

-
- 1: **Input:** Signal: \mathbf{y} , dictionary \mathbf{D} , stopping rule threshold
 - 2: Let \mathbf{d}_j , $1 \leq j \leq N$, denote the j -th column (atom) of the dictionary matrix \mathbf{D}
 - 3: **Initialization:** Set $k=0$, the number of iterations
 - 4: Initial solution: $\hat{\mathbf{x}}^{(0)} = 0$
 - 5: Initial Solution Support $\mathbf{S}^{(0)} = \text{support}\{\hat{\mathbf{x}}^{(0)}\} = 0$
 - 6: Initial residual: $\mathbf{r}^{(0)} = \mathbf{y}$
 - 7: **Repeat** ($k = k + 1$) and perform:
 - 8: Atom selection:
 - 9: Compute the current correlation: $\mathbf{c}_j^{(k)} = \langle \mathbf{d}_j, \mathbf{r}^{(k)} \rangle$;
 - 10: Identify the index \hat{j} such that: $\hat{j} = \underset{j}{\text{max}} |\mathbf{c}_j^{(k)}|$
 - 11: Update the support $\mathbf{S}^{(k)} = \mathbf{S}^{(k-1)} \cup \hat{j}$
 - 12: Update the matrix $\mathbf{D}_{\mathbf{S}^{(k)}} = [0, \dots, \mathbf{d}_i, \dots, 0, \dots, \mathbf{d}_j, \dots, 0]$
 - 13: Update the solution $\hat{\mathbf{x}}^{(k)} = (\mathbf{D}_{\mathbf{S}^{(k)}}^T \mathbf{D}_{\mathbf{S}^{(k)}})^{-1} \mathbf{D}_{\mathbf{S}^{(k)}}^T \mathbf{y}$
 - 14: Residual update step:
 - 15: Update $\mathbf{r}^{(k)} = \mathbf{y} - \mathbf{D}_{\mathbf{S}^{(k)}} \hat{\mathbf{x}}^{(k)}$;
 - 16: **Stopping rule** ($|\mathbf{r}_j| < \text{threshold value}$)
-

that contains the columns from \mathbf{D} that belong to this support. The updated solution gives the $\hat{\mathbf{x}}^{(k)}$ that solves the minimization problem $\|\mathbf{y} - \mathbf{D}_{\mathbf{S}^{(k)}} \mathbf{x}\|_2^2$. The algorithm can be stopped after a predetermined number of steps, hence after having selected a fixed number of atoms. Alternatively, the stopping rule can be based on the norm of the residual, or on the maximal inner product computed in the next atom selection stage. The complexity of the OMP algorithm is of order $\mathcal{O}(NT(T + K))$ where T is the total number of iterations (TROPP, 2004b).

As a representative method in the greedy algorithm family, the OMP has been widely used due to its simplicity and competitive performance. There have been some studies to improve the computational efficiency and recovery performance on the OMP algorithm. Some enhancements to the basic greedy framework are: 1) selecting multiple columns per iteration 2) pruning the set of active columns at each step 3) solving the least squares problems iteratively, and 4) theoretical analysis using the Restricted Isometry Property² (RIP) (CANDÈS et al., 2005) bound.

Examples of OMP algorithm extensions are, among others, the Regularized Orthogonal Matching Pursuit (ROMP) (NEEDELL et al., 2009b), subspace pursuit (SP) algorithm (DAI et al., 2009), Compressive Sampling Matched Pursuit (CoSaMP) (NEEDELL et al., 2009a) and Stagewise Orthogonal Matching Pursuit (StOMP) (DONOHO et al., 2012).

Modern pursuit methods are closely related to iterative thresholding algorithms. Among thresholding approaches, iterative hard thresholding (IHT) (BLUMENSATH et al., 2009) is the simplest. This algorithm is not based on OMP. In IHT, a non-linear operator $H_n(\cdot)$ is used to reduce the value of the ℓ^0 norm at each iteration by changing all but the largest n entries to 0. A property of the IHT algorithm is the robustness to observation noise.

2. The restricted isometry property (RIP) characterizes matrices which are nearly orthonormal, at least when operating on sparse vectors. It is a concept widely used to prove many theorems in the field of compressed sensing.

2.3.2 Convex relaxation methods

The idea in convex relaxation problems is to replace the ℓ^0 -norm by the ℓ^1 -norm resulting in a convex optimization in the optimization problem solved by (2.8). This is commonly known in the literature as Basis Pursuit (BP) methods (CHEN et al., 1998). Hence solutions to the Sparsest Representation problem reduces to solving:

$$\arg \min_{\mathbf{x}} \|\mathbf{x}\|_1 \quad s.t. \quad \mathbf{y} - \mathbf{D}\mathbf{x} \quad (2.9)$$

and the subset selection problem:

$$\arg \min_{\mathbf{x}} \frac{1}{2} \|\mathbf{y} - \mathbf{D}\mathbf{x}\|_2^2 + \lambda \|\mathbf{x}\|_1 \quad (2.10)$$

lead to the BP representations. Equation (2.10) is typically called ℓ^1 -regularized least-squares (ℓ^1 -LS) sparse coding model (LI et al., 2013) and coincides with the well-known LASSO model (TIBSHIRANI, 1994), where $\lambda \geq 0$ is a regularization parameter whose value governs the sparsity of the solution: large values typically produce sparser results (TROPPE et al., 2010), while small values lead to a solution approaching to the LS solution, i.e. a dense solution. The use of ℓ^1 solvers (BP method) is more stable and accurate compared to greedy algorithms, however, there are cases where the convergence is not reached in a reasonable amount of time (CHEN et al., 1998). Thus, approximating the solution of ℓ^0 minimization problems by greedy algorithms are still considered to be more practical than the ℓ^1 solvers. The computational cost for solving BP is of order $\mathcal{O}(N^2 K^{3/2})$ (SALMAN et al., 2009).

2.3.3 Bayesian methods

The Bayesian approach assumes that the signal's coefficients in the alternative space are random variables with a sparse promoting prior distribution (LI et al., 2013; SCHNITER et al., 2009; WIPF et al., 2004). Sparse coding is statistically formulated as:

$$\mathbf{y} = \mathbf{D}\mathbf{x} + \varepsilon \quad (2.11)$$

where ε is an error term. The Sparse coding problem has the following constraints:

- The error term is Gaussian distributed with mean zero and isotropic covariance, that is $\varepsilon \sim N(0, \mathbf{\Phi})$ where $\mathbf{\Phi} = \varphi \mathbf{I}$, where φ is a positive scalar.
- The dictionary atoms are usually Gaussian distributed, that is $\mathbf{d}_i \sim N(0, \mathbf{\Delta})$, where $\mathbf{\Delta} = \mathbf{I}$. The coefficient vector should follows a sparsity-inducing distribution.
- \mathbf{x} is independent of ε .

Bayesian approaches to the sparse approximation problem have typically been divided into two categories (WIPF et al., 2004): (i) *maximum a posteriori* MAP estimation using a fixed family of prior and (ii) empirical Bayesian approaches (Sparse Bayesian Learning).

The MAP problem statement is defined as:

$$\begin{aligned}\hat{\mathbf{x}} &= \arg \max_{\mathbf{x}} P(\mathbf{x}|\mathbf{y}) &= \arg \max_{\mathbf{x}} P(\mathbf{y}|\mathbf{x})P(\mathbf{x}) \\ &= \arg \min_{\mathbf{x}} \left[-\log[P(\mathbf{y}|\mathbf{x})] - \log[P(\mathbf{x})] \right],\end{aligned}\quad (2.12)$$

where $P(\mathbf{x})$ represent the probability distribution function assumed as a priori distribution for the coefficients of \mathbf{x} . For example, assuming a Laplacian prior with zero mean and isotropic variance on the coefficient vector:

$$P(\mathbf{x}|\gamma) = \frac{1}{(2\gamma)^k} e^{-\frac{\|\mathbf{x}\|_1}{\gamma}} \quad (2.13)$$

the MAP estimation is equivalent to the standard ℓ^1 norm regularized problem in equation 2.10. Assuming a moderately sparse prior such as the Laplacian, the resultant posterior is simplified but not sufficiently sparse.

The Sparse Bayesian Learning Model (SBL) employs a flexible, parameterized prior that is learned from the data. It assumes an independent zero-mean Gaussian noise model, with variance σ^2 , giving a multivariate Gaussian likelihood of the target vector \mathbf{y} :

$$P(\mathbf{y}|\mathbf{x}; \sigma^2) = (2\pi\sigma^2)^{-\frac{N}{2}} e^{-\frac{1}{2\sigma^2}\|\mathbf{y}-\mathbf{D}\mathbf{x}\|^2} \quad (2.14)$$

The prior over the coefficients \mathbf{x} is mean-zero Gaussian:

$$P(\mathbf{x}|\boldsymbol{\alpha}) = (2\pi)^{-M/2} \prod_{m=1}^M \alpha_m^{1/2} e^{-\frac{\alpha_m x_m^2}{2}} \quad (2.15)$$

where the key to the model sparsity is the use of M independent hyperparameters $\boldsymbol{\alpha} = (\alpha_1, \dots, \alpha_m)^T$, one per coefficient vector, which moderate the strength of the prior.

The use of SBL framework shows good promise to achieve the global minimum as the maximally sparse solution (WIPF, 2006). However, the SBL model fall behind in terms of solid theoretical justification and rigorous analysis in the context of sparse estimation problems. The connections between various families of Bayesian algorithms remain a problem addressed in the literature. In a later section, we will see how the use of different prior (gaussian or uniform) on the sparse coefficient vector can be applied also over the dictionary atoms (LI et al., 2013), which leads to various sparse representation models.

2.3.4 Non-convex optimization methods

A weaker notion of sparsity can be built on the notion of approximately representing a vector using a small number of non-zeros; this can be quantified by the ℓ^p norms ($p < 2$), which measure the trade-off between the number of non-zeros and the ℓ^2 error of reconstruction (BRUCKSTEIN et al., 2009). In the set of ℓ^p norms, the choice $p = 1$ gives a convex functional, while every choice $0 < p < 1$ yields non-convex functional. In (CHARTRAND, 2007; SAAB et al., 2008) is demonstrated that by replacing the ℓ^1 norm with the ℓ^p norm with $p < 1$, exact reconstruction is possible with substantially fewer measurements.

2.3.5 Other methods

Other methods known as "brute force" methods explore through all potential approximations to find the global optimum. Exhaustive searches quickly become computationally intractable as the problem size becomes large, and more sophisticated techniques, such as branch-and bound, do not accelerate the pursuit to be considered a practical method (MILLER, 2002).

2.4 Design of the dictionary

As we have seen, a good compromise between the error in approximation and the computational cost in approximation of sparse representation of signals, depends on the algorithm used to solve the sparse approximation problem. It is also connected to the dictionary in which the decomposition is realized. The definition of dictionaries thus establishes an important step and is the main object of a large number of contributions (AHARON et al., 2006; ENGAN et al., 1999, 2007; KREUTZ-DELGADO et al., 2003; LEWICKI et al., 2000; OLSHAUSEN et al., 1997).

We have introduced the concept of an overcomplete dictionary $\mathbf{D} = [\mathbf{d}_1, \mathbf{d}_2, \mathbf{d}_3, \dots, \mathbf{d}_K] \in \mathbb{R}^{N \times K}$ that contains K elementary signals or atoms for columns, with $K > N$ and usually $K \gg N$. If the dictionary spans the signal space, the dictionary is complete or total (TROPP, 2004b). In this case, every signal can be approximated with zero error using a linear combination of atoms. If the atoms form a linearly dependent set, then the dictionary is redundant. In this case, every signal has an infinite number of best approximations. For a dictionary to be complete, it is necessary that $K \geq N$. For a dictionary to be redundant, it is sufficient that $K > N$. In many modern applications, the dictionary is both complete and redundant.

The limits that may be assumed on sparsity (BARCHIESI et al., 2013; TROPP, 2004a) depends on the properties of the dictionary \mathbf{D} . We can mention two basic measures of quality in the dictionary:

- The Mutual Coherence of a dictionary \mathbf{D} , denoted by $\mu(\mathbf{D})$, is defined as the maximal absolute scalar product between two different normalized atoms of \mathbf{D} ,

$$\mu(\mathbf{D}) = \arg \max_{i \neq j} |\mathbf{d}_i^T \mathbf{d}_j| \quad (2.16)$$

For an orthogonal matrix \mathbf{D} , $\mu(\mathbf{D}) = 0$. In an overcomplete matrix ($K > N$), $\mu(\mathbf{D}) > 0$.

- The Spark of a dictionary \mathbf{D} , denoted by $\sigma(\mathbf{D})$, is the smallest number of columns that form a linearly dependent set.

Also, we can mention two properties related to the previous measures:

- A necessary and sufficient condition for every linear combination of m atoms to have a unique m -term representation (TROPP, 2004a) is:

$$m < \frac{\sigma(\mathbf{D})}{2} \quad (2.17)$$

- If \mathbf{D} is a coherent dictionary consisting of L orthonormal bases, the relation between $\mu(\mathbf{D})$ and $\sigma(\mathbf{D})$ is (GRIBONVAL et al., 2003):

$$\sigma(\mathbf{D}) \geq [1 + \frac{1}{L-1}] \mu(\mathbf{D})^{-1} \quad (2.18)$$

The main goal in sparse signal representation, is to find an overcomplete basis or dictionary \mathbf{D} that is good for representing a given set of vectors as sparsely as possible. Two major approaches have been followed to answer this issue. The first is to use some standard overcomplete basis, such as Wavelets, Curvelets, Contourlets, steerable Wavelet filters, short-time-Fourier and the DCT basis. The success of such dictionaries in applications depends on how suitable they are to sparsely describe the signals to analyze. The second approach is to obtain an overcomplete basis from a given set of vectors through training. These approaches are relevant for Dictionary Learning techniques. While choosing a prespecified standard basis is appealing due to its simplicity, the training based approach intuitively appears to be a better option as it generates dictionaries that are well suited to the class of signals in the training set and, therefore, more suitable to the problem at hand. The next subsections develop these two problems.

2.4.1 Standard overcomplete basis

Earlier works made use of traditional dictionaries, such as the Fourier and Wavelet dictionaries, but they are not well equipped for representing more complex natural and high-dimensional signal data. To overcome this apparent limitation, dictionaries constructed from a mathematical model of the data, commonly called analytic dictionaries emerged. An exhaustive pursuit of a set of basis functions can become an inconvenience if these atoms have a weak correlation with the signal. The choice of atoms depends on the application for which we intend the use of the sparse representation. It has proved useful, even essential, to have atoms having the same characteristics as the signal source for which we try to model. In the case of image analysis, the modeling of boundaries will be obvious if atoms present themselves a structure visually close to a boundary.

To better encircle the decisive character of the choice of atoms, we briefly present the most basic characteristic atoms, as well as their advantages and inconveniences. An extensive study can be found in (RUBINSTEIN et al., 2010a):

2.4.1.1 The Fast Fourier Transform (FFT)

The Fourier transform presents a number of properties that make it suitable for invariant feature extraction for pattern recognition. The Fourier basis describes a signal in terms of its global frequency content, as a combination of orthogonal waveforms:

$$\mathcal{F} = \{\phi_n(x) = e^{inx}\}_{n \in \mathbb{Z}} \quad (2.19)$$

where \mathbb{Z} denotes the set of integer values. A signal is approximated in this basis by projecting it onto the K lowest frequency atoms, which has a strong smoothing and noise-reducing effect.

However, the lack of time localization makes it difficult to represent discontinuities. Digital signal processing has become the mainstream in signal processing, and only discrete transforms can be implemented in the digital domain, the discrete version of the Fourier transform (DFT) is frequently used as an intermediate step in more elaborated signal processing techniques. The classic example of this is the Fast Fourier Transform (FFT) popularized in 1965 by (COOLEY et al., 1965).

In details, a dictionary of FFT is a collection of sinusoidal waveforms indexed by $r = (\omega, \nu)$, where $\omega \in [0, 2\pi)$ is an angular frequency variable and $\nu = \{0, 1\}$ indicates phase type, sine or cosine:

$$\begin{aligned} g(\omega, 0) &= \cos(\omega t) \\ g(\omega, 1) &= \sin(\omega t) \end{aligned} \tag{2.20}$$

For the standard Fourier dictionary, r varies through the set of all cosines with Fourier frequencies $\omega_k = 2\pi k/N$, $k = 0, \dots, N/2$, and all sines with Fourier frequencies ω_k , $k = 1, \dots, N/2 - 1$, meaning that the dictionary consists of N atoms conforming an orthogonal basis. If the frequencies are divided into more than N components, generating a dictionary with more than N atoms, the higher frequency resolution can be also obtained. For example, for cosines with frequencies $\omega_k = \pi k/N$, $k = 0, \dots, N$ and sines frequencies ω_k , $k = 1, \dots, N - 1$, the dictionary will contain $2N$ atoms with higher frequency resolution, meaning that the dictionary is overcomplete. Meanwhile, the decomposition algorithm will not be FFT. Instead, optimization techniques based on sparse representation should be employed (cf. subsection 2.3).

2.4.1.2 Wavelets

Wavelets are time-located functions that cup up data into different frequency components, and then study each component with a resolution matched to its scale. The idea is similar to the Fourier Transform where the approximation of functions is based on the superposition of sines and cosines functions. Generally, Wavelets have properties that make them useful for signal processing. Wavelets are more useful for describing signals with discontinuities because of their time-localized behavior (both Fourier and Wavelet transforms are frequency-localized, but Wavelets have an additional time-localization property). For this reason, many types of signals in practice may be non-sparse in the Fourier domain, but very sparse in the Wavelet domain.

In many practical applications a sampled version of the continuous Wavelets is used: the discrete Wavelet transform (DWT). The DWT is an implementation of the Wavelet transform using a discrete set of the Wavelet scales and translations obeying some defined rules. For instance a 2D discrete Wavelet transform for image processing can be constructed from Wavelet orthonormal bases of one-dimensional signals. Three mother Wavelets denoted as $\psi^1(x)$, $\psi^2(x)$ and $\psi^3(x)$, related to horizontal, vertical and diagonal directions respectively ($\psi^3(x) = \psi^1(x) * \psi^2(x)$), with $x = (x_1, x_2) \in \mathbb{R}^2$, are dilated and translated by dyadic scales (or level j) 2^j and $2^j n$

respectively, with $n = (n_1, n_2) \in \mathbb{Z}^2$. This yields an orthonormal basis of the space $L^2(\mathbb{R}^2)$ of finite energy functions $f(x) = f(x_1, x_2)$:

$$\left\{ \psi_{j,n}^k(x) = \frac{1}{2^j} \psi^k\left(\frac{x - 2^j n}{2^j}\right) \right\}_{j \in \mathbb{Z}, n \in \mathbb{Z}^2, 1 \leq k \leq 3} \quad (2.21)$$

When j, n can take values in \mathbb{R} , the set of Wavelets represents an overcomplete frame and is called undecimated Wavelet basis. For example, in Figure 2.2, a set of Wavelet Haar atoms in an overcomplete dictionary is shown. The set of Haar Wavelet includes separable basis functions, having steps of various sizes and in all locations. The support of a Wavelet $\psi_{j,n}^k$ is a square of width proportional to the scale 2^j . 2D Wavelet bases are discretized to define orthonormal bases of images including N pixels. Figure 2.3, shows an image (Lena) with its third level of decomposition using the Haar Wavelet transform.

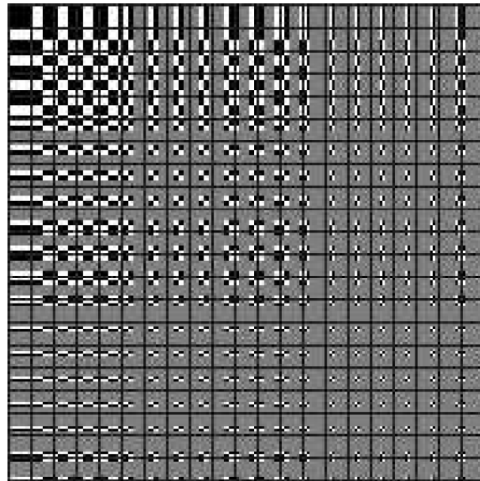


FIGURE 2.2– Wavelet Haar atoms in an overcomplete dictionary.

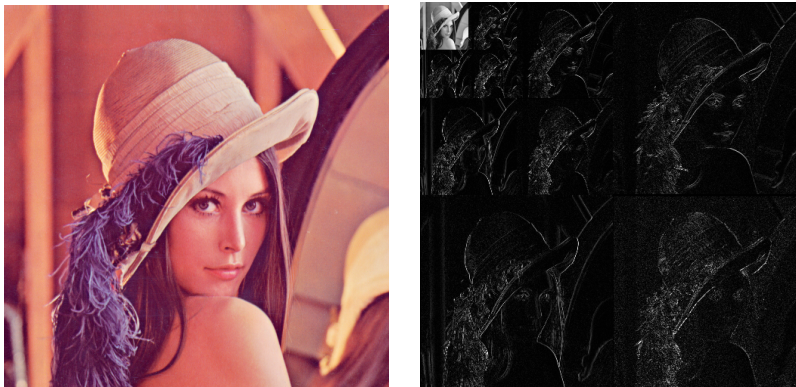


FIGURE 2.3– Image lena and its third level Wavelet decomposition using Haar Wavelet transform.

2.4.1.3 Curvelets

The Curvelet transform is a multiscale directional transform that allows near optimal non-adaptive sparse representation of objects with curved singularities. Unlike 2D Wavelets, which are tensor product of 1D Wavelets, Curvelets are intrinsically defined in 2D and are highly anisotropic. Each Curvelet atom is associated with a triplet index j, l, k representing scale, direction and location. Each Curvelet atom is a well-localized needle-shaped function, oscillating along one direction and smoothed in the direction orthogonal to the first. The continuous Curvelet in 2D with scale j , angle index l , and location $k = (k_1, k_2)$ (also called translation parameter) is defined as:

$$\phi_{j,l,k} = 2^{j/2} \phi_j \left(\mathbf{M}_j \mathbf{R}_{\theta_{j,l}} x - k \right) \quad (2.22)$$

where \mathbf{M}_j is the dilation matrix and $\mathbf{R}_{\theta_{j,l}}$ is the rotation matrix:

$$\mathbf{M}_j = \begin{pmatrix} 2^{2j} & 0 \\ 0 & 2^{2j} \end{pmatrix}, \quad \mathbf{R}_{\theta_{j,l}} = \begin{pmatrix} \cos \theta_{j,l} & \sin \theta_{j,l} \\ -\sin \theta_{j,l} & \cos \theta_{j,l} \end{pmatrix} \quad (2.23)$$

and $\theta_{j,l}$ is the l th angle at scale j :

$$\theta_{j,l} = 2\pi 2^{-j} l \quad (2.24)$$

The mother function of scale j , ϕ_j , is rotated, dilated and shifted to generate the other Curvelets at the same scale.

2.4.2 Dictionary Learning (DL)

Dictionary learning is a recent approach to dictionary design that has been strongly influenced by the latest advances in sparse representation theory and algorithms. This approach suggests the use of machine learning based techniques to infer the dictionary from a set of examples. In this case, the dictionary is typically represented as an explicit matrix, and a training algorithm is employed to adapt the matrix coefficients to the examples. The most recent training methods are focusing on ℓ^0 and ℓ^1 sparsity measures, which lead to simple formulations and enable the use of recently developed efficient sparse coding techniques (cf. 2.3). Main algorithms of this type include the method of optimal directions (MOD) (ENGAN et al., 1999), the K-SVD algorithm (AHARON et al., 2006), and others algorithms based on parametric approaches that will be summarized in this section. An illustration of the Dictionary Learning problem is shown in Figure 2.4.

Next, we briefly introduce the basic framework for DL. Let $\mathbf{Y} = [\mathbf{y}_1, \mathbf{y}_2, \dots, \mathbf{y}_N] \in \mathbb{R}^{n \times N}$ be a data matrix (a finite training set of signals) where each column is a n -dimensional input signal. Learning a reconstructive dictionary \mathbf{D} with K items for sparse signal representation of \mathbf{Y} can be accomplished by solving (AHARON et al., 2006):

$$\langle \mathbf{D}, \mathbf{X} \rangle = \arg \min_{\mathbf{D}, \mathbf{X}} \|\mathbf{Y} - \mathbf{D}\mathbf{X}\|_F^2 \quad s.t. \quad \forall i, \|\mathbf{x}_i\|_0 \leq T, \quad (2.25)$$

where: $\mathbf{D} = [\mathbf{d}_1, \mathbf{d}_2, \mathbf{d}_3, \dots, \mathbf{d}_K] \in \mathbb{R}^{n \times K}$ ($K > n$, making the dictionary over-complete) is the dictionary to be learned from the data samples \mathbf{Y} . The N -column vector $\mathbf{X} = [\mathbf{x}_1, \mathbf{x}_2, \dots, \mathbf{x}_N] \in$

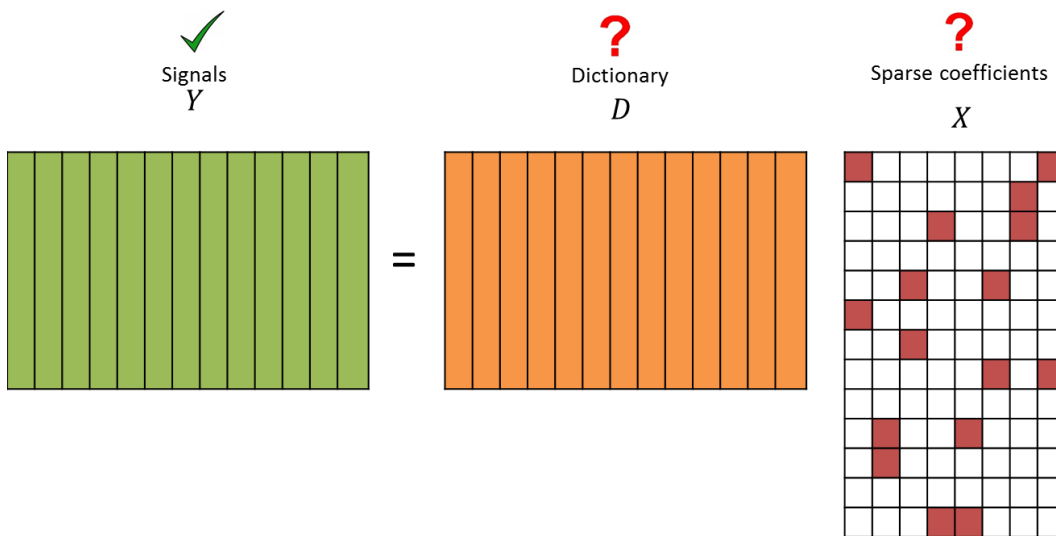


FIGURE 2.4— An illustration of the Dictionary Learning (DL) process.

$\mathbb{R}^{K \times N}$ are the sparse codes coefficients of input signals \mathbf{Y} . T is a sparsity constraint parameter (each signal has fewer than T items in its decomposition). $\|\mathbf{Y} - \mathbf{D}\mathbf{X}\|_F$ denotes the reconstruction error and $\|\mathbf{x}\|_0$ denotes the ℓ^0 -norm that counts the number of non-zero elements of \mathbf{X} . The Frobenius norm $\|\cdot\|_F$ defined as $\|\mathbf{A}\|_F = \sqrt{\sum_{ij} \mathbf{A}_{ij}^2}$ is an indication of the reconstruction error. The construction of \mathbf{D} is achieved by minimizing the reconstruction error and satisfying simultaneously the sparsity constraint.

In the next subsections, we present a brief description of the most commonly used DL algorithms found in the literature. In (TOSIC et al., 2011) a classification of dictionary learning algorithms is presented in three main directions: i) probabilistic learning methods; ii) learning methods based on clustering or vector quantization; and iii) methods for learning dictionaries with a particular construction.

2.4.2.1 Probabilistic methods

Probabilistic and non-probabilistic approaches have been adopted for the derivation of DL algorithms. Maximum likelihood (ML) dictionary learning method for natural images was introduced in (OLSHAUSEN et al., 1997) under the sparse approximation assumption. In (LEWICKI et al., 2000) another ML algorithm is presented, which uses the Laplacian prior to enforce sparsity. Given the training examples $\mathbf{Y} \in \mathbb{R}^{n \times N}$, to obtain the likelihood function $P(\mathbf{Y}|\mathbf{D})$ and seek the dictionary \mathbf{D} that maximizes it, two assumptions are necessary: the first one is that the measurements are drawn independently, therefore:

$$P(\mathbf{Y}|\mathbf{D}) = \prod_{i=1}^N P(\mathbf{y}_i|\mathbf{D}) \quad (2.26)$$

The second one is critical and refers to the coefficient vector \mathbf{x} which is considered as a random vector with prior distribution $P(\mathbf{x})$. The components of the likelihood function are computed using the relation:

$$P(\mathbf{y}_i|\mathbf{D}) = \int P(\mathbf{y}_i, \mathbf{x}|\mathbf{D})d\mathbf{x} = \int P(\mathbf{y}_i|\mathbf{x}, \mathbf{D}) \cdot P(\mathbf{x})d\mathbf{x} \quad (2.27)$$

Formally, the goal of ML learning method is to maximize the likelihood that signals have efficient sparse representations in a redundant dictionary given by the matrix \mathbf{D} . This can be accomplished by finding the overcomplete dictionary $\hat{\mathbf{D}}$ such that

$$\hat{\mathbf{D}} = \arg \max_{\mathbf{D}} \left[\log \int_{\mathbf{X}} P(\mathbf{Y}|\mathbf{X}, \mathbf{D}) \cdot P(\mathbf{X})d\mathbf{X} \right] \quad (2.28)$$

Here, all the examples \mathbf{y}_i are concatenated as columns to construct the data matrix \mathbf{Y} . Likewise, the representations coefficient vectors \mathbf{x}_i are gathered together to build the matrix \mathbf{X} . The optimization problem in 2.28 can be reduced to an energy minimization problem where it is possible to compute an estimation $\hat{\mathbf{X}}$:

$$(\hat{\mathbf{D}}, \hat{\mathbf{X}}) = \arg \min_{\mathbf{D}, \mathbf{X}} \left[-\log[P(\mathbf{Y}|\mathbf{X}, \mathbf{D}) \cdot P(\mathbf{X})] \right] \quad (2.29)$$

$$= \arg \min_{\mathbf{D}, \mathbf{X}} \left[\|\mathbf{Y} - \mathbf{D}\mathbf{X}\|_2^2 + \lambda\|\mathbf{X}\|_1 \right] \quad (2.30)$$

This problem can be solved by iterating between two steps. In the first step (sparse approximation step), \mathbf{D} is kept constant and the energy function is minimized with respect to a set of coefficient vectors \mathbf{x}_i . It can be solved, for example, by convex optimization for each vector \mathbf{y}_i . The second step (dictionary update step), keeps the sparse codes coefficients \mathbf{x}_i constant, while performing, for example, the gradient descent on \mathbf{D} to minimize the average energy.

The probabilistic inference approach in overcomplete dictionary learning has subsequently been adopted by other researchers. For simplicity, the two-step optimization structure has been preserved in most of these works, and the modifications usually appeared in either the sparse approximation step, or the dictionary update step, or in both, for example, the method of optimal directions (MOD)(ENGAN et al., 1999). It uses the OMP or FOCUSS³ optimization (GORODNITSKY et al., 1997) algorithm in the sparse coding stage and introduces an analytic solution of the quadratic problem in the dictionary update step given by $\mathbf{D} = \mathbf{Y}\mathbf{X}^+$, with \mathbf{X}^+ denoting the Moore-Penrose pseudo-inverse.

The same researchers that conceived the MOD method also suggested a maximum a-posteriori probability (MAP) setting for the training of dictionaries. Instead of maximizing the likelihood $P(\mathbf{Y}|\mathbf{D})$, the MAP method maximizes the posterior probability $P(\mathbf{D}|\mathbf{Y})$.

3. FOCUSS stands for FOcal Underdetermined System Solver: an algorithm designed to obtain sub-optimally sparse solutions to the $m \times n$, underdetermined linear inverse problem: $\mathbf{A}\mathbf{x} = \mathbf{y}$

2.4.2.2 Clustering-based methods

A slightly different family of dictionary learning techniques is based on Vector Quantization (VQ)⁴ achieved by K-means clustering (TOSIC et al., 2011). In clustering, a set of descriptive vectors $\{\mathbf{d}_k\}_{k=1}^K$ of the searched dictionary is learned, and each sample is represented by one and only one of those vectors (the one closest to it, based on the ℓ^2 distance measure). In contrast, in sparse representations, each example is represented as a linear combination of several vectors $\{\mathbf{d}_k\}_{k=1}^K$. A generalization of the K-means algorithm for dictionary learning, called the K-SVD algorithm, has been proposed by (AHARON et al., 2006).

K-SVD

The K-SVD algorithm takes its name from the Singular-Value-Decomposition (SVD) process that forms the core of the atom update step, and which is repeated K times, as the number of atoms.

Suppose \mathbf{M} is a real or complex $m \times n$ matrix. Then there exists a factorization of the form $\mathbf{M} = \mathbf{U}\mathbf{\Delta}\mathbf{V}^*$ where \mathbf{U} is a real or complex $m \times m$ unitary matrix, $\mathbf{\Delta}$ is a $m \times n$ diagonal matrix with non-negative real numbers on the diagonal, and the $n \times n$ unitary matrix \mathbf{V}^* denotes the conjugate transpose of the $n \times n$ unitary matrix \mathbf{V} . Such a factorization is called a singular value decomposition of \mathbf{M} . The diagonal entries δ_{ii} of $\mathbf{\Delta}$ are known as the singular values of \mathbf{M} . A common convention is to list the singular values in descending order. In this case, the diagonal matrix $\mathbf{\Delta}$ is uniquely determined by \mathbf{M} .

Similar to the MOD algorithm, in the K-SVD algorithm, the objective function in (2.25) is iteratively solved in two stages. The main contribution of the K-SVD is that the dictionary update, rather than using a matrix inversion, is performed atom-by-atom in a simple and efficient process. Further acceleration is provided by updating both the current atom and its associated sparse coefficients simultaneously. The result is a fast and efficient algorithm which is less demanding than the MOD method.

As shown in Algorithm 3, the approximation is based on the singular value decomposition (SVD) described before. A more detailed description can be found in (AHARON et al., 2006).

Dictionaries learned with K-SVD have been initially used in synthetic signals to test whether the algorithm recovers the original dictionary that generate the data. Then the K-SVD algorithm has been applied on natural image data with two different main goals: filling in missing pixels (inpainting) and compression. K-SVD has been widely used in other signal processing tasks like denoising (ELAD et al., 2006), image restoration (MAIRAL et al., 2008a) and signal separation (ABOLGHASEMI et al., 2011). Some extensions of the K-SVD algorithm are: the Shift-Invariant K-SVD algorithm (MAILHÉ et al., 2008), useful to represent long signals where the same pattern can appear several times at different positions, and the Non-negative K-SVD algorithm (AHARON et al., 2005), that suits signals generated under an additive model with positive atoms.

4. Vector quantization (VQ) is a classical quantization technique from signal processing which allows the modelling of probability density functions by the distribution of prototype vectors. It was originally used for data compression.

Algorithm 3 K-SVD

-
- 1: **Input:** Random normalized dictionary matrix $\mathbf{D} \in \mathbb{R}^{n \times K}$, Input Signals: $\mathbf{Y} \in \mathbb{R}^{n \times N}$,
 - 2: **Initialization:**
 - 3: $J=1$
 - 4: **Repeat until convergence:**
 - 5: Sparse Coding Stage:
 - 6: Use any pursuit based algorithm to compute the coefficient vectors \mathbf{x}_i , for each
 - 7: example \mathbf{y}_i , by approximating the solution of
 - 8: $i = 1, 2, \dots, N, \quad \arg \min_{\mathbf{x}_i} \|\mathbf{y}_i - \mathbf{D}\mathbf{x}_i\|_2^2 \quad s.t. \quad \|\mathbf{x}_i\|_0 \leq T$
 - 9: Codebook Update Stage:
 - 10: For each column $k = 1, 2, \dots, K \in \mathbf{D}^{(J-1)}$, update it by
 - 11: - Define the group of examples (indices) that use the atom \mathbf{d}_k ,
 - 12: $\omega_k = \{i | 1 \leq i \leq N, \mathbf{x}_T^k(i) \neq 0\}$.
 - 13: - Compute the overall representation error matrix, \mathbf{E}_k , by
 - 14:
$$\mathbf{E}_k = \mathbf{Y} - \sum_{j \neq k} \mathbf{d}_j \mathbf{x}_T^j$$
 - 15: - Restrict \mathbf{E}_k by choosing only the columns index in ω_k corresponding to those
 - 16: elements that initially used \mathbf{d}_k in their representation, and obtain \mathbf{E}_k^R
 - 17: - Apply SVD decomposition $\mathbf{E}_k^R = \mathbf{U}\mathbf{\Delta}\mathbf{V}^T$. Choose the update dictionary
 - 18: column $\hat{\mathbf{d}}_k$ to be the first column of \mathbf{U} . Update the coefficient
 - 19: vector \mathbf{x}_R^k to be the first column of \mathbf{V} multiplied by $\delta(1, 1)$
 - 20: **Set** $J = J + 1$
-

In later sections, we will see that the K-SVD algorithm is also used in the construction of discriminative dictionaries for classification tasks (JIANG et al., 2013b).

2.4.2.3 Parametric training methods

A parametric dictionary is constructed typically driven by prior on the structure of the data or to the target usage of the learned dictionary. The advantages of parametric dictionaries reside in the short description of the atoms. Parametric dictionary learning tries to find better parameters for atoms based on some criteria yielding to better and more adaptive representations of signals. It also gains the benefits of dictionary design approaches which are the simplicity and better matching to the structure of a special class of signals. An important advantage of parametric dictionary learning is that only the parameters of an atom (which is as few as 5 parameters in typical applications) should be stored instead of all the samples of the atom. So, it is very well suited to the applications with large matrix dimensions (ATAEE et al., 2010). Some examples of parametric dictionary structures are related to: Translation-Invariant Dictionaries, Multiscale Dictionaries and Sparse Dictionaries. A widely description can be found in (RUBINSTEIN et al., 2010a).

As we have seen, most important methods for DL include the maximum likelihood method, the method of optimal direction MOD and the K-SVD algorithm. Among these, the K-SVD algorithm has been the most popularly used technique for dictionary learning. It provides a good trade-off between sparsity and convergence (RIBHU et al., 2012).

2.5 Applications of the sparse representation

Recent advances in information technologies have produced massive high-dimensional data that demands efficient processing and analysis. The new theory of sparse representation and Compressive Sensing (CS) (BARANIUK, 2007; CANDÈS et al., 2006; DONOHO, 2006) provides a rigorous mathematical framework for studying high dimensional data, and also provides computationally feasible ways to uncover the structures of the data. The field of sparse representations and the use of redundant dictionaries has been drawing a considerable attention lately. Applications of this theory range from conventional audio/image/video processing tasks (denoising, deblurring, inpainting, compression, and super-resolution) to speech and object recognition (source separation and classification); from multimedia data mining to bioinformatic data decoding; from correcting error for corrupted data (face recognition despite occlusion) to detecting activities and events through a large network of sensors and computers. In (BARANIUK et al., 2010), a special issue called *Applications of Sparse Representation and Compressive sensing* resumes important topics from 15 papers grouped into three categories: The first one surveys theory and algorithms of Compressive Sensing (CS) and Sparse representation. The second one, highlights some of the conventional applications of compressive sensing in signal processing, including images audio, music, radar, and astronomical data. The final category shows how the sparsity promoting and compressive sensing techniques have started to create tremendous impact on a much broader range of engineering fields, including but not limited to pattern recognition, machine learning, communications, sensor networks, and imaging sensors.

This section aims at providing a few representative examples of the application of this theory in the field of image processing. Furthermore, in the next Chapter we present a state-of-the-art of the application of this theory in Medical Imaging. Figure 2.5 illustrates some applications of Sparse representation in this domain.

2.5.1 Image super-resolution

Image resolution describes the details contained in an image; the higher the resolution, the more details can be captured. High resolution image offers a high pixel density per area and thereby more details about the original scene. The need for high resolution is common in computer vision applications for better performance in pattern recognition and analysis of images. Enhancing the resolution of an image can be addressed by using signal processing or machine learning techniques to post-process the captured images. These techniques are specifically referred as super-resolution (SR) reconstruction and it is specially helpful in many practical applications such as medical imaging, remote sensing, video surveillance and video standard conversion. Image super-resolution is arguably one of the most classical inverse problems in image processing and is, by nature, intrinsically under-determined (ELAD et al., 2010). The problem can be simply stated as that of recovering a high-resolution image $\mathbf{x} \in \mathbb{R}^n$ from its low-resolution version $\mathbf{y} \in \mathbb{R}^q$ (with

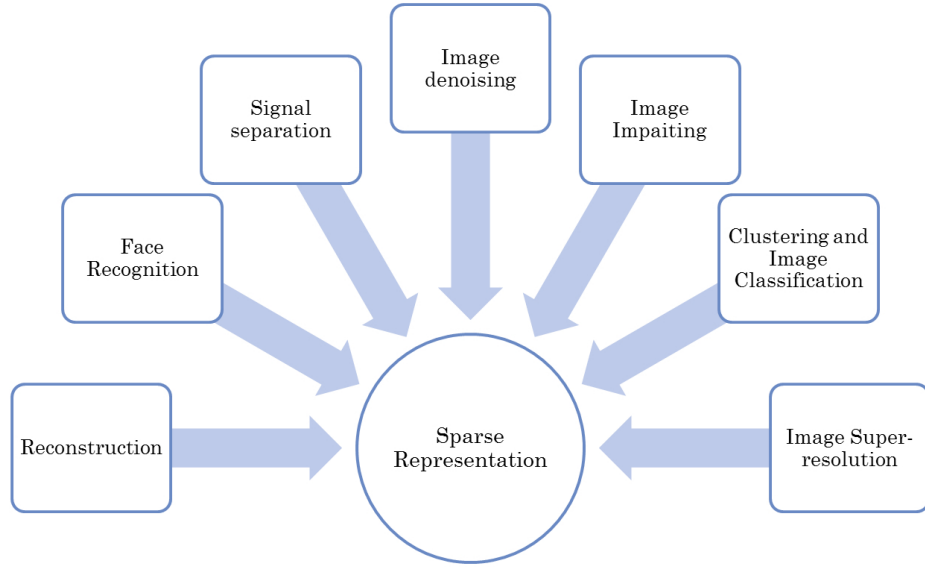


FIGURE 2.5– Applications of Sparse representation in image processing.

$q < n$). A relation between these two versions can be modeled by:

$$\mathbf{y} = \mathbf{S}\mathbf{H}\mathbf{x} = \mathbf{L}\mathbf{x}, \quad (2.31)$$

where \mathbf{H} is a linear filter that models certain low-pass filtering operation (blurring, e.g., with a Gaussian kernel), \mathbf{S} is a down-sampling operator, and $\mathbf{L} = \mathbf{S}\mathbf{H}$. The dimension of \mathbf{y} is significantly smaller than that of \mathbf{x} , thus there are infinitely many possible vectors \mathbf{x} that satisfy the above equation.

With respect to such a dictionary of high-resolution patches, denoted as \mathbf{D}_h , we may assume that any high-resolution image patch has a sparse representation,

$$\mathbf{x} = \mathbf{D}_h\boldsymbol{\alpha}, \quad (2.32)$$

for some $\boldsymbol{\alpha}$ with $\|\boldsymbol{\alpha}\|_0 \leq k$. Thus, the super-resolution problem becomes that of recovering $\boldsymbol{\alpha}$ from low-dimensional measurements

$$\mathbf{y} = \mathbf{L}\mathbf{x} = \mathbf{L}\mathbf{D}_h\boldsymbol{\alpha} \quad (2.33)$$

Notice that $\mathbf{D}_l = \mathbf{L}\mathbf{D}_h$ can be seen as a dictionary of corresponding low-resolution image patches. We may thus attempt to recover $\boldsymbol{\alpha}$ by solving an error constrained approximation problem (Equation 2.6) or a subset selection problem (Equation 2.8). Some contributions in this topic can be found in (J. YANG et al., 2008; J. ZHANG et al., 2012; ZHU et al., 2014)

2.5.2 Image inpainting

Image inpainting refers to the desire to fill-in missing values in an image, based on their surrounding neighbors. (SHEN et al., 2009) consider the problem of image inpainting from the view point of sequential incomplete signal recovery under the assumption that every image patch admits a sparse representation over a redundant dictionary. As for the identity of \mathbf{D} , a prespecified dictionary could be used, such as a redundant DCT, or gather many patch examples and learn a dictionary that sparsifies them. In the sparse representation modeling the core inpainting problem can be formulated as the optimization problem:

$$\arg \min_{\boldsymbol{\alpha}} \frac{1}{2} \|\mathbf{y} - \mathbf{M}\mathbf{D}\boldsymbol{\alpha}\|_2^2 + \lambda \|\boldsymbol{\alpha}\|_0, \quad (2.34)$$

where \mathbf{M} is a diagonal mask matrix of size $n \times n$, with 1-s for existing pixels, and 0-es elsewhere. It is further assumed that in the missing pixels, the image y is set to zero. Some contributions in this topic can be found in (ELAD et al., 2005; FADILI et al., 2009; OGAWA et al., 2013; SHEN et al., 2009)

2.5.3 Image Denoising

The problem to estimate \mathbf{x} from an observed noisy version under the sparsity prior has two essential issues: firstly, to find a dictionary which permits a sparse representation regarding the fact that the samples are noisy; secondly, to find the coefficients of this sparse representation. Let \mathbf{y} be an observed image, a noisy version of an unknown underlying clean image \mathbf{x} , i.e., $\mathbf{y} = \mathbf{x} + \nu$, where ν is an additive white Gaussian noise with known variance σ_ν^2 . The main aims of an image denoising algorithm is to achieve both noise reduction and feature preservation. In this context, Wavelet-based methods are of particular interest. In the Wavelet domain, the noise is uniformly spread throughout coefficients while most of the image information is concentrated in a few large ones. The denoising problem in the sparse representation of signals can be addressed by using, for instance, the Discrete Wavelet Transform (DWT). In this case the denoising problem can be formulated as:

$$\hat{\boldsymbol{\alpha}} = \arg \min_{\boldsymbol{\alpha}} \lambda \|\boldsymbol{\alpha}\|_p^p + \frac{1}{2} \|\boldsymbol{\alpha} - \boldsymbol{\beta}\|_2^2, \quad (2.35)$$

where $\boldsymbol{\beta} = \mathbf{T}\mathbf{y}$ is the DWT of the noisy image, \mathbf{T} is an orthogonal matrix containing the Wavelet bases, i.e., $\mathbf{x} = \mathbf{T}^T \boldsymbol{\alpha}$. The final image estimate is obtained as $\hat{\mathbf{x}} = \mathbf{T}^T \hat{\boldsymbol{\alpha}}$.

A second approach for image denoising is using dictionaries suitably adapted to the data. Rather than working on the image as a whole, the sparse and redundant representation model can be adopted on small image patches of size $\sqrt{N} \times \sqrt{N}$. Every patch in a given image (with overlaps) is expected to have a sparse representation with respect to a dictionary \mathbf{D} . The core of denoising using learned dictionaries can be formulated as:

$$\arg \min_{\mathbf{x}, \{\boldsymbol{\alpha}_i\}_{i \in \Omega}} \frac{1}{2} \|\mathbf{x} - \mathbf{y}\|_2^2 + \sum_{i \in \Omega} \|\boldsymbol{\alpha}_i\|_0^0 \quad s.t. \quad \|\mathbf{R}_i \mathbf{x} - \mathbf{D}\boldsymbol{\alpha}_i\|_2 \leq \delta, \quad \forall i \in \Omega. \quad (2.36)$$

In this formulation, the domain of the image is defined as Ω , and the index locations are represented by i . The operator \mathbf{R}_i extracts a patch of size $\sqrt{n} \times \sqrt{n}$ from location i . For each patch a representation α_i is constructed that should be both sparse and represent $\mathbf{R}_i \mathbf{x}$ within a pre-specified error.

To obtain a clean image estimate $\hat{\mathbf{x}}$, first the set of representations $\{\alpha_i\}_{i \in \Omega}$ must be obtained. Then, $\hat{\mathbf{x}}$ can be computed by fixing these representations and solving

$$\arg \min_{\mathbf{x}} \frac{1}{2} \|\mathbf{x} - \mathbf{y}\|_2^2 + \lambda \|\mathbf{R}_i \mathbf{x} - \mathbf{D} \alpha_i\|_2 \quad (2.37)$$

More details of this problem can be found in (ELAD et al., 2010). Related works in image denoising are reported in (ELAD et al., 2006; SUCHITHRA et al., 2013; VALIOLLAHZADEH et al., 2009).

2.5.4 Signal Separation

Source separation problems in digital signal processing are those in which several signals have been mixed together into a combined signal and the objective is to recover the original component signals from the combined signal. The problem of signal separation consists in the observation $\mathbf{y} = \mathbf{x}_1 + \mathbf{x}_2 + \nu$ that is composed of two signals, \mathbf{x}_1 and \mathbf{x}_2 , to be separated, along with additive noise ν . \mathbf{x}_1 and \mathbf{x}_2 have sparse representations with respect to two known and different dictionaries \mathbf{D}_1 and \mathbf{D}_2 , respectively. Separation can be achieved by finding the two sparsest representations $\hat{\alpha}_1$ and $\hat{\alpha}_2$ that can explain \mathbf{y} .

$$\{\hat{\alpha}_1, \hat{\alpha}_2\} = \arg \min_{\alpha_1, \alpha_2} \|\alpha_1\|_0 + \|\alpha_2\|_0 \quad s.t. \quad \|\mathbf{D}_1 \alpha_1 + \mathbf{D}_2 \alpha_2 - \mathbf{y}\|_2^2 \leq n \sigma_\nu^2 \quad (2.38)$$

The error bound $n \sigma_\nu^2$ is a direct consequence of the knowledge of the noise power.

Solution to the above problem can be addressed in different ways. One option is an iterated path by considering an alternated denoising problem, where $\hat{\alpha}_1$ is estimated as the denoising of the signal $\mathbf{y} + \mathbf{x}_2$, while $\hat{\alpha}_2$ is obtained when denoising $\mathbf{y} + \mathbf{x}_1$. Other methods can be found in (SHOHAM et al., 2008) where a review of algorithms for signal separation exploiting sparse representations is presented, with application to texture image separation. This work is based on greedy Morphological Component Analysis (MCA) algorithms (ELAD et al., 2005).

2.5.5 Clustering and Image classification

Classification based on sparse representation involves the use of different algorithms to learn dictionaries from the labeled training dataset and then use the features of the sparse decomposition of the testing signal for classification. We devote a complete description of this topic in the next section. Regarding to clustering, some authors (RAMIREZ et al., 2010) present the basis framework for clustering datasets that are well represented in the sparse modeling framework with a set of learned dictionaries. Given K clusters, the method learns K dictionaries for representing the data, and then associates each signal to the dictionary for which the “best”

sparse decomposition is obtained. The basis clustering framework can be defined as:

$$\arg \min_{\mathbf{D}_i, C_i} \sum_{i=1}^K \sum_{\mathbf{y}_j \in C_i} \mathcal{R}(\mathbf{y}_j, \mathbf{D}_i) \quad (2.39)$$

where $\mathbf{D}_i = [\mathbf{d}_1 | \mathbf{d}_2 | \dots | \mathbf{d}_{k_i}] \in \mathbf{R}^{n \times k_i}$ is a dictionary of k_i atoms associated with the class C_i , $\mathbf{y}_j \in \mathbf{R}^n$ are the data vectors, and \mathcal{R} is a function that measures the goodness of the sparse decomposition for the signal \mathbf{y}_j under the dictionary \mathbf{D}_i . A cost function $\mathcal{R}(\mathbf{y}, \mathbf{D}) = \arg \min_{\mathbf{x}} \|\mathbf{y} - \mathbf{D}\mathbf{x}\|_2^2 + \lambda \|\mathbf{x}\|_1$, can be considered as a measure of performance. It takes into account both the reconstruction error and the complexity of the sparse decomposition. Other measures include a term that promotes incoherence between dictionaries that, with an initialization procedure that combines sparse coding, dictionary learning and spectral clustering is used for unsupervised clustering (RAMIREZ et al., 2010).

As we have seen, sparse representation becomes an important topic of pattern recognition and computer vision. Notice that sparse coefficients could also be interpreted as features, therefore it is natural to explore the benefits of using sparse representation and DL for classification.

We aim to show how this technique is useful dealing with two specific problems we are interested in this work: classification of LV wall motion and detection of cardiac fibrosis in cardiac medical images. In the next section we describe some DL-based classification methods with emphasis in two representative models: discriminative dictionary learning methods and dictionary learning based on kernels for classification.

2.6 DL-based classification methods

The primary goal of pattern recognition is supervised or unsupervised classification (JAIN et al., 2000). Classifier design is one of the most popular technologies. The goal of supervised learning is to build a concise model of the distribution of class labels in terms of predictor features (KOTSIAKIS, 2007). Sparse representations are originally trained to contain sufficient information for reconstruction, however, from the point of view of signal classification, sparse representation is a reconstructive approach. In (WRIGHT et al., 2009) sparse representation is applied to classification by exploiting the sparse representation based classification (SRC) algorithm. For SRC, a test sample is represented as a sparse combination of training samples, and its sparse representation coefficient is obtained by solving the sparse representation problem. The test sample is assigned to the class that minimizes the residual between itself and the reconstruction signal represented by training samples of this class. The SRC algorithm is presented in Table 2.1, where for each class i , $\delta_i : \mathbb{R}^n \rightarrow \mathbb{R}^n$ is a characteristic function that selects the coefficients associated with the i -th class, thus, for $\mathbf{x} \in \mathbb{R}^n$, $\delta_i(\mathbf{x}) \in \mathbb{R}^n$, is a new vector whose only non-zero entries are the entries in \mathbf{x} that are associated with class i .

TABLE 2.1– Sparse Representation Classification SRC algorithm

Input: A matrix of training samples $\mathbf{A} = [\mathbf{A}_1 \mathbf{A}_2 \dots \mathbf{A}_k] \in \mathbb{R}^{m \times n}$ for k classes
A test sample $\mathbf{y} \in \mathbb{R}^m$, and an optimal error tolerance $\varepsilon > 0$
Normalize the columns of \mathbf{A} to have unit ℓ^2 -norm.
Solve the ℓ^1 -minimization problem:
$\hat{\mathbf{x}}_1 = \arg \min_{\mathbf{x}} \ \mathbf{x}\ _1 \quad s.t. \quad \mathbf{y} = \mathbf{A}\mathbf{x}$
or alternative solve
$\hat{\mathbf{x}}_1 = \arg \min_{\mathbf{x}} \ \mathbf{x}\ _1 \quad s.t. \quad \ \mathbf{y} - \mathbf{A}\mathbf{x}\ _2 \leq \varepsilon$
Compute the residuals $\mathbf{r}_i(\mathbf{y}) = \ \mathbf{y} - \mathbf{A}\delta_i(\hat{\mathbf{x}}_1)\ _2$, for $i = 1, \dots, k$.
Output: $identity(\mathbf{y}) = \arg \min_i \mathbf{r}_i(\mathbf{y})$

Later several algorithms (RAMIREZ et al., 2010; M. YANG et al., 2010) have emerged from the same framework. A particular extension of the SRC framework is the Kernel Sparse representation based classification KSRC (YIN et al., 2012) for high dimensional signals. In KSRC, samples are mapped into a high dimensional feature space firstly and then SRC is performed in this new feature space by utilizing a kernel based classification approach. The discrimination criteria in KSRC algorithm is incorporated with the assumption that sparse representation coefficient in the high dimensional feature space contains more effective discriminating information than sparse representation coefficient in the original feature space.

Another work related to Sparse representation with kernels is presented in (GAO et al., 2013), (KSR) which consists in a sparse coding technique in a high dimensional feature space mapped by an implicit mapping function. They incorporates KSR into spatial pyramid matching (SPM), achieving a good performance for image classification.

The SRC algorithm has achieved competitive performance on face recognition. However the performance of classification of SRC has been improved by using discriminative dictionaries based on Dictionary Learning (DL) (CAI et al., 2014). Recent works in DL (RODRIGUEZ et al., 2008), (MAIRAL et al., 2008b), make the sparse signal decomposition discriminative. Discrimination criteria was introduced in the framework of sparse representation of signals by (HUANG et al., 2007) and into the framework of Dictionary Learning by (RODRIGUEZ et al., 2008). Major contribution of these works in DL is the introduction of a metric which includes both reconstruction and discrimination terms in the dictionary learning process, benefiting from the best of both discriminative and reconstructive worlds.

Formally, a DL-based classification approach consists of two steps: a training step based on a DL model and a prediction step based on the sparse codes coefficients \mathbf{X} obtained in the training step. In the general framework of DL for classification, the set of signals \mathbf{Y} is mapped to its high dimensional feature (sparse coefficient) using a learned dictionary \mathbf{D} , which could make the hidden patterns more prominent and easier to capture. A classifier \mathbf{W} is then used to predict the label vector \mathbf{l} of the test data. The key in this problem is to design \mathbf{D} and \mathbf{X} with discriminative properties (discriminative dictionary learning) by adding extra constraints $f_{\mathbf{X}}(\cdot)$

(over the sparse coefficients) and/or $f_{\mathbf{D}}(\cdot)$ (over the dictionary atoms). Now the optimization problem in 2.25 becomes:

$$\langle \mathbf{D}, \mathbf{X} \rangle = \arg \min_{\mathbf{D}, \mathbf{X}} \|\mathbf{Y} - \mathbf{D}\mathbf{X}\|_F^2 + \lambda_1 f_{\mathbf{X}}(\mathbf{X}) + \lambda_2 f_{\mathbf{D}}(\mathbf{D}) \quad s.t. \quad \forall i, \|\mathbf{x}_i\|_0 \leq T, \quad (2.40)$$

The parameters λ_1 and λ_2 balances the contribution of each term. The function $f_{\mathbf{X}}(\cdot)$ could be a logistic function (MAIRAL et al., 2012), a linear classifier (RODRIGUEZ et al., 2008), (Q. ZHANG et al., 2010), a label consistency term (JIANG et al., 2013a), a low rank constraint (Y. ZHANG et al., 2013) or Fisher discrimination criterion (M. YANG et al., 2014). An example of $f_{\mathbf{D}}(\cdot)$ is to force the sub-dictionaries for different classes to be as incoherent as possible (RAMIREZ et al., 2010). Most of these methods correspond to discriminative dictionary learning approaches that are described later.

In the next subsection we describe two specific DL approaches extensively used in natural images. We search the benefits of using dictionaries, directly learned from a set of training medical images, that better capture the distribution of the data and later, can be used in statistical inference tasks such as classification and detection. Specifically, we addressed two specific DL approaches in the scope of this thesis: the first one corresponds to discriminative dictionary learning approaches and the second one corresponds to a dictionary learning algorithm based on kernel in which a simple classifier is trained over the sparse code coefficients of the input data. These approaches will be adapted for the classification of LV wall motion in cardiac cine MRI. The DL algorithm based on kernel in combination with clustering, will be used for detection of cardiac fibrosis in late gadolinium enhanced MRI. To the best of our knowledge these approaches have not been used in cardiac medical images for the proposed applications.

2.6.1 Discriminative DL

The classification task based on dictionary learning framework consists in learn a classification-oriented dictionary in a supervised learning fashion by exploring the label information of the training data. In (WANG et al., 2014), a classification-oriented dictionary learning model is presented in three scenarios:

- First scenario uses the labeling information to learn class-specific sub-dictionaries, by which way, the discrimination power of the overall dictionary concatenated by the sub-dictionaries is improved. Most of the algorithms in this scenario originates from SRC method which uses the original training images as a predefined dictionary. In this group we can found the Metaface learning method (M. YANG et al., 2010) that learns a class-specific dictionary for each class, thus the dictionary becomes more compact and more discriminative than the originated by the SRC algorithm which is not effective to represent query images when the dictionary is too large and also due to the noisy information in the training data. Another method in this scenario is the dictionary learning with structure incoherence (DLSI) (RAMIREZ et al., 2010) which promotes learning class-specific sub-dictionaries for each class with a structural incoherence penalty term to make the sub-dictionaries as independent

as possible. These approaches usually exploit reconstruction-based classifier for the final classification, i.e. reconstructing the novel signal by each class-specific dictionary and identifying the signal to the class whose sub-dictionary produces the smallest reconstruction error.

- Methods from the second scenario apply the labeling information to a criterion on the coefficients and thus propagate the discrimination power to the dictionary. Methods in the second scenario drive the sparse coefficients more discriminative to enhance the discrimination power of the overall dictionary. In this group we have the Supervised DL method proposed by (MAIRAL et al., 2009) which adds a logistic loss function on the sparse coefficients to the DL framework, achieving good performances in hand-written digit recognition and texture classification. Other method in this scenario is the discriminative K-SVD algorithm (D-KSVD) (Q. ZHANG et al., 2010) which embeds a linear classifier on the sparse coefficients into the DL framework achieving good performance in face recognition. However, the performance of this algorithm is further improved by the Label Consistent K-SVD algorithm (LC-KSVD) (JIANG et al., 2013b) which adds a label consistence term on D-KSVD thus driving the sparse coefficients more discriminative. This algorithm achieves impressive results on face recognition and object classification.
- The third scenario inherits the advantages of the above scenarios by using the label information on the updating of both the dictionary and the coefficients. Methods in this scenario simultaneously learn class-specific sub-dictionaries and make the coefficients more discriminative. They concern for instance, the Fisher Discriminant DL algorithm (FDDL) (M. YANG et al., 2014) which makes the coefficients more discriminative based on Fisher criterion achieving good performance on face recognition, digit recognition and gender classification. More recent in (WANG et al., 2014), a DL approach is proposed to explicitly learn a class-specific dictionary (called particularity) for each category that captures the most discriminative features of this category, and simultaneously learns a common pattern pool (called commonality), whose atoms are shared by all the categories and only contribute to representation of the data rather than discrimination. This method achieves very competitive performances on various classification tasks, such as face recognition, hand-written digit recognition, scene classification and object categorization.

In the next subsection, we describe two specific discriminative dictionary learning algorithms: the first one, from the second scenario where the discrimination of the learned dictionary is enforced by imposing structural constraints on the dictionary: the Label Consistent K-SVD algorithm (LC-KSVD) (JIANG et al., 2013a), and the second one, a technique in the third scenario where the discrimination is enforced by imposing a discrimination term on the sparse decomposition vectors: the Fisher discriminant DL algorithm (M. YANG et al., 2014). In this thesis, both algorithms are adapted for the specific task of classification of LV wall motion in cardiac MRI.

2.6.1.1 Label consistent K-SVD (LC-KSVD)

The Label Consistent K-SVD (LC-KSVD) algorithm (JIANG et al., 2013a) learns a discriminative dictionary for sparse coding. Let $\mathbf{Y} \in \mathbb{R}^{n \times N}$ be a data matrix (a finite training set of signals) where each column is a n -dimensional input signal, $\mathbf{H} = [\mathbf{h}_1, \dots, \mathbf{h}_N]^T \in \mathbb{R}^{m \times N}$ are the class labels of the input signals \mathbf{Y} with $\mathbf{h}_i = [0, 0 \dots 1 \dots 0, 0] \in \mathbb{R}^m$ is a label vector corresponding to an input signal \mathbf{y}_i , where the non-zero position indicates the class of \mathbf{y}_i . m represents the number of classes. To obtain a discriminative dictionary $\mathbf{D} = [\mathbf{d}_1, \mathbf{d}_2, \mathbf{d}_3, \dots, \mathbf{d}_K] \in \mathbb{R}^{n \times K}$ with K atoms and the coefficient matrix $\mathbf{X} = [\mathbf{x}_1, \mathbf{x}_2, \dots, \mathbf{x}_N] \in \mathbb{R}^{K \times N}$ of input signals \mathbf{Y} , the LC-KSVD algorithm, in addition to using class labels of training data, introduces a label consistent constraint called discriminative sparse-code error, and combine it with the reconstruction error $\|\mathbf{Y} - \mathbf{D}\mathbf{X}\|$ and the classification error to form a unified objective function as follows:

$$\begin{aligned} \langle \mathbf{D}, \mathbf{W}, \mathbf{A}, \mathbf{X} \rangle &= \arg \min_{\mathbf{D}, \mathbf{W}, \mathbf{A}, \mathbf{X}} \|\mathbf{Y} - \mathbf{D}\mathbf{X}\|_2^2 + \\ &\quad \alpha \|\mathbf{Q} - \mathbf{A}\mathbf{X}\|_2^2 + \beta \|\mathbf{H} - \mathbf{W}\mathbf{X}\|_2^2 \\ &\quad s.t. \quad \forall i, \|\mathbf{x}_i\|_0 \leq T, \end{aligned} \quad (2.41)$$

where, $\|\mathbf{Q} - \mathbf{A}\mathbf{X}\|$ represent the discriminative sparse-code error, and $\|\mathbf{H} - \mathbf{W}\mathbf{X}\|$ represents the classification error.

$\mathbf{Q} = [\mathbf{q}_1, \dots, \mathbf{q}_N] \in \mathbb{R}^{K \times N}$ are the discriminative sparse codes of input signals \mathbf{Y} for classification and $\mathbf{A} = [\mathbf{a}_1, \mathbf{a}_2, \dots, \mathbf{a}_K] \in \mathbb{R}^{K \times K}$ is a linear transformation matrix. A column \mathbf{q}_i has non-zero values only where the corresponding dictionary elements are from the same class as the i -th signal \mathbf{y}_i . The linear transformation, $g(\mathbf{x}; \mathbf{A}) = \mathbf{A}\mathbf{x}$, maps the original sparse codes coefficients \mathbf{x} to be most discriminative in the sparse feature space \mathbb{R}^K . $\mathbf{W} \in \mathbb{R}^{m \times K}$ denotes the classifier parameters to be learned. α and β are scalar parameters controlling the relative contribution of the corresponding terms. The discriminative sparse-code error term can make the sparse codes discriminative between classes while the classification error term supports learning an optimal classifier.

Intuitively, the final classification mechanism is very fast due to the obtained classifier parameter matrix $\hat{\mathbf{W}}$. An advantage of this approach is that a test sample is classified just by evaluating the expression:

$$\hat{j} = \arg \max_j (\mathbf{l} = \hat{\mathbf{W}}\mathbf{x}_i), \quad (2.42)$$

where \mathbf{x}_i is the sparse representation of the tested signal \mathbf{y}_i , \hat{j} is the respective estimated label and $\mathbf{l} \in \mathbb{R}^m$ is the class label vector.

The LC-KSVD approach is summarized in Algorithm 4. Further implementation details can be found in the original paper (JIANG et al., 2013b).

Algorithm 4 Label Consistent K-SVD algorithm (LC-KSVD)

-
- 1: **Input:** A matrix of input signals \mathbf{Y}
 - 2: The discriminative sparse codes \mathbf{Q}
 - 3: The class labels of input signals \mathbf{H}
 - 4: Parameters: α, β, T, K
 - 5: **Compute** $\mathbf{D}^{(0)}$ by combining class-specific dictionary items for each class using
 - 6: the original K-SVD algorithm
 - 7: **Compute** Sparse codes $\mathbf{X}^{(0)}$ for \mathbf{Y} using:
 - 8: $\arg \min_{\mathbf{x}} \|\mathbf{y}_i - \mathbf{D}\mathbf{x}\|_2^2 \quad s.t. \quad \|\mathbf{x}\|_0 \leq T$
 - 9: **Compute** $\mathbf{A}^{(0)}$ and $\mathbf{W}^{(0)}$ by using the solution to a multivariate regression model:
 - 10: $\mathbf{A} = \mathbf{Q}\mathbf{X}^T(\mathbf{X}\mathbf{X}^T + \lambda_2\mathbf{I})^{-1}$
 - 11: $\mathbf{W} = \mathbf{H}\mathbf{X}^T(\mathbf{X}\mathbf{X}^T + \lambda_1\mathbf{I})^{-1}$
 - 12: **Initialize:**
 - 13:
$$\mathbf{Y}_{new} = \begin{pmatrix} \mathbf{Y} \\ \sqrt{\alpha}\mathbf{Q}\sqrt{\beta}\mathbf{H} \end{pmatrix} \quad \mathbf{D}_{new} = \begin{pmatrix} \mathbf{D}^{(0)} \\ \sqrt{\alpha}\mathbf{A}^{(0)} \\ \sqrt{\beta}\mathbf{W}^{(0)} \end{pmatrix}$$
 - 14: **Update** \mathbf{D}_{new} by solving
 - 15: $\langle \mathbf{D}_{new}, \mathbf{X} \rangle = \arg \min_{\mathbf{D}_{new}, \mathbf{X}} \|\mathbf{Y}_{new} - \mathbf{D}_{new}\mathbf{X}\|_2^2 \quad s.t. \quad \|\mathbf{x}_i\|_0 \leq T$
 - 16: **Obtain** $\hat{\mathbf{D}}, \hat{\mathbf{A}}, \hat{\mathbf{W}}$ from \mathbf{D}_{new} by:
 - 17:
$$\hat{\mathbf{D}} = \left\{ \frac{\mathbf{d}_1}{\|\mathbf{d}_1\|_2} \dots \frac{\mathbf{d}_K}{\|\mathbf{d}_K\|_2} \right\}, \quad \hat{\mathbf{A}} = \left\{ \frac{\mathbf{a}_1}{\|\mathbf{a}_1\|_2} \dots \frac{\mathbf{a}_K}{\|\mathbf{a}_K\|_2} \right\}, \quad \hat{\mathbf{W}} = \left\{ \frac{\mathbf{w}_1}{\|\mathbf{w}_1\|_2} \dots \frac{\mathbf{w}_K}{\|\mathbf{w}_K\|_2} \right\}$$
 - 18: **Output:** For a test signal \mathbf{y}_i first compute its sparse representation $\hat{\mathbf{x}}_i$
 - 19: Estimate the label with the linear predictive classifier
 - 20:
$$j = \arg \max_j (\mathbf{l} = \hat{\mathbf{W}}\hat{\mathbf{x}}_i)$$
-

2.6.1.2 Fisher Discriminant DL (FD-DL)

Instead of learning a shared dictionary to all classes, the FD-DL algorithm (M. YANG et al., 2014), proposes to learn a structured dictionary $\mathbf{D} = [\mathbf{D}_1 | \mathbf{D}_2 | \dots | \mathbf{D}_m]$, where \mathbf{D}_i is the class-specified sub-dictionary associated with class i , and m is the total number of classes.

Denoting by $\mathbf{Y} = [\mathbf{Y}_1 | \mathbf{Y}_2 | \dots | \mathbf{Y}_m]$ the set of training samples, where \mathbf{Y}_i is the sub-set of the training samples from the i -th class. Furthermore, let \mathbf{X} be the coding coefficient matrix of \mathbf{Y} over \mathbf{D} i.e., $\mathbf{X} = [\mathbf{X}_1 | \mathbf{X}_2 | \dots | \mathbf{X}_m]$, where \mathbf{X}_i is the sub-matrix containing the sparse coding coefficients of \mathbf{Y}_i over \mathbf{D} . They proposed to obtain the dictionary \mathbf{D} and the coding coefficient matrix \mathbf{X} by solving:

$$(\mathbf{D}, \mathbf{X}) = \arg \min_{\mathbf{D}, \mathbf{X}} \{r(\mathbf{Y}, \mathbf{D}, \mathbf{X}) + \lambda_1 \|\mathbf{X}\|_1 + \lambda_2 \|f(\mathbf{X})\|_1\}, \quad (2.43)$$

where $r(\mathbf{Y}, \mathbf{D}, \mathbf{X})$ is the discriminative fidelity term, $\|\mathbf{X}\|_1$ is the sparsity constraint, $f(\mathbf{X})$ is a discrimination constraint imposed on the coefficient matrix \mathbf{X} , and λ_1 and λ_2 are regularization parameters. As mentioned in (M. YANG et al., 2014), the discrimination ability of FD-DL is two-folds.

Firstly, each sub-dictionary of the trained full dictionary has good representation power to the samples from the corresponding class, and it is expected that it has poor representation

power to the samples from other classes. This is achieved by the discriminative fidelity term that is defined as:

$$r(\mathbf{Y}_i, \mathbf{D}, \mathbf{X}_i) = \|\mathbf{Y}_i - \mathbf{D}\mathbf{X}_i\|_F^2 + \|\mathbf{Y}_i - \mathbf{D}_i\mathbf{X}_i^i\|_F^2 + \sum_{j=1, j \neq i}^m \|\mathbf{D}_j\mathbf{X}_i^j\|_F^2 \quad (2.44)$$

where the representation coefficients \mathbf{X}_i of \mathbf{Y}_i over \mathbf{D}_i are written as \mathbf{X}_i^i and over \mathbf{D}_j are written as \mathbf{X}_i^j .

The dictionary \mathbf{D} should represent well \mathbf{Y}_i which is assured by the first term. Then, since \mathbf{D}_i is associated with the i -th class, it is expected that \mathbf{Y}_i could be well represented by \mathbf{D}_i but not by \mathbf{D}_j , $j \neq i$. This implies that \mathbf{X}_i^i should have some significant coefficients such that $\|\mathbf{Y}_i - \mathbf{D}_i\mathbf{X}_i^i\|_F^2$ is small, while \mathbf{X}_i^j should have very small coefficients such that $\|\mathbf{D}_j\mathbf{X}_i^j\|_F^2$ is small.

Secondly, based on the Fisher discrimination criterion, FD-DL will result in discriminative coefficients by minimizing the within-class scatter of \mathbf{X} denoted by $S_W(\mathbf{X})$ and maximizing the between-class scatter of \mathbf{X} denoted by $S_B(\mathbf{X})$. The Fisher discrimination criterion is introduced by the discriminative coefficient term $f(\mathbf{X})$ defined as:

$$f(\mathbf{X}) = tr(S_W(\mathbf{X})) - tr(S_B(\mathbf{X})) + \eta\|\mathbf{X}\|_F^2 \quad (2.45)$$

The FD-DL is presented in Algorithm 5. It is divided into two sub-problems: updating \mathbf{X} by fixing \mathbf{D} ; and updating \mathbf{D} by fixing \mathbf{X} . An Iterative Projection Method (IPM) (ROSASCO et al., 2009) is used to solve the first problem, while the second problem (step 3) is solved by employing the algorithm for meta-face learning proposed by the same authors of the FD-DL algorithm in (M. YANG et al., 2010). Further implementation details can be found in the original paper in (M. YANG et al., 2014).

Once the discriminative dictionary \mathbf{D} is learned, a testing sample \mathbf{y} can be classified by coding it over \mathbf{D} . In this case, the sparse coding coefficients $\hat{\boldsymbol{\alpha}}$ can be obtained by solving:

$$\hat{\boldsymbol{\alpha}} = \arg \min_{\boldsymbol{\alpha}} \{\|\mathbf{y} - \mathbf{D}\boldsymbol{\alpha}\|_2^2 + \gamma\|\boldsymbol{\alpha}\|_1\}, \quad (2.46)$$

where γ is a constant. Let $\hat{\boldsymbol{\alpha}} = [\hat{\boldsymbol{\alpha}}_1^T, \hat{\boldsymbol{\alpha}}_2^T, \dots, \hat{\boldsymbol{\alpha}}_m^T]^T$, be the sparse representation of the testing sample in \mathbf{D} , where $\hat{\boldsymbol{\alpha}}_i$ is the coefficient vector associated with sub-dictionary \mathbf{D}_i . The metric for final classification is defined as:

$$e_i = \|\mathbf{y} - \mathbf{D}_i\hat{\boldsymbol{\alpha}}_i\|_2^2 + w \cdot \|\hat{\boldsymbol{\alpha}} - \mathbf{m}_i\|_2^2, \quad (2.47)$$

where the first term is the reconstruction error by class i , the second term is the distance between the coefficient vector $\hat{\boldsymbol{\alpha}}$ and the learned mean vector \mathbf{m}_i of class i , and w is a weight to balance the contribution of both terms. The testing sample is classified to the class that outputs the smallest error e_i . The metric for final classification in Equation (2.47) is used when the number of training samples of each class is relatively small. It is known as Global classifier. When the number of training samples of each class is relatively large, the algorithm uses a Local classifier. In this case the learned dictionary \mathbf{D}_i is able to well span the sample space of class i , and thus

Algorithm 5 Fisher Discrimination Dictionary Learning (FD-DL)

-
- 1: **Input:** A matrix of input signals \mathbf{Y} , m = number of classes
 - 2: **Initialization of \mathbf{D} .**
 - 3: Initialize all the p_i atoms of each \mathbf{D}_i as random vectors with unit ℓ^2 -norm.
 - 4: **Update** the sparse coding coefficients \mathbf{X} .
 - 5: Fix \mathbf{D} and solve \mathbf{X}_i , $i = 1, 2, \dots, m$, one by one by solving
 - 6: $J(\mathbf{X}_i) = \arg \min_{(\mathbf{X}_i)} \left\{ r(\mathbf{Y}_i, \mathbf{D}, \mathbf{X}_i) + \lambda_1 \|\mathbf{X}_i\|_1 + \lambda_2 f_i(\mathbf{X}_i) \right\}$, with
 - 7: $r(\mathbf{Y}_i, \mathbf{D}, \mathbf{X}_i) = \|\mathbf{Y}_i - \mathbf{D}\mathbf{X}_i\|_F^2 + \|\mathbf{Y}_i - \mathbf{D}_i\mathbf{X}_i^i\|_F^2 + \sum_{j=1, j \neq i}^m \|\mathbf{D}_j\mathbf{X}_i^j\|_F^2$, and
 - 8: $f_i(\mathbf{X}_i) = \|\mathbf{X}_i - \mathbf{M}_i\|_F^2 - \sum_{k=1}^m \|\mathbf{M}_k - \mathbf{M}\|_F^2 + \eta \|\mathbf{X}_i\|_F^2$,
 - 9: where \mathbf{M}_k and \mathbf{M} are the mean vector matrices of class k and all classes, respectively.
 - 10: **Updating dictionary \mathbf{D} .**
 - 11: Fix \mathbf{X} and update each \mathbf{D}_i , $i = 1, 2, \dots, m$, by solving:
 - 12: $J(\mathbf{D}_i) = \arg \min_{(\mathbf{D}_i)} \left\{ \|\mathbf{Y} - \mathbf{D}_i\mathbf{X}^i - \sum_{j=1, j \neq i}^m \mathbf{D}_j\mathbf{X}^j\|_F^2 + \|\mathbf{Y}_i - \mathbf{D}_i\mathbf{X}_i^i\|_F^2 + \sum_{j=1, j \neq i}^m \|\mathbf{D}_i\mathbf{X}_j^i\|_F^2 \right\}$
 - 13: **Output.** Return to step 2 until the values of $J(\mathbf{D}, \mathbf{X})$ in adjacent iterations are close
 - 14: enough or the maximum number of iterations is reached. Output \mathbf{D} and \mathbf{X} .
-

directly code the testing sample \mathbf{y} by \mathbf{D}_i to reduce the computational cost and the interference of other dictionaries. The sparse coding coefficients can be obtained by solving:

$$\hat{\boldsymbol{\alpha}} = \arg \min_{\boldsymbol{\alpha}} \left\{ \|\mathbf{y} - \mathbf{D}_i\boldsymbol{\alpha}\|_2^2 + \gamma_1 \|\boldsymbol{\alpha}\|_1 + \gamma_2 \|\boldsymbol{\alpha} - \mathbf{m}_i^i\|_2^2 \right\}, \quad (2.48)$$

where γ_1 and γ_2 are constants. The metric for final classification is defined as:

$$e_i = \|\mathbf{y} - \mathbf{D}_i\hat{\boldsymbol{\alpha}}\|_2^2 + \gamma_1 \|\hat{\boldsymbol{\alpha}}\|_1 + \gamma_2 \|\hat{\boldsymbol{\alpha}} - \mathbf{m}_i^i\|_2^2, \quad (2.49)$$

2.6.2 Kernel-based DL for classification

The DL-based classification approach consists of two steps: a training step based on a DL model and a prediction step based on the sparse codes coefficients \mathbf{X} obtained in the training step. The sparse coding problem for sparse representation can be obtained by solving a ℓ^1 -regularized ℓ^1 least squares (ℓ^1 -LS) sparse coding model:

$$\mathbf{x} = \min_{\mathbf{x}} \frac{1}{2} \|\mathbf{y} - \mathbf{D}\mathbf{x}\|_2^2 + \lambda \|\mathbf{x}\|_1 \quad (2.50)$$

Where $\mathbf{y} \in \mathbb{R}^n$ is a new signal and $\mathbf{D} = [\mathbf{d}_1, \mathbf{d}_2, \mathbf{d}_3, \dots, \mathbf{d}_K] \in \mathbb{R}^{n \times K}$ with K atoms, is a given dictionary.

Let $\mathbf{Y} \in \mathbb{R}^{n \times N}$ be a data matrix (a finite training set of signals) where each column is a n -dimensional input signal. A dictionary $\mathbf{D} = [\mathbf{d}_1, \mathbf{d}_2, \mathbf{d}_3, \dots, \mathbf{d}_K] \in \mathbb{R}^{n \times K}$ with K atoms and the coefficient matrix $\mathbf{X} = [\mathbf{x}_1, \mathbf{x}_2, \dots, \mathbf{x}_N] \in \mathbb{R}^{K \times N}$ of input signals \mathbf{Y} , can be obtained with a generalized DL model where sparse representation is introduced from a Bayesian viewpoint

assuming Gaussian prior or Uniform prior over the dictionary atoms. The models proposed by (Li et al., 2013) using both priors: Gaussian and Uniform are presented in Equations (6.2) and (2.52) respectively:

$$\min_{\mathbf{D}, \mathbf{X}} \frac{1}{2} \|\mathbf{Y} - \mathbf{D}\mathbf{X}\|_F^2 + \frac{\alpha}{2} \text{trace}(\mathbf{D}^T \mathbf{D}) + \lambda \sum_{i=1}^N \|\mathbf{x}_i\|_1, \quad (2.51)$$

$$\min_{\mathbf{D}, \mathbf{X}} \frac{1}{2} \|\mathbf{Y} - \mathbf{D}\mathbf{X}\|_F^2 + \lambda \sum_{i=1}^N \|\mathbf{x}_i\|_1 \quad \text{s.t.} \quad d_i^T d_i = 1, \\ i = 1, \dots, k, \quad (2.52)$$

Classification based on DL can be performed by training a classifier over the sparse training coefficients matrix \mathbf{X} . Several methods can be applied: Nearest Neighbor (*NN*) rule, weighted *K-NN* rule or the nearest subspace (*NS*) rule. The class label of new p test instances can be predicted using the classifier obtained in the training step and the learned dictionary \mathbf{D} . As the selected classifier is trained based on the sparse coefficients of the input data, the test data need to be represented in the same space of representation (sparse coefficients) over the learned dictionary. To this end, the sparse coefficients matrix \mathbf{X} for the new test instances can be obtained by solving a l_1 -regularized least squares problem reformulated to the following smooth constrained quadratic problem (*QP*):

$$\min_{\mathbf{X}, \mathbf{U}} \sum_{i=1}^p \frac{1}{2} \mathbf{x}_i^T \mathbf{H} \mathbf{x}_i + \mathbf{g}_i^T \mathbf{x}_i + \lambda^T \mathbf{u}_i \quad \text{s.t.} \quad -\mathbf{U} \leq \mathbf{X} \leq \mathbf{U}, \quad (2.53)$$

where $\mathbf{H}_{k \times k} = \mathbf{D}^T \mathbf{D}$, $\mathbf{g} = -\mathbf{D}^T \mathbf{Y}$ and \mathbf{u}_i is an auxiliary vector variable to squeeze \mathbf{x}_i towards to zero. The sparse coefficients matrix \mathbf{X} for the new test instances, can be also obtained by solving the Non negative Quadratic Problem (*NNQP*):

$$\min_{\mathbf{X}} \sum_{i=1}^p \frac{1}{2} \mathbf{x}_i^T \mathbf{H} \mathbf{x}_i + \mathbf{g}_i^T \mathbf{x}_i \quad \text{s.t.} \quad \mathbf{X} \geq 0 \quad (2.54)$$

As the optimizations of the above problems only require inner products between the instances instead of the original data, the sparse coding problem can be solved by replacing inner products to kernel functions.

We refer this algorithm as KSRDL (Kernel Sparse Representation DL) (Li et al., 2013) and is presented in Algorithm 7, it uses the generic framework for DL based on kernels presented in Algorithm 6.

2.7 Support Vector Machines (SVM)-based classification

The idea behind SVMs is to map the original data points from the input space to a high-dimensional, or even infinite-dimensional, feature space such that the classification problem becomes simpler in the feature space. In SVM, original data is shown as vectors $\mathbf{x}_i \in R^d$ with

Algorithm 6 The generic dictionary learning framework algorithm based on kernels

- 1: **Input:** $K = \mathbf{Y}^T \mathbf{Y}$, dictionary size K , λ
 - 2: **Initialize** \mathbf{X} and $\mathbf{R} = \mathbf{D}^T \mathbf{D}$ randomly;
 - 3: **Update** \mathbf{X} by solving Equation (2.53), or (6.3)
 - 4: For Gaussian prior over \mathbf{D} :
 - 5: Update $\mathbf{R} = \mathbf{X}^\dagger \mathbf{Y}^T \mathbf{Y} \mathbf{X}^*$; wher \dagger denotes the hermitian operator
 - 6: For Uniform prior over \mathbf{D} :
 - 7: Update $\mathbf{R} = \mathbf{X}^\dagger \mathbf{Y}^T \mathbf{Y} \mathbf{X}^*$;
 - 8: Normalize \mathbf{R} by $\mathbf{R} = \mathbf{R} / \sqrt{\text{diag}(\mathbf{R}) \text{diag}(\mathbf{R})^T}$;
 - 9: Update the residual of the DL model
 - 10: Return to step 2 until residual $\leq \varepsilon$ or the maximum number of iterations is reached
 - 11: **Output:** $\mathbf{R} = \mathbf{D}^T \mathbf{D}$, \mathbf{X}
-

Algorithm 7 Dictionary-learning-based classification KSRDL

- 1: **Input:** $\mathbf{Y} \in \mathbb{R}^{n \times N}$: N training instances, c the class labels, $\mathbf{B} \in \mathbb{R}^{n \times p}$: p new instances,
 - 2: k : dictionary size
 - 3: **Training step:**
 - 4: 1: Normalize each training instance to have unit ℓ^2 norm
 - 5: 2: Learn dictionary inner product $\mathbf{D}^T \mathbf{D}$ and sparse coefficient matrix \mathbf{X}
 - 6: of training instances by Algorithm 6.
 - 7: 3: Train a classifier $f(\theta)$ using \mathbf{X} (in the feature space spanned by columns of \mathbf{D}).
 - 8: **Prediction step:**
 - 9: 1: Normalize each new instance to have unit ℓ^2 norm.
 - 10: 2: Obtain the sparse coefficient matrix \mathbf{X} of the new instances by solving
 - 11: Equation (2.53), or (6.3).
 - 12: 3: Predict the class labels of \mathbf{X} using the classifier $f(\theta)$ learned in the training phase.
 - 13: **Output:** the predicted class labels of the p new instances
-

its respective class label $y_i \in (-1, +1)$. The d -dimensional input vector from the input/original space is mapped to the d_h -dimensional feature space using a linear or non linear function $\Phi(\cdot) : \mathbb{R}^d \rightarrow \mathbb{R}^{d_h}$, with $d_h \gg d$.

The separating hyperplane in the feature space is defined as $\mathbf{w}^T \Phi(\mathbf{x}) + b = 0$ where \mathbf{w} is an unknown hyperplane with the same dimension as $\Phi(\mathbf{x})$ and $b \in \mathbb{R}$ is the bias. A test data point \mathbf{x} is assigned to the first class if $f(\mathbf{x}) = \text{sign}(\mathbf{w}^T \Phi(\mathbf{x}) + b)$ equals $+1$ or to the second class if $f(\mathbf{x})$ equals -1 . SVMs are based on the maximum margin principle, and aim at constructing a hyperplane with maximal distance between the two classes (LUTS et al., 2010). The optimization problem for SVMs is written as:

$$\min_{\mathbf{w}, \xi, b} \zeta_1(\mathbf{w}, \xi) = \frac{1}{2} \mathbf{w}^T \mathbf{w} + C \sum_{i=1}^N \xi_i, \text{ s.t.} \quad (2.55)$$

$$y_i(\mathbf{w}^T \Phi(\mathbf{x}_i) + b) \geq 1 - \xi_i, \quad \xi_i \geq 0, \quad i = 1, \dots, N, \quad (2.56)$$

where C is a positive regularization constant and $y_i \in \{-1, +1\}$ is the class label related to th i -th training sample. The regularization constant in the cost function defines the trade-off

between a large margin and misclassification error. The value of ξ_i indicates the distance of \mathbf{x}_i with respect to the decision boundary.

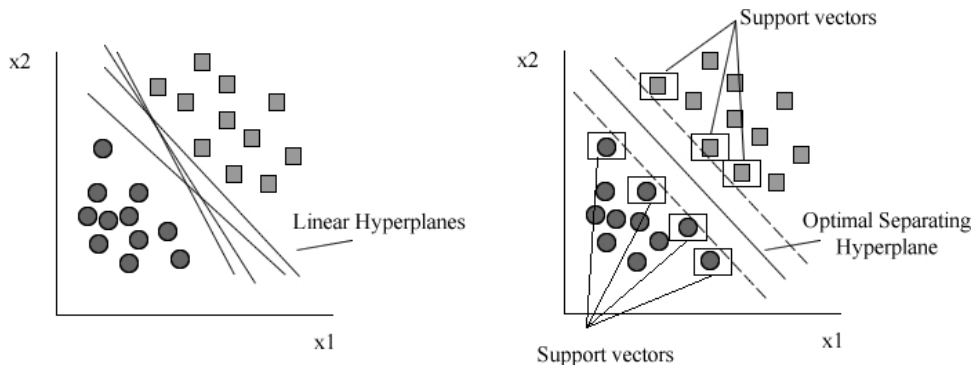


FIGURE 2.6— Separating hyperplanes in a SVM classification problem with two classes. a) the data can be separated by many linear hyperplanes. b) Optimal separating hyperplane.

The optimization problem for SVMs can be written in the dual space using Lagrange multipliers $\alpha_{n_i} > 0$. The solution for the Lagrange multipliers is obtained by solving a quadratic programming problem (LUTS et al., 2010). Finally, the SVM classifier is reduced to:

$$f(\mathbf{x}) = \text{sign} \left(\sum_{i=1}^N \alpha_{n_i} y_{n_i} K(\mathbf{x}, \mathbf{x}_{n_i}) + b \right), \quad (2.57)$$

where N represents the number of training samples and \mathbf{x}_{n_i} are referred to as the support vectors (Figure 2.6). These data points are located close to the decision boundary and contribute to the construction of the separating hyperplane. $K(\mathbf{x}, \mathbf{x}_{n_i})$ is the kernel function that can be, among others,

$$\begin{aligned} K(\mathbf{x}, \mathbf{z}) &= \mathbf{x}^T \mathbf{z}, \text{ linear kernel,} \\ K(\mathbf{x}, \mathbf{z}) &= \exp(-\|\mathbf{x} - \mathbf{z}\|_2^2 / \sigma^2), \text{ RBF kernel,} \end{aligned}$$

where $K(\cdot, \cdot)$ is positive definite for all σ values in the RBF (radial basis function) kernel case. We use traditional SVM in order to evaluate the sparseness of the model where a large number of the resulting Lagrange multipliers are equal to zero. Thus, the sum in (2.57) only takes a few non-zero α_{n_i} values, *i.e.*, the Support Values (SV), that are the data points that are closest to the optimal separating hyperplane.

2.8 Conclusion

We have reviewed sparse representations as a new model that harnesses the local low-dimensional structure of natural images. While image representation and reconstruction have been the most popular goal of sparse modeling and dictionary learning, other important image science applications are starting to be addressed by this framework, in particular, classification.

In medical imaging, the use of sparse representation is verified with the success of the Compressive Sensing theory in the field of reconstruction. Other applications of Sparse representations and Dictionary Learning in medical imaging cover, among others, denoising, segmentation and fusion. As we have mentioned, we are interested in taking advantage of sparse representation and dictionary learning; dealing with two specific problems we are interested in this work: classification of LV wall motion and detection of cardiac fibrosis in cardiac medical images.

We have seen that by incorporating discriminative terms on the DL objective function or by mapping the sparse representation of samples in new feature spaces, the classification task can be addressed; therefore the proposed applications in the field of medical imaging could be addressed.

In the next chapter, we will review the state-of-the-art of sparse representations and Dictionary learning in medical imaging. We will note that classification in cardiac cine MRI for the assessment of LV wall motion and fibrosis detection in LGE-MRI, are tasks that has not yet been addressed by the framework of Dictionary learning.

References

- ABOLGHASEMI, V., S. FERDOWSI, and S. SANEI (2011). “Sparse multichannel source separation using incoherent K-SVD method”. In: *2011 IEEE Statistical Signal Processing Workshop (SSP)*, pp. 477–480.
- AHARON, M., M. ELAD, and A. BRUCKSTEIN (2005). “K-SVD and its non-negative variant for dictionary design”. In: *Proc. SPIE*. Vol. 5914, pp. 327–339.
- (2006). “K-SVD: An Algorithm for Designing Overcomplete Dictionaries for Sparse Representation”. In: *IEEE Transactions on Signal Processing* 54.11, pp. 4311–4322.
- ATAEE, M., H. ZAYYANI, M. BABAIE-ZADEH, and C. JUTTEN (2010). “Parametric dictionary learning using steepest descent”. In: *2010 IEEE International Conference on Acoustics Speech and Signal Processing (ICASSP)*, pp. 1978–1981.
- BARANIUK, R. (2007). “Compressive Sensing [Lecture Notes]”. In: *IEEE Signal Processing Magazine* 24.4, pp. 118–121.
- BARANIUK, R., E. CANDÈS, M. ELAD, and Y. MA (2010). “Applications of Sparse Representation and Compressive Sensing [Scanning the Issue]”. In: *Proceedings of the IEEE* 98.6, pp. 906–909.
- BARCHIESI, D. and M. PLUMBLEY (2013). “Learning Incoherent Dictionaries for Sparse Approximation Using Iterative Projections and Rotations”. In: *IEEE Transactions on Signal Processing* 61.8, pp. 2055–2065.
- BLUMENSATH, T. and M. E. DAVIES (2009). “Iterative hard thresholding for compressed sensing”. In: *Applied and Computational Harmonic Analysis* 27.3, pp. 265–274.
- BRUCKSTEIN, A., D. DONOHO, and M. ELAD (2009). “From Sparse Solutions of Systems of Equations to Sparse Modeling of Signals and Images”. In: *SIAM Rev.* 51.1, pp. 34–81.
- CAI, S., W. ZUO, L. ZHANG, X. FENG, and P. WANG (2014). “Support Vector Guided Dictionary Learning”. In: *Computer Vision – ECCV 2014*. Ed. by D. FLEET, T. PAJDLA, B. SCHIELE,

- and T. TUYTELAARS. Lecture Notes in Computer Science 8692. Springer International Publishing, pp. 624–639.
- CANDÈS, E., J. ROMBERG, and T. TAO (2006). “Robust uncertainty principles: exact signal reconstruction from highly incomplete frequency information”. In: *IEEE Transactions on Information Theory* 52.2, pp. 489–509.
- CANDÈS, E. and T. TAO (2005). “Decoding by linear programming”. In: *IEEE Transactions on Information Theory* 51.12, pp. 4203–4215.
- CHARTRAND, R. (2007). “Exact Reconstruction of Sparse Signals via Nonconvex Minimization”. In: *IEEE Signal Processing Letters* 14.10, pp. 707–710.
- CHEN, S., D. DONOHO, and M. SAUNDERS (1998). “Atomic Decomposition by Basis Pursuit”. In: *SIAM Journal on Scientific Computing* 20.1, pp. 33–61.
- COOLEY, J. W. and J. W. TUKEY (1965). “An Algorithm for the Machine Calculation of Complex Fourier Series”. In: *Mathematics of Computation* 19.90, pp. 297–301.
- DAI, W. and O. MILENKOVIC (2009). “Subspace Pursuit for Compressive Sensing Signal Reconstruction”. In: *IEEE Transactions on Information Theory* 55.5, pp. 2230–2249.
- DONOHO, D. (2006). “Compressed sensing”. In: *IEEE Transaction on Information Theory* 52, pp. 1289–1306.
- DONOHO, D., Y. TSAIG, I. DRORI, and J. STARCK (2012). “Sparse Solution of Underdetermined Systems of Linear Equations by Stagewise Orthogonal Matching Pursuit”. In: *IEEE Transactions on Information Theory* 58.2, pp. 1094–1121.
- ELAD, M. and M. AHARON (2006). “Image Denoising Via Sparse and Redundant Representations Over Learned Dictionaries”. In: *IEEE Transactions on Image Processing* 15.12, pp. 3736–3745.
- ELAD, M., M. FIGUEIREDO, and Y. MA (2010). “On the Role of Sparse and Redundant Representations in Image Processing”. In: *Proceedings of the IEEE* 98.6, pp. 972–982.
- ELAD, M., J. STARCK, P. QUERRE, and D. DONOHO (2005). “Simultaneous cartoon and texture image inpainting using morphological component analysis (MCA)”. In: *Applied and Computational Harmonic Analysis* 19.3, pp. 340–358.
- ENGAN, K., S. AASE, and H. H. (1999). “Method of optimal directions for frame design”. In: *Acoustics, Speech, and Signal Processing, 1999. Proceedings., 1999 IEEE International Conference on*. Vol. 5, 2443–2446 vol.5.
- ENGAN, K., K. SKRETTING, and H. H. (2007). “Family of iterative LS-based dictionary learning algorithms, ILS-DLA, for sparse signal representation”. In: *Digit. Signal Process.* 17.1, pp. 32–49.
- FADILI, M. J., J.-L. STARCK, and F. MURTAGH (2009). “Inpainting and Zooming Using Sparse Representations”. In: *The Computer Journal* 52.1, pp. 64–79.
- GAO, S., I. W.-H. TSANG, and L.-T. CHIA (2013). “Sparse Representation With Kernels”. In: *IEEE Transactions on Image Processing* 22.2, pp. 423–434.
- GORODNITSKY, I. and B. RAO (1997). “Sparse signal reconstruction from limited data using FO-CUSS: a re-weighted minimum norm algorithm”. In: *IEEE Transactions on Signal Processing* 45.3, pp. 600–616.

- GRIBONVAL, R. and M. NIELSEN (2003). “Sparse representations in unions of bases”. In: *IEEE Transactions on Information Theory* 49.12, pp. 3320–3325.
- HUANG, K. and S. AVIYENTE (2007). “Sparse Representation for Signal Classification”. In: *Advances in Neural Information Processing Systems 19*. Ed. by B. SCHÓLKOPF, J. PLATT, and T. HOFFMAN. MIT Press, pp. 609–616.
- JAIN, A. K., R. P. W. DUIN, and J. MAO (2000). “Statistical Pattern Recognition: A Review”. In: *IEEE Transactions on Pattern Analysis and Machine Intelligence* 22.1, pp. 4–37.
- JIANG, Z., Z. LIN, and L. S. DAVIS (2013a). “Label Consistent K-SVD: Learning a Discriminative Dictionary for Recognition”. In: *IEEE Transactions on Pattern Analysis and Machine Intelligence* 35.11, pp. 2651–2664.
- JIANG, Z., Z. LIN, and L. DAVIS (2013b). “Label Consistent K-SVD: Learning a Discriminative Dictionary for Recognition”. In: *IEEE Transactions on Pattern Analysis and Machine Intelligence* 35.11, pp. 2651–2664.
- KOTSIANTIS, S. B. (2007). “Supervised Machine Learning: A Review of Classification Techniques”. In: *Proceedings of the 2007 Conference on Emerging Artificial Intelligence Applications in Computer Engineering: Real World AI Systems with Applications in eHealth, HCI, Information Retrieval and Pervasive Technologies*. Amsterdam, The Netherlands, The Netherlands: IOS Press, pp. 3–24.
- KREUTZ-DELGADO, K., J. MURRAY, B. RAO, K. ENGAN, T. LEE, and T. SEJNOWSKI (2003). “Dictionary Learning Algorithms for Sparse Representation”. In: *Neural computation* 15.2, pp. 349–396.
- LEWICKI, M. S. and T. J. SEJNOWSKI (2000). “Learning Overcomplete Representations”. In: *Neural Computation* 12.2, pp. 337–365.
- LI, Y. and A. NGOM (2013). “Sparse representation approaches for the classification of high-dimensional biological data”. In: *BMC Systems Biology* 7.Suppl 4, S6.
- LUTS, J., F. OJEDA, R. V. DE PLAS, B. D. MOOR, S. V. HUFFEL, and J. A. K. SUYKENS (2010). “A tutorial on support vector machine-based methods for classification problems in chemometrics”. In: *Analytica Chimica Acta* 665 (2), pp. 129–145.
- MAILHÉ, B., S. LESAGE, R. GRIBONVAL, F. BIMBOT, and P. VANDERGHEYNST (2008). “Shift-invariant dictionary learning for sparse representations: extending K-SVD”. In: 5 p.
- MAIRAL, J., F. BACH, and J. PONCE (2012). “Task-Driven Dictionary Learning”. In: *IEEE Transactions on Pattern Analysis and Machine Intelligence* 34.4. arXiv: 1009.5358, pp. 791–804.
- MAIRAL, J., M. ELAD, and G. SAPIRO (2008a). “Sparse Representation for Color Image Restoration”. In: *IEEE Transactions on Image Processing* 17.1, pp. 53–69.
- MAIRAL, J., B. F., P. J., S. G., and Z. A. (2008b). “Supervised Dictionary Learning”. In: *CoRR* abs/0809.3083.
- MAIRAL, J., P. J., G. S., A. ZISSERMAN, and B. F. (2009). “Supervised Dictionary Learning”. In: *Advances in Neural Information Processing Systems 21*. Ed. by D. KOLLER, D. SCHUURMANS, Y. BENGIO, and L. BOTTOU. Curran Associates, Inc., pp. 1033–1040.

- MALLAT, S. and Z. ZHANG (1993). “Matching pursuits with time-frequency dictionaries”. In: *IEEE Transactions on Signal Processing* 41.12, pp. 3397–3415.
- MILLER, A. (2002). *Subset Selection in Regression*. CRC Press.
- NEEDELL, D. and J. TROPP (2009a). “CoSaMP: Iterative signal recovery from incomplete and inaccurate samples”. In: *Applied and Computational Harmonic Analysis* 26.3, pp. 301–321.
- NEEDELL, D. and R. VERSHYNIN (2009b). “Uniform Uncertainty Principle and Signal Recovery via l_0 Regularized Orthogonal Matching Pursuit”. In: *Found. Comput. Math.* 9.3, pp. 317–334.
- OGAWA, T. and M. HASEYAMA (2013). “Image inpainting based on sparse representations with a perceptual metric”. In: *EURASIP Journal on Advances in Signal Processing* 2013.1, pp. 1–26.
- OLSHAUSEN, B. A. and D. J. FIELD (1997). “Sparse coding with an overcomplete basis set: A strategy employed by V1?” In: *Vision Research* 37.23, pp. 3311–3325.
- PATI, Y., R. REZAIIFAR, and P. KRISHNAPRASAD (1993). “Orthogonal matching pursuit: recursive function approximation with applications to wavelet decomposition”. In: 40–44 vol.1.
- RAMIREZ, I., P. SPRECHMANN, and G. SAPIRO (2010). “Classification and clustering via dictionary learning with structured incoherence and shared features”. In: *2010 IEEE Conference on Computer Vision and Pattern Recognition (CVPR)*, pp. 3501–3508.
- RIBHU, R. and D. GHOSH (2012). “Dictionary design for sparse signal representations using K-SVD with sparse Bayesian learning”. In: *2012 IEEE 11th International Conference on Signal Processing (ICSP)*. Vol. 1, pp. 21–25.
- RODRIGUEZ, F. and G. SAPIRO (2008). *Sparse representations for image classification: Learning discriminative and reconstructive non-parametric dictionaries*. Tech. rep. DTIC Document.
- ROSASCO, L., A. VERRI, M. SANTORO, S. MOSCI, and S. VILLA (2009). *Iterative Projection Methods for Structured Sparsity Regularization*. Tech. rep. MIT Technical Reports, MIT-CSAIL-TR-2009-050, CBCL-282.
- RUBINSTEIN, R., A. BRUCKSTEIN, and M. ELAD (2010a). “Dictionaries for Sparse Representation Modeling”. In: *Proceedings of the IEEE* 98.6, pp. 1045–1057.
- RUBINSTEIN, R., M. ZIBULEVSKY, and M. ELAD (2010b). “Double Sparsity: Learning Sparse Dictionaries for Sparse Signal Approximation”. In: *Signal Processing, IEEE Transactions on* 58.3, pp. 1553–1564.
- SAAB, R., R. CHARTRAND, and O. YILMAZ (2008). “Stable sparse approximations via nonconvex optimization”. In: *IEEE International Conference on Acoustics, Speech and Signal Processing, 2008. ICASSP 2008*, pp. 3885–3888.
- SALMAN, A. and J. ROMBERG (2009). “Basis pursuit with sequential measurements and time varying signals”. In: *2009 3rd IEEE International Workshop on Computational Advances in Multi-Sensor Adaptive Processing (CAMSAP)*, pp. 293–296.
- SCHNITER, P., L. C. POTTER, and J. ZINIEL (2009). *Fast Bayesian Matching Pursuit: Model Uncertainty and Parameter Estimation for Sparse Linear Models*.

- SHEN, B., W. HU, Y. ZHANG, and Y.-J. ZHANG (2009). “Image inpainting via sparse representation”. In: *Acoustics, Speech and Signal Processing, 2009. ICASSP 2009. IEEE International Conference on*, pp. 697–700.
- SHOHAM, N. and M. ELAD (2008). “Algorithms for signal separation exploiting sparse representations, with application to texture image separation”. In: *Electrical and Electronics Engineers in Israel, 2008. IEEEI 2008. IEEE 25th Convention of*, pp. 538–542.
- SUCHITHRA, M., P. SUKANYA, P. PRABHA, O. SIKHA, V. SOWMYA, and K. SOMAN (2013). “An experimental study on application of Orthogonal Matching Pursuit algorithm for image denoising”. In: *2013 International Multi-Conference on Automation, Computing, Communication, Control and Compressed Sensing (iMac4s)*, pp. 729–736.
- TIBSHIRANI, R. (1994). “Regression Shrinkage and Selection Via the Lasso”. In: *Journal of the Royal Statistical Society, Series B* 58, pp. 267–288.
- TOSIC, I. and P. FROSSARD (2011). “Dictionary Learning”. In: *IEEE Signal Processing Magazine* 28.2, pp. 27–38.
- TROPP, J. (2004a). “Greed is good: algorithmic results for sparse approximation”. In: *IEEE Transactions on Information Theory* 50.10, pp. 2231–2242.
- (2004b). “Topics in sparse approximation”. PhD thesis. The University of Texas at Austin.
- TROPP, J. and A. GILBERT (2007). “Signal recovery from random measurements via Orthogonal Matching Pursuit”. In: *IEEE Transactions on Information Theory* 53, pp. 4655–4666.
- TROPP, J. and S. WRIGHT (2010). “Computational Methods for Sparse Solution of Linear Inverse Problems”. In: *Proceedings of the IEEE* 98.6, pp. 948–958.
- VALIOLLAHZADEH, S., H. FIROUZI, M. BABAIE-ZADEH, and C. JUTTEN (2009). “Image denoising using sparse representations”. In: *Independent Component Analysis and Signal Separation*. Springer, pp. 557–564.
- WANG, D. and S. KONG (2014). “A classification-oriented dictionary learning model: Explicitly learning the particularity and commonality across categories”. In: *Pattern Recognition* 47.2, pp. 885–898.
- WIPF, D. (2006). “Bayesian methods for finding sparse representations”. PhD thesis. University of California, San Diego.
- WIPF, D. and B. RAO (2004). “Sparse Bayesian Learning for Basis Selection”. In: *IEEE Transactions on Signal Processing* 52.8, pp. 2153–2164.
- WRIGHT, J., Y. MA, J. MAIRAL, G. SAPIRO, T. HUANG, and S. YAN (2010). “Sparse Representation for Computer Vision and Pattern Recognition”. In: *Proceedings of the IEEE* 98.6, pp. 1031–1044.
- WRIGHT, J., A. YANG, A. GANESH, S. SASTRY, and Y. MA (2009). “Robust Face Recognition via Sparse Representation”. In: *IEEE Transactions on Pattern Analysis and Machine Intelligence* 31.2, pp. 210–227.
- YANG, J., J. WRIGHT, T. HUANG, and Y. MA (2008). “Image super-resolution as sparse representation of raw image patches”. In: *IEEE Conference on Computer Vision and Pattern Recognition, 2008. CVPR 2008*, pp. 1–8.

- YANG, M., Z. LEI, J. YANG, and D. ZHANG (2010). “Metaface learning for sparse representation based face recognition.” In: *ICIP*. IEEE, pp. 1601–1604.
- YANG, M., L. ZHANG, X. FENG, and D. ZHANG (2014). “Sparse Representation Based Fisher Discrimination Dictionary Learning for Image Classification”. In: *International Journal of Computer Vision* 109.3, pp. 209–232.
- YIN, J., Z. LIU, Z. JIN, and W. YANG (2012). “Kernel sparse representation based classification”. In: *Neurocomputing* 77.1, pp. 120–128.
- ZHANG, J., C. ZHAO, R. XIONG, S. MA, and D. ZHAO (2012). “Image Super-Resolution via Dual-Dictionary Learning And Sparse Representation”. In: *arXiv:1208.3723 [cs]*. arXiv: 1208.3723.
- ZHANG, Q. and B. LI (2010). “Discriminative k-svd for dictionary learning in face recognition”. In: *Computer Vision and Pattern Recognition (CVPR), 2010 IEEE Conference on*. IEEE, pp. 2691–2698.
- ZHANG, Y., Z. JIANG, and L. DAVIS (2013). “Learning Structured Low-Rank Representations for Image Classification”. In: *2013 IEEE Conference on Computer Vision and Pattern Recognition (CVPR)*, pp. 676–683.
- ZHU, Z., F. GUO, H. YU, and C. CHEN (2014). “Fast Single Image Super-Resolution via Self-Example Learning and Sparse Representation”. In: *IEEE Transactions on Multimedia* 16.8, pp. 2178–2190.

Sparse representation in Medical Imaging: State-of-the-art

3.1 Introduction

Confirming what has been observed for natural images, we would like to show how in medical imaging, sparse representation and dictionaries, directly learned from a set of training images, can better capture the distribution of the data and later, can be used in statistical inference tasks such as classification. Sparse representation and dictionary learning are closely related to each other in the framework of compress sensing theory. Some successful applications in medical imaging have been recently explored for sparse representation and DL approaches. They concerned, among others, image reconstruction, image denoising, image fusion, image segmentation, multimodal images analysis and classification. A brief overview of recent works is given in this chapter.

3.2 Related work

3.2.1 Image reconstruction

The field of sparse reconstruction has seen hugely development over the pass decade. A multitude of reconstruction formulations exploiting sparsity in many different ways have been proposed. One of the greatest areas of success for Compressed Sensing (CS) has been medical imaging, particularly Magnetic Resonance Imaging (MRI). CS has important applications also in Computed Tomography (KUDO et al., 2013), PET (S. CHEN et al., 2015), SPECT (ZHAO et al., 2012), ultrasound (QUINSAC et al., 2010) and optical imaging. A special issue reports cutting-edge results on CS for biomedical imaging can be found in (G. WANG et al., 2011).

The sparsity of Magnetic Resonance (MR) images in some transform domain (Wavelets, Finite Differences, Contourlets, etc.), or equivalently, MR images admitting a sparse representation in some dictionaries, are the key to accurate CS reconstruction. In (RAVISHANKAR et al.,

2011), a novel framework for adaptively learning the dictionary and reconstructing the image simultaneously from highly undersampled k-space data was proposed. The reconstruction algorithm learns the sparsifying dictionary, and uses it to remove aliasing and noise in one step, and subsequently restores and fills-in the k-space data in the other step. Numerical experiments were conducted on MR images for several anatomical regions with a variety of sampling schemes. Recently, in (SONG et al., 2014), reconstruction of MR images is performed by 3D dual-dictionary learning. They proposed a DL scheme at two different resolution levels, using a high-resolution dictionary trained with a full-data reconstructed series and a low-resolution dictionary co-trained with corresponding undersampled reconstructed volumes. Thus, the inherent correspondence between the two resolution levels is fully exploited to improve the reconstruction quality. Experiments were performed in dynamic cardiac imaging and abdominal imaging. A comprehensive review of CS in cardiac MRI can be found in (GAMPER et al., 2008; LUSTIG et al., 2007).

In Computed Tomography, the sparse CT, inspired by compressed sensing, means to introduce a prior information of image sparsity into CT reconstruction to reduce the input projections so as to reduce the potential menace of incremental X-ray dose to patients' health. Relevant works are reported in (LAROQUE et al., 2008; M. LI et al., 2002; XU et al., 2012). A review of reconstruction techniques in CT can be found in (KUDO et al., 2013).

3.2.2 Image denoising

The noise in medical images makes interpretation of images more difficult. Denoising is often necessary before analyzing (Segmentation, Classification and Detection of diseases or injury) medical images. Denoising methods can be used for reducing multiplicative or additive noise. Some works have been reported by employing sparse representation and dictionary learning in this task:

In (BAO et al., 2009) a sparse representation-based method for denoising cardiac diffusion tensor(DT)-MRI images has been developed. The proposed method, firstly generates a dictionary of multiple bases (Haar Wavelet and cosine transform) according to the features of the observed image. A segmentation algorithm based on non-stationary degree detector is then introduced to make the selection of atoms in the dictionary adapted to the image features. The denoising is achieved by gradually approximating the underlying image using the atoms selected from the generated dictionary.

The experiments in (RUBINSTEIN et al., 2010), are focused on the specific task of image denoising in 3D computed tomography (CT) imagery provided by the NIH Visible Human Project - Head CT volume. They extract the training blocks from a noisy version of the CT volume and compare the generalization performance of K-SVD versus Sparse K-SVD. The initial dictionary for both methods is the overcomplete Discrete Cosine Transform (DCT) dictionary. The sparse dictionary is trained using either 8, 16, or 24 coefficients per atom. Experiments were also performed with CT Ankle volumes.

Also in the denoising task (STAGLIANÒ et al., 2011) performed the tests on MR images of three different anatomical regions: wrist, brain and kidneys. All experiments were made comparing the performances of K-SVD dictionary, l_1 -DL dictionary (both learned from data) and a data-independent DCT dictionary.

In (S. LI et al., 2012a), the authors perform denoising experiments on a) synthetic data, b) data corrupted by Gaussian Noise: two 3-D CT images: Male-Head and Female-Ankle, and two 3-D MR images: Brain and Heart, c) 3-D CT Images from male pelvis corrupted by Poisson Noise and d) Real Noisy 3-D Ultrasound Images from liver. An algorithm named multiple clusters pursuit (MCP) is proposed in the sparse coding step and then, the dictionary updating stage is performed using SVD. Instead of using traditional 3-D medical image denoising method where each slice is independently processed with different learned dictionaries, they propose the joint 3-D operation to sufficiently utilize both the intraslice and interslice correlations in the slices, by processing patches from the same slice and nearby slices jointly.

In (S. LI et al., 2012b) a Dictionary Learning with Group Sparsity and Graph Regularization (DL-GSGR) is applied into 3-D medical image denoising. Denoising on experiments on synthetic MR images from the simulated database BrainWeb (KWAN et al., 1999) contaminated by Gaussian and Rician noise are performed. The denoising results show that their proposed approach is superior to several popular 2-D denoising methods (K-SVD, Non-local means (NLM), and Block-matching and 3D filtering (BM3D)) and 3-D denoising methods (3-D K-SVD and Video block matching 3-D filtering (VBM3D)) in high noise level.

In (YANG et al., 2013), a method based on dictionary learning is proposed in order to improve abdomen tumor low-dose CT (LDCT) image quality. The objective is two-fold, this is, to suppress the mottled noise and streak artifacts while enhancing the structure edges especially on tumors or lesions. The method makes use of a patch based DL processing by using a pre-computed general dictionary that was preliminary trained from a high quality standard-dose CT (SDCT) abdomen reference image. Then, a contrast restoration unsharp filtering is applied.

In (Y. CHEN et al., 2014), Low-dose computed tomography (LDCT) images are processed in order to suppress artifacts and reduce noise. Orientation and scale information on artifacts is exploited to train artifact atoms, which are then combined with tissue feature atoms to build three discriminative dictionaries. Then, a general dictionary learning processing is applied to further reduce the noise and residual artifacts. Experiments were performed on a large set of abdominal and mediastinum CT images.

3.2.3 Image Fusion

Medical image fusion is the process of registering and combining multiple images from single or multiple imaging modalities to improve the imaging quality and reduce randomness and redundancy in order to increase the clinical applicability of medical images for diagnosis and assessment of medical problems. A survey of the state of the art in medical fusion can be found in (JAMES et al., 2014). In this area few works related to sparse representation and dictionary learning have been recently reported:

In (S. LI et al., 2012b), a medical image fusion method called group sparse representation with learned dictionary-based image fusion method (GSLDF) is proposed. The method learns the dictionary using the Dictionary Learning with Group Sparsity and Graph Regularization (DL-GSGR) proposed by the same authors for denoising. Such dictionary contains abundant features, such as points, lines, and corners, which can extract effectively the salient features of the different modalities. The proposed fusion method was applied over CT image, proton-density PD-MR image, and T2-MR image of the brain. The experimental results on fusion demonstrate that their method surpasses the multiresolution analysis based methods (Discrete Wavelet Transform DWT, Stationary Wavelet Transform SWT, and Non-subsampled Contourlet Transform NSCT) and the Simultaneous orthogonal matching pursuit (SOMP) method.

3.2.4 Image Segmentation

Segmentation is a fundamental problem in image processing, medical image analysis and computer vision. The aims of segmentation in case of medical images are, among others: to study anatomical structures (for instance, cardiac structures), identify Region of Interest (i.e., locate tumor, lesion and other abnormalities), measure tissue volume to determine growth up of tumor (also decreased in size of tumor with treatment), help in treatment planning prior to radiation therapy (i.e. radiation dose calculation). Although a number of algorithms have been proposed in the field of medical image segmentation, it continues to be a complex and challenging problem. Several state of the art surveys exist for segmentation (ERDT et al., 2012; LEE et al., 2015; SHARMA et al., 2010). In the field of sparse representation and dictionary learning some works have been reported:

In (ZHANG et al., 2012a), a Deformable segmentation via sparse representation and dictionary learning was proposed. The method is based on the sparse shape composition (SSC) model proposed in (ZHANG et al., 2011). K-SVD is used to learn a compact but still informative shape dictionary. An affinity propagation method is used to partition the surface into small sub-regions, on which the sparse shape composition is performed locally. The method is applied on a diverse set of biomedical image analysis problems: 2D lung localization in X-ray, 3D liver segmentation in PET-CT, and 3D Rat Cerebellum Segmentation in Magnetic Resonance Microscopy.

Based on the (SSC) model proposed in (ZHANG et al., 2011), the K-SVD algorithm was also used to construct an initial shape dictionary for lung localization in X-Ray and for cardiac segmentation in dynamic MRI (ZHANG et al., 2012b). When new training shapes are considered, instead of re-constructing the initial dictionary, they update the existing one using a block-coordinates descent approach. Using the updated dictionary, sparse shape composition can be gracefully scaled up to model shape priors from a large number of training shapes without sacrificing run-time efficiency.

In (GAO et al., 2012), a supervised sparse representation based classification method for segmentation of prostate in CT images was proposed. Feature selection is combined with dictionary learning technique to train two discriminant sub-dictionaries which overcome the limitation of the traditional Sparse representation classification (SRC) that works well when

there are no similar elements between sub-dictionaries. Context features are further incorporated into SRC to refine the classification results (especially the prostate boundary) in an iterative scheme. A residue-based linear regression model is finally learned to increase the classification performance and extend the traditional SRC from hard classification to soft classification. The method has been evaluated on a CT dataset consisting of 15 patients and 230 CT images.

In (JULAZADEH et al., 2012), an approach for segmenting lateral ventricle in MR images of the brain utilizing sparse representation solutions is presented. The method takes advantage of K-SVD dictionary learning algorithm to create two distinct over complete dictionaries for each class (the cerebral cortex class using a DCT initial dictionary and the lateral ventricle class using the training data images patches) and it uses sparse representation classification (SRC) algorithm to sparsely represent the image as well as discriminating the two different classes in the image.

(KHALILZADEH et al., 2013) proposed a method of fully automatic detection and segmentation of the brain tissues in MR images. Using K-SVD they obtained two dictionaries for target and non-target classes. They suggested to define a sparse factor for segmentation. At first, the average value of intensity level is computed for each class according to the reconstruction error method. Then, it is segmented by using sparse and distance factors.

In (L. WANG et al., 2013), a subject-specific atlas from a library of aligned, manually segmented images by using sparse representation in a patch-based fashion was constructed. Then, the spatial consistency in the subject-specific atlas is further enforced by considering the similarities of a patch with its neighboring patches. Finally, this subject-specific atlas is integrated into a coupled level set framework for surface-based neonatal brain segmentation.

In (TONG et al., 2013), a segmentation strategy based on image reconstruction has been proposed. They proposed a Fixed Discriminative Dictionary Learning for Segmentation (F-DDLS) strategy, which can learn dictionaries offline and perform segmentations online. The proposed approach belongs to supervised learning methods by exploiting the discriminative information in the patch library extracted from atlases. The proposed method has been evaluated for the hippocampus segmentation of 80 healthy subjects from the International Consortium for Brain Mapping (ICBM) database and 202 images obtained from the Alzheimer’s Disease Neuroimaging Initiative (ADNI) database.

In (HUANG et al., 2014), a dynamical appearance model based on sparse representation and dictionary learning for tracking both endocardial and epicardial contours of the left ventricle in echocardiographic sequences is presented. The contour tracker is initialized with a manual tracing of the first frame. The approach is validated on twenty-six 4D canine echocardiographic images acquired from both healthy and post-infarct canines.

In (OZAN OKTAY et al., 2014), a new spectral representation for echocardiography images based on sparse reconstruction of dictionary atom spectral embeddings is presented. Echo images are first sparsely reconstructed with dictionary atoms for speckle reduction learned with the K-SVD algorithm. Secondly, a spectral representation is extracted from the processed images by mapping image patches to the manifold space of the dictionary atoms. Then, atlas labels

are propagated to the target image by deformable registration using the spectral representation. The proposed spectral representation is used in image registration to perform multi-atlas LV segmentation on a set of 3D echo cardiac image sequences acquired from 30 subjects.

In (X. WANG et al., 2014), an online discriminative multi-atlas learning method for isointense infant brain tissue segmentation is presented. A multi-kernel learning is used to map image patches into discriminative kernel spaces for producing corresponding probability maps to model a label of each sample in these spaces. Then, an online DL is proposed to build the atlas that handles the intra-class compactness and inter-class separability simultaneously. Finally sparse coding is used to select only a small number of candidate patches that best represent the target patch.

In (ROSAS-ROMERO et al., 2014), the segmentation of endocardium in ultrasound images from rats is performed with sparse representation over learned redundant dictionaries. Experiments show that the performance of dictionaries directly built with manually extracted atoms outperforms that of trained dictionaries (reconstructive and discriminative) with K-SVD methods. The total number of entries per atom is $N=23$ which includes gray level information, spatial coordinates, statistical information and contour information. Endocardium segmentation is done with a patch-by-patch classification process and a patch size of 3×3 .

3.2.5 Multimodal images analysis

Multimodal signal analysis has received an increased interest in the last years. Multi-modal signals are sets of heterogeneous signals originating from the same phenomenon but captured using different sensors. Multimodal dictionaries (MONACI et al., 2007) is a novel model of multimodal signals based on their sparse decomposition over a dictionary of recurrent multi-modal structures. In medical images, this model can be applied to super resolution (Y.-H. WANG et al., 2012), multi-modal image registration (CAO et al., 2014) and tissue synthesis (ROY et al., 2011).

In (ROY et al., 2011) a method to synthesize missing MR tissue contrasts from available acquired images using an atlas containing the desired contrast and a patch-based compressed sensing strategy is described. The proposed method is called MIMECS: MR image example-based contrast synthesis. This method addresses the problem of intensity standardization over pulse sequences or scanners and synthesizes different MR contrast images for a given subject from two different MR contrasts.

In (Y.-H. WANG et al., 2012) sparse representation is used to generate high resolution in MR images of the brain. MRI image super-resolution is divided into two steps: 1) based on the sparsity prior, they find the sparse representation for each local patch, respecting spatial compatibility between neighbors; 2) use the result from this local sparse representation to further regularize and refine the entire image using the reconstruction constraint. Results of sparse representation in one MR image is compared with popular Bicubic interpolation method.

A robust multimodal dictionary learning method for multimodal images was proposed in (CAO et al., 2013) with a probabilistic model for dictionary learning which discriminates between corresponding and non-corresponding patches. The problem of learning a dictionary in presence

of problematic image patches is casted as a likelihood maximization problem and it is solved with a variant of the EM algorithm. The method was tested on synthetic images and also in correlative microscope images with the application in multimodal registration.

(MA et al., 2013) proposed a new model to recover images suffering from blur and Poisson noise. It is based on the mixture of two priors: a patch-based sparse representation prior over a learned dictionary inspired by the K-SVD algorithm for Gaussian noise removal, and the pixel-based Total Variation (TV) regularization. Experiments were performed over MR images coming from: Ankle, Brain, Mouse intestine and Neck.

(CAO et al., 2014) propose an image registration method for correlative microscopy. They use a sparse representation model to obtain image analogies. The method makes use of corresponding image training patches of two different imaging modalities to learn a dictionary capturing appearance relations. The approach was tested in backscattered electron (BSE) scanning electron microscopy (SEM)/confocal and transmission electron microscopy (TEM)/confocal images.

3.2.6 Classification

Clinicians are often interested in early diagnosis of pathologies (classification) and in learning the progression of a disease (regression). Classification of objects such as lesions into certain categories (e.g., abnormal or normal, lesions or non-lesions) is one of the most popular uses of machine learning in medical image analysis. From a methodological point of view, current techniques for classification varies from applying standard machine learning algorithms to medical imaging datasets (e.g. support vector machines). Some works using dictionary learning and sparse representation for classification in medical images have been reported:

(ZHENG et al., 2011) presents a Metasample-Based sparse representation method for tumor classification using gene expression data. A set of metasamples are extracted from the training samples, and then an input testing sample is represented as the linear combination of these metasamples by l_1 -regularized least square method. Classification is achieved by using a discriminating function defined on the representation coefficients. This approach can be seen as the combination of SRC and metasample-based clustering. Experiments were performed over Acute leukemia data, Colon cancer data, Prostate cancer data and Diffuse large B-cell lymphomas data.

In (DESHPANDE et al., 2014; WEISS et al., 2013) the detection of Multiple sclerosis (MS) lesions using dictionary learning is performed. Experiments were performed in FLAIR MR images, T1 (T1-wMPRAGE) and T2-weighted, (T2-w) and Proton Density (PD) sequences. The manual segmented images obtained from neurological experts are referred to as ground truth lesion masks. Three approaches of classification were proposed: a) using Single Dictionary learned from healthy and lesion class patches: For a given test patch, they calculate the sparse coefficients and reconstruction error, and assign the patch to the lesion class if this error is greater than a chosen threshold. The threshold is selected by observing the histogram of the error map. b) using class specific dictionaries for healthy and lesion classes, respectively where classification is based on the error minimization. c) using class specific dictionaries of different

lengths: they allow dictionaries with high length for healthy class data and study its effect on MS lesion classification.

In (SHI et al., 2013) a multimodal sparse representation-based classification (mSRC), is proposed for classifying lung needle biopsy images. Features of three modalities (shape, color, and texture) are extracted from segmented cell nuclei. In a training phase, three discriminative subdictionaries corresponding to the three feature modalities are jointly learned by a genetic algorithm guided by multimodal dictionary learning approach. The dictionary learning aims to select the topmost discriminative samples and encourage large disagreement among different subdictionaries. In the testing phase, when a new image is analyzed, a hierarchical fusion strategy is applied, which first predicts the labels of the cell nuclei by fusing three modalities, then predicts the label of the image by majority voting. The method is evaluated on a real image set of 4372 cell nuclei regions segmented from 271 images.

In (VAROL et al., 2014) a novel approach for Computational Anatomy (CA) is proposed. CA is an emerging discipline focused on the quantitative analysis of variability of biological shape. This is achieved by solving a supervised dictionary learning problem for block-sparse signals. Structured sparsity allows the grouping of instances across different independent samples, while label supervision allows for discriminative dictionaries. The block structure of dictionaries allows constructing multiple classifiers that treat each dictionary block as a basis of a subspace that spans a separate band of information.

In (M. SRINIVAS et al., 2014) a method for classification of medical images captured by different modalities is proposed, "Content Based Medical Image Retrieval (CBMIR)", based on multi-scale wavelet representation using Online Dictionary Learning (ODL). Wavelet features extracted from an image provide discrimination useful for classification of medical images, namely, diffusion tensor imaging (DTI), magnetic resonance imaging (MRI), magnetic resonance angiography (MRA) and functional magnetic resonance imaging (fMRI). An experimental analysis performed on a set of images from the International Consortium for Brain Mapping (ICBM) medical database. Each class (modality) consists of 5587 training and 1482 testing images. Other classifiers, namely, SVM, NN and Bayes were also examined.

(U. SRINIVAS et al., 2014) proposed a simultaneous sparsity model for histopathological image representation and classification. Classification is performed by solving a newly formulated simultaneous sparsity-based optimization problem extended from the SRC algorithm by designing three color dictionaries, corresponding to the RGB channels. Experiments were performed on two image data sets: 1) mammalian tissue images and 2) human intraductal breast lesions.

More recently in (GUO et al., 2015), a fully automatic classification method based on the sparse representation is proposed to distinguish intracardiac tumor and thrombi in echocardiography. A globally denoising method is employed to remove the speckle and preserve the anatomical structure in the mass area. Subsequently, the contour of the mass and its connected atrial wall are described by the K-singular value decomposition and a modified active contour model. Finally, the motion, the boundary as well as the texture features are processed by a sparse representation classifier using the SRC algorithm to distinguish two masses. The method was

applied in ninety-seven clinical echocardiogram sequences with an accuracy of 96.91% on the classification of intracardiac tumors and thrombi.

3.2.7 Other applications

Change detection in medical images was proposed in (NIKA et al., 2014) based on adaptive dictionary learning techniques. The proposed AEDL, Adaptive EigenBlock Dictionary Learning, algorithm captures local spatial difference between the reference and test images via detecting the significant changes between the test and the reference image linearly modeled by a local dictionary trained from the reference and the test images and reconstructed by local sparse minimization processes. Experiments were performed in synthetic images and two real T2 weighted MR images of the brain taken in 2010 and 2012 taken from brainWeb: (simulated brain database). AEDL algorithm finds the significant changes related to the new MS lesion formation and ignores changes shown from the absolute difference.

In (S. LI et al., 2014) a dictionary based sinogram inpainting method is proposed to compensate the artifact problem in CT sparse reconstruction. The patch-based dictionary is first learned by applying K-SVD algorithm with database composed by the patches from simulated CT sinogram. The learned dictionary is then used to inpaint the missing sinogram data which is then used in final image reconstruction via the classical analytic Filtered Back Projection (FBP) reconstruction.

3.3 Conclusions

We have presented a survey of the sparsity techniques used in medical imaging. Most of the applications for denoising, involves the use of dictionaries trained with known basis as DCT or dictionaries learned using K-SVD algorithm. In the case of supervised sparse representation for segmentation and classification most of the methods are based on the framework of the SRC algorithm. Image modalities involves MRI, CT, Ultrasound and microscopy images. In cardiac medical images works are focused on segmentation on epicardial and endocardial contours of LV in echocardiography images. In cardiac MRI, to our knowledge, there is not works based on sparse representation and Dictionary learning for classification tasks, so the work presented in this research is the first in proposing the use of dictionary learning for LV wall motion classification in cardiac medical images. As we have mentioned, the choice of atoms depends on the application for which we intend the use of the sparse representation. For example, for face recognition features usually are patches from the images, we have also constated that DCT basis are well adapted for denoising tasks. In the case of assessment of LV wall motion, features must represent the spatial and temporal variation of the LV cavity providing discriminative information that could help in the characterization of LV cardiac function abnormalities. In the next chapter, we briefly describe the problem of assessment LV wall motion in cardiac cine MRI that usually involves the segmentation of the epicardial and endocardial boundaries. The first contribution of this research is also presented in the next chapter with a feature extraction method from

sequences cine-MRI in short-axis view for the assessment of LV function. Later, we will see how these features will be used as input atoms in the training of discriminative dictionaries to classify normal or abnormal regional LV movement. A second contribution is also depicted for the detection of cardiac fibrosis in MRI.

References

- BAO, L. J., Y. M. ZHU, W. Y. LIU, P. CROISILLE, Z. B. PU, M. ROBINI, and I. E. MAGNIN (2009). “Denoising human cardiac diffusion tensor magnetic resonance images using sparse representation combined with segmentation”. In: *Physics in Medicine and Biology* 54.6, p. 1435.
- CAO, T., V. JOJIC, S. MODLA, D. POWELL, K. CZYMMEK, and M. NIETHAMMER (2013). “Robust Multimodal Dictionary Learning”. In: *Medical Image Computing and Computer-Assisted Intervention-MICCAI 2013*. Ed. by K. MORI, I. SAKUMA, Y. SATO, C. BARILLOT, and N. NAVAB. Lecture Notes in Computer Science 8149. Springer Berlin Heidelberg, pp. 259–266.
- CAO, T., C. ZACH, S. MODLA, D. POWELL, K. CZYMMEK, and M. NIETHAMMER (2014). “Multi-modal registration for correlative microscopy using image analogies”. In: *Medical Image Analysis* 18.6, pp. 914–926.
- CHEN, S., H. LIU, P. SHI, and Y. CHEN (2015). “Sparse representation and dictionary learning penalized image reconstruction for positron emission tomography”. In: *Physics in Medicine and Biology* 60.2, p. 807.
- CHEN, Y., L. SHI, Q. FENG, J. YANG, H. SHU, L. LUO, J.-L. COATRIEUX, and W. CHEN (2014). “Artifact Suppressed Dictionary Learning for Low-Dose CT Image Processing”. In: *IEEE Transactions on Medical Imaging* 33.12, pp. 2271–2292.
- DESHPANDE, H., P. MAUREL, and C. BARILLOT (2014). “Detection of Multiple Sclerosis Lesions using Sparse Representations and Dictionary Learning”. In: *2nd International Workshop on Sparsity Techniques in Medical Imaging (STMI), MICCAI 2014*. 71-79. Boston, MA, United States.
- ERDT, M., S. STEGER, and G. SAKAS (2012). “Regmentation: A New View of Image Segmentation and Registration”. In: *Journal of Radiation Oncology Informatics* 4.1, pp. 1–23.
- GAMPER, U., P. BOESIGER, and S. KOZERKE (2008). “Compressed sensing in dynamic MRI”. In: *Magnetic Resonance in Medicine: Official Journal of the Society of Magnetic Resonance in Medicine / Society of Magnetic Resonance in Medicine* 59.2, pp. 365–373.
- GAO, Y., S. LIAO, and D. SHEN (2012). “Prostate segmentation by sparse representation based classification”. In: *Medical image computing and computer-assisted intervention: MICCAI - International Conference on Medical Image Computing and Computer-Assisted Intervention* 15.Pt 3, pp. 451–458.

- GUO, Y., Y. WANG, D. KONG, and X. SHU (2015). “Automatic Classification of Intracardiac Tumor and Thrombi in Echocardiography Based on Sparse Representation”. In: *IEEE Journal of Biomedical and Health Informatics* 19.2, pp. 601–611.
- HUANG, X., D. P. DIONE, C. B. COMPAS, X. PAPADEMETRIS, B. A. LIN, A. BREGASI, A. J. SINUSAS, L. H. STAIB, and J. S. DUNCAN (2014). “Contour tracking in echocardiographic sequences via sparse representation and dictionary learning”. In: *Medical Image Analysis* 18.2, pp. 253–271.
- JAMES, A. P. and B. V. DASARATHY (2014). “Medical image fusion: A survey of the state of the art”. In: *Information Fusion*. Special Issue on Information Fusion in Medical Image Computing and Systems 19, pp. 4–19.
- JULAZADEH, A., J. ALIREZAIE, and P. BABYN (2012). “A novel automated approach for segmenting lateral ventricle in MR images of the brain using sparse representation classification and dictionary learning”. In: *2012 11th International Conference on Information Science, Signal Processing and their Applications (ISSPA)*, pp. 888–893.
- KHALILZADEH, M. M., E. FATEMIZADEH, and H. BEHNAM (2013). “Automatic segmentation of brain MRI in high-dimensional local and non-local feature space based on sparse representation”. In: *Magnetic Resonance Imaging* 31.5, pp. 733–741.
- KUDO, H., T. SUZUKI, and E. A. RASHED (2013). “Image reconstruction for sparse-view CT and interior CT—introduction to compressed sensing and differentiated backprojection”. In: *Quantitative Imaging in Medicine and Surgery* 3.3, pp. 147–161.
- KWAN, R.-S., A. EVANS, and G. PIKE (1999). “MRI simulation-based evaluation of image-processing and classification methods”. In: *IEEE Transactions on Medical Imaging* 18.11, pp. 1085–1097.
- LAROQUE, S. J., E. Y. SIDKY, and X. PAN (2008). “Accurate image reconstruction from few-view and limited-angle data in diffraction tomography”. In: *Journal of the Optical Society of America. A, Optics, image science, and vision* 25.7, pp. 1772–1782.
- LEE, L. K., S. C. LIEW, and W. J. THONG (2015). “A Review of Image Segmentation Methodologies in Medical Image”. In: *Advanced Computer and Communication Engineering Technology*. Ed. by H. A. SULAIMAN, M. A. OTHMAN, M. F. I. OTHMAN, Y. A. RAHIM, and N. C. PEE. Lecture Notes in Electrical Engineering 315. Springer International Publishing, pp. 1069–1080.
- LI, M., H. YANG, and H. KUDO (2002). “An accurate iterative reconstruction algorithm for sparse objects: application to 3D blood vessel reconstruction from a limited number of projections”. In: *Physics in Medicine and Biology* 47.15, pp. 2599–2609.
- LI, S., L. FANG, and H. YIN (2012a). “An efficient dictionary learning algorithm and its application to 3-D medical image denoising”. In: *IEEE transactions on bio-medical engineering* 59.2, pp. 417–427.
- LI, S., H. YIN, and L. FANG (2012b). “Group-Sparse Representation With Dictionary Learning for Medical Image Denoising and Fusion”. In: *IEEE Transactions on Biomedical Engineering* 59.12, pp. 3450–3459.

- LI, S., Q. CAO, Y. CHEN, Y. HU, L. LUO, and C. TOUMOULIN (2014). “Dictionary learning based sinogram inpainting for CT sparse reconstruction”. In: *Optik - International Journal for Light and Electron Optics* 125.12, pp. 2862–2867.
- LUSTIG, M., D. D., and P. J. (2007). “Sparse MRI: The application of compressed sensing for rapid MR imaging”. In: *Magnetic Resonance in Medicine* 58 (6), pp. 1182–1195.
- MA, L., L. MOISAN, J. YU, and T. ZENG (2013). “A dictionary learning approach for Poisson image deblurring”. In: *IEEE transactions on medical imaging* 32.7, pp. 1277–1289.
- MONACI, G., P. JOST, P. VANDERGHEYNST, B. MAILHÉ, S. LESAGE, and R. GRIBONVAL (2007). “Learning multimodal dictionaries”. In: *IEEE transactions on image processing: a publication of the IEEE Signal Processing Society* 16.9, pp. 2272–2283.
- NIKA, V., P. BABYN, and H. ZHU (2014). “Change detection of medical images using dictionary learning techniques and PCA”. In: *Proc. SPIE 9035, Medical Imaging*. Vol. 9035, pages.
- OZAN OKTAY, WENZHE SHI, JOSE CABALLERO, KEVIN KERAUDREN, and DANIEL RUECKERT (2014). *Sparsity Based Spectral Embedding: Application to Multi-Atlas Echocardiography Segmentation*. Tech. rep. MICCAI 2014 Workshop - Sparsity Techniques in Medical Imaging (STMI).
- QUINSAC, C., A. BASARAB, J. GIRAULT, and D. KOUAME (2010). “Compressed sensing of ultrasound images: Sampling of spatial and frequency domains”. In: *2010 IEEE Workshop on Signal Processing Systems (SIPS)*, pp. 231–236.
- RAVISHANKAR, S. and Y. BRESLER (2011). “Image Reconstruction From Highly Undersampled k-Space Data by Dictionary Learning”. In: *IEEE Transactions on Medical Imaging* 30.5, pp. 1028–1041.
- ROSAS-ROMERO, R. and H. D. TAGARE (2014). “Segmentation of endocardium in ultrasound images based on sparse representation over learned redundant dictionaries”. In: *Engineering Applications of Artificial Intelligence* 29, pp. 201–210.
- ROY, S., A. CARASS, and J. PRINCE (2011). “A compressed sensing approach for MR tissue contrast synthesis”. In: *Information Processing in Medical Imaging: Proceedings of the ... Conference 22*, pp. 371–383.
- RUBINSTEIN, R., M. ZIBULEVSKY, and M. ELAD (2010). “Double Sparsity: Learning Sparse Dictionaries for Sparse Signal Approximation”. In: *Signal Processing, IEEE Transactions on* 58.3, pp. 1553–1564.
- SHARMA, N. and L. M. AGGARWAL (2010). “Automated medical image segmentation techniques”. In: *Journal of Medical Physics / Association of Medical Physicists of India* 35.1, pp. 3–14.
- SHI, Y., Y. GAO, Y. YANG, Y. ZHANG, and D. WANG (2013). “Multimodal sparse representation-based classification for lung needle biopsy images”. In: *IEEE transactions on bio-medical engineering* 60.10, pp. 2675–2685.
- SONG, Y., Z. ZHU, Y. LU, Q. LIU, and J. ZHAO (2014). “Reconstruction of magnetic resonance imaging by three-dimensional dual-dictionary learning”. In: *Magnetic Resonance in Medicine* 71.3, pp. 1285–1298.

- SRINIVAS, M. and C. MOHAN (2014). “Medical images modality classification using multi-scale dictionary learning”. In: *2014 19th International Conference on Digital Signal Processing (DSP)*, pp. 621–625.
- SRINIVAS, U., H. MOUSAVI, V. MONGA, A. HATTEL, and B. JAYARAO (2014). “Simultaneous Sparsity Model for Histopathological Image Representation and Classification”. In: *IEEE Transactions on Medical Imaging* 33.5, pp. 1163–1179.
- STAGLIANÒ, A., G. CHIUSANO, C. BASSO, and M. SANTORO (2011). “Learning Adaptive and Sparse Representations of Medical Images”. In: *Medical Computer Vision. Recognition Techniques and Applications in Medical Imaging*. Ed. by B. MENZE, G. LANGS, Z. TU, and A. CRIMINISI. Vol. 6533. Lecture Notes in Computer Science. Springer Berlin Heidelberg, pp. 130–140.
- TONG, T., R. WOLZ, P. COUPÉ, J. V. HAJNAL, D. RUECKERT, and ALZHEIMER’S DISEASE NEUROIMAGING INITIATIVE (2013). “Segmentation of MR images via discriminative dictionary learning and sparse coding: application to hippocampus labeling”. In: *NeuroImage* 76, pp. 11–23.
- VAROL, E. and C. DAVATZIKOS (2014). “Supervised Block Sparse Dictionary Learning for Simultaneous Clustering and Classification in Computational Anatomy”. In: *Medical Image Computing and Computer-Assisted Intervention – MICCAI 2014*. Ed. by P. GOLLAND, N. HATA, C. BARILLOT, J. HORNEGGER, and R. HOWE. Lecture Notes in Computer Science 8674. Springer International Publishing, pp. 446–453.
- WANG, G., Y. BRESLER, and V. NTZIACHRISTOS (2011). “Guest Editorial Compressive Sensing for Biomedical Imaging”. In: *IEEE Transactions on Medical Imaging* 30.5, pp. 1013–1016.
- WANG, L., F. SHI, G. LI, W. LIN, J. GILMORE, and D. SHEN (2013). “Patch-driven neonatal brain MRI segmentation with sparse representation and level sets”. In: *2013 IEEE 10th International Symposium on Biomedical Imaging (ISBI)*, pp. 1090–1093.
- WANG, X., L. WANG, H.-I. SUK, and D. SHEN (2014). “Online Discriminative Multi-atlas Learning for Isointense Infant Brain Segmentation”. In: *Machine Learning in Medical Imaging*. Ed. by G. WU, D. ZHANG, and L. ZHOU. Lecture Notes in Computer Science 8679. Springer International Publishing, pp. 297–305.
- WANG, Y.-H., J.-B. LI, and P. FU (2012). “Medical Image Super-resolution Analysis with Sparse Representation”. In: *2012 Eighth International Conference on Intelligent Information Hiding and Multimedia Signal Processing (IIH-MSP)*, pp. 106–109.
- WEISS, N., D. RUECKERT, and A. RAO (2013). “Multiple Sclerosis Lesion Segmentation Using Dictionary Learning and Sparse Coding”. In: *Medical Image Computing and Computer-Assisted Intervention – MICCAI 2013*. Ed. by K. MORI, I. SAKUMA, Y. SATO, C. BARILLOT, and N. NAVAB. Lecture Notes in Computer Science 8149. Springer Berlin Heidelberg, pp. 735–742.
- XU, Q., H. YU, X. MOU, L. ZHANG, J. HSIEH, and G. WANG (2012). “Low-dose X-ray CT reconstruction via dictionary learning”. In: *IEEE transactions on medical imaging* 31.9, pp. 1682–1697.

- YANG, C., F. YU, L. LUO, and C. TOUMOULIN (2013). “Improving abdomen tumor low-dose CT images using dictionary learning based patch processing and unsharp filtering”. In: *Conference Proceedings 2013*, pp. 4014–4017.
- ZHANG, S., Y. ZHAN, M. DEWAN, J. HUANG, D. N. METAXAS, and X. S. ZHOU (2011). “Deformable segmentation via sparse shape representation”. In: *Medical image computing and computer-assisted intervention: MICCAI ... International Conference on Medical Image Computing and Computer-Assisted Intervention 14.Pt 2*, pp. 451–458.
- ZHANG, S., Y. ZHAN, and D. N. METAXAS (2012a). “Deformable segmentation via sparse representation and dictionary learning”. In: *Medical Image Analysis 16.7*, pp. 1385–1396.
- ZHANG, S., Y. ZHAN, Y. ZHOU, M. UZUNBAS, and D. N. METAXAS (2012b). “Shape prior modeling using sparse representation and online dictionary learning”. In: *Medical image computing and computer-assisted intervention: MICCAI ... International Conference on Medical Image Computing and Computer-Assisted Intervention 15.Pt 3*, pp. 435–442.
- ZHAO, B., H. DING, Y. LU, G. WANG, J. ZHAO, and S. MOLLOI (2012). “Dual-dictionary learning-based iterative image reconstruction for spectral computed tomography application”. In: *Physics in Medicine and Biology 57.24*, pp. 8217–8229.
- ZHENG, C.-H., L. ZHANG, T.-Y. NG, S. C. K. SHIU, and D.-S. HUANG (2011). “Metasample-based sparse representation for tumor classification”. In: *IEEE/ACM transactions on computational biology and bioinformatics / IEEE, ACM 8.5*, pp. 1273–1282.

Feature extraction and Dictionary Learning for the Assessment of LV wall motion in cardiac MRI

4.1 Introduction

Cardiovascular disease (CVD) is in general the leading cause of death worldwide (MEMBERS et al., 2012). 17.3 million people died from CVDs in 2008, representing 30% of all global deaths that year, according to the World Health Organization (WHO, 2014). By 2010, CVDs caused 223 deaths per 100 thousand individuals in France (about 27% of total deceases)¹, being the first cause of decease in the country for women and the second for men. CVDs affects the heart, the blood vessels or both. In this work, we address two specific problems in the context of CVDs, specifically: 1) the assessment of Left Ventricle (LV) wall motion in patients with heart failure (HF) and 2) the cardiac fibrosis detection in patients with hypertrophic cardiomyopathy (HCM). Both pathologies are studied in cardiac magnetic resonance imaging (MRI). We propose to use sparse representation and Dictionary learning (DL) methods in medical imaging to address those specific issues. In the previous chapters we have reviewed these techniques and we have seen that they have not been applied in the context of the problems of interest. For a better understanding of the remainder of this study, a brief review of the anatomy, electrical and mechanical function of the human cardiovascular system is first given in section 4.2. The principal issue of this study is depicted in section 4.3: the assessment of LV wall motion in patients with HF. Furthermore, a description of the cardiac imaging modalities used here is presented in section 4.4. A brief state-of-the-art for the assessment of cardiac left ventricular function in cardiac cine-MRI is presented in section 4.5. In section 4.6, we present our proposed approach, that represents a novel approach based on dynamic images combined with DL techniques to classify local normal/abnormal wall

1. Source INSEE "L'Institut national de la statistique et des études économiques", sheet "Causes de décès 2010".

motion in LV function in cardiac cine-MRI. The results of this approach will be presented in Chapter 5.

4.2 The Cardiovascular system

The cardiovascular system is one of the most vital systems in the body. Its prime responsibility is the circulation of blood to cells throughout the body. The blood provides oxygen from the lungs to the cells and transfers carbon dioxide from the cells to the lungs. The circulation of the blood is achieved by the heart which forces the blood through the blood vessels. The circulation of the blood can be divided into two stages: the pulmonary circulation and the systemic circulation. During the pulmonary circulation the blood is carried out from the heart to the lungs. In the lungs, oxygen is absorbed and carbon dioxide is removed from the blood. During the systemic circulation the blood is pumped by the heart to the cells in the body (SIMON, 2005).

4.2.1 Heart anatomy

The heart (Figure 4.1) is located into the thoracic cavity in a zone called mediastinum, between the lungs and the diaphragm. An average adult human heart weights between 300 g and 350 g. The heart is a hollow organ with four chambers separated by valves and surrounded by muscles which squeeze and relax to pump the blood around the body. The four chambers are: the right atrium (RA), the right ventricle (RV), the left atrium (LA) and the left ventricle (LV). Although a single organ, the heart functions as two separate pumps namely the right heart (RA and RV) and the left heart (LA and LV). The left heart is responsible for the systemic circulation and the right heart is responsible for the pulmonary circulation (FILIPOIU, 2013).

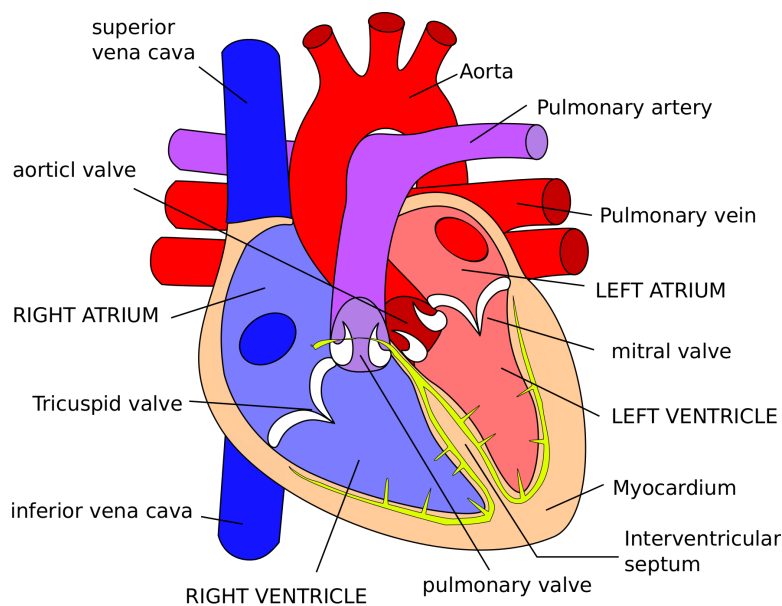


FIGURE 4.1– A schematic illustration of the heart. Modified From: (SIMON, 2005)

The atrium receives blood from the veins and aids its flow into the ventricle which forces it into the arteries. Therefore, the blood coming from the body enters the right atrium, flows to the right ventricle (RV) and exits towards the lungs. After absorbing the necessary oxygen, the blood returns to the heart through the left atrium and then it is propelled to the body by the left ventricle (LV). The atria can also contract like the ventricles but their main function is to act as reservoirs which are filled with blood flowing back through the veins to the heart. The contraction in the RV and LV is longer and stronger than in atria in a healthy heart.

LV geometry can be roughly depicted with a truncated ellipsoid with the base plane intersecting the mitral and aortic valves (cf. Figure 4.1 and 4.2). The vertex of this ellipsoid will correspond to the apex. The axis perpendicular to the base and containing the apex is called the long axis. In cardiac imaging, planar images lying in planes parallel to this axis are called long-axis-view (LAX) images and those perpendicular to the long axis are called short-axis-view (SAX) images. The basal, mid-cavity (middle) and apical terms indicate the location of the SAX planes on the long axis of the left ventricle.

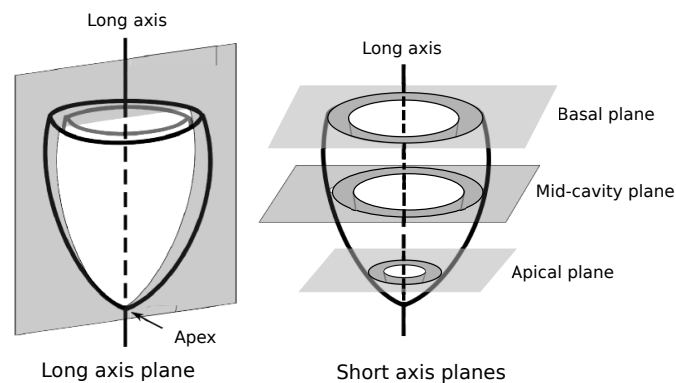


FIGURE 4.2– Left ventricular long axis, apex and illustration of the long-axis (LAX) and the short-axis (SAX). Modified from (BETANCUR, 2014).

RV and LV are bounded by a thick muscle called myocardium (10 mm for a healthy LV), an interventricular septum, two atrioventricular valves (mitral and tricuspid valves, respectively), and two semilunar valves (pulmonary and aortic valves, respectively) (cf. Figure 4.1). The inner surface of the myocardium is the endocardium, while the outer surface is the epicardium.

The pumping action of the heart is achieved by the contraction and relaxation of the cardiac muscle. The coordinated pumping action of the atria and the ventricles is controlled by an electrical system that is contained in the heart muscle. The myocardium is made up of cardiomyocytes (cells) that arrange into fibers. Cardiomyocytes are unique in the human body due to their characteristics. They are contractile yet cannot remain in contraction, independent and good conductors (i.e. cell excitation is transmitted to neighbors). Cardiomyocytes are irrigated by micro arteries and excited by the autonomic nervous system. Myocardial fibers are arranged into spiral and circular bundles. Fiber disposition locally determines the favored direction to transmit cells excitation to neighbors.

4.2.2 Electrical function

The cardiac muscle has the ability to contract without nervous input. The action potential for each heart beat is generated by a pacemaker node in the right atrium and is transmitted through the heart along specialized pathways (i.e., Purkinje fibers, which are divided into the left and right branches). Figure 4.3, shows an illustrative example of the electrical function of the heart. The pacemaker is a small area in the wall of the right atrium, near the entrance of the superior vena cava, known as sinoatrial node (SA) or Keith-Flack node. The electrical impulse originated by the SA node spreads radially across both atria, and then reaches the atrio-ventricular (AV) node and the specialized conduction bundles in the ventricle. From the terminal buttons of the Purkinje fibers, the electrical impulse spreads to the cardiomyocytes, leading to a coordinated depolarization (and further contraction) of right and left ventricles from the apex towards the base. Each cardiac cell is characterized by a transmembrane voltage due to an unbalanced ionic concentration of sodium Na^+ , potassium K^+ and calcium Ca^{++} in the intra- and extracellular space, respectively; this leads to values of -80mV inside the cell and $+20\text{mV}$ outside the cell membrane.

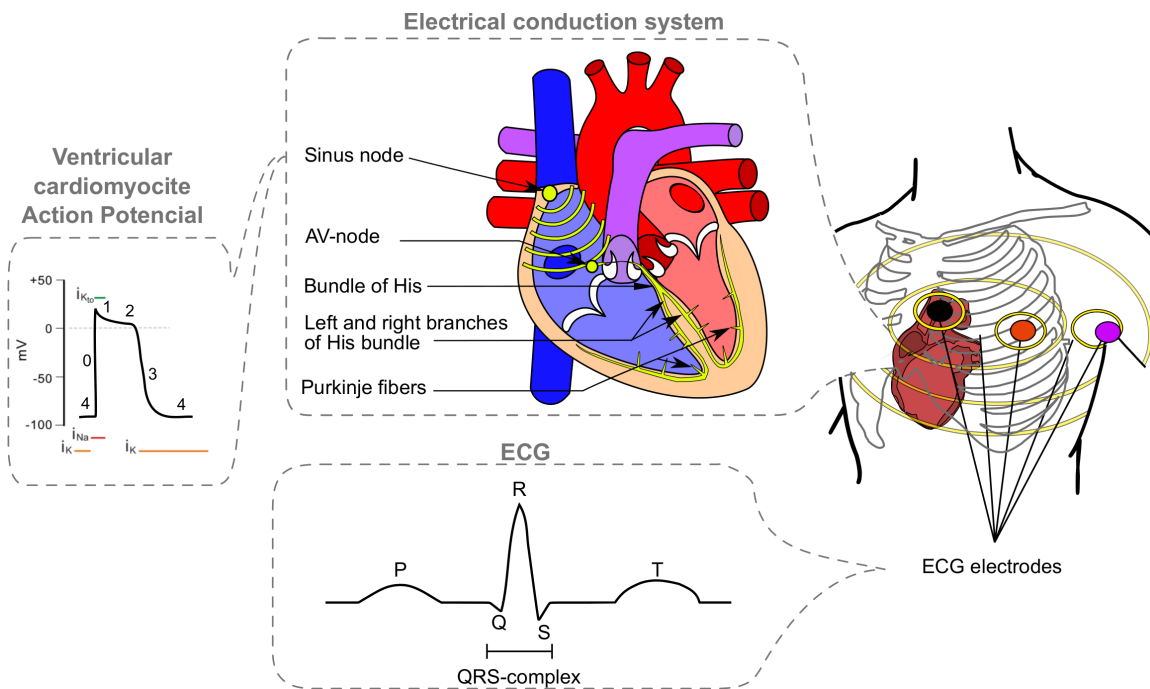


FIGURE 4.3– Electrical function of the heart. (Top-middle) Electrical conduction system: impulses originating at sinus node travels to atria and then convey at the AV-node to then propagate towards the right and left ventricles through the bundle of His, its left and right branches, and the Purkinje fibers. (Bottom-middle) Schematic representation of an electrocardiogram (ECG) for a healthy heart in sinus rhythm. The ECG depicts the global electrical function of the heart. (Left) Ventricular cardiomyocyte action potential: phase 0 = rapid inward Na^+ conductance, phase 1= Initial repolarization, K^+ moving out, phase 2 = Inward Ca^{++} current (main); plateau phase, phase 3 = repolarization; outward K^+ current (main), phase 4 = Inward & outward K^+ current equal. Modified from (BETANCUR, 2014).

During stimulation, the polarity of transmembrane voltage changes, generating an action potential, that is a reflection of each cell's electrical activity. It has certain phases (Figure 4.3-left)):

Rapid depolarization An electrical excitation of the cell above a given activation threshold causes a rapid inversion of its polarization or depolarization (phase 0).

Beginning of repolarization Characterized by a fast and acute return to equilibrium (phase 1).

Plateau The repolarization slows down into a "plateau" phase where the voltage does not change significantly (phase 2).

Rapid repolarization Fast decrease of cardiomyocyte's voltage until equilibrium is reached (phase 3).

Resting membrane potential The action potential intracellular and extracellular concentrations of ions are restored (phase 4).

The electrocardiogram (ECG) depicts the electrical activity of the heart. Figure 4.3 bottom-middle provides a schematic illustration of a standard ECG record at resting heart rate. The ECG can be decomposed into the P-wave representing atria depolarization (contraction), the QRS-complex corresponding to ventricular depolarization (contraction), and the T-wave corresponding to ventricular repolarization (relaxation). Atria repolarization is masked by the QRS complex.

4.2.3 Mechanical function

In normal conditions the human heart beats between 65 to 75 times per minute, which means that each heart beat lasts around 0.85 sec. Each heart beat is considered as a cardiac cycle which is separated into a contraction phase (systole) and a relaxation phase (diastole) of the atria and ventricles.

To analyze systole and diastole in more detail, the cardiac cycle is usually divided into seven phases. Figure 4.4 provides an example of the volume of the left ventricle during each phase of the cardiac cycle. In addition, it shows the relationship between the ECG signal, the ventricular volume and the cardiac pressure during the cardiac cycle. The seven phases of the cardiac cycle are (KLABUNDE, 2011):

Atrial contraction The atrial contraction is initiated by the electrical depolarization of the atria (P wave). As the atria contract, the pressure within the atrial chambers increases. The pressure gradient which is generated across the open AV valves causes a rapid flow of blood into the ventricles.

Isovolumetric contraction The isovolumetric contraction is initiated by the ventricular depolarization (QRS complex). During the isovolumetric contraction all the valves are closed and the volume of the ventricles remains the same. However, there is a rapid increase in the intraventricular pressure due to depolarization of the ventricle.

Rapid ejection In the rapid ejection phase, the intraventricular pressures exceed the pressures within the aorta and pulmonary artery. This causes the aortic and pulmonic valves to open and blood is ejected out of the ventricles.

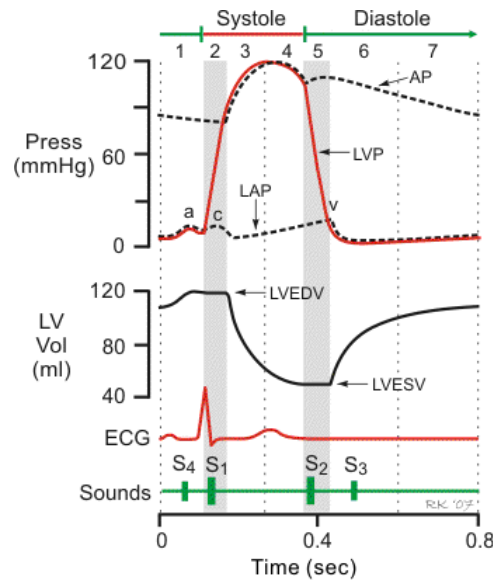


FIGURE 4.4— An example of the pressure and volume of the heart during the cardiac cycle (LVEDV= left ventricular end-diastolic volume, LVESV= left ventricular end-systolic volume, LAP= left atrial pressure, LVP= left ventricular pressure, AP= aortic pressure). From: (KLABUNDE, 2011)

Reduced ejection After the rapid ejection phase, ventricular repolarisation occurs (T wave) causing the ventricular tension to fall and the rate of ventricular emptying to be reduced. This is called the reduced ejection phase. In this phase the ventricular pressure falls below the blood pressure in the outflow tracts. However, the blood continues to flow due to its kinetic energy.

Isovolumetric relaxation When the total energy of the blood within the ventricles is less than the energy of the blood in the outflow tracts, the aortic and pulmonic valves close (isovolumetric relaxation phase). During this phase, the ventricular pressures decrease. However, the atrial pressures continue to rise due to venous return. The volumes of the ventricles remain constant since all the valves are closed. The volume of the blood which remains in the ventricle is called the end-systolic volume. In the left ventricle the end-systolic volume is about 50ml.

Rapid ventricular filling The rapid ventricular filling occurs when the ventricular pressures fall below the atrial pressures. Then, the AV valves open and the ventricular filling begins. The ventricles continue to relax, despite blood inflow, which causes intraventricular pressure to continue falling by a few additional mmHg. The opening of the AV valves and the rapid flow of blood cause a rapid fall in the atrial pressure.

Reduced ventricular filling In reduced ventricular filling phase, the ventricular pressure rises as the ventricles fill with blood. This reduces the pressure gradient across the AV valves so that the rate of the filling falls. The aortic pressure (and pulmonary arterial pressure) continue to fall.

Figure 4.4 also shows the phases when the four basic heart sounds can be heard during a cardiac auscultation. The most fundamental heart sounds are the first and second sounds: S1 and S2. S1 is caused by closure of the mitral and tricuspid valves at the beginning of isovolumetric ventricular contraction. S2 is caused by closure of the aortic and pulmonic valves at the beginning of isovolumetric ventricular relaxation. The third heart sound (S3), when audible, occurs early in ventricular filling. The fourth heart sound (S4), when audible, is caused by vibration of the ventricular wall during atrial contraction.

The performance of the heart can be studied by examining the relationship between the cardiac volume and the cardiac pressure. A number of global measurements are important in clinical practice. For instance, the stroke volume (SV) is the amount of blood ejected by the left ventricle in one contraction, it is calculated by the difference of the ventricular volumes at the end-diastole (LVEDV) and end-systole (LVESV). The stroke volume multiplied by the heart rate is the cardiac output, which represents the amount of blood pumped by the heart per minute. The ratio of the stroke volume to the end diastolic volume is the Ejection Fraction (EF). Another global measure is the Left ventricular mass that is generally calculated as the difference between the epicardium delimited volume and the left ventricular chamber volume multiplied by an estimate of myocardial density. The volume of the left ventricle, the ejection fraction and the Left ventricular mass are considered as relevant measures of cardiac performance (O'DELL et al., 2000). The performance of the heart is not only assessed by global indicators. Local indicators can also be studied to describe regional myocardial function.

The regional myocardial function is commonly scored following a standard issued by the American Heart Association (CERQUEIRA et al., 2002), which suggests selecting representative 2D cardiac slices (planes) in the short axis (SAX) view (cf. 4.2) to generate 17 standardized LV segments. The segmented model of the LV suggested by the AHA was developed for improving communication between imaging modalities for research and clinical purposes. The segment model is applicable for MRI, CT, positron emission tomography (PET), coronary angiography, and echocardiography (cf. Chapter 5). The AHA segment model is a polar plot where data from each slice is represented as a concentric ring with apical slices located at the center of the plot while the most-basal slice is on the outside. As can be seen in Figure 4.5, basal and mid-cavity planes are divided into 6 segments each one, whereas the apical slice has 4 segments, and the 17th segment is the apex.

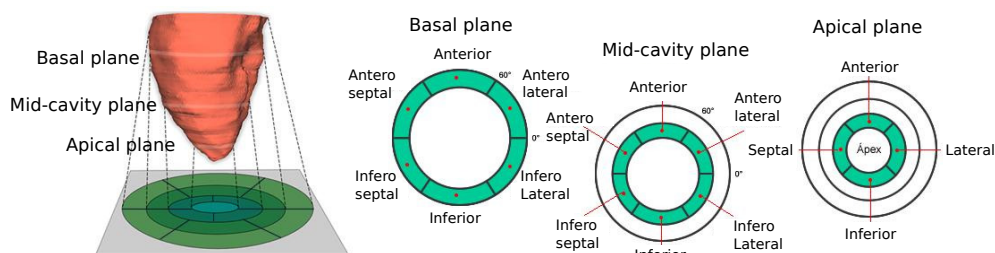


FIGURE 4.5– AHA 17 segment representation

Local parameters that describe the regional myocardial function can include: Regional Ejection Fraction, Myocardial thickening, Local speed of movement, Spatio-temporal evolution and Strain.

Both, global and local clinical parameters, can be obtained from diverse cardiac imaging modalities, which include echocardiography, CT (Computed Tomography), coronary angiography, nuclear imaging (SPECT/PET) and cardiac Magnetic Resonance Imaging (MRI). The diagnosis, treatment and follow-up of cardiac pathologies can rely on these image modalities (cf. Chapter 5).

In the next subsection we introduce the most common pathologies that affect the cardiovascular system. In this chapter, we focus on abnormal cardiac LV wall motion that is an early finding in multiple cardiac pathologies and its diagnosis is of critical importance (GARCIA-FERNANDEZ et al., 2003).

The left ventricle motion during the systolic phase is considered as the combination of five types of movements: 1) translation, 2) rotation, 3) torsion, 4) longitudinal shortening, and 5) radial contraction (GONZALEZ et al., 2010). These components are not uniform throughout the left ventricular cavity. For instance, the longitudinal shortening movement with respect to the anatomical axis (aortic valve-apex) is significantly asymmetric. During systole, the plane of the mitral valve descends 1 to 2 centimeters towards the apex in adults with normal cardiac function, but the apex barely moves towards the base of the heart. In normal cases, the longitudinal shortening and radial contraction are the most important in both ventricles, followed by the torsion (cf. Figure 4.6). In pathological cases, these movements can be affected differently accordingly to the pathology.

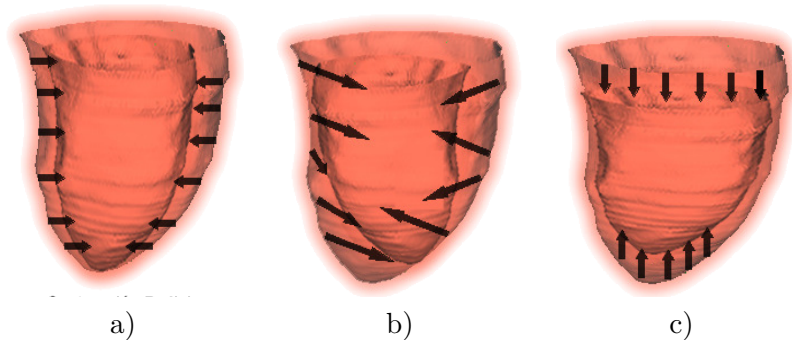


FIGURE 4.6— Components to describe LV wall motion: a) Radial contraction, b) Circumferential strain and c) Longitudinal contraction.

4.3 Cardiac Pathologies: Heart Failure

Cardiovascular diseases (CVDs) are a group of disorders of the heart and blood vessels and they mainly include: Ischaemic heart disease or coronary artery disease (e.g. heart attack), Cerebrovascular disease (e.g. stroke), Diseases of the aorta and arteries, including hypertension and peripheral vascular disease, Congenital heart disease, Rheumatic heart disease, Cardiomyopathies and Cardiac arrhythmias (WHO, 2011).

An estimated 17.5 million people died from CVDs in 2012, representing 31% of all global deaths. Of these deaths, an estimated 7.4 million were due to coronary heart disease and 6.7 million were due to stroke (WHO, 2014).

Cardiomyopathy, or heart muscle disease, is a type of progressive heart disease in which the heart is abnormally enlarged, thickened, and/or stiffened. As a result, the heart muscle's ability to pump blood is weakened, often causing Heart Failure (HF) and the backup of blood into the lungs or rest of the body. The disease can also cause abnormal heart rhythms.

Heart failure (HF) is the end stage of CVD and is the most expensive CVD-related condition with respect to health care costs of which the largest component is related to repeated hospitalizations. HF may be associated with a wide spectrum of LV functional abnormalities, which may range from patients with normal LV size and preserved Ejection fraction (EF) to those with severe dilatation and/or markedly reduced EF (YANCY et al., 2013).

Heart failure symptoms include changes to ventricular size and function due to both chemical and mechanical factors (JESSUP et al., 2003). Remodeling occurs in response to myocardial infarction, cardiomyopathy, hypertension, or valvular heart disease. If a patient had a myocardial infarction, where a major vessel supplying blood the myocardium is blocked; the downstream myocardium supplied by the blocked vessel undergoes necrosis and is replaced over time by fibrotic tissue in an attempt to heal the infarct. The fibrous tissue has different mechanical and contractile properties than healthy myocardium, so an myocardial infarction, often leads to abnormal loading conditions throughout the ventricle resulting in dilatation and hypertrophy (cf. Chapter 7); increasing end diastolic volumes and limiting the ability of the heart to pump effectively (SUTTON et al., 2000).

As the heart's pumping becomes less effective, blood may back up in other areas of the body. Fluid may build up in the lungs, liver, gastrointestinal tract, and the arms and legs. This is called Congestive Heart Failure (CHF). The New York Heart Association (NYHA) functional classification is widely used and accepted. It is based on exercise capacity and symptoms of the disease and places patients in one of four categories based on how much they are limited during physical activity. Table 4.1 shows a functional classification according the presence and severity of HF provided by the New York Heart Association (NYHA), and also by the American College of Cardiology Foundation (ACCF)/ American Heart Association (AHA).

Changes to the ventricular wall as a result of remodeling can also disrupt the electrical activation network within the heart. These disruptions can result in atrial fibrillation or irregular ventricular activation and contraction. Underlying electrical conduction issues manifest themselves

TABLE 4.1– Comparison of ACCF/AHA Stages of HF and NYHA Functional Classifications. From (YANCY et al., 2013)

ACCF/AHA Stages of HF		NYHA Functional classification	
A	At high risk for HF but without structural heart disease or symptoms of HF	None	
B	Structural heart disease but without signs or symptoms of HF	I	No limitation of physical activity. Ordinary physical activity does not cause symptoms of HF.
C	Structural heart disease with prior or current symptoms of HF	I	No limitation of physical activity. Ordinary physical activity does not cause symptoms of HF.
		II	Slight limitation of physical activity. Comfortable at rest, but ordinary physical activity results in symptoms of HF.
		III	Marked limitation of physical activity. Comfortable at rest, but less than ordinary activity causes symptoms of HF.
		IV	Unable to carry on any physical activity without symptoms of HF, or symptoms of HF at rest.
D	Refractory HF requiring specialized interventions	IV	Unable to carry on any physical activity without symptoms of HF, or symptoms of HF at rest.

as changes in the contraction timing of the heart, which decreases the ejection fraction (EF) and further diminishes the pumping efficiency of the heart.

Although heart failure can manifest itself in a variety of ways, cardiac dyssynchrony affects 30 to 50% of heart failure patients (DE SUTTER et al., 2005). Dyssynchrony is indicative of a disruption in the conduction pathway of the heart caused by ischemia, inflammation, fibrosis, and aging. These disruptions cause different parts of the heart to be activated at different times. Because mechanical contraction requires electrical activation, irregular electrical activation leads to discoordinate mechanical contraction of the heart.

Mechanical dyssynchrony is when regions of the heart contract at different times. There are several general types of mechanical dyssynchrony. Inter-ventricular dyssynchrony is a difference in contraction times between the left and right ventricles. Atrio-ventricular mechanical dyssynchrony is characterized by an abnormal delay between atrial and ventricular activation, which can result in a shortened diastolic filling period and a decreased stroke volume. Intra-ventricular dyssynchrony is of particular interest in heart failure patients, it is the discoordinate mechanical contraction of different regions within the same ventricle (HAWKINS et al., 2006).

It is estimated that up to 40% of patients with cardiomyopathy and congestive heart failure (CHF) have an uncoordinated ventricular contraction caused by electrical delay, most often in the left bundle branch (TRUPP, 2006). This is known as left bundle branch block (LBBB).

Because the electrical signal to the left ventricle is delayed by LBBB, the right ventricle begins to contract a fraction of a second before the left ventricle instead of simultaneously. The result is an asynchronous contraction of the ventricles. This uncoordinated ventricular contraction further reduces the pumping efficiency of an already weakened heart muscle in HF patients. The electrical delay is visible on an electrocardiogram (ECG) (cf. Figure 4.3) as widening of the QRS complex and helps to identify patients who might benefit from cardiac resynchronization therapy (CRT).

Cardiac resynchronization therapy (CRT) is a treatment option for heart failure patients with cardiac dyssynchrony. From HF population, it is estimated that between 30% and 40% suffer from cardiac dyssynchrony which is associated with a decrease in ejection fraction and worsened prognosis. CRT utilizes a biventricular pacemaker to electrically stimulate the myocardium in an effort to restore synchronous electrical activation and improve cardiac output.

Currently, there are four major criteria that must be met for a patient to qualify for CRT implantation:

- QRS Duration > 120 ms: QRS duration is a measure of the electrical dyssynchrony of the heart. Without electrical dyssynchrony, the simultaneous stimulation of the septal and lateral walls of the LV will have no effect.
- Ejection Fraction $< 35\%$: A healthy ejection fraction is greater than 50%. A low EF is indicative of inefficient cardiac function.
- NYHA HF Functional Class III-IV: *The New York Heart Association (NYHA) functional classification* (cf. Table 4.1) serves to determine the effect that heart failure has on patient activity and comfort. Patients classified as Class III-IV are considered to have moderate to severe heart failure.
- Optimal Medical Therapy for at least 3 Months: Before resorting to an implantable device, it is necessary to ensure that the patient cannot benefit from guided pharmacological treatments.

There have been a large number of randomized clinical trials that demonstrate the efficacy of CRT; however, at least 30% of patients undergoing CRT do not benefit from the treatment. Currently, there are a widely used definitions of response to CRT (FORNWALT et al., 2010). The major two categories of response criteria are clinical response and quantitative response. Clinical response criteria to CRT is focused on detecting improvement of symptoms in heart failure patients. Most commonly ways to assess clinical response criteria are: i) the *New York Heart Association Functional Classification*, in which a responder to CRT is a patient who improves by at least one heart failure class six months after device implantation, ii) *The Minnesota Living with Heart Failure Questionnaire*, which consists of 21 questions covering a wide range of daily activities to determine the effect of heart failure symptoms on the patient's daily routine, and iii) *The Six-minute Hall Walk Distance*, that measure of how heart failure affects an individual's susceptibility to fatigue due to physical activity.

In addition to clinical criteria, there are a variety of quantitative measures that have been used in the literature to classify patients as responders or non-responders to CRT. Quantitative measures typically identify signs of reverse remodelling including improved cardiac output and decreased cardiac volumes. Some quantitative criteria to assess CRT response are: i) LV Ejection Fraction (LVEF) increased by at least 5% (absolute) or 15%, ii) LV End Systolic Volume (LVESV) decreased by at least 10% - 15%, iii) LV End Diastolic Volume (LVEDV) decreased by 15% or more, and iv) Stroke Volume (SV) increased by at least 15%.

There must be additional factors that contribute to an individual's response to CRT. It is thought that the presence of mechanical dyssynchrony, the amount and location of myocardial scar, and coronary vein anatomy play a role in a patient's response to CRT.

Clinically, Echography/Ultrasound (US) is the most common modality used to assess mechanical dyssynchrony of the heart. Another technique that can assess mechanical dyssynchrony, determines the presence and distribution of myocardial scar tissue, and discerns the proximal parts of coronary vein anatomy is Magnetic Resonance Imaging. Hence, MRI is a potentially powerful tool for CRT patient selection.

In the next section we briefly describe two cardiac modalities techniques addressed in this thesis: cardiac MRI, that is currently used in medical imaging for the assessment of LV function, and Echocardiography, that is considered as the standard of reference for cardiac mechanical analysis.

4.4 Imaging of the Cardiovascular System

The main imaging modalities of the cardiovascular system are: X-Ray, Ultrasound (US), Positron Emission Tomography (PET), Single Photon Emission Computed Tomography (SPECT), Computed Tomography (CT) and Magnetic Resonance Imaging (MRI). Each imaging modality provides a different type of information and is used for specific purposes. This work focuses on cardiovascular magnetic resonance images (CMRI) and echocardiography (US, ultrasound imaging) which are widely used in clinical routine to characterize cardiac motion abnormalities taking advantage of their high temporal resolution. They provide complementary information about cardiac anatomy, myocardial structure and mechanical function. Several MRI-based techniques or specific sequences can be employed to detect mechanical dyssynchrony and assess cardiac LV motion including myocardial tagging, phase contrast tissue velocity mapping and cardiac cine-MRI. Late Gadolinium Enhanced (LGE) cardiac magnetic resonance imaging is used to determine the presence and distribution of myocardial scar/fibrosis tissue. As this work is also focused on the detection of cardiac fibrosis, this cardiac MRI sequence will be described in Chapter 7. Cardiac cine-MRI mode is used in this study for the assessment of LV wall motion and is described below.

4.4.1 Cardiac Magnetic Resonance Imaging (cMRI)

Cardiac Magnetic Resonance Imaging (MRI) is currently used in medical imaging for the assessment of LV function (KIRSCHBAUM et al., 2011). It is also used to evaluate cardiac morphology and myocardial substrate. One of the main advantages of cardiac MRI is the lack of ionizing radiation, which is substantial with SPECT and computed tomography (CT) scanning. High-quality imaging can be achieved in most patients in all orientations, for all cardiac chambers and wall segments including the left and right ventricles.

Cardiac MR images are commonly acquired at a magnetic field strength of 1.5T and 3T (tesla); commercial systems are available between 0.2T–7T. This strong constant magnetic field is applied to align the magnetization of hydrogen atoms of the organ being scanned. The hydrogen nuclei are then excited by applying another magnetic field at a certain frequency (RF field) that deflects their magnetization from this alignment. The signal emitted from these excited nuclei, when they realign to their initial configuration, is measured by RF sensors and used to form an image. In MR imaging, signals received from a particular tissue (e.g., heart muscle, fat, etc) are determined by the density of hydrogen atoms (proton density), and by two distinct MR relaxation parameters, longitudinal relaxation time (T1) and transverse relaxation time (T2). Proton density, T1, and T2 are significantly varied for different tissue types, and are used to generate contrast in MR images. Also, image contrast can be modified by modulating the way the radiofrequency signals are applied (the MR sequence). An MR imaging sequence refers to a specific combination of radiofrequency pulses, magnetic gradient field switches, and data acquisitions with temporal synchronization, all used to generate the MRI image.

The most recent standard protocol for cardiac MR employs the Steady-State Free Precession (SSFP) sequence. This sequence provides the best contrast between myocardium (dark) and the blood in the chamber (white) for imaging cardiac function. For a better visualization, fat suppression sequences may be applied to allow signal from fat to be specifically suppressed with special pre-pulses. To assess heart function, a full cardiac cycle is divided into 20-30 frames, each consisting of 10-12 slices corresponding to a specific plane of the heart.

In a cardiac-cine MRI study, 3 main cardiac imaging planes are identified: the short axis (SAX), the horizontal long axis also known as a 4-chamber view (LAX-4CH), and the vertical long axis also known as a 2-chamber view (LAX-2CH). The standard imaging plane SAX used for LV assessments is perpendicular to the long axis of the heart (apex-base). Figure 4.7 shows an example of the three main image planes of acquisition in cardiac MRI. Spin echo sequences acquire a static anatomic image with black blood, providing information about heart morphology (cardiac cavities and vessels appear black contrasting with myocardial and vessel walls in gray). On the other hand, gradient echo sequences enable to acquire dynamic images (called cine) with white blood and gray myocardium, allowing to analyse heart dynamics.

Cardiac cine-MRI is particularly appropriate to study global and regional ventricular function (GAROT, 2005; KIRSCHBAUM et al., 2011; SARWAR et al., 2008). The strength of cardiac MRI, as compared with CT scanning, is its superior temporal and contrast resolution. However, the spatial resolution of CT scanning is superior (LIN, 2008). A typical cardiac cine-MRI will have a

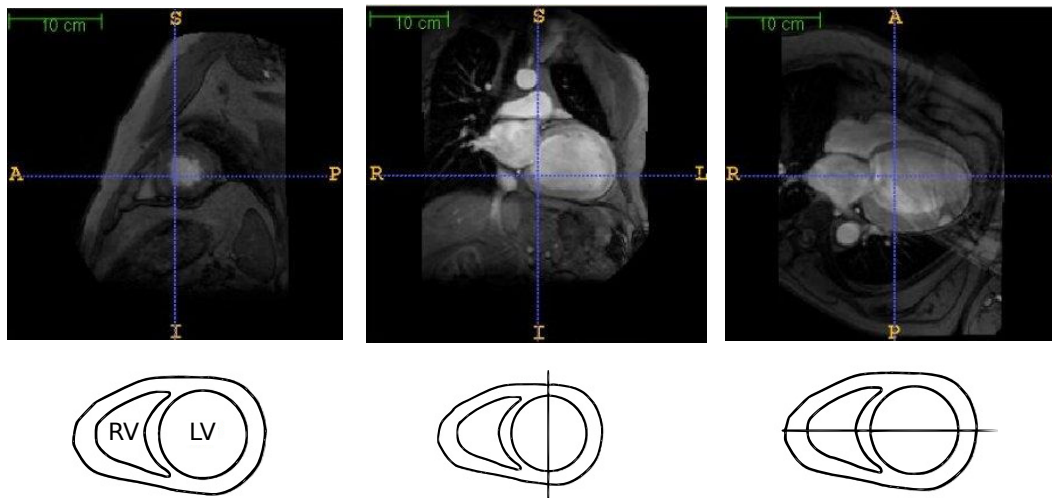


FIGURE 4.7— Cardiac Imaging plane in MRI: (left) Short-axis plane SAX; (middle) Vertical long axis plane (2-chamber view) LAX-2CH; (right) Horizontal long axis (4-chamber view) LAX-4CH.

temporal resolution of 30 ms, a spatial resolution of 1.5 mm (in-plane) and a slice thickness of 8 to 10 mm. Capturing an image of the heart that is unaffected by motion requires the image to be acquired in just a few tens of milliseconds. However, to achieve acceptable image quality, the image acquisition time becomes too long to “freeze” heart motion. Therefore, cMRI signals are acquired over multiple heartbeats, synchronizing the signal acquisition to a particular time point in the cardiac cycle using the ECG. There are two main techniques for synchronising the measurement of MR data with the cardiac cycle.

Prospective gating techniques wait for the trigger signal to start acquisition of data. The data are acquired using excitations at a fixed time points in the cardiac cycle. The data collection is paused at the end of the cardiac cycle and the sequence waits for the next trigger signal. The R wave of the ECG signal corresponds to the beginning of the contraction phase of the heart (cf. Figure 4.8). After a small time interval, t_{delay} , the first frame of the image sequence is acquired. After the acquisition of the first frame, frames are acquired every t_{offset} msec. In retrospective gating, data collection is done continuously throughout the entire cardiac cycle. Then, the recorded trigger signal is used to retrospectively assign the data to the different positions in the cardiac cycle.

A cardiac cine-MRI study is performed in different slices routinely divided in three spatial planes: basal, mid-cavity and apical (cf. 4.2.1). Figure 4.9 shows different cardiac cine MRI acquisitions in a short axis view at different planes for one patient.

4.4.2 Echocardiography (US)

Ultrasound (US) employs pulsed, high frequency sound waves. When an ultrasound wave meets an interface of differing echogenicity, the wave is reflected, refracted and absorbed. The reflected sound waves are sensed by the transducer (which also emits the sound waves) and then, processed to produce the image. The ultrasound beam can be aimed at specific directions and

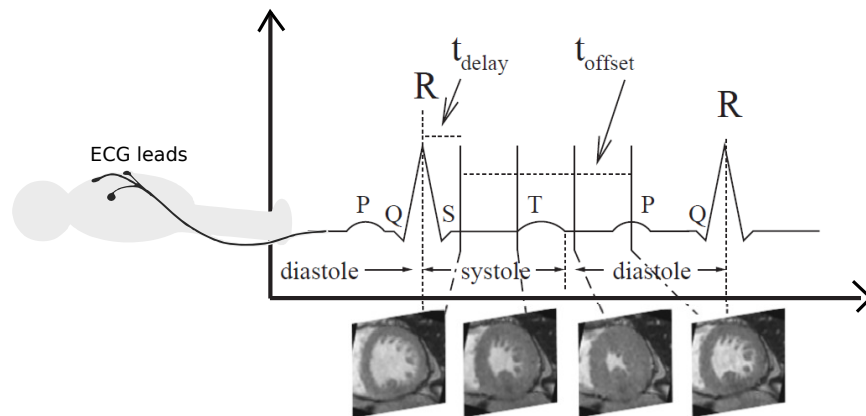


FIGURE 4.8– ECG synchronization of imaging pulse sequences. Adapted from: (PERPERIDIS, 2005)

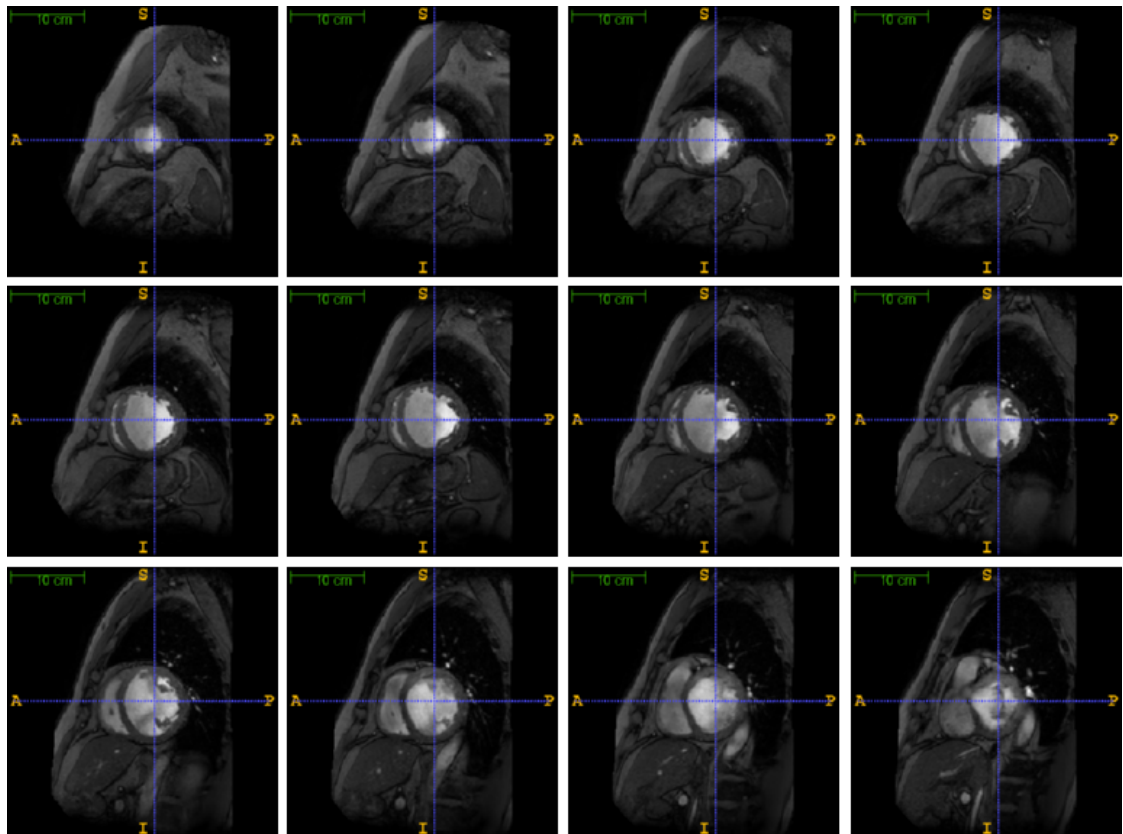


FIGURE 4.9– Different spatial acquisitions in short axis view, from apical plane (top left) to basal planes (bottom right)

obeys the laws of optics with regards to refraction, reflection and transmission. The intensity of the ultrasound beam decreases as it travels away from the ultrasound source due to divergence, absorption, scatter and reflection of the wave energy at tissue interfaces. Stronger reflections

are returned when the ultrasound beam is perpendicular to the imaged structure. Ultrasound is frequently used for the imaging of the heart (echocardiography).

Echocardiography is more frequently used to evaluate cardiac chamber size, wall thickness, wall motion, valve configuration, global and regional motion and the proximal great vessels. Ultrasound has a high temporal resolution and is widely used in clinical routine. It is also more portable and less expensive than other modalities. However, the signal to noise ratio of the US images is low. Figure 4.10, shows an example of three Transthoracic echocardiographic (TTE-US) images at end-diastole.

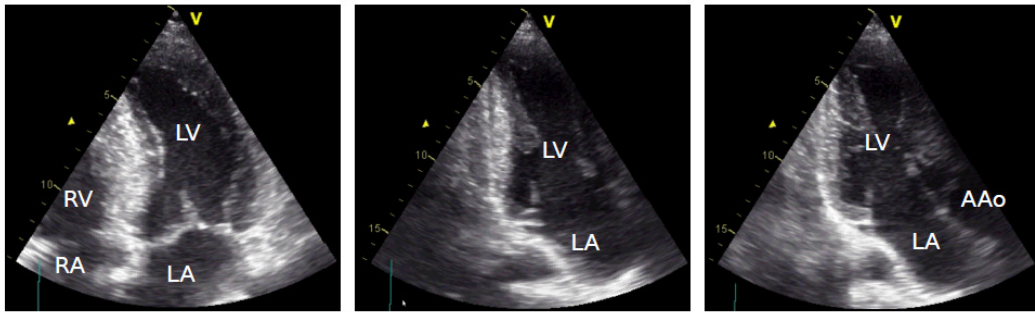


FIGURE 4.10– Transthoracic echocardiographic (TTE-US) images at end-diastole. From left to right: apical four chambers view (4CH), apical two chambers view (2CH), and apical three chambers view (3CH). Acronyms – AAo: ascending aorta, LA: left atrium, LV: left ventricle, RA: right atrium, RV: right ventricle. From: (BETANCUR, 2014)

There are three types of echocardiography: M-mode US, B-mode (brightness) US and Doppler mode US. The M-mode provides one dimensional view (depth) into the heart. The B-mode US uses an array of transducers which allows a plane of tissue to be imaged, thus making the anatomical relationships between different structures easier to appreciate than with the M-mode imaging. Doppler imaging allows the evaluation of blood flow patterns (direction and velocity) by detecting frequency changes occurring when ultrasound waves reflect off individual blood cells moving towards or away from the transducer. Tissue Doppler imaging (TDI) is an echocardiographic technique that uses Doppler principles to measure the velocity of myocardial motion (HO et al., 2006). TDI can be performed in pulsed-wave and color modes. Pulsed-wave TDI is used to measure peak myocardial velocities and is particularly well suited to the measurement of long-axis ventricular motion because the longitudinally oriented endocardial fibers are most parallel to the ultrasound beam in the apical views. Similar to TDI, Two Dimensional (2D) speckle tracking echocardiography (STE) (BLESSBERGER et al., 2010), permits offline calculation of myocardial velocities and deformation parameters such as strain and strain rate (SR), with a regional analysis by anatomical segments.

In Speckle tracking echocardiography (STE), echoes are locally modified by an interference pattern and natural acoustic reflections called as a whole speckle noise. This speckle is particular for a given portion of a tissue being a sort of local acoustic signature of a particular subregion. A technique called speckle tracking tracks this speckle frame to frame and ultimately resolves it

into angle-independent two-dimensional strain-based sequences. STE provides both quantitative and qualitative information about tissue deformation and motion (BLESSBERGER et al., 2010). Displacement, velocity, deformation (strain), tissue kinetics (tissue velocity imaging or tissue synchronization imaging) are examples of what can be analyzed with STE. Moreover, today it is possible to have their extension to 3D echocardiography (e.g. to compute surface strain) (MAFFESSANTI et al., 2009). The strain is calculated for each segment of the LV as the relative average of deformation between two points along the predetermined directions of the coordinate system of the heart. These deformation and strain measures are computed in circumferential, longitudinal and radial directions.

Radial deformation represents myocardial deformation towards the center of the LV cavity, and therefore indicates the LV thickening and thinning motion during the cardiac cycle. Longitudinal deformation represents motion from the base to the apex. Circumferential deformation is defined as the change of the radius in the short axis, perpendicular to the radial and long axes. Longitudinal deformation is assessed from the apical views while circumferential and radial deformation are assessed from short axis views of the left ventricle. Longitudinal and circumferential strain, are expressed as a negative value and occur, simultaneously, to the deformation in the radial direction. The radial strain is represented as a positive value.

The assessment of 2D strains by STE is a semiautomatic method that requires the cardiologist to define a few points along the endocardial border. Furthermore, the sampling region of interest (ROI), that is automatically defined by the echo system from the endocardial delineation, needs to be adjusted to ensure that most of the wall thickness is incorporated in the analysis and to avoid the pericardium, as depicted in Figure 4.11-top left panel.

Then, strains are computed by tracking the local speckle from the defined regions. Regional strain is defined as the fractional or percentage change in a myocardial region in comparison to its original dimension, along a direction. From this, it can be obtained both a 2D mapping of the region's deformation during a heartbeat and local strain curves (2D plot of myocardial deformation over time), as depicted in Figure 4.11.

The recent advances in the development of Ultrasound imaging enable the acquisition of 3D images which overcome some limitations of the conventional 2D Ultrasound imaging. 3D Ultrasound imaging (FENSTER et al., 2001; MAFFESSANTI et al., 2009) has the potential to provide real time 3D visualizations of the heart and a regional measure of strain. However, the temporal resolution is lower than those of 2D ultrasound imaging. According to current clinical literature on 2D-STE technology, single plane acquisition must be performed with a temporal resolution ranging from 50 up to 80-90 frames/sec. 2D STE temporal resolution is two to three times higher than 3D-STE resolution.

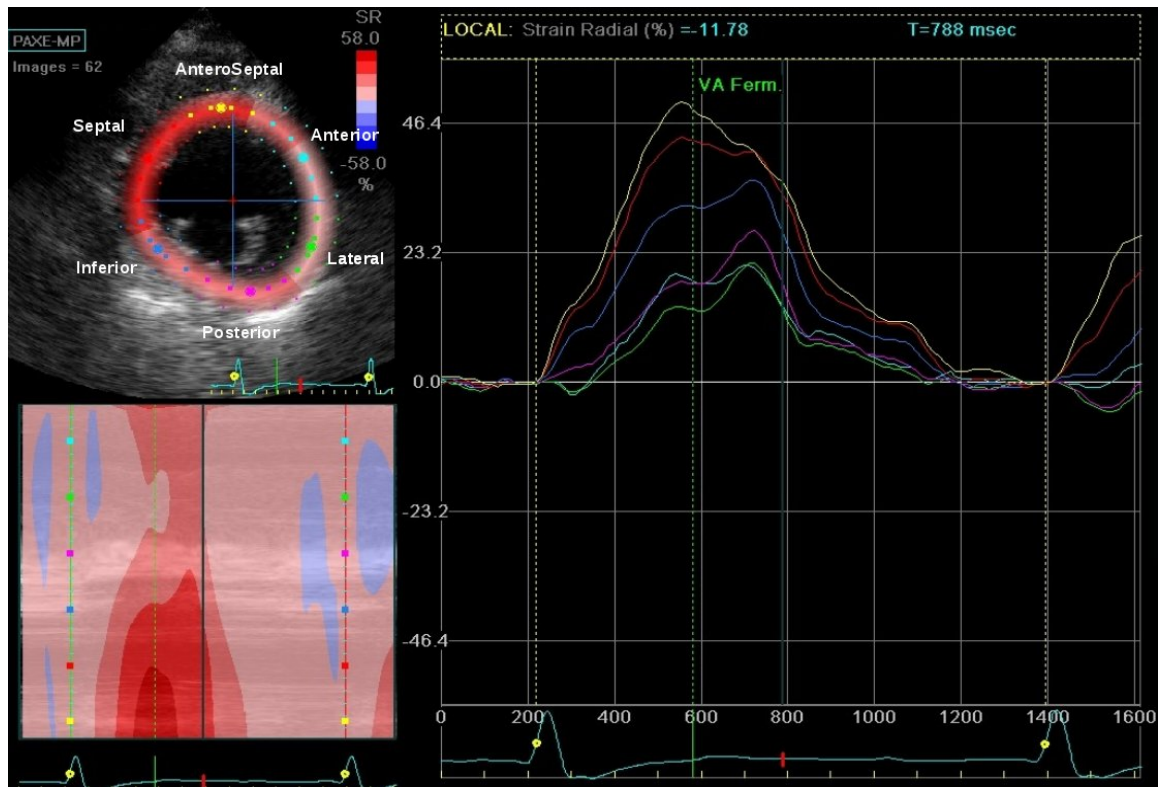


FIGURE 4.11— Speckle tracking echocardiography from a pathologic patient in the short axis view. Top-Left panel: A region of interest is indicated in a two-dimensional grey-scale image. The colours of the region of interest correspond with the colours of the time-strain curves in the right panel. Bottom-left panel: Bidimensional map of the myocardial deformation during a cardiac cycle. In abscissa: time in ms; in ordinate: radial strain along STE trace from antero-septal (bottom) to anterior (top) regions. Right panel: Time-radial strain curves of the different segments of the left ventricle. Acronyms – VA ferm: aortic valve closure, SR: radial strain

4.5 The assessment of cardiac Left Ventricular (LV) function in cardiac cine-MRI: a brief state-of-the-art

In clinical practice, assessment of the LV in cardiac cine-MRI relies mainly on manual segmentations as well as visual analysis and interpretations of wall motion. Several clinical studies have shown that visual assessments are inaccurate and subject-dependent (LU et al., 2009). Manual segmentation of the LV is prone to intra- and inter-observer variability, therefore, automatic assessment methods have become a major area of research (PETITJEAN et al., 2011). Assessment of the LV includes two main steps:

Global assessment of the LV: Cardiac magnetic resonance (CMR) evaluation of global left ventricular (LV) function is routinely performed based on measurements of LV volumes, ejection fraction and mass (cf. 4.2.3). These parameters are calculated from semi-automatically traced endocardial and epicardial boundaries using commercial software. Cardiac Magnetic Resonance (CMR) imaging provides accurate and reproducible methods to perform physio-

logical studies such as left ventricular ejection fraction (LVEF) estimation considered as an important prognostic marker and used to evaluate the cardiac function globally.

Regional assessment of the LV: CMR diagnosis of regional LV dysfunction is based on the interpretation of regional wall motion. This interpretation relies on integrating spatial and temporal information, which is subjective and requires extensive training and experience and is realized in clinical practice by radiologists or cardiologists. The parameters used to study regional function (cf. 4.2.3) are ventricular wall thickness, systolic thickening, and longitudinal and circumferential motion or wall shortening (SAN ROMÁN et al., 2009; SARWAR et al., 2008). These assessments can be performed either qualitatively or quantitatively. While a quantitative evaluation of ventricular volumes and EF is commonly utilized in the clinical setting, regional LVEF is typically evaluated on a qualitative basis only by visually assessing segmental LV thickening and motion of the 17 LV segments. Typically, segments will be scored as normal, hypokinetic, akinetic, or dyskinetic. Some clinicians employ a semi-quantitative scale whereby the regional wall motion of individual segments is graded as follows: normal = 0; hypokinesia = 1; akinesia = 2; and dyskinesia = 3. Hypokinesia is defined as impaired thickening and motion; akinesia is defined by absent thickening and motion; and dyskinesia is defined as paradoxical outward motion of the segment during systole.

Automatic diagnosis of LV regional dysfunction has attracted significant research. Below, we present some representative methods that have been proposed to the automatic assessment of LV wall motion in cardiac MRI. They are grouped in three categories:

4.5.1 Methods based on shape statistics

These methods are based on Landmark-based statistical shape analysis. Landmarks (anatomical points) are homologous points with point-to-point correspondences between shapes, which can be defined either mathematically, anatomically or manually. These methods provide a statistical shape modeling of cardiac contraction:

In (ORDAS et al., 2005), a 3D statistical model-based algorithm (3D-ASM) is used to segment the left ventricle in short- and long-axis cine-MRI. The segmentation process uses an optimized fuzzy inference strategy to provide the appearance (grey-level) model necessary to deform the shape model, and conduct the segmentation. Subsequent functional analysis includes the assessment of LV global functional indexes like e.g. time-volume curves, ejection fraction, stroke volume and cardiac output, as well as regional function parameters, like segmental wall motion, thickening and dyssynchrony delays. Experiments in the three planes, were performed in a group of 18 MRI studies, 10 healthy subjects and 8 patients candidate to Cardiac Resynchronization Therapy.

In (HUANG et al., 2006), cardiac magnetic resonance imaging data from 20 patients are analysed, in which half have heart failure. Two spatio-temporal ventricular motion models are proposed to analyze the mechanical dyssynchrony: radial motion series and wall motion series.

The radial motion series model is constructed based on the distances calculated from the LV center to points located in the endocardial border obtained using a surface tracking technique. The wall motion series model is constructed from wall thickness changes obtained using spherical harmonic (SPHARM) description combined with surface alignment method. This algorithm is applied in the context of CRT and a hierarchical agglomerative clustering technique is applied to the motion series to find candidate pacing sites based on the determination of the most delayed contraction sites of the LV.

In (BOYER et al., 2006), an approach for the spatio-temporal shape analysis of ventricular wall motion is presented, by demonstrating the feasibility of detecting intra-ventricular dyssynchrony in the left ventricle (LV) from short-axis MRI data using only one midventricular sequence. Using a statistical pattern recognition approach, based on Principal Component Analysis and Linear Discriminant Analysis, they have designed a classifier for intra-ventricular dyssynchrony detection from the shape descriptors extracted using a deformable model method with a complex Fourier series parametrization. The shape descriptors correspond to the spatial frequency components of the contour points from the combination of N ellipses obtained following a snake-like approach. The short-axis, cine MRI database used in this experiments comprises 33 studies: dyssynchronous samples correspond to 14 patients with intra-ventricular dyssynchrony in the LV; non-dyssynchronous samples correspond to 10 healthy subjects and 9 patients with dysfunctions other than intra-ventricular dyssynchrony.

In (SUINESIAPUTRA et al., 2009), a statistical model-based method to automatically detect regional wall motion abnormalities is proposed. The model uses as input parameters myocardial contractility patterns from a framework where all shapes contract from a reference shape constructed with the endocardial and epicardial contours at end-diastole (ED) and end-systole (ES). 44 short-axis magnetic resonance images were selected from healthy volunteers to train a statistical model of normal myocardial contraction using independent component analysis (ICA). A classification algorithm was constructed from the ICA components to automatically detect and localize abnormal contracting regions of the myocardium. The algorithm was validated on 45 patients suffering from ischemic heart disease. Two validations were performed; one with visual wall motion scores (VWMS) and the other with wall thickening (WT) used as references. WT was calculated by using dedicated quantitative MR measurement software (MR Analytical Software System MASS v. 5.0, Medis, Leiden, the Netherlands). Best accuracy of the ICA-based method was obtained in the mid-cavity plane with almost 90% in WT benchmarking and 67% in VWMS benchmarking.

In (SLIMAN et al., 2010), the myocardial function is assessed by estimating the left ventricle (LV) wall thickening based on a 4D tracking approach that tracks the LV wall during the cardiac cycle. Initially, the proposed 4D approach tracks the surface points on the LV wall by solving a 3D Laplace equation between each two subsequent LV surfaces. The initial locations of the tracked LV surface points are iteratively adjusted through an energy minimization cost function using a generalized Gauss-Markov random field image model. Using the iteratively adjusted solution of the 3D Laplace equation, the myocardial wall thickening is estimated by co-allocation

of the corresponding points, or by matching between the endocardium and epicardium surfaces of the LV wall.

In (LEKADIR et al., 2011) the myocardial assessment in MRI is focused on statistical modeling based on spatio-temporal interlandmark relationships. Experiments were performed for the interpretation of 4-D cardiac MRI data in a set of 28 subjects identified as normal, 11 datasets mildly abnormal and 11 identified as severely diseased. For each subject, eight uniformly distributed cine frames were delineated by an expert observer using 136 landmarks for each surface. The upper and lower LV/RV junction points were manually defined in all short-axis images and time frames. Inter-landmark constraints are first introduced based on a statistical generalization of barycentric coordinates. A combinatorial sequential search is then developed for optimal tracking of the dynamic boundaries based on the A^* algorithm (a graph search algorithm based on a best-first and heuristic approach, which can find efficiently solutions to least-cost path problems). The multivariate variables are used to encode existing patterns between varying regions of the dynamic shape by using a Boolean consistency measure. Trained tolerance regions that are resistant to the selected set of training examples are constructed to describe normal motion properties. They are subsequently used within an iterative algorithm to accurately identify the abnormal landmarks and derive a dysfunction surface map for highlighting regional dysfunctions.

4.5.2 Methods based on image features extraction

These methods are based with the hypothesis that motion patterns of normal LV segments should be deviated away from motion patterns of the abnormal LV segments. Patterns correspond to features extracted directly from the cardiac MRI sequences.

In (LU et al., 2009), a pattern recognition technique built upon intra-segment correlation using a normalization scheme that maps each LV slice to polar coordinates with fixed size, intensity level, and position is proposed. Following the normalization, an intra-segment correlation based classifier was used for recognition of segments with abnormal regional LV wall motion. The features used in this experiment correspond to rectangle images obtained in the end diastolic frame in which the left edge represents the line from the LV center to a reference point located in the epicardial border previously delineated, the row represents the radial distance (normalized by the distance to the epicardium for that radial line) and the column is the counterclockwise polar angle. Experiments were performed on cardiac studies from 17 subjects, 12 with abnormal wall motion and 5 control subjects, only in the basal plane.

In (PUNITHAKUMAR et al., 2010b), LV contours previously delineated were processed using a Kalman filter, given a cyclic dynamic model. Then, wall motion was quantitatively analyzed by constructing distributions of the radial distance estimates of the LV cavity. Three information theoretic abnormality detection criteria are proposed: the first one is based on the Shannon's differential entropy (SDE), a second one is based on Rényi entropy and a third one is based on Fisher information. Experiments were performed on segmented LV cavities of short-axis MRI obtained from 30 subjects. Later in (PUNITHAKUMAR et al., 2010a, 2013), the work was

extended to other features: normalized radial distance, radial velocity, segment arc length, segment area and wall thickness. A naive Bayes classifier algorithm is constructed from the Shannon's differential entropy of the features to automatically detect abnormal functional regions of the myocardium. Using 174 segmented short-axis magnetic resonance cine images obtained from 58 subjects (21 normal and 37 abnormal), the proposed approach is quantitatively evaluated by comparison with ground truth classifications by radiologists over 928 myocardial segments. The overall classification accuracy was 87.1%

In (XAVIER et al., 2012), myocardial motion was estimated by using a modified phase-based optical flow technique. Myocardial velocity is measured in centimeter per second in each studied pixel and visualized as coloured vectors superimposed on MRI images. The vector field represents the local velocity measurements of the various structures within the images. Tracking of points of interest then allows a quantitative analysis of the myocardial displacement through time-radial velocity curves, providing clinicians metrics for the assessment of myocardial wall abnormalities. Eleven normal hearts and one heart presenting a severe parietal dyssynchrony were used to evaluate the method leading to a regional measurement of the time-velocity course of myocardial displacement in different segments of the heart wall.

In (AFSHIN et al., 2014), a set of statistical MRI features, based on the Bhattacharyya measure of similarity between distributions, is constructed for all the regional segments and all the frames in the cardiac study. The statistical features, over a cardiac cycle, are related to the proportion of blood within each segment, characterizing the segmental contraction. Starting with the manual segmentation of endo- and epi-cardial boundaries in the first frame, the method searches the optimal direction along which the proposed image features are most descriptive via a linear discriminant analysis. Then, using the results as inputs to a linear support vector machine classifier, they obtain an abnormality assessment of each of the standard cardiac segments. Experiments, in the three planes, were performed over 58 subjects, 21 normal and 37 abnormal hearts, obtaining an overall classification accuracy about 86.09%.

4.5.3 Methods based on parametric imaging-based quantification

This methodology relies on the reader's ability to integrate spatial and temporal information on LV wall motion by creating parametric images from which motion abnormalities can be easily identified.

(CAIANI et al., 2006, 2004) used parametric images of the dynamic loops of cardiac MR images to improve the accuracy and reduces the interobserver variability of the detection of regional wall motion abnormalities by non-cardiologists. Parametric analysis of main LV motion was also presented in (KACHENOURA et al., 2007) in cine MR images for the evaluation of regional myocardial function. The parametric analysis of main motion (PAMM) in echocardiography (RUIZ et al., 2005) was adapted to short-axis MR images and a new quantitative process was proposed to extract the segmental mean contraction times and the mean radial velocities from the parametric images. This cardiac assessment approach was applied to short-axis slices in 22 subjects: 8 controls, 13 myocardial infarctions, and one left bundle branch block (LBBB).

Later in (EL BERBARI et al., 2009) the method was applied to 36 healthy subjects. This type of approaches have as a preliminary step, the segmentation of the cardiac cavity.

Recently, in (SUEVER et al., 2014) radial displacement curves (RDCs) are generated throughout the LV that represent the distance from the LV centroid to different points in the endocardial border previously delineated. A parameter based on cross-correlation was used to determine the delay time between each RDC and a patient-specific reference. Maps of regional dyssynchrony are constructed to identify the latest-contracting segment in the LV. The method was tested in 10 normal individuals and 10 patients candidate for CRT.

Despite this impressive research effort that has been devoted to automatic detection, localization and quantification of regional LV abnormality, the problem is still challenging. Methods based on shape statistics are sensitive to the quality of the myocardial contours, as they have the myocardial contours as input. In these models myocardial shapes are subsampled into a number of landmark points from which the statistical models are estimated. Some of these methods exploit all the cardiac sequence while others base their analysis only on two phases (ES and ED) (ORDAS et al., 2005; SLIMAN et al., 2010; SUINESIAPUTRA et al., 2009). The method proposed in (AFSHIN et al., 2014) exploits all the sequence, however it needs the segmentation of epicardial and endocardial boundaries at the first frame of the cardiac cycle. Others methods use only the epicardial boundaries (LU et al., 2009).

All of the informative features proposed in the previous techniques contribute to the discrimination of LV wall motion abnormality. Different pattern recognition techniques have been employed: in (AFSHIN et al., 2014), Linear Discriminant Analysis (LDA) is combined with linear SVM. In (PUNITHAKUMAR et al., 2010a), Shannon’s Differential Entropy (SDE) is used with a Naive Bayes classifier. In (SUINESIAPUTRA et al., 2009), wall thickening and visual wall motion scoring are used for Independent Component Analysis (ICA). A classifier based on intra-segment correlation measure is proposed in (LU et al., 2009) and finally, Principal Component Analysis (PCA) combined with a classifier based on the Mahalanobis distance is used in (GARCIA-BARNES et al., 2010).

In the next section, we introduce our proposed approach that is based on dynamic images and machine learning techniques to obtain a binary classification between normal and abnormal LV wall motion in cine-MRI. Furthermore, we propose to use a classification approach based on discriminative dictionary learning techniques that, to the best of our knowledge, has never been used for the classification of LV wall motion in cardiac cine-MRI.

4.6 The proposed method

We propose a novel approach based on dynamic images combined with discriminative dictionary learning (DL) techniques to classify local normal/abnormal wall motion in Left Ventricle (LV) function in cardiac cine-Magnetic Resonance Imaging (MRI). The proposed

method exploits the partial information obtained from all temporal cardiac phases and anatomical segments in a spatio-temporal representation without the need of LV boundaries segmentation.

4.6.1 Overall scheme

An overview of the proposed method can be seen in Figure 4.12. Firstly, cardiac cine-MRI sequences in short axis view are collected from two populations: pathologic and control subjects. Secondly, the subsequent process can be explained in three main stages:

Pre-processing stage: A region of interest (ROI) is defined at the first frame of each sequence in order to keep only the LV cavity. Then, the ROI is projected in all the sequence and is spatially normalized according to the AHA representation to identify different anatomical segments.

Feature extraction stage: An automated spatio-temporal image extraction procedure is performed with the construction of three novel representations: i) diametral spatio-temporal profiles, ii) radial spatio-temporal profiles, and iii) time signal intensity curve parameters extracted from the radial profiles. Based on these three new types of representation, three respective approaches have been proposed in this work. They are all based on Dictionary Learning-based classification.

Dictionary Learning-based classification stage: In each case, the proposed representation is taken as input atoms for the training of DL approaches to provide a classification of local LV wall motion. The results are presented in parametric images known as bull-eyes.

Our global proposed approach deals with four main problems that limit the application of pattern recognition techniques to the problem of detecting abnormal LV wall motion (LU et al., 2009):

- Normalization of the LV's size, shape, intensity level and position: A subject's LV changes size, shape, intensity level and position throughout the cardiac cycle and implies intra-subject variation. Furthermore, there is an additional inter-subject variation to consider.
- Temporal normalization between datasets: the number of phases in the datasets in study can be different. The LV wall motion features can be extracted only after defining a temporal normalization among the phases and subjects.
- Feature extraction that is sensitive to wall motion but not sensitive to the thickness variation of the myocardium across subjects.
- Discrimination of normal and abnormal wall motion and selection of a classification criterion.

The first problem is handled in the preprocessing step. The second is handled in the feature extraction stage that concerns LV wall motion features. In this stage, we based our method on the hypothesis that the construction of spatio-temporal profiles allows the analysis of the radial motions of LV's walls during all the cardiac cycle. In short-axis cine-MRI, a radial motion profile represents relative contraction between endocardium and epicardium and reflects an important part of the wall's mechanical activation (HUANG et al., 2006). Because the heart contracts and

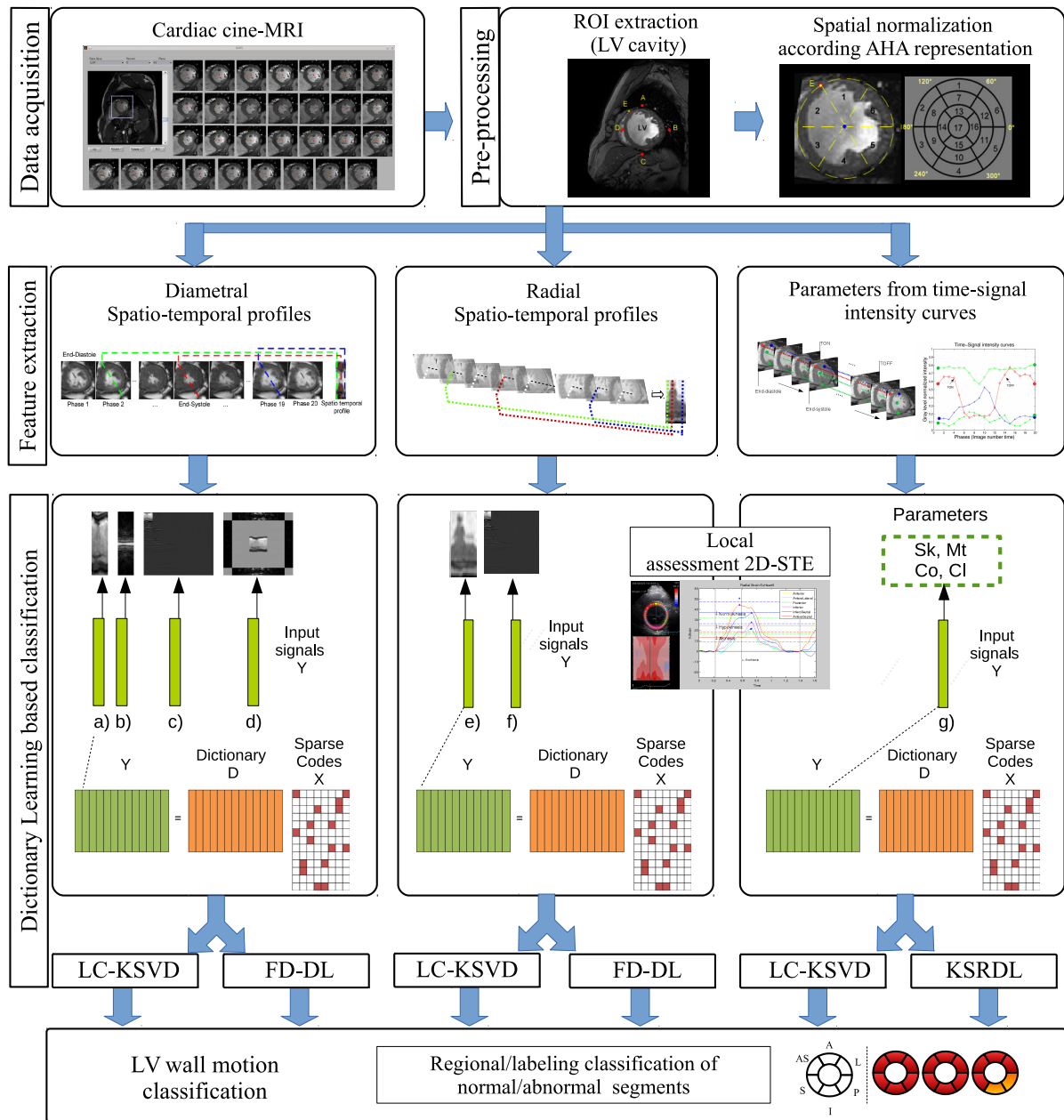


FIGURE 4.12– Overall scheme of the adaptation of DL approaches for local LV wall motion classification in cardiac cine-MRI: 1) Data acquisition stage corresponds to acquisitions of cardiac cine-MRI sequences in short-axis view from two populations: pathologic and control subjects. 2) *Pre-processing stage*, involves the ROI extraction of the LV cavity and spatial normalization procedures. 3) *Feature extraction stage*, corresponds to the three proposed spatio-temporal representations: Diametral profiles, radial profiles and parameters extracted from time-signal intensity curves in the radial profiles. 4) *The classification based on Dictionary Learning*, with three different approaches according the spatio-temporal representation used as input signals: First approach compares two discriminative DL classification algorithms: LC-KSVD with FD-DL using diametral spatio-temporal profiles as inputs in one of the following representations: a) gray level (original domain), b) Fourier domain, c) Wavelet domain or d) Curvelet domain. Second approach also compares the LC-KSVD with the FD-DL algorithm using radial spatio-temporal profiles in one of the following representations: e) gray level (original domain) or f) wavelet domain. Third approach compares the LC-KSVD algorithm with the KSRDL algorithm using g) combinations of parameters extracted from the radial spatio-temporal profiles. The three approaches search for the LV wall motion classification and the regional labeling of normal/abnormal LV anatomical segments.

dilates also along both the long and short axes of the image stack, the radial motion series can approximately describe the spatio-temporal wall motion from two-dimensional view (HUANG et al., 2006). For a normal heart, all the radial motions are approximately similar to one another because the different LV anatomical segments tend to contract synchronously. However, for a failing heart, different LV segments may have different contraction behaviors.

The interpretation of regional wall motion relies on integrating spatial and temporal information, which is subjective and requires extensive training and experience (CAIANI et al., 2006). The proposed representations exploit the spatio-temporal information in a familiar, easily understandable, visual format. Three type of features are proposed and used in this work:

The first proposed feature used corresponds to **diametral spatio temporal profiles** that show the temporal evolution of epicardium and endocardium at the same time in opposite LV anatomical segments, exploiting thus, the spatial relation exhibited by radial motion profiles at the same orientation. The study of contraction in opposite segments has been exploited in echocardiography for dyssynchrony analysis. Radial dyssynchrony is defined as the differences in peak strain between the anterior septum and posterior wall (SUFFOLETTO et al., 2006). The parasternal short-axis views in echocardiography at the mid-cavity LV level is used for radial dyssynchrony analysis. Several works have shown septal wall-to-free wall mechanical activation as a major feature of dyssynchrony (DOHI et al., 2005; SADE et al., 2004; SUFFOLETTO et al., 2006). Several studies have demonstrated the value of speckle tracking strain imaging in predicting response to CRT, for example, in (DELGADO et al., 2008), a total of 161 patients undergoing CRT implantation were studied. A time difference between peak radial strain of the anteroseptal and posterior segments upper than 130 ms predicted CRT response with a sensitivity and specificity of 83% and 80%, respectively.

Dyssynchrony analysis, that is performed in opposite segments in echocardiography has been exploited again in cine MRI by (XAVIER, 2010). In this work, the parasternal short-axis view in M-mode echocardiography was considered equivalent to the short axis view in cardiac MRI. Preliminary results of dyssynchrony were obtained by measuring different parameters in 6 points located between the inferoseptal and lateral segment, between the inferoseptal and anterior segment and finally between anteroseptal and posterior segments. The method is based on optical flow and allowed the definition of a Septal-Posterior Wall Motion Delay parameter with a correlation of 0.9 between the value obtained by echocardiography and the one obtained by the MRI study. The method was applied in a set of 9 normal subjects and 15 patients, 5 with long QRS and 10 with small QRS.

Following this target in mind and taking advantage that 2D speckle tracking echocardiography studies were available for a subset of patients in this work, **a second proposed feature** is based on the construction of **radial spatio-temporal profiles** where motion of LV's walls is observed for each segment of the LV cavity. Furthermore, we propose the assessment of these profiles with the analysis of radial strain curves obtained from the 2D-STE studies, where a profile is classified as normal or abnormal (akinetic or hypokinetic cases). By incorporating the radial strain information we can detect more accurately, LV wall motion abnormalities in

independent anatomical segments of the LV.

A third feature for LV wall motion classification is based on the idea that information of contraction is given by specific information extracted from the radial spatio-temporal profiles that can be described as quantitative parameters. By using these parameters to represent each profile, we can reduce the data size and the training and testing times in the classification process. From the cine-MRI sequence, **Time-signal intensity curves (TSICs)** are extracted from the radial spatio-temporal profiles in each anatomical segment. Different parameters are then defined from these curves that reflect dynamic information of the LV contraction.

The proposed methods to discriminate normal and abnormal wall motion are defined according to the type of previous proposed features that are given as input atoms in the training of dictionary learning algorithms for classification. By this way, the Label Consistent K-SVD DL algorithm and the Fisher Discriminative DL algorithm described in sections 2.6.1.1 and 2.6.1.2 respectively, are adapted for the classification of LV wall motion using diametral and radial profiles. A kernel based DL algorithm (KSRDL), described in section 2.6.2, is used with the third type of features or parameters that are extracted from the radial spatio-temporal profiles. We have shown in previous chapters that these algorithms provide good classification performance and generalization when they are used with natural images. Furthermore, they have not yet been applied in medical imaging. For comparison purposes, our methods will be compared with support vector machines using linear and radial basis function (RBF) kernels.

In the next sections we describe the steps of the proposed method in detail.

4.6.2 Pre-processing stage

This stage comprises the extraction of a region of interest to extract the LV cavity and a spatial normalization of the LV's size and position with the objective to analyze inter-subjects variations.

4.6.2.1 ROI extraction

A cardiac cine-MRI sequence contains S temporal frames usually between 25 and 40, each frame comprising R slices routinely divided in three spatial levels: basal, mid-cavity and apical. The short axis view of any of these slices shows a cross-section of the left and right ventricle. For each patient, and for each slice, the center of the LV and the anterior intersection between the two ventricles are determined with the placement of 5 points selected manually by the user in a reference frame at the end-diastolic phase in each slice: basal, mid-cavity and apical. As shown in Figure 4.13, the first 4 points (labeled as A, B, C, D) located outside the epicardial border respectively in the anterior, lateral, inferior and septal wall at the end-diastolic phase, are used to calculate the LV centroid, and the fifth point (E) is placed in the anterior intersection of the left ventricle and the right ventricle. It should be pointed out that the selection of these points is the only user assistance required by the proposed approach.

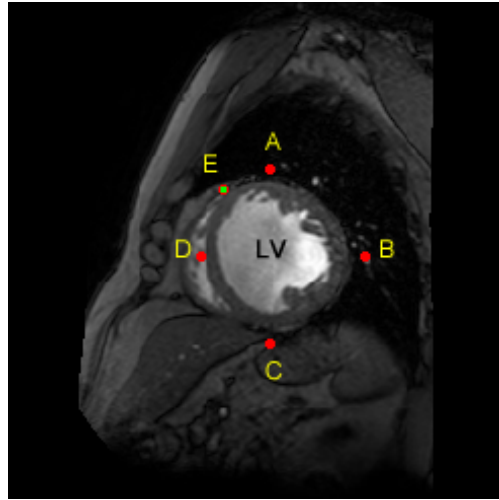


FIGURE 4.13– Region of interest for normal/abnormal wall motion classification. The 4 points (A,B,C,D) that enclose the LV cardiac cavity and the intersection point (E) between the two ventricles in a short axis plane.

4.6.2.2 Spatial normalization according to American Heart Association 17-Segment Model (AHA)

Because of the diversity of the body positions of patients in the scanner and different heart positions in the thorax, we have to normalize different heart positions. This normalization is based on the AHA 17 segment model (CERQUEIRA et al., 2002) (cf. 4.2.3). Figure 4.14 shows the location of the point E at the three short axis planes used for the spatial normalization of the LV according to the AHA representation. By this way, a reference axis crossing points E and the LV centroid is used as reference in order to spatially normalize different heart positions to the same reference. Following the procedure described in (LU et al., 2009), we can identify different segments in the short axis slices: basal, mid-cavity and apical (cf. Figure 4.14-right).

For basal and mid-cavity planes, 6 anatomical segments (cf. Figure 4.14-middle and left) are identified: anterior (n° 1 and 7), antero septal (n° 2 and 8), infero septal (n° 3 and 9), inferior (n° 4 and 10), posterior/infero-lateral (n° 5 and 11), and lateral/antero-lateral segments (n° 6 and 12). For apical plane 4 segments are identified: anterior (n° 13), septal (n° 14), inferior (n° 15) and lateral (n° 16).

4.6.3 Feature extraction stage

In this stage, the three proposed representations are described. They are constructed without the need of segmentation of the LV cavity. Furthermore, they exploit all the information of the cardiac cycle and inherently dispose discriminatory information for cardiac LV wall motion characterization.

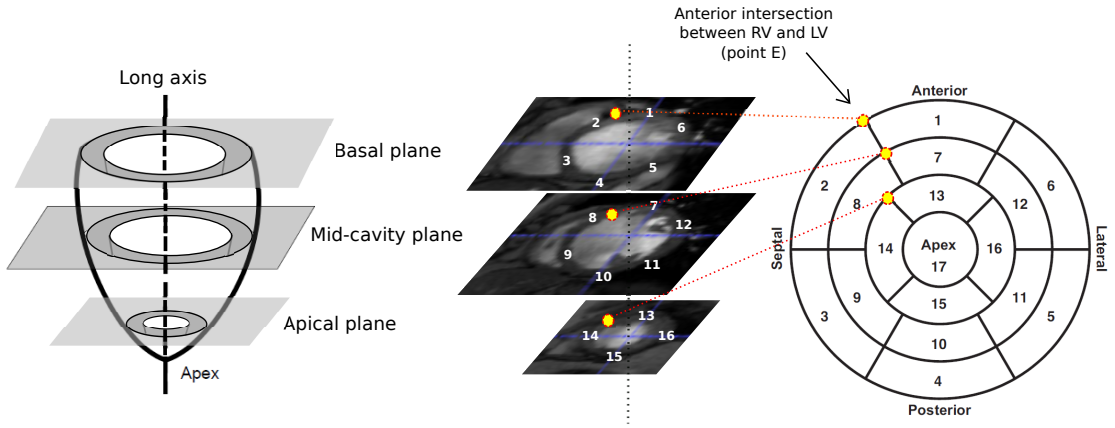


FIGURE 4.14– Spatial normalization according to AHA model. The figure shows the anterior intersection between RV and LV (point E) in three short axis planes. For basal and mid-cavity planes: 1-7. Anterior, 2-8. Antero-Septal, 3-9. infero-Septal, 4-10. Inferior, 5-11. Infero-Lateral, 6-12. Antero-Lateral. For apical plane: 13. Anterior, 14. Septal, 15. Inferior, 16. Lateral

4.6.3.1 Extraction of Diametral Spatio-temporal profiles

Diametrical lines are traced passing by the LV centroid from a point outside the epicardial border in a segment to its opposite side, e.g. from antero-lateral to infero-septal, from anterior to inferior or from antero-septal to infero-lateral segments. The spatio-temporal image extraction is applied for different angular positions. As it can be seen in Figure 4.15, it begins from a horizontal diametrical line taken as reference at 0° , then with an angular step $\Delta\theta$, we repeat the process setting $\theta_i = \theta_{i-1} + \Delta\theta$, $i = 1, \dots, 360$, with $\theta_0 = 0^\circ$ by rotating the diametrical line along the counterclockwise direction with the center of the line coinciding with the LV centroid, leading thus to a 360° spatio-temporal scan of the heart.

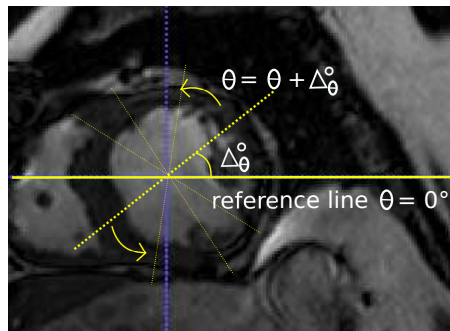


FIGURE 4.15– Rotation of the diametrical line for the extraction of diametral spatio-temporal profiles.

Each line is mapped into the next temporal frame or phase of the heartbeat in the same orientation (Figure 4.16). The image's gray levels along each diametrical line are concatenated for all the cardiac sequence to obtain a temporal image $I \in \mathbb{R}^{P \times col}$, where P denotes the length of the diametrical line (the number of crossed pixels) and col represents the number of phases in the

cardiac cycle. This image is called a spatio-temporal profile and shows the temporal evolution of the contraction in opposite segments in AHA model (CERQUEIRA et al., 2002), going through the entire cardiac cycle. Thus, for the i -th row, $I_{i,j}$, $j = 1, 2, \dots, col$, shows the temporal evolution on a single pixel along the sequence (the phases), while for a fix column j , $I_{i,j}$, $i = 1, 2, \dots, P$, shows the set of pixels that lies on a diametrical line for a fixed phase (MANTILLA et al., 2013b). Figure 4.16 shows an illustrative example of the construction of the spatio-temporal image for the Antero-lateral to Infero-septal segment in the LV.

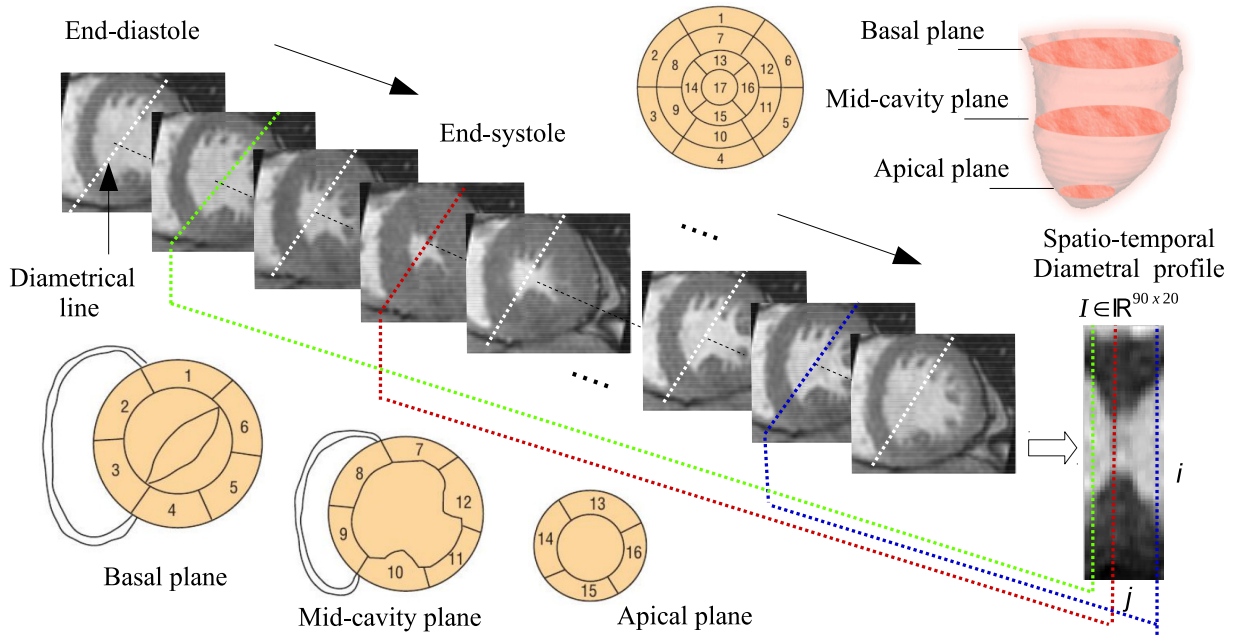


FIGURE 4.16— Example of the construction of the spatio-temporal image from a diametrical profile across opposite segments for a control patient. The diametrical line crosses Anterolateral and inferoseptal segments. The spatio-temporal profile is obtained from end-diastolic phase to the end of the cardiac cycle going through the end-systolic phase. In the same figure, Spatial normalization according to the AHA 17 myocardial Segments (CERQUEIRA et al., 2002): basal and mid-cavity planes: 1 and 7, Anterior; 2 and 8, Antero-Septal; 3 and 9, Infero-Septal; 4 and 10, Inferior; 5 and 11, Infero-Lateral; 6 and 12, Antero-Lateral. For apical plane: 13, Anterior; 14, Septal; 15, Inferior and 16, Lateral. 17 is the apex.

Spatio-temporal normalization: For the normalization of the LV's size among patients, we have observed the length of the diametrical lines at the end-diastolic phase in the basal short axis plane in all the patients. We select this reference plane because at the basal plane the LV ventricle presents the bigger size. The diametral line holds between 80 and 112 points for all the patients, then we select a reference average of 90 points. Thus, every spatio-temporal image is linearly interpolated along the y direction to 90 points, leading to the same length of the diametrical line, thus we have interpolated images $I' \in \mathbb{R}^{90 \times col}$.

Since the number of phases in the acquisition stage differs for each patient group, we perform an interpolation along the x direction to 20 points using bicubic interpolation method, leading to a spatio-temporal image $I'' \in \mathbb{R}^{90 \times 20}$. This procedure is applied independently for each image

profile and allows to normalize the images spatially for both intra- and inter-subject comparisons (GARCIA-BARNES et al., 2010; LU et al., 2009).

Intensity normalization: In order to normalize the intensity differences across slices, phases, subjects and data sets, each spatio-temporal image is normalized. For that purpose, each pixel in each spatio-temporal image is set to $(I''_{i,j} - \mu) / \sigma$, where, $I''_{i,j}$ is the interpolated pixel intensity value (after spatio-temporal normalization), μ and σ are, respectively, the mean and the standard deviation of the spatio-temporal image $I'' \in \mathbb{R}^{90 \times 20}$ (LU et al., 2009).

For each patient we obtain a set of $I_M^R \in \mathbb{R}^{90 \times 20}$, diametral normalized spatio-temporal profiles, where $R \in \{1, 2, 3\}$ each associated with a short axis slice level (apical, medial and basal) and $M \in \{1, \dots, 360\}$, $\Delta\theta = 1^\circ$, each associated with a profile orientation in the 360° scans of the LV. Although we only take profiles between 0° and 180° since a diametral profile covers two opposite segments in the LV cavity.

Once spatio-temporal profiles are extracted, the objective is to detect changes between healthy and pathological patients. Figure 4.17, shows an example of three spatio temporal profiles from two patients (Figure 4.17-a) and b)) and one healthy subject (Figure 4.17-c)). We handle the hypothesis that in healthy subjects, contraction is synchronous in opposite segments. As can be seen in the spatio-temporal profile shown in Figure 4.17-(c), the arrows move uniformly in opposite segments showing the contraction and then relaxation of the ventricular walls.

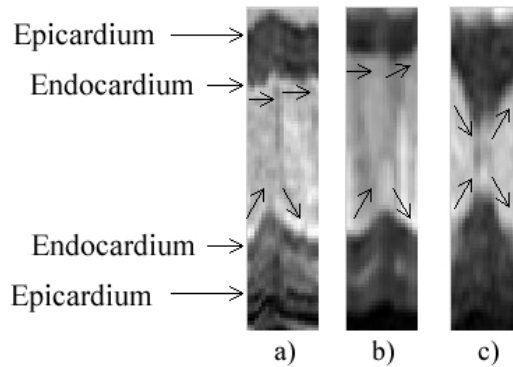


FIGURE 4.17– Spatio-temporal image profiles examples from patients (a) and (b), and healthy subject (c) data. In (a) and (b) asynchronous motion contraction is observed with the arrows (inside the spatio-temporal profile) that follow a non uniform movement, while in (c) synchronous contraction wall motion is observed in the opposite segments. The arrows moves uniformly in opposite segments showing the contraction and then relaxation of the ventricular walls.

Furthermore, in pathological patients normal contraction can be observed only in one segment, while in its opposite segment, contraction can occurs i) with a relative delay (late contraction or early contraction), ii) synchronous but with low amplitude or iii) maybe there is absence of contraction. For instance, for the spatio-temporal profiles shown in Figure 4.17-(a) and (b), asynchronous motion contraction is observed with the arrows that follow a non uniform movement. In one segment it seems that contraction of epi-and endocardium follows a normal motion while in its opposite segment the same behavior can not be appreciated.

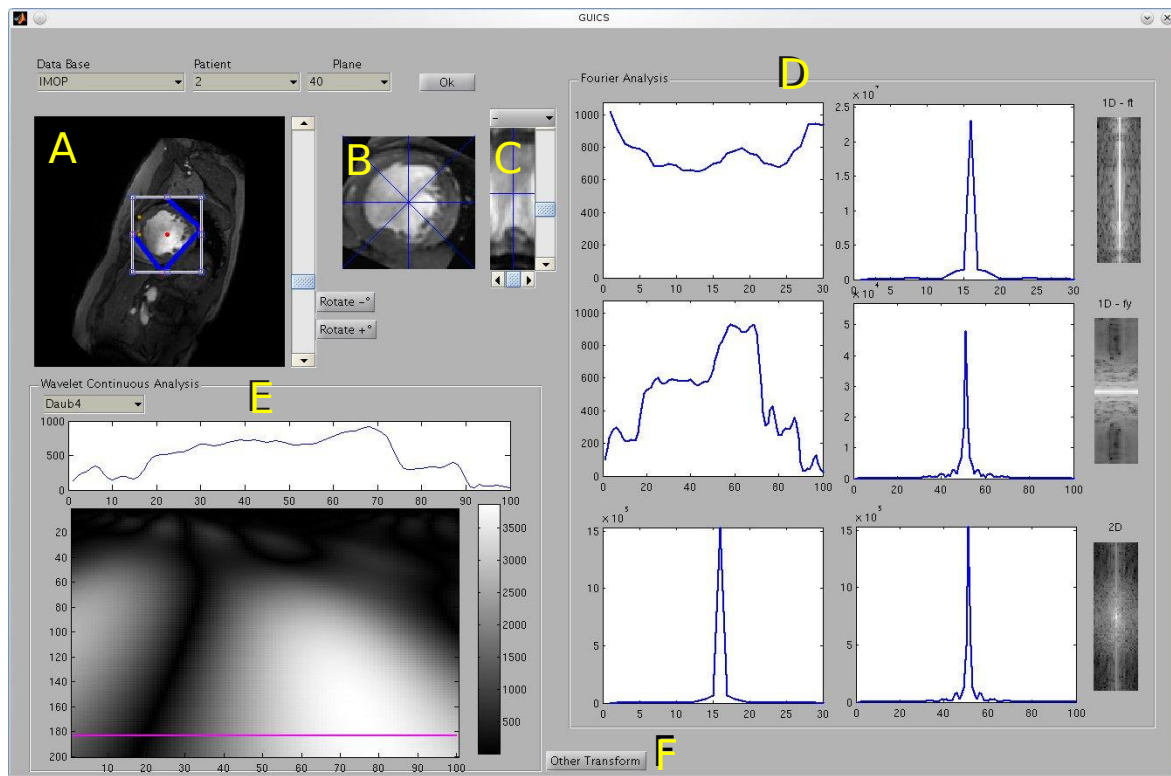


FIGURE 4.18– Graphical User Interface (GUI) for profiles extraction in CMR databases. Panel (A) shows a short-axis MR view at slice 40 (middle) of a patient. Panel (B) shows the extracted-normalized region-of-interest (ROI) and 4 highlighted diametrical lines in blue. Panel (C) shows the spatio-temporal image from the horizontal diametrical line in the ROI. Panel (D) shows gray level intensity curves of the highlighted row and column in the spatio-temporal image and the corresponding Fourier representation along the columns (1D FFT- y), rows(1D FFT- t) and 2D-FFT. Panel (E) shows an intensity curve of the highlighted column and its correspondent continuous Wavelet representation. The button “Other transform” (F) allows the visualization of Discrete Wavelet transform or Curvelet transform of the spatio-temporal image.

To facilitate the study of the cardiac cine-MRI sequences and the spatio-temporal profile extraction, we developed a Graphical User Interface (GUI) in Matlab[®] that is shown in Figure 4.18 (MANTILLA et al., 2013a). The application allows us to select a patient and a slice of interest (base, middle, or apex), then, the region of interest (ROI) can be defined by the user. The GUI shows different panels, where the representation of the spatio-temporal profiles in different domains is observed.

In this stage, relevant features are extracted from the whole spatio-temporal image. We apply four modes of information representation on the given image. Considering that Dictionary learning will be applied in next steps, we apply the most basic characteristic atoms (cf. 2.4.1): Fourier, Wavelet and Curvelet, with the assumption that in those domains the data may be sparse and more suitable for classification purposes.

In the first mode of representation, information of the gray level (original image domain) is taken.

The second mode of representation is performed in the Fourier domain: i) 1-Dimensional Fast Fourier Transform along the rows of the spatio-temporal profile (FFT- x), ii) 1-Dimensional Fast Fourier Transform along the columns of the spatio-temporal profile (FFT- y), and iii) 2-Dimensional Fast Fourier Transform (FFT-2D). The respective representations are shown in Figure 4.18-panel D.

In the third mode of representation, a three-level db4 2-Dimensional discrete Wavelet Transform is applied, following the sparsifying transform used in the thresholding experiment described in (LUSTIG et al., 2007). The sparsifying transform is an operator mapping a vector of image data to a sparse vector. In (LUSTIG et al., 2007) the Wavelet transform has obtained slight advantage in performance compared to the Discrete Cosine Transform (DCT) and finite-differences on two representative MR images at reconstructions involving 5-10% of the coefficients.

Finally 2D Curvelet transform (CANDÈS et al., 2005) with 3 levels of decomposition is also applied.

Figure 4.19 shows an example of a spatio-temporal profile and its respective representation in other domains.

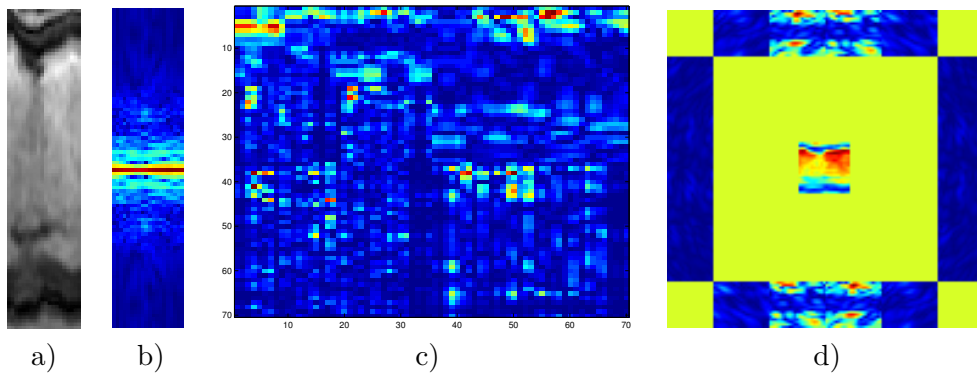


FIGURE 4.19— (a) Spatio-Temporal profile and its respective representation on other bases: (b) 1-Dimensional FFT- y , (c) Wavelet and (d) Curvelet domains.

4.6.3.2 Extraction of Radial Spatio-temporal profiles

Similar to the diametral profile extraction procedure described above, radial lines are traced from the LV centroid to a point outside of the epicardial border. This line is mapped into the next frame of the heartbeat in the same orientation. The image's gray levels along the radial line are concatenated to obtain a temporal image $I \in \mathbb{R}^{P \times S}$, where P denotes the length of the radial line and S represents the number of temporal frames in a cardiac cycle. Figure 4.20, shows an illustrative example of the construction of a radial spatio-temporal image from the LV centroid to a point in the Infero-septal segment in the LV.

The spatio-temporal image extraction begins with a horizontal radial line taken as reference at 0° , then with an angular step $\Delta\theta$, we repeat the process setting $\theta_i = \theta_{i-1} + \Delta\theta$, with $\theta_0 = 0^\circ$ by

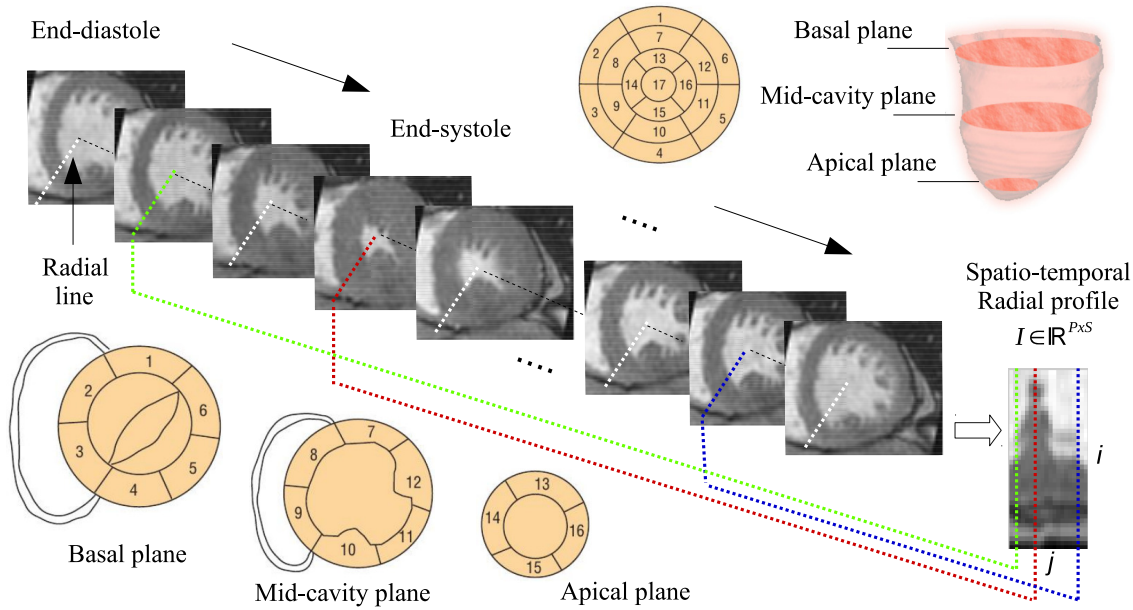


FIGURE 4.20— Example of construction of the spatio-temporal image from a radial profile in the inferoseptal segment for a control patient. Each radial profile is obtained from end-diastole phase during one cardiac cycle going through the end-systole phase. In the same figure, Spatial normalization according to the AHA 17 myocardial Segments (CERQUEIRA et al., 2002): basal and mid-cavity planes: 1 and 7, Anterior; 2 and 8, Antero-Septal; 3 and 9, Infero-Septal; 4 and 10, Inferior; 5 and 11, Infero-Lateral; 6 and 12, Antero-Lateral. For apical plane: 13, Anterior; 14, Septal; 15, Inferior and 16, Lateral. 17 is the apex.

rotating the radial line along the counterclockwise direction fixing the LV centroid, leading thus to a 360° spatio-temporal scan of the LV.

For spatio-temporal normalization, the same procedure used for diametral profiles is applied for radial profiles. Every spatio-temporal image is linearly interpolated along the y direction to 40 points (by evaluating the average length of the radial lines at the mid-cavity plane for all the patients at the end-diastolic phase), leading to the same length of the radial line, thus we obtained interpolated images $I' \in \mathbb{R}^{40 \times S}$. Furthermore, since the number of phases in the acquisition stage differs from each patient group, we perform an interpolation along the x direction to 20 points using bicubic interpolation method leading to a spatio-temporal image $I'' \in \mathbb{R}^{40 \times 20}$.

Then, we follow the same normalization procedure for diametral spatio-temporal profiles in order to normalize the intensity differences across slices, phases and subjects. Each pixel in each radial spatio-temporal image is set to $(I''_{i,j} - \mu) / \sigma$, where, $I''_{i,j}$ is the interpolated pixel intensity value, μ and σ are, respectively, the mean and the standard deviation of the radial spatio-temporal image.

For each patient we obtain a set of $I_M^R \in \mathbb{R}^{40 \times 20}$, radial normalized spatio-temporal profiles, where $R \in \{1, 2, 3\}$ each associated with a SAX slice (apical, medial and basal) and $M \in \{1, \dots, 360\}$, $\Delta\theta = 1^\circ$, each associated with a profile orientation in the 360° scans of the LV.

Similarly to diametral profiles, after several experiments, we have chosen to apply two mode of information representation on the given image $I_M^R \in \mathbb{R}^{40 \times 20}$. In the first mode of representation,

features are extracted directly on the gray level domain (original image domain). In the second mode of representation, feature extraction is performed with a three-level db4 2-Dimensional discrete Wavelet Transform obtaining a new representation $\Psi_M^R \in \mathbb{R}^{64 \times 64}$.

Unlike diametral profiles for which we have chosen three standard overcomplete basis: Fourier, Wavelet and Curvelet domains, after several experiments we have found that Fourier and Curvelet domains were not be able to give a competitive performance for classification compared to Wavelet. This is due to the characteristics of the profiles that must retain not only frequency-localized information, but also time-localization information given by Wavelet coefficients and not by Fourier coefficients. As Curvelets well represent objects with curved singularities, in the case of spatio-temporal profiles, they lack of this particularity.

Figure 4.21, shows an example of a spatio-temporal profile and its respective representation in the Wavelet domain.

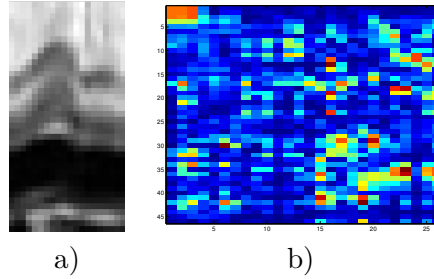


FIGURE 4.21– (a) Radial Spatio-Temporal profile and its respective representation on the (b) Wavelet domain.

4.6.3.3 Extraction of parameters from radial Spatio-temporal profiles

Initially, from a radial image profile $I_M \in \mathbb{R}^{40 \times 20}$, where $M \in \{1, \dots, 360\}$, $\Delta\theta = 1^\circ$, each associated with a radial profile orientation in the 360° scans of the LV, we extract the set of pixels that lies on a radial line for a fixed row, i.e., for the i -th row, $I_{i,j}$, $j = 1, 2, \dots, 20$ represents a time-signal intensity curve. It shows the temporal evolution on a single pixel during the cardiac cycle. This type of curve has been extracted directly from the cardiac cine-MRI sequence in (KACHENOURA et al., 2007). Figure 4.22, shows an illustrative example based on the method proposed in (KACHENOURA et al., 2007), where four patterns of time-signal intensity curves corresponding to four pixels located near the endocardial wall are shown. Their evolution from the end-diastolic image to the end of the cardiac cycle passing through the end systolic phase are also illustrated in the same figure.

These type of curves are also identified in the proposed radial spatio-temporal profiles. They are called Time-Signal Intensity Curves (TSICs). For each TSIC obtained in a single radial image profile, we performed the interpretation of parametric images proposed in (KACHENOURA et al., 2007). Figure 4.23-right shows 4 TSICs extracted from the image profile shown on the left.

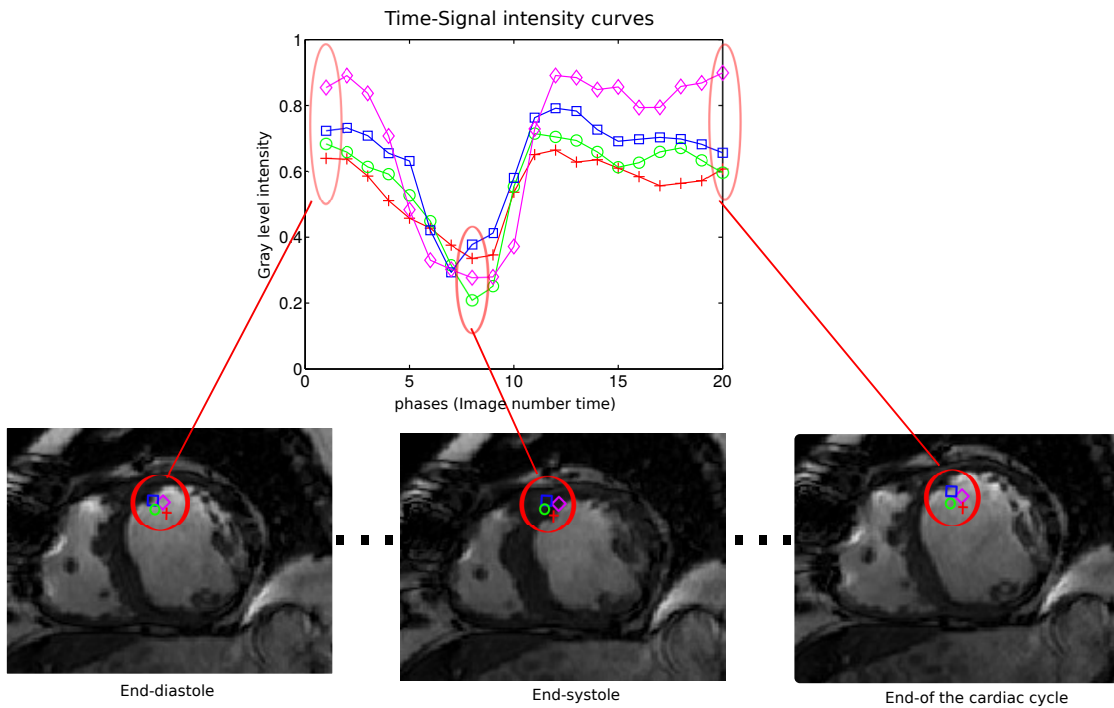


FIGURE 4.22— Four patterns of time-signal intensity curves (top) are shown according to the distance of the corresponding pixels to the endocardial wall and its evolution from the the end-diastole image to the end of the cardiac cycle passing through the end systolic phase (bottom). Adapted from (KACHENOURA et al., 2007).

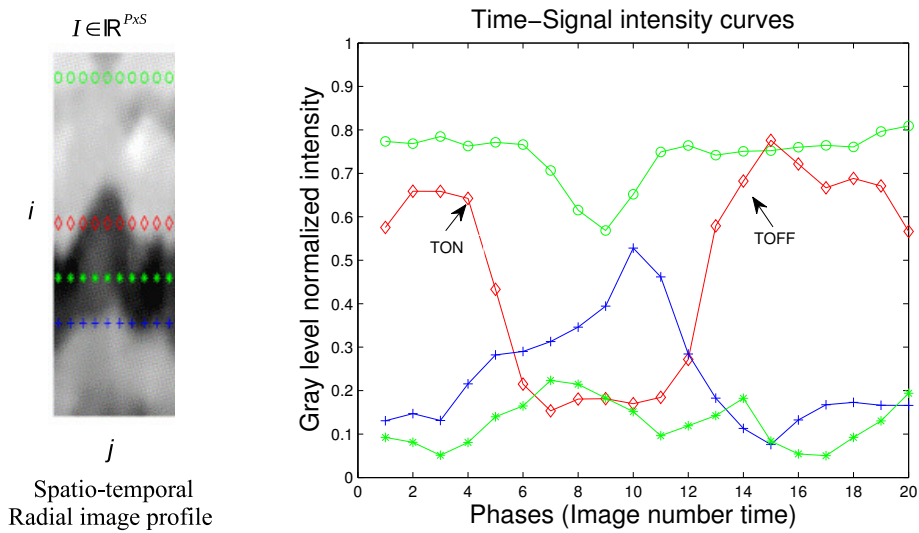


FIGURE 4.23— A spatio-temporal profile (left) and 4 patterns of TSICs (right). The green color line at the top of the graphic, corresponds to a pixel located inside the cavity. The red color line corresponds to a pixel located near the endocardial border. The blue color line corresponds to a pixel located outside the epicardial border. The green color line at the bottom of the graphic, corresponds to a pixel located between endocardium and epicardium.

A total of three types of TSICs $C(x, y, t)$ associated with the pixel $c(x, y)$ are observed (KACHENOURA et al., 2007) and different colors are assigned to label each one:

Green color is assigned to the pixel points that remain within the myocardium during the whole cardiac cycle and to the pixels that remain inside the cavity. Red color labels the pixels from curves that present a decreasing then increasing shape, reflecting the contraction of the LV cavity while blue color is assigned to the pixels from curves that present an increasing then decreasing shape with low amplitude.

Following a threshold operator based on the amplitude of the TSICs, we select only the curves that reflect the contraction of the ventricular cavity, i.e., red curves. After constructing the histogram of these curves, we find out that the form of the distribution follows a Gaussian probability density function (p.d.f.). By this way, a Gaussian p.d.f. is fitted to each inverted TSIC labeled in red. Gaussian p.d.f. is given by:

$$f(t) = \frac{1}{\sigma(c)\sqrt{2\pi}} e^{-\frac{(t - \mu(c))^2}{2\sigma(c)^2}} \quad (4.1)$$

where, $\mu(c)$ and $\sigma(c)$ are the mean and the standard deviation of the distribution with the corresponding variance $\sigma(c)^2$.

We obtain the optimal values $\sigma(c)$ and $\mu(c)$ for the new function $f(t)$ using an iterative Least-Mean-Square (LMS) algorithm for the c -th red curve that is of interest. The new curves constructed with the optimal values of $\sigma(c)$ and $\mu(c)$ are called FTSICs (Fitted Time-Signal Intensity curves). An example of a FTSIC is shown in Figure 4.24 where two representative transition time values TON and TOFF are shown. TON represents the time when the contraction begins and TOFF represents the time of the end of the endocardial movement.

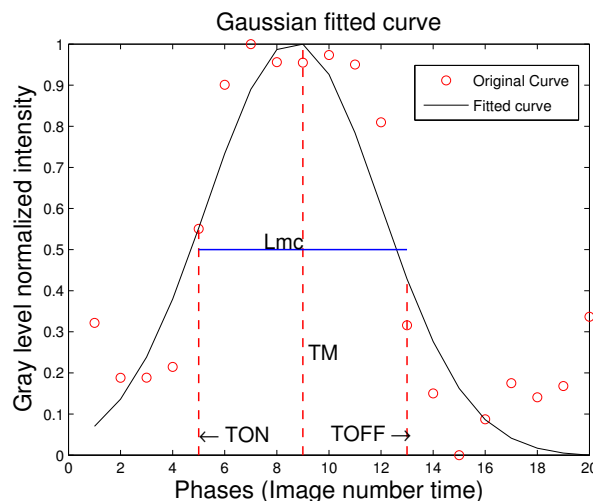


FIGURE 4.24— A Gaussian p.d.f. function fitted to a selected TSIC. TON represents the time when the contraction begins and TOFF represents the time of the end of the endocardial movement. TM is the time of the maximum peak in the curve. Lmc is the mid-height width value.

These parameters were firstly identified in TSICs from cine MRI in (KACHENOURA et al., 2007) by adapting the parametric analysis of main motion proposed in echocardiography in (RUIZ et al., 2005). This analysis is based on a nonlinear transition model defined by an adaptive window function and allowed the estimation of the time parameters TON and TOFF values and two amplitude parameters.

Following this target in mind, we calculate the parameters $TON(c)$ and $TOFF(c)$ from the FTSICs using the parameters $\sigma(c)$, $\mu(c)$ and the time characteristics L_{mc} and TM, which are the mid-height width and the maximum time on the FTSIC (cf. Figure 4.24).

The mid-height width is calculated as:

$$L_{mc} = 2\sqrt{2\ln 2}\sigma \approx 2.355\sigma \quad (4.2)$$

Formally, for a pixel c initially inside the cavity, close to the endocardial border, the transition times $TON(c)$ and $TOFF(c)$ are defined as:

$$TON(c) = TM - \mu - \frac{\sigma \cdot L_{mc}}{2}, \quad (4.3)$$

$$TOFF(c) = TM - \mu + \frac{\sigma \cdot L_{mc}}{2}, \quad (4.4)$$

where, $TON(c)$ represents the time when the contraction begins and $TOFF(c)$ represents the time of the end of the endocardial movement over the pixel c .

From a clinical point of view, the mean transition time $Mt=(TON + TOFF)/2$ was considered more informative with regard to characterizing the wall motion (RUIZ et al., 2005).

We follow the hypothesis that by using this type of parameters like the mean transition time parameter proposed by (KACHENOURA et al., 2007), we can perform the task of LV wall motion classification more accurately than using all the information contained in the spatio-temporal profiles.

Thus, in this step, four parameters are then proposed in this work: An average clustered curve parameter, a skewness parameter and a Cross correlation parameter. Furthermore, we propose to use the Mean transition time parameter proposed by (KACHENOURA et al., 2007), calculated over the clustered curve. The extraction of these parameters are described below (MANTILLA et al., 2015):

Average clustered curve (C1): Each anatomical segment of the left ventricle is divided into 6 angular subregions of ten consecutive profiles as shown in Figure 4.25. A multisignal 1-D clustering process based on Wavelets (MISITI et al., 2007), splits the set of all the FTSICs from radial profiles in each angular subregion into two clusters, then the average of the signals in the largest cluster is computed representing the largest group of signals with a similar contraction pattern. Thus, each image profile in an angular subregion is represented by a reference clustered signal of length 20, $Cl_M \in \mathbb{R}^{20}$, where $M \in \{1, \dots, 360\}$, $\Delta\theta = 1^\circ$, each associated with a radial profile orientation in the 360° scans of the LV.

In Figure 4.25, FTSICs from profiles in a selected sub-region in the anterolateral segment, are clustered into two groups shown in red and blue. In the same figure the average signal

of the cluster with maximum size is shown in black and is chosen to represent the behavior of the anatomical segment.

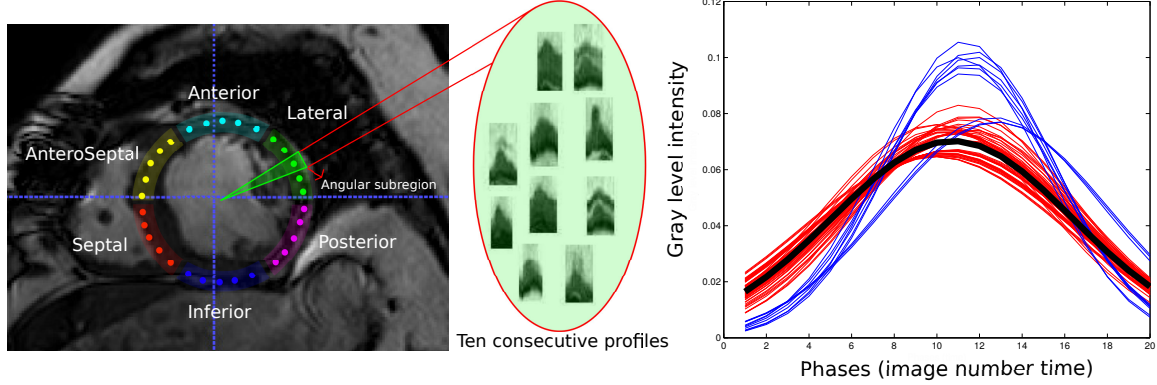


FIGURE 4.25— Example of an angular subregion of 10° (left) in the anterolateral segment where 10 radial spatio-temporal profiles can be extracted (middle). Time-signal intensity curves from the radial spatio-temporal profiles in the selected sub-region are shown in the right. The 2 clusters in red and blue after multisignal 1-D clustering and its respective reference signal in black (right).

The Skewness parameter (Sk): In (RUIZ et al., 2005), the boundaries of the transition times were analyzed in accordance with physiological criteria. For the cardiac cycle beginning at the end-diastolic point, the transition corresponding to the time TON occurs during the systolic phase. The duration of the systolic phase is considered not larger than half the duration of the cardiac cycle. We propose to analyze the position of the TON parameter in terms of symmetry of the FTSICs.

Figure 4.26, shows the histogram of the maximum peak in FTSICs for abnormal and normal profiles. For normal profiles mostly of the maximum peak in the curves appears slightly leftward and nonsymmetrical which means that the TON parameter is located at the first half of the cardiac cycle. In the case of abnormal profiles, the maximum peak in the curves appears slightly to the right and more balanced which means that the TON parameter is located at the end of the first half of the cardiac cycle or at the beginning of the second half of the cardiac cycle. These observations are in accordance to the physiological criteria described before for the healthy population.

From the profiles in a subregion in a particular segment, after experimentation, 5 random FTSICs are selected. In this case every FTSIC is represented by a single value, thus each image profile is represented by 5 values of Skewness, $Sk_M \in \mathbb{R}^5$, where $M \in \{1, \dots, 360\}$, $\Delta\theta = 1^\circ$, each associated with a radial profile orientation in the 360° scans of the LV.

For univariate data x_1, x_2, \dots, x_N , the formula for skewness is:

$$Sk = \sum_{i=1}^N \frac{(x_i - \bar{x})^3}{s^3} \quad (4.5)$$

where \bar{x} is the mean, s is the standard deviation, and N is the number of data points.

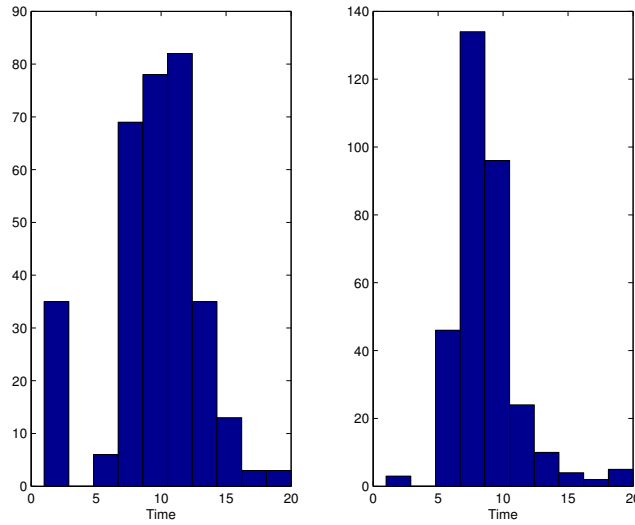


FIGURE 4.26– Histogram of maximum peak time in time-signal intensity curves from abnormal profiles (left) and normal profiles (right)

The Cross Correlation parameter (Co): A parameter based on cross-correlation analysis is calculated between each average clustered curve (Cl) and a patient-specific reference. To define this reference we have performed a global multisignal 1-D clustering based on Wavelets (MISITI et al., 2007) overall the FTSICs from all the image profiles that belong to the control subjects. The average of the cluster with maximum size is a patient-specific reference from the healthy population. Cross-correlation is then computed between each average clustered curve (Cl) and the normal reference. Thus, every spatio-temporal image profile is represented by a single value of correlation. $Co_M \in \mathbb{R}^1$, where $M \in \{1, \dots, 360\}$, $\Delta\theta = 1^\circ$, each associated with a radial profile orientation in the 360° scans of the LV.

The Mean transition time parameter (Mt) As we have mentioned before, we propose to use the Mean transition time parameter proposed by (KACHENOURA et al., 2007), calculated over the clustered curve (Cl). Thus, every spatio-temporal image profile depicted by a clustered curve, is represented by a single value of Mean transition time $Mt_M \in \mathbb{R}^1$, where $M \in \{1, \dots, 360\}$, $\Delta\theta = 1^\circ$, each associated with a radial profile orientation in the 360° scans of the LV.

4.6.4 Dictionary Learning-based classification

We aim at classifying whether a LV anatomical segment presents wall motion abnormality or not using the proposed spatio-temporal profiles. These profiles are taken as input vectors in the SVM models and are also taken as initial atoms of the dictionaries in the LC-KSVD, FD-DL and KSRDL algorithms, all of them previously described in Chapter 2 (cf. Section 2.6).

To recall (cf. 2.4.2), Figure 4.27 shows an illustrative example of the proposed method of classification using the basic framework of DL. In this figure, input signals $\mathbf{Y} = [\mathbf{y}_1, \mathbf{y}_2, \dots, \mathbf{y}_N] \in \mathbb{R}^{n \times N}$ are represented as a data matrix where each column is a n -dimensional input signal

(vectorized spatio-temporal representations) and N is the number of profiles.

Note that in the parametric approach, \mathbf{Y} represents a data matrix of parameters where each column is a vector of concatenated parameters extracted from the radial spatio-temporal profiles.

The Sparse coefficients $\mathbf{X} = [\mathbf{x}_1, \mathbf{x}_2, \dots, \mathbf{x}_N] \in \mathbb{R}^{K \times N}$ represent the sparse codes coefficients of input signals \mathbf{Y} , i.e, $\mathbf{x}_i \in \mathbb{R}^K$, $i = 1, \dots, N$, is the sparse representation of size K of the vectorized spatio-temporal profile $\mathbf{Y}_i \in \mathbb{R}^n$.

The dictionary $\mathbf{D} = [\mathbf{d}_1, \mathbf{d}_2, \mathbf{d}_3, \dots, \mathbf{d}_K] \in \mathbb{R}^{n \times K}$, with K items for sparse signal representation of \mathbf{Y} constrained by a sparsity parameter T ($\|\mathbf{x}_i\|_0 \leq T$), is the dictionary to be learned from the data samples.

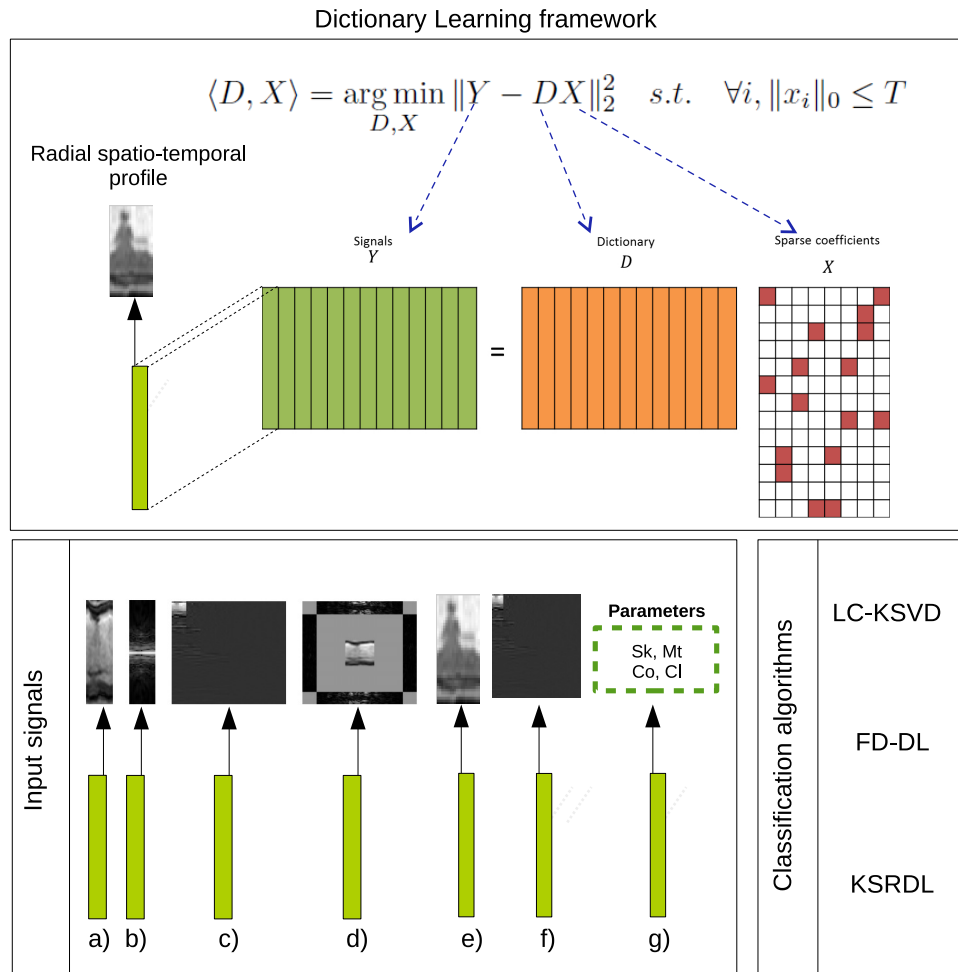


FIGURE 4.27– Illustrative scheme for DL based framework for LV wall motion classification. Top panel: the DL framework using radial spatio-temporal profiles as input signals. Left bottom panel: The different possible representations of the input signals \mathbf{y}_i : a) a diametral spatio-temporal profile and its representation in a) gray level domain, b) Fourier domain, c) Wavelet domain, d) Curvelet domain, a radial spatio-temporal profile and its representation in e) gray level domain, f) Wavelet domain, g) parameters extracted from the radial profiles. Bottom right panel: the three DL classification techniques.

The Sparse coefficients \mathbf{X} and the dictionary \mathbf{D} , are learned by adapting the following three specific DL-based classification algorithms for LV wall motion classification:

Label Consistent LC-KSVD algorithm: The first discriminative DL technique adapted for LV wall motion classification is the Label Consistent DL (LC-KSVD) algorithm (JIANG et al., 2013), which presents two variants (cf. 2.6.1.1): the first one, denoted here as LC-KSVD1 (Equation 4.6) takes only one structural constraint on the dictionary, that is represented by $\|\mathbf{Q} - \mathbf{A}\mathbf{X}\|_2^2$, the discriminative sparse-code error term; the second one, named LC-KSVD2 (Equation 4.7), takes two structural constraints on the dictionary: the discriminative sparse-code error term and the classification error that is represented by $\|\mathbf{H} - \mathbf{W}\mathbf{X}\|_2^2$. Their respective optimization problems are:

$$\begin{aligned} \langle \mathbf{D}, \mathbf{A}, \mathbf{X} \rangle &= \arg \min_{\mathbf{D}, \mathbf{W}, \mathbf{A}, \mathbf{X}} \|\mathbf{Y} - \mathbf{D}\mathbf{X}\|_2^2 + \alpha \|\mathbf{Q} - \mathbf{A}\mathbf{X}\|_2^2 \\ &s.t. \quad \forall i, \|\mathbf{x}_i\|_0 \leq T, \end{aligned} \quad (4.6)$$

$$\begin{aligned} \langle \mathbf{D}, \mathbf{W}, \mathbf{A}, \mathbf{X} \rangle &= \arg \min_{\mathbf{D}, \mathbf{W}, \mathbf{A}, \mathbf{X}} \|\mathbf{Y} - \mathbf{D}\mathbf{X}\|_2^2 + \\ &\alpha \|\mathbf{Q} - \mathbf{A}\mathbf{X}\|_2^2 + \beta \|\mathbf{H} - \mathbf{W}\mathbf{X}\|_2^2 \\ &s.t. \quad \forall i, \|\mathbf{x}_i\|_0 \leq T, \end{aligned} \quad (4.7)$$

where, $\mathbf{Q} = [\mathbf{q}_1 \dots \mathbf{q}_N] \in \mathbb{R}^{K \times N}$ are the discriminative sparse codes of the input data \mathbf{Y} (vectorized spatio-temporal representations) for classification and \mathbf{A} is a linear transformation matrix to be obtained as part of the solution of the optimization problem.

The linear transformation, $g(\mathbf{x}; \mathbf{A}) = \mathbf{A}\mathbf{x}$, transforms the original sparse codes coefficients \mathbf{X} to be most discriminative in the sparse feature space \mathbb{R}^K .

$\mathbf{W} \in \mathbb{R}^{m \times K}$ denotes the classifier parameters, where m is the number of classes ($m = 2$, normal/abnormal spatio-temporal representations).

$\mathbf{H} = [\mathbf{h}_1, \dots, \mathbf{h}_N] \in \mathbb{R}^{m \times N}$ are the class labels of input profiles \mathbf{Y} . α is the weight for label constraint term and β is the weight for classification error term.

The K-SVD algorithm (AHARON et al., 2006) is used to find the optimal solution for all parameters \mathbf{D} , \mathbf{W} , \mathbf{A} and \mathbf{X} simultaneously, whereas \mathbf{Q} and \mathbf{H} matrices are initialized in a supervised manner based on the original labels for each class. To recall (cf. 2.6.1.1), the dictionary \mathbf{D} is initialized by computing several iterations of the K-SVD algorithm within each class and then combine all the outputs (i.e. dictionary items learning from each class) of each K-SVD. \mathbf{W} and \mathbf{A} are initialized by computing ridge regression models. Finally, given the initialized \mathbf{D} , the original K-SVD algorithm is applied to compute the sparse codes \mathbf{X} of training signals \mathbf{Y} .

An illustrative example of the matrices \mathbf{Q} and \mathbf{H} for the binary classification of 8 diametral spatio-temporal profiles (4 from the abnormal class and 4 from the normal class) is shown in Figure 4.28-left, where each column of \mathbf{Q} corresponds to a discriminative sparse code for an input profile. In the same figure (top-right), an illustrative example of the initial dictionary for LC-KSVD algorithm is shown.

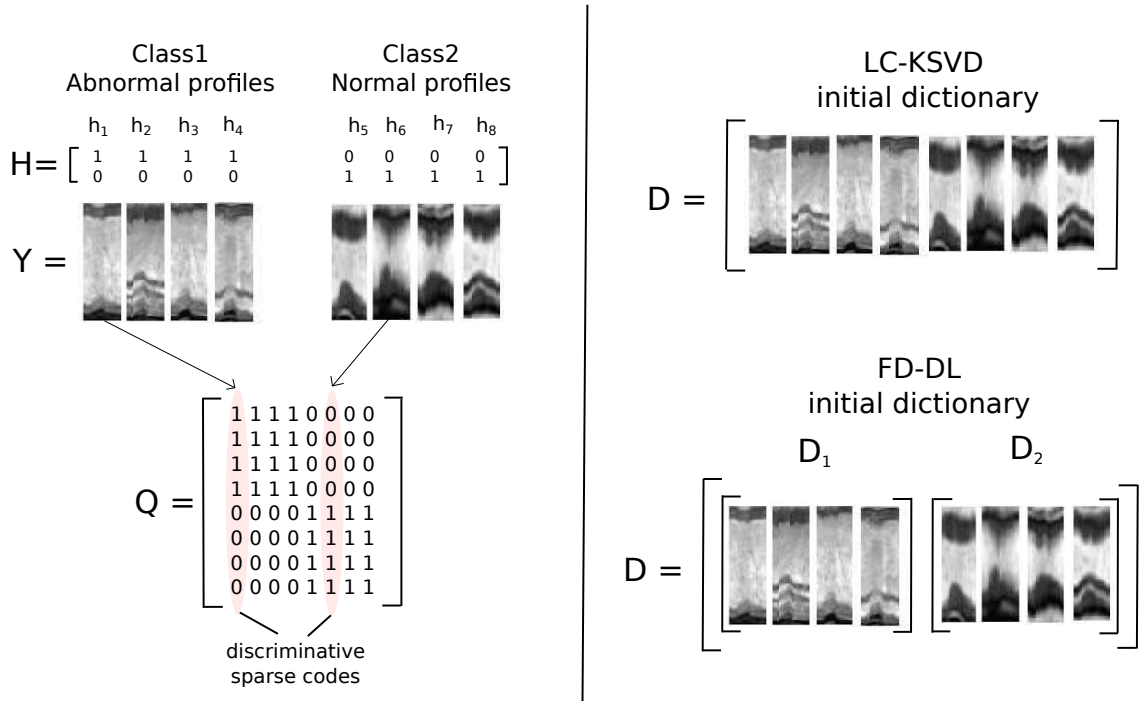


FIGURE 4.28— Left: An illustrative example of the “discriminative” sparse codes matrix Q for an initial dictionary of size 8 in the LC-KSVD algorithm. Each column q_i is a “discriminative” sparse code corresponding to an input profile y_i if the non-zero values of q_i occur at those indices where the input profile y_i and the dictionary item d_k share the same label. The input signals Y correspond to 8 diametral spatio-temporal profiles with their respective class labels H : class 1 corresponds to abnormal spatio-temporal profiles with $h_i = [1, 0]^T$, while class 2 corresponds to normal spatio-temporal profiles with $h_i = [0, 1]^T$. Top right: the initial dictionary of the LC-KSVD algorithm $D = [d_1, d_2, d_3, \dots, d_8] \in \mathbb{R}^{n \times 8}$. Bottom right: The initial structured dictionary for the FD-DL algorithm: $D = [D_1 | D_2]$.

Fisher discriminant FD-DL algorithm: The second discriminative DL technique which has been adapted for the classification of radial spatio-temporal profiles is the Fisher Discriminative DL (FD-DL) algorithm (YANG et al., 2014) (cf. 2.6.1.2). It proposes to learn a structured dictionary $D = [D_1 | D_2]$, where D_1 is the class-specified sub-dictionary associated with class of abnormal profiles, and D_2 is the class-specified sub-dictionary associated with class of normal profiles. In the Figure 4.28-bottom right, an initial structured dictionary for the FD-DL algorithm with 8 diametral spatio-temporal profiles (4 from the abnormal class and 4 from the normal class) is shown.

Denoting by $Y = [Y_1 | Y_2]$ the set of training profiles (abnormal/normal respectively). Furthermore, let X be the coding coefficient matrix of Y over D i.e., $X = [X_1 | X_2]$, where X_1 and X_2 are the sub-matrix containing the sparse coding coefficients of Y_1 and Y_2 over D respectively. They propose to obtain the dictionary D and the coding coefficient matrix X by solving:

$$(D, X) = \arg \min_{D, X} \{r(Y, D, X) + \lambda_1 \|X\|_1 + \lambda_2 \|f(X)\|_1\}, \quad (4.8)$$

where $r(\mathbf{Y}, \mathbf{D}, \mathbf{X})$ is the discriminative fidelity term, $\|\mathbf{X}\|_1$ is the sparsity constraint, $f(\mathbf{X})$ is a discrimination constraint imposed on the coefficient matrix \mathbf{X} , and λ_1 and λ_2 are regularization parameters.

In the FD-DL algorithm, the Fisher discrimination criterion is imposed on the coding coefficients \mathbf{X} to make them discriminative. To this end, the DL process grants that the sparse coding coefficients keeps small intra-class scatter but big inter-class scatter. At the same time it grants that each class-specific sub-dictionary in the whole structured dictionary keeps good representation ability to the training samples from the associated class but poor representation ability for other classes.

Kernel-based KSRDL algorithm: The third algorithm for LV wall motion classification is adapted by using the parametric inputs. It correspond to the Kernel Sparse Representation DL algorithm (LI et al., 2013) (cf. 2.6.2). Here, the input signals \mathbf{Y} represent a data matrix of parameters where each column is a vector of concatenated parameters extracted from the radial spatio-temporal profiles.

Classification is performed by training a K-Nearest Neighbor classifier over the sparse training coefficients matrix \mathbf{X} learned by the kernel-based DL algorithm with Gaussian prior over the atoms of the Dictionary \mathbf{D} :

$$\min_{\mathbf{D}, \mathbf{X}} \frac{1}{2} \|\mathbf{Y} - \mathbf{D}\mathbf{X}\|_F^2 + \frac{\alpha}{2} \text{trace}(\mathbf{D}^T \mathbf{D}) + \lambda \sum_{i=1}^N \|\mathbf{x}_i\|_1, \quad (4.9)$$

In this case the KSRDL algorithm is applied using a radial basis RBF mapping function with $\sigma = 1$ that replaces the inner products in the DL model. The sparse coefficients matrix \mathbf{X} are obtained by solving the Non negative Quadratic Problem (*NNQP*):

$$\min_{\mathbf{X}} \sum_{i=1}^p \frac{1}{2} \mathbf{x}_i^T \mathbf{H} \mathbf{x}_i + \mathbf{g}_i^T \mathbf{x}_i \quad s.t. \quad \mathbf{X} \geq 0 \quad (4.10)$$

where $\mathbf{H}_{k \times k} = \mathbf{D}^T \mathbf{D}$ and $\mathbf{g} = -\mathbf{D}^T \mathbf{Y}$. The class label of the new test instances is predicted using the classifier obtained in the training step and the learned dictionary \mathbf{D} .

4.7 Conclusion

This chapter described the clinical context of this work, the main components of the cardiac function and the principal issue that is focused on LV wall motion abnormalities characterization in cardiac cine-MRI for heart failure patients. A brief description of the imaging modalities that are used in this work for the assessment of left ventricular function was presented, including: Echocardiography and cardiac MRI. Different works of the literature to assess LV wall motion in cardiac MRI have been reported. Finally the proposed method has been presented. This method differs from those methods reported in the literature in two points: firstly, it differs in the feature extraction procedure which exploits all the information contained in the cardiac cycle without the need of segmentation of the epicardial and endocardial boundaries. The proposed features

are: i) diametral spatio-temporal profiles, ii) radial spatio-temporal profiles, and iii) time signal intensity curve parameters extracted from the radial profiles. This kind of representation has not been previously reported for the classification of LV wall motion in cardiac MRI. It differs secondly, by the use of DL techniques for classification of LV wall motion in cardiac MRI. The application of the DL algorithms and the results are presented in the next chapter.

References

- AFSHIN, M., I. BEN AYED, K. PUNITHAKUMAR, M. LAW, A. ISLAM, A. GOELA, T. PETERS, and N. SHUO LI (2014). “Regional assessment of cardiac left ventricular myocardial function via MRI statistical features”. In: *IEEE Transaction in Medical Imaging* 33.2, pp. 481–494.
- AHARON, M., M. ELAD, and A. BRUCKSTEIN (2006). “K-SVD: An Algorithm for Designing Overcomplete Dictionaries for Sparse Representation”. In: *IEEE Transactions on Signal Processing* 54.11, pp. 4311–4322.
- BETANCUR, J. (2014). “Multimodal image registration for the characterization of the hypertrophic cardiomyopathy and the cardiac asynchronism”. PhD thesis. Université Rennes 1.
- BLESSBERGER, H. and T. BINDER (2010). “Two dimensional speckle tracking echocardiography: basic principles”. In: *Heart* 96.9, pp. 716–722.
- BOYER, K., P. F. U. GOTARDO, J. SALTZ, and S. RAMAN (2006). “On the detection of intraventricular dyssynchrony in the left ventricle from routine cardiac MRI”. In: *Biomedical Imaging: Nano to Macro, 2006. 3rd IEEE International Symposium on*, pp. 169–172.
- CAIANI, E., E. TOLEDO, P. MACENEANEY, D. BARDO, S. CERUTTI, R. LANG, and V. MOR-AVI (2006). “Automated Interpretation of Regional Left Ventricular Wall Motion from Cardiac Magnetic Resonance Images”. In: *Journal of Cardiovascular Magnetic Resonance* 8.3, pp. 427–433.
- CAIANI, E., E. TOLEDO, P. MACENEANEY, K. A. COLLINS, R. M. LANG, and V. MOR-AVI (2004). “The role of still-frame parametric imaging in magnetic resonance assessment of left ventricular wall motion by non-cardiologists.” In: *J Cardiovasc Magn Reson* 6.3, pp. 619–25.
- CANDÈS, E., D. L., D. D., and Y. L. (2005). *Fast Discrete Curvelet Transforms*.
- CERQUEIRA, M. D., N. J. WEISSMAN, V. DILSIZIAN, A. K. JACOBS, S. KAUL, W. K. LASKEY, D. J. PENNELL, J. A. RUMBERGER, T. RYAN, M. S. VERANI, and AMERICAN HEART ASSOCIATION WRITING GROUP ON MYOCARDIAL SEGMENTATION AND REGISTRATION FOR CARDIAC IMAGING (2002). “Standardized Myocardial Segmentation and Nomenclature for Tomographic Imaging of the Heart: A Statement for Healthcare Professionals from the Cardiac Imaging Committee of the Council on Clinical Cardiology of the American Heart Association”. In: *Circulation* 105.4, pp. 539–542.
- DE SUTTER, J., N. R. VAN DE VEIRE, L. MUYLDERMANS, T. DE BACKER, E. HOFFER, M. VAERENBERG, B. PAELINCK, P. DECOODT, L. GABRIEL, T. C. GILBERT, and G. VAN CAMP (2005). “Prevalence of Mechanical Dyssynchrony in Patients With Heart Failure

- and Preserved Left Ventricular Function (a Report from the Belgian Multicenter Registry on Dyssynchrony)”. In: *American Journal of Cardiology* 96.11, pp. 1543–1548.
- DELGADO, V., C. YPENBURG, R. J. VAN BOMMEL, L. F. TOPS, S. A. MOLLEMA, N. A. MARSAN, G. B. BLEEKER, M. J. SCHALIJ, and J. J. BAX (2008). “Assessment of left ventricular dyssynchrony by speckle tracking strain imaging comparison between longitudinal, circumferential, and radial strain in cardiac resynchronization therapy”. In: *Journal of the American College of Cardiology* 51.20, pp. 1944–1952.
- DOHI, K., M. S. SUFFOLETTO, D. SCHWARTZMAN, L. GANZ, M. R. PINSKY, and J. GORCSAN (2005). “Utility of echocardiographic radial strain imaging to quantify left ventricular dyssynchrony and predict acute response to cardiac resynchronization therapy”. In: *The American Journal of Cardiology* 96.1, pp. 112–116.
- EL BERBARI, R., N. KACHENOURA, A. REDHEUIL, A. GIRON, E. MOUSSEAUX, A. HERMENT, I. BLOCH, and F. FROUIN (2009). “Automated estimation of regional mean transition times and radial velocities from cine magnetic resonance images: evaluation in normal subjects”. In: *J Magn Reson Imaging* 30.1, pp. 236–242.
- FENSTER, A., D. B. DOWNEY, and H. N. CARDINAL (2001). “Three-dimensional ultrasound imaging”. In: *Physics in Medicine and Biology* 46.5, R67–99.
- FILIPOIU, F. M. (2013). *Atlas of Heart Anatomy and Development*. Springer Science and Business Media.
- FORNWALT, B. K., W. W. SPRAGUE, P. BEDELL, J. D. SUEVER, B. GERRITSE, J. D. MERLINO, D. A. FYFE, A. R. LEÓN, and J. N. OSHINSKI (2010). “Agreement is poor among current criteria used to define response to cardiac resynchronization therapy”. In: *Circulation* 121.18, pp. 1985–1991.
- GARCIA-BARNES, J., D. GIL, L. BADIELLA, A. HERNÁNDEZ-SABATÉ, F. CARRERAS, S. PUJADAS, and E. MARTÍ (2010). “A Normalized Framework for the Design of Feature Spaces Assessing the Left Ventricular Function”. In: *IEEE Transactions on Medical Imaging* 29.3, pp. 733–745.
- GARCIA-FERNANDEZ, M. A., J. BERMEJO, E. PEREZ-DAVID, T. LOPEZ-FERNANDEZ, M. J. LEDESMA, P. CASO, N. MALPICA, A. SANTOS, M. MORENO, and M. DESCO (2003). “New techniques for the assessment of regional left ventricular wall motion”. In: *Echocardiography (Mount Kisco, N.Y.)* 20.7, pp. 659–672.
- GAROT, J. (2005). “Apport de l’IRM à l’évaluation des cardiopathies ischémiques”. In: *MT Cardio* 1.2, pp. 148–157.
- GONZALEZ, F. A. and E. ROMERO, eds. (2010). *Biomedical Image Analysis and Machine Learning Technologies: Applications and Techniques*. IGI Global.
- HAWKINS, N. M., M. C. PETRIE, M. R. MACDONALD, K. J. HOGG, and J. J. V. McMURRAY (2006). “Selecting patients for cardiac resynchronization therapy: electrical or mechanical dyssynchrony?” In: *European Heart Journal* 27.11, pp. 1270–1281.
- HO, C. Y. and S. D. SOLOMON (2006). “A Clinician’s Guide to Tissue Doppler Imaging”. In: *Circulation* 113.10, e396–e398.

- HUANG, H., L. SHEN, R. ZHANG, F. MAKEDON, B. HETTLEMAN, and J. PEARLMAN (2006). “Cardiac Motion Analysis to Improve Pacing Site Selection in CRT”. In: *Academic Radiology* 13.9, pp. 1124–1134.
- JESSUP, M. and S. BROZENA (2003). “Heart failure”. In: *The New England Journal of Medicine* 348.20, pp. 2007–2018.
- JIANG, Z., Z. LIN, and L. S. DAVIS (2013). “Label Consistent K-SVD: Learning a Discriminative Dictionary for Recognition”. In: *IEEE Transactions on Pattern Analysis and Machine Intelligence* 35.11, pp. 2651–2664.
- KACHENOURA, N., A. REDHEUIL, D. BALVAY, C. RUIZ-DOMINGUEZ, A. HERMENT, E. MOUSSEAU, and F. FROUIN (2007). “Evaluation of regional myocardial function using automated wall motion analysis of cine MR images: Contribution of parametric images, contraction times, and radial velocities.” In: *J Magn Reson Imaging* 26.4, pp. 1127–1132.
- KIRSCHBAUM, S., P. DE FEYTER, and R. VAN GEUNS (2011). “Cardiac magnetic resonance imaging in stable ischaemic heart disease.” In: *Neth Heart J* 19.5, pp. 229–35.
- KLABUNDE, R. (2011). *Cardiovascular Physiology Concepts*. Lippincott Williams & Wilkins.
- LEKADIR, K., N. KEENAN, D. PENNELL, and G.-Z. YANG (2011). “An Inter-Landmark Approach to 4-D Shape Extraction and Interpretation: Application to Myocardial Motion Assessment in MRI”. In: *IEEE Transactions on Medical Imaging* 30.1, pp. 52–68.
- LI, Y. and A. NGOM (2013). “Sparse representation approaches for the classification of high-dimensional biological data”. In: *BMC Systems Biology* 7.Suppl 4, S6.
- LIN, E. C. (2008). “Cardiac MRI - Technical Aspects Primer”.
- LU, Y., P. RADAU, K. CONNELLY, A. DICK, and G. WRIGHT (2009). “Pattern Recognition of Abnormal Left Ventricle Wall Motion in Cardiac MR”. In: *Proceedings of the 12th International Conference on Medical Image Computing and Computer-Assisted Intervention: Part II. MICCAI '09*. London, UK: Springer-Verlag, pp. 750–758.
- LUSTIG, M., D. D., and P. J. (2007). “Sparse MRI: The application of compressed sensing for rapid MR imaging”. In: *Magnetic Resonance in Medicine* 58 (6), pp. 1182–1195.
- MAFFESSANTI, F., H.-J. NESSER, L. WEINERT, R. STERINGER-MASCHERBAUER, J. NIEL, W. GORISSEN, L. SUGENG, R. M. LANG, and V. MOR-AVI (2009). “Quantitative evaluation of regional left ventricular function using three-dimensional speckle tracking echocardiography in patients with and without heart disease”. In: *The American Journal of Cardiology* 104.12, pp. 1755–1762.
- MANTILLA, J., M. GARREAU, J.-J. BELLANGER, and J. L. PAREDES (2013a). “Automated classification of LV regional wall motion based on spatio-temporal profiles from cardiac cine magnetic resonance imaging”. In: *Proc. SPIE*. Vol. 8922, pages.
- (2013b). “Machine Learning Techniques for LV Wall Motion Classification Based on Spatio-temporal Profiles from Cardiac Cine MRI”. In: *IEEE Machine Learning and Applications (ICMLA), 2013 12th International Conference on*. Vol. 1, pp. 167–172.
- MANTILLA, J., J. PAREDES, J.-J. BELLANGER, E. DONAL, C. LECLERCQ, R. MEDINA, and M. GARREAU (2015). “Classification of LV wall motion in cardiac MRI using kernel Dictionary

- Learning with a parametric approach”. In: *37th Annual International Conference of the IEEE Engineering in Medicine and Biology Society (EMBS)*. (in press), pp. 7292–7295.
- MEMBERS, W. G., V. L. ROGER, A. S. GO, D. M. LLOYD-JONES, E. J. BENJAMIN, J. D. BERRY, W. B. BORDEN, D. M. BRAVATA, S. DAI, E. S. FORD, C. S. FOX, H. J. FULLERTON, C. GILLESPIE, S. M. HAILPERN, J. A. HEIT, V. J. HOWARD, B. M. KISSELA, S. J. KITTNER, D. T. LACKLAND, J. H. LICHTMAN, L. D. LISABETH, D. M. MAKUC, G. M. MARCUS, A. MARELLI, D. B. MATCHAR, C. S. MOY, D. MOZAFFARIAN, M. E. MUSSOLINO, G. NICHOL, N. P. PAYNTER, E. Z. SOLIMAN, P. D. SORLIE, N. SOTOODEHNIA, T. N. TURAN, S. S. VIRANI, N. D. WONG, D. WOO, and M. B. TURNER (2012). “Heart Disease and Stroke Statistics—2012 Update A Report From the American Heart Association”. In: *Circulation* 125.1, e2–e220.
- MISITI, M., Y. MISITI, G. OPPENHEIM, and J.-M. POGGI (2007). “Clustering Signals Using Wavelets”. In: *Computational and Ambient Intelligence*. Ed. by F. SANDOVAL, A. PRIETO, J. CABESTANY, and M. GRAÑA. Lecture Notes in Computer Science 4507. Springer Berlin Heidelberg, pp. 514–521.
- O’DELL, W. G. and A. D. MCCULLOCH (2000). “Imaging Three-Dimensional Cardiac Function”. In: *Annual Review of Biomedical Engineering* 2.1, pp. 431–456.
- ORDAS, S. and A. FRANGI (2005). “Automatic Quantitative Analysis of Myocardial Wall Motion and Thickening from Long-and Short-Axis Cine MRI Studies.” In: *Conf Proc IEEE Eng Med Biol Soc* 7, pp. 7028–31.
- PERPERIDIS, D. (2005). “Spatio-temporal registration and modelling of the heart using cardiovascular MR imaging”. PhD thesis. University of London.
- PETITJEAN, C. and J.-N. N. DACHER (2011). “A review of segmentation methods in short axis cardiac MR images.” In: *Medical image analysis* 15.2, pp. 169–184.
- PUNITHAKUMAR, K., I. AYED, A. ISLAM, I. ROSS, and S. LI (2010a). “Regional Heart Motion Abnormality Detection via Information Measures and Unscented Kalman Filtering”. In: *Medical Image Computing and Computer-Assisted Intervention – MICCAI 2010*. Ed. by T. JIANG, N. NAVAB, J. PLUIM, and M. VIERGEVER. Vol. 6361. Lecture Notes in Computer Science. Springer Berlin Heidelberg, pp. 409–417.
- PUNITHAKUMAR, K., I. BEN AYED, A. ISLAM, A. GOELA, I. G. ROSS, J. CHONG, and S. LI (2013). “Regional heart motion abnormality detection: An information theoretic approach”. In: *Medical Image Analysis* 17.3, pp. 311–324.
- PUNITHAKUMAR, K., I. BEN AYED, I. G. ROSS, A. ISLAM, J. CHONG, and S. LI (2010b). “Detection of left ventricular motion abnormality via information measures and bayesian filtering”. In: *IEEE Transactions on information technology in biomedicine: a publication of the IEEE Engineering in Medicine and Biology Society* 14.4, pp. 1106–1113.
- RUIZ, C., N. KACHENOURA, A. DE CESARE, A. DELOUCHE, P. LIM, O. GÉRARD, A. HERMENT, B. DIEBOLD, and F. FROUIN (2005). “Assessment of left ventricular contraction by parametric analysis of main motion (PAMM): theory and application for echocardiography.” In: *Phys Med Biol* 50.14, pp. 3277–3296.

- SADE, L. E., H. KANZAKI, D. SEVERYN, K. DOHI, and J. GORCSAN (2004). “Quantification of radial mechanical dyssynchrony in patients with left bundle branch block and idiopathic dilated cardiomyopathy without conduction delay by tissue displacement imaging”. In: *The American Journal of Cardiology* 94.4, pp. 514–518.
- SAN ROMÁN, J. A., J. CANDELL-RIERA, R. ARNOLD, P. L. SÁNCHEZ, S. AGUADÉ-BRUIX, J. BERMEJO, A. REVILLA, A. VILLA, H. CUÉLLAR, C. HERNÁNDEZ, and F. FERNÁNDEZ-AVILÉS (2009). “Quantitative Analysis of Left Ventricular Function as a Tool in Clinical Research. Theoretical Basis and Methodology”. In: *Revista Española de Cardiología (English Edition)* 62.5, pp. 535–551.
- SARWAR, A., M. D. SHAPIRO, S. ABBARA, and R. C. CURY (2008). “Cardiac magnetic resonance imaging for the evaluation of ventricular function”. In: *Seminars in Roentgenology* 43.3, pp. 183–192.
- SIMON, A. (2005). “Cardiac motion extraction and characterization in multislice computed tomography.” Theses. Université Rennes 1.
- SLIMAN, H., A. ELNAKIB, G. BEACHE, A. ELMAGHRABY, and A. EL-BAZ (2010). “Assessment of Myocardial Function from Cine Cardiac MRI Using a Novel 4D Tracking Approach”. In: *Journal of Computer Science and Systems Biology* 7.5, pp. 169–173.
- SUEVER, J. D., B. K. FORNWALT, L. R. NEUMAN, J. G. DELFINO, M. S. LLOYD, and J. N. OSHINSKI (2014). “Method to create regional mechanical dyssynchrony maps from short-axis cine steady-state free-precession images”. In: *Journal of Magnetic Resonance Imaging* 39.4, pp. 958–965.
- SUFFOLETTO, M. S., K. DOHI, M. CANNESON, S. SABA, and J. GORCSAN (2006). “Novel Speckle-Tracking Radial Strain From Routine Black-and-White Echocardiographic Images to Quantify Dyssynchrony and Predict Response to Cardiac Resynchronization Therapy”. In: *Circulation* 113.7, pp. 960–968.
- SUINESIAPUTRA, A., A. F. FRANGI, T. A. M. KAANDORP, H. J. LAMB, J. J. BAX, J. H. C. REIBER, and B. P. F. LELIEVELDT (2009). “Automated Detection of Regional Wall Motion Abnormalities Based on a Statistical Model Applied to Multi-Slice Short-Axis Cardiac MR Images.” In: *IEEE Transactions on Medical Imaging* 4.28, pp. 595–607.
- SUTTON, M. G. S. J. and N. SHARPE (2000). “Left Ventricular Remodeling After Myocardial Infarction Pathophysiology and Therapy”. In: *Circulation* 101.25, pp. 2981–2988.
- TRUPP, R. J. (2006). “Cardiac Resynchronization Therapy: A Practical Guide for Patient Management After Device Implantation, Part II”. In: *Congestive Heart Failure* 12.4, pp. 219–222.
- WHO (2011). *Global atlas on cardiovascular disease prevention and control*.
- (2014). *Global status report on noncommunicable diseases 2014*. World Health Organization.
- XAVIER, M. (2010). “Quantitative study of cardiac wall motion from cine-MRI using frequency-based optical flow methods”. Theses. Université de Bourgogne.
- XAVIER, M., A. LALANDE, P. M. WALKER, F. BRUNOTTE, and L. LEGRAND (2012). “An adapted optical flow algorithm for robust quantification of cardiac wall motion from standard

- cine-MR examinations”. In: *IEEE Transactions on information technology in biomedicine: a publication of the IEEE Engineering in Medicine and Biology Society* 16.5, pp. 859–868.
- YANCY, C. W., M. JESSUP, B. BOZKURT, J. BUTLER, D. E. CASEY, M. H. DRAZNER, G. C. FONAROW, S. A. GERACI, T. HORWICH, J. L. JANUZZI, M. R. JOHNSON, E. K. KASPER, W. C. LEVY, F. A. MASOUDI, P. E. MCBRIDE, J. J. V. McMURRAY, J. E. MITCHELL, P. N. PETERSON, B. RIEGEL, F. SAM, L. W. STEVENSON, W. H. W. TANG, E. J. TSAI, and B. L. WILKOFF (2013). “2013 ACCF/AHA Guideline for the Management of Heart Failure A Report of the American College of Cardiology Foundation/American Heart Association Task Force on Practice Guidelines”. In: *Circulation* 128.16, e240–e327.
- YANG, M., L. ZHANG, X. FENG, and D. ZHANG (2014). “Sparse Representation Based Fisher Discrimination Dictionary Learning for Image Classification”. In: *International Journal of Computer Vision* 109.3, pp. 209–232.

Dictionary Learning for LV wall motion classification based on Spatio-temporal profiles: Experiments and Results

5.1 Introduction

In this Chapter we present the experimental part and the results of the proposed method for LV wall motion classification, based on Spatio-temporal profiles and DL approaches. The description of the study population and the used protocol of evaluation are first described. Then, experimental results using the proposed features with discriminative dictionary learning DL algorithms for LV wall motion classification are presented. Furthermore, these results are compared with the results obtained using classical classification methods based on Support Vector Machines (SVMs) using two different kernels. The classification techniques are quantitatively evaluated in terms of accuracy, sensitivity, specificity, complexity (sparseness in SVMs and sparsity constraint in DL techniques) and computing times (training and testing). The end of this chapter presents a conclusion, elements of discussion of the proposed approach, limitations and perspectives of this study.

5.2 Study population

For this study, cardiac short-axis MR images were collected from four databases: two groups of data patients that were acquired from clinical protocols in national and international research projects; and two groups of healthy subjects obtained from two challenges of MICCAI¹ the

1. MICCAI - Medical image computing and computer-assisted intervention

Cardiac MR Left Ventricle Segmentation Challenge MICCAI 2009 (RADAU et al., 2009) and the first Cardiac Motion Analysis Challenge MICCAI 2011 (TOBON-GOMEZ et al., 2013). Next, we describe in details these datasets.

5.2.1 Patient data

This study included 14 patients who met accepted clinical criteria for CRT: NYHA Class III or IV heart failure, LV Ejection Fraction (LVEF) $< 35\%$, and optimal medical therapy for at least one month. All patients used in this study had a QRS duration ≥ 120 ms and present LV wall motion abnormalities. From these patients, 6 belong to the IMOP² project and 8 belong to the EuHeart³ project, that are two research projects in the context of CRT optimization for which the Laboratory of Signal and Image Processing (LTSI⁴, INSERM-U1099⁵) participated.

IMOP (2005–2008) was a project funded by the French Ministry of Research. The goal of this project was to analyze different approaches to improve the exploitation of multisensor acquisitions from CRT candidate patients (anatomical, electrical, hemodynamical and mechanical), in order to optimize Biventricular (BIV) device implantation, by following up these candidates at pre-, per- and post-operative stages (TAVARD et al., 2014).

The European project euHeart (WEESE et al., 2013), lead by Philips Research and Philips Healthcare, combined sixteen industrial, clinical and academic partners, including INSERM-U1099 (i.e. the LTSI) in cooperation with the CHU-Pontchaillou. The specific objective of euHeart was to improve diagnosis, treatment planning and delivery, and optimization of implantable devices by making patient-specific cardiac models using clinical measurements. euHeart partners were organized into different work-packages (WPs). Each WP in the application group of the project focused on a particular cardiovascular disease and in the optimization of cardiovascular therapies into the clinical environment. LTSI-INSERM U1099 was involved in one WP focused on CRT. The goal of this WP was the same as those defined in the context of IMOP project (MARCHESSEAU et al., 2013).

These database patients have been chosen initially for two objectives: 1) to show the capability of classification of normal and abnormal LV motion; 2) to see the possibilities to classify responder and non-responder patients. This second goal is more difficult to reach, because it needs a sufficient number of cases with information of response in each class. This study is limited to the first goal.

2. ANR CIC-IT *n*_o 04 187-188-189-190. Acronym from the French "utilité de l'Imagerie Médicale dans l'Optimisation de la Pose de prothèses cardiaques implantables", utility of medical imaging in the optimization of the implantation of implantable cardiac prosthesis.

3. euHeart: Personalised and Integrated Cardiac Care, FP7/2008-2012

4. Acronym from the French "Laboratoire Traitement du Signal et de l'Image" from the University of Rennes 1.

5. LTSI is the research unit number 1099 into the French Institute of Health and Medical Research (INSERM, acronym from the French "Institut national de la santé et de la recherche médicale").

5.2.1.1 Image Data

Cardiac magnetic resonance: CMR images included cine-SAX and cine-LAX (4CH, 2CH). CMR images were acquired with a Philips Achieva 3T machine using cardiac SENSE Coil (multicoil). Cine-CMR images were acquired in: Restrospective ECG-gated (RR-interval) mode, with breath-hold and multiplanar SAX, 4CH and 2CH views. Typical parameters for this acquisition were:

- Acquisition: Gradient echo (bTFE sequence), repetition time $TR=3.69$ ms, echo time $TE=1.85$ ms, flip angle $FA=45^\circ$,
- Resolution: 30 cardiac phases in IMOP, 40 and 60 cardiac phases for SAX and LAX views in euHeart, respectively. 256×256 pixels (in-plane) with 10 slices for SAX and 2 slices for LAX views. In-plane pixel size= 1.25×1.25 mm², slice thickness= 7 mm, spacing between slices = 9 mm,

For this study only the cine-SAX images have been used.

Echocardiography: Trans-thoracic echocardiography TTE US acquisitions included parasternal apical LAX (4CH, 2CH, 3CH) and SAX images. A cardiologist, expert in echocardiography, performed TTE acquisitions pre/post-implantation (3 and/or 6 months). The end-systolic phase was annotated in US acquisitions. STE traces and regional strain curves have been computed and exported using an echoPAC clinical workstation software (GE). Only SAX images have been used in this work.

Among the 14 patients, radial strain tracings from 2D-STE were available only for 3 patients in the IMOP database and for 6 patients in the euHeart database and only at mid-cavity slice.

5.2.2 Control Subjects

Two groups of data have been chosen from MICCAI challenges: For the first group, data provided in the Cardiac MR Left Ventricle Segmentation Challenge MICCAI 2009 (RADAU et al., 2009) comprise 45 cardiac cine-MR datasets from a mixed of patients and pathologies: healthy, hypertrophy, heart failure with infarction and heart failure without infarction. The subset of the data were first used for automated myocardium segmentation challenge from short-axis MRI, held by a MICCAI workshop in 2009. Cine steady state free precession (SSFP) MR short axis (SAX) images were obtained with a 1.5T GE Signa MRI. All the images were obtained during 10-15 second breath-holds with a temporal resolution of 20 cardiac phases over the heart cycle. 6 to 12 SAX images were obtained from the atrioventricular ring to the apex (slice thickness= 8 mm, spacing between slices= 8 mm, spatial resolution= 256×256). For this study we have selected 6 patient studies corresponding to one of the group of healthy subjects.

For the second group, the control data in the Cardiac Motion Analysis Challenge that was held at the 2011 MICCAI workshop entitled "Statistical Atlases and Computational Models of the Heart: Imaging and Modelling Challenges" (STACOM'11) (TOBON-GOMEZ et al., 2013), consisted of fifteen healthy volunteers without clinical history of cardiac disease. This challenge

has been organized by the Cardiac Atlas Project (CAP)⁶. The data were acquired at the Division of Imaging Sciences and Biomedical Engineering, King’s College London, United Kingdom. The MR datasets were acquired using a 3T Philips Achieva System (Philips Healthcare, Best, The Netherlands). The MR sequences were cine Steady State Free Precession (SSFP). SSFP datasets were scanned in multiple views (TR/TE = 2.9/1.5 ms, flip angle = 40°). All images were acquired during breath-holds of approximately 15 s with a temporal resolution of 30 cardiac phases over the heart cycle and were gated to the signal ECG. Eleven to 16 SAX images were obtained from the atrioventricular ring to the apex (slice thickness=8mm, spacing between slices=8mm, in-plane pixel size=1.25 × 1.25 mm², matrix= 256×256). For this study we have chosen randomly a set of 9 studies from this database.

In summary, for this work we had at our disposal 14 patients with cardiac dyssynchrony and 15 control subjects. Cardiac cine MR images in short axis view are available for all the population, while 2D-STE in short axis are available only for 9 patients.

In the next section, we present the protocol that has been defined for the evaluation of our methods for the LV wall motion assessment.

5.3 Evaluation protocol

As we mentioned in Chapter 4, the discrimination of normal and abnormal wall motion is performed with the use of the proposed features (radial/diametral spatio-temporal profiles or parameters extracted from the radial profiles) as input atoms in the training of discriminative dictionary learning algorithms. To this end, we propose an evaluation protocol based on the information available from the population described before and the kind of feature used for training the classifiers. Figure 5.1, shows an overview of the proposed protocol that is defined according four criteria:

Global or Local evaluation: The first aspect is related to the level of the label associated to the proposed feature for LV motion assessment. A global and simple criterium can be established: i) by considering all the features extracted from pathological subjects, as features with abnormal motion without considering regional analysis, and ii) by considering all the features extracted from control subjects, as features with normal motion. This criterium could be biased by the fact that in pathological subjects, some regions or anatomical segments of the LV could present normal motion whereas others are abnormal. A more accurate criterium consists to be local in labeling the features by anatomical regions, as it is realized in clinical analysis, by incorporating visual assessment of cardiologists or other measures like strain measures that can be extracted in STE images. In this work, we

6. The Cardiac Atlas Project (CAP) was funded by the National Heart, Lung and Blood Institute, USA, part of the National Institutes of Health. (R01HL087773). The Cardiac Atlas Project (CAP) has established a large-scale database of cardiac imaging examinations and associated clinical data in order to develop a shareable, web-accessible, structural and functional atlas of the normal and pathological heart for clinical, research and educational purposes.

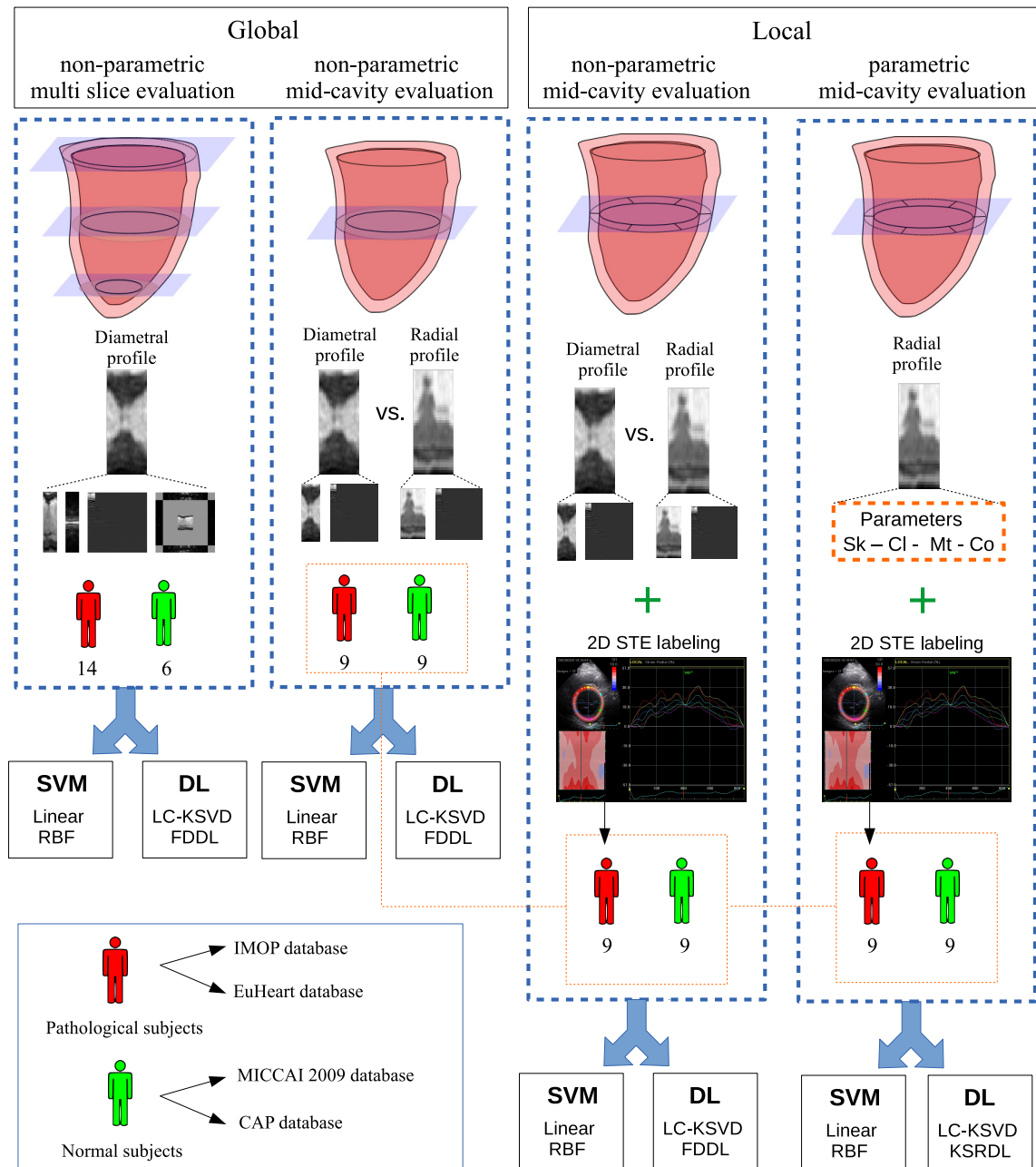


FIGURE 5.1– Overview of the proposed evaluation protocol at two levels: Global and Local evaluation. In Global evaluation, patient global status (Normal/Pathologic) is taken as ground truth to label the spatio-temporal profiles for each patient. In Local evaluation, local strain information from 2D-STE (normal/abnormal) is taken as ground truth to label the spatio-temporal profiles per anatomical LV segment in each patient. Non-parametric inputs, correspond to spatio-temporal representations: diametral profiles or radial profiles in the Gray level domain (original domain), as well as, in Fourier, Wavelet or Curvelet domains, while parametric input corresponds to the parameters extracted from the radial spatio-temporal profiles (Curve Skewness (Sk), Curve clustering (Cl), Mean transition time (Mt), and Cross Correlation parameter (Co)). Multislice evaluation, is performed in a population of 20 subjects (14 pathologic and 6 control) at three anatomical planes: basal, mid-cavity and apical. Mid-cavity evaluation is performed in a population of 18 subjects: 9 patients with 2D-STE studies and 9 control subjects.

take advantage of the radial strain traces available for 9 patients at the mid-cavity slice, provided by the 2D-STE study.

We propose two levels of evaluation at Global and Local. In a Global evaluation level, patient global status (Normal/Pathologic) is taken as ground truth to label the spatio-temporal profiles for each patient. In a Local evaluation level that is more realistic, extracted local strain information from 2D-STE (normal/abnormal) per anatomical segment in each patient, is taken as ground truth to label the spatio-temporal profiles.

Non-parametric or parametric inputs: Non-parametric inputs correspond to diametral or radial spatio-temporal profiles, while Parametric input, corresponds to the parameters extracted from the radial spatio-temporal profiles (Curve Skewness (Sk), Curve clustering (Cl), Mean transition time (Mt), and Cross Correlation parameter (Co)).

Non-parametric diametral spatio-temporal inputs are represented in the Gray level (original) domain as well as, in Fourier, Wavelet and Curvelet domains, in the case of global evaluation. For local evaluation, they are represented in the original and Wavelet domains.

In the case of radial spatio-temporal inputs and local evaluation, they are represented in the Gray level/original and Wavelet domains.

Multi-slice/mid-cavity evaluation: Multi-slice evaluation is performed at three anatomical planes: basal, mid-cavity and apical. Global evaluation with Non-parametric diametral spatio-temporal inputs is considered to evaluate the LV motion in these three planes.

Single mid-cavity evaluation is performed in accordance with available information of local strain provided by 2D-STE only at the mid-cavity plane for some patients in the study. In this case, non parametric and parametric inputs are considered.

SVM and DL classifiers: Non-parametric or parametric features are taken as input atoms in the training of different machine learning techniques. Firstly, as we mentioned in the previous chapter, two discriminative dictionary learning algorithms are adapted for LV wall motion classification: the first one, the Label Consistent K-SVD algorithm (LC-KSVD) (JIANG et al., 2013), and a second one, the Fisher discriminant DL algorithm (FD-DL) (YANG et al., 2014). These two algorithms take as input atoms the diametral or the radial spatio-temporal profiles.

Secondly, another type of DL algorithm based on kernels, the KSRDL algorithm (LI et al., 2013), is adapted for LV wall motion classification using parameters extracted from the radial spatio-temporal profiles. For comparison, LC-KSVD is also used with the parametric inputs.

Classical classification based on Support Vector Machines (SVMs) with two different kernels, linear and RBF kernels, is performed for comparison purposes.

To summarize, we propose the following levels of evaluation:

Global non-parametric multi-slice evaluation using diametral profiles with the global status of the patient (Normal/Pathologic) as ground truth.

Global non-parametric mid-cavity evaluation comparing diametral with radial spatio-temporal profiles with the global status of the patient (Normal/Pathologic) as ground truth.

Local non-parametric mid-cavity evaluation comparing diametral with radial spatio-temporal profiles with the local radial strain information from 2D-STE as ground truth.

Local parametric mid-cavity evaluation using parameters extracted from spatio-temporal radial profiles with the local radial strain information from 2D-STE as ground truth.

This scheme of evaluation allows to measure the benefit of parametric compared to the non-parametric local approaches, the benefit of local compared to global analysis and the difference between multi-slice and mid-cavity evaluation, by using SVM and DL approaches.

We have described in the previous chapter the Non-parametric and parametric feature extraction and the adaptation of the DL algorithms for the task of LV wall motion classification using the proposed spatio-temporal representations. In the next subsections, global and local aspects of evaluation are firstly described by the local 2D-STE Radial strain assessment. Secondly, the selection of the correct number of profiles and different measures of performance are presented. Finally, we present the obtained results and the evaluation of the mentioned classifiers before to conclude.

5.3.1 2D-STE Radial strain assessment for local evaluation

The definition of normal values of local LV motion is of critical importance to the clinical application. Based on Echocardiography modality and specifically in Speckle Tracking mode (STE), various studies have been focused on defining these ranges. In (FINE et al., 2013), 2D echocardiography is performed in 186 healthy adults free of cardiovascular disease or risk factors, followed by a comprehensive ventricular myocardial strain analysis. Mean segmental peak systolic LV radial strain values and their corresponding standard deviation reported in this study are shown in Table 5.1.

TABLE 5.1– Normal Mean segmental peak systolic LV radial strain values reported in (FINE et al., 2013)

Radial	Strain(%)
All segments	44.8 ± 21.7
Anterior	40.2 ± 30.0
Anteroseptal	52.2 ± 63.4
Inferior	42.0 ± 22.5
Lateral	42.5 ± 33.5
Posterior	47.4 ± 23.6
Septal	44.8 ± 32.6
<i>p</i> -value	0.078

In (YINGCHONCHAROEN et al., 2013), a review analysis of 24 articles, 12 articles with a total of 568 patients were eligible for global radial strain analysis, the results of normal values of strain are ranged from 35.1% to 59.0% (mean, 47.3%, confidence interval of 95%, from 43.6% to

51.0%). In (BECKER et al., 2006), an analysis of myocardial deformation was performed in 64 patients of which, 54 patients suffer from ischaemic heart disease with a myocardial infarction and 10 participants with normal LV motion confirmed by cardiac cine-MRI. Tracking of acoustic markers was used to calculate radial and circumferential strain, and strain rate within 2D echocardiographic images for each LV segment in a 16 segment model. Then, cardiac MRI was performed to define segmental LV function as normokinetic, hypokinetic or akinetic. Table 5.2 shows the results of radial strain obtained in this analysis reported for the overall set of LV segments.

TABLE 5.2– Radial strain related to regional LV function defined by cardiac magnetic resonance imaging reported in (BECKER et al., 2006)

	Radial Strain(%)
Normal kinesis (n=399 segments)	36.8 ± 10.5
Hypokinesis (n=392 segments)	24.1 ± 7.5
Akinesis (n=110 segments)	13.4 ± 4.8
<i>p</i> Value	<0.01

In this work, we have at our disposal both the cardiac cine-MRI study and the 2D-STE study for a total of 9 patients. Based on the reference values shown in Table 5.2, with a relative variability of $8.7 \pm 7.1\%$ for peak systolic radial strain between 2D-STE and cardiac cine-MRI (BECKER et al., 2006), we catalogue a particular segment in a cardiac cine-MRI study as normal if the peak systolic radial strain curve of this segment in the STE data presents normal kinesis, or abnormal if the peak systolic radial strain curve presents hypokinesis or akinesis.

First, a correspondence between cine-MRI and 2D-STE studies is needed. A visual inspection supported by the medical reports of the 9 patients was performed in order to find a correspondence between the SAX plane used in the 2D-STE study and the SAX plane selected in the cine-MRI study. This inspection is in particular, based on the visualization of the papillary muscles observed in both images.

Note that, due to the standard deviation into the ranges, a peak radial strain value can fall in two overlapping zones i.e. normal kinesis or hypokinesis, thus, the range with the mean value closest to the peak value in study is selected. These observations have been established with the help supervision of a cardiologist and have been confirmed with information obtained in the cine-MRI studies assessed by physicians in the medical reports.

Figure 5.2 shows the 2D-STE study for one example of data corresponding to the EuHeart5 patient. Radial strain curves from this patient are shown in Figure 5.3 with the respective range zones of normal kinesis, hypokinesis and akinesis. To illustrate the result of this assessment, a set of 6 radial spatio-temporal profiles per anatomical segment of this patient is presented in Figure 5.4. The graphical user interface (GUI) that has been developed allows us the labeling of a profile based on the strain given by the 2D-STE study (normal/abnormal) (MANTILLA et al., 2015c). For example, radial profiles in the anteroseptal (AS), septal (S) and inferior (I)

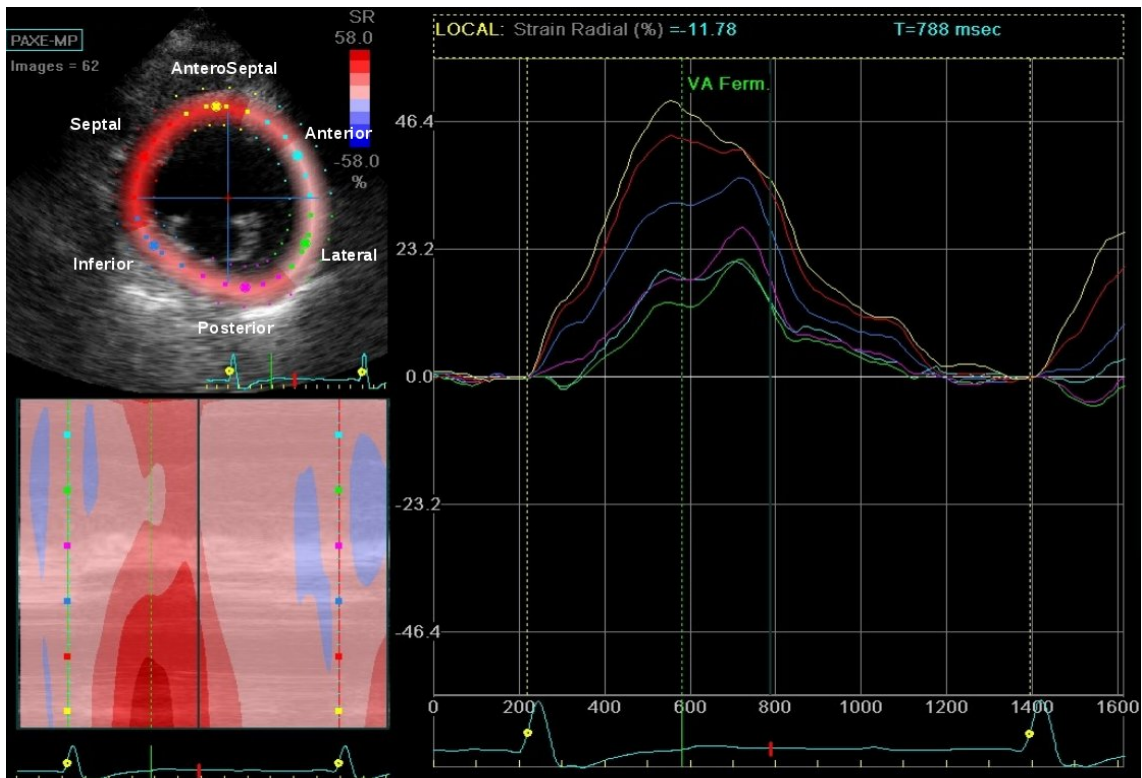


FIGURE 5.2– Radial strain tracings for one cardiac cycle obtained from the short axis view in the EuHeart5 patient. There are six tracings for the six evaluated anatomical segments within the circumference.

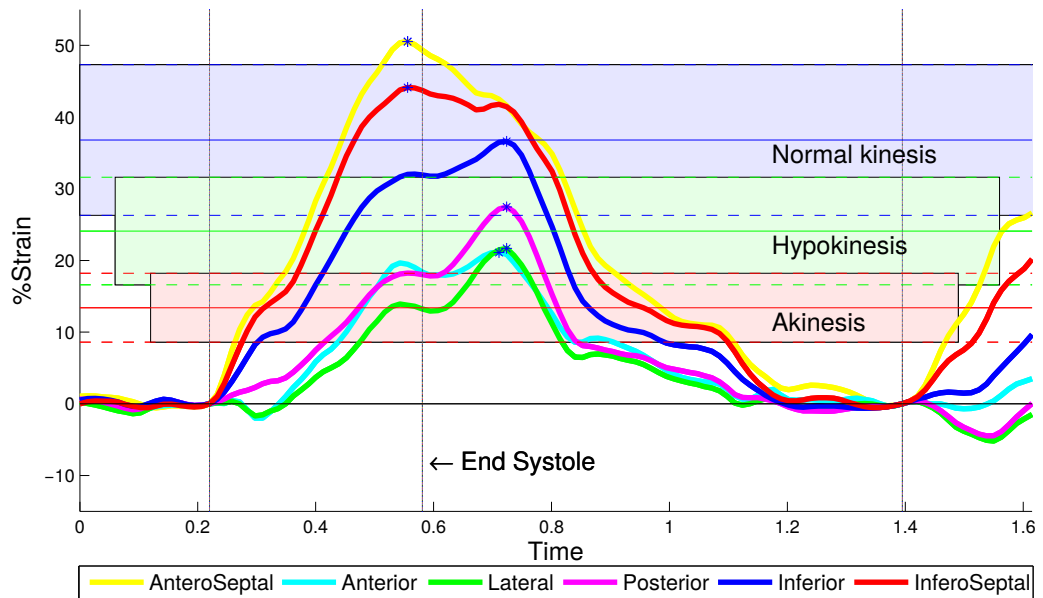


FIGURE 5.3– Radial strain tracings for the EuHeart5 patient.

anatomical segments shown in the GUI, are identified as profiles with normal segment contraction according to the information of local strain given by the 2D-STE study.

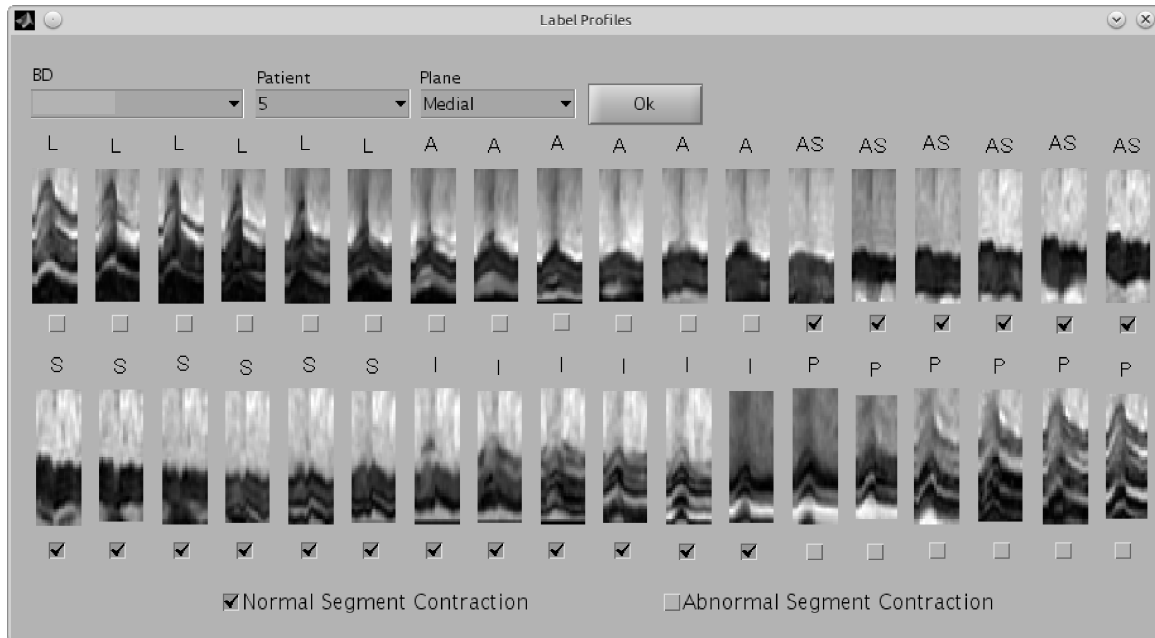


FIGURE 5.4— Radial spatio-temporal profiles obtained from the short axis view in a pathologic patient. Labels of the profiles are performed with the assessment of the radial strain tracings for the six evaluated segments in the 2D-STE study (L=Lateral, A=Anterior, AS=AnteroSeptal, S=Septal, I=Inferior, P=Posterior). Profiles of the anterior, anteroposeptal and inferoseptal segments are labeled as normal segment contraction while the others are labeled as abnormal.

We assume that all the segments from subjects of the healthy group have normal contraction, consequently all the segments of the control subjects are cataloged as normal kinesis. With the procedure described before, we can precise the mode of Local evaluation of radial and diametral spatio-temporal profiles of the pathologic population.

Local radial spatio-temporal evaluation: In this case, anatomical segments can be directly matched with the corresponding radial profiles. Table 5.3, shows the group of 9 patients with the respective anatomical regions cataloged accordingly the assessment of radial strain. As we can see, 5 of the 9 pathological patients present hypokinesia or akinesia in all segments, while the other 4 patients present segments with normal kinesis, hypokinesia or akinesia. In the same Table, EF denotes Ejection Fraction. To better illustrate this assessment, in Figure 5.5 parametric images at mid-cavity SAX plane known as bull-eyes are shown for the 9 patients in study (cf. 4.2.3). These images represent the ground truth in the assessment of LV anatomical segments provided by the 2D-STE study.

Local diametral spatio-temporal evaluation: Local evaluation using diametral spatio-temporal profiles needs the definition of a criterium to label each pair of opposite LV anatomical segments.

TABLE 5.3– LV anatomical segments assessed by 2D-STE in the pathological group in the mid-cavity SAX plane.

Patient	Segments						EF
	AS	A	L	P	I	S	
IMOP0	Akin	Akin	Akin	Akin	Akin	Akin	8%
IMOP4	Akin	Akin	Hypo	Akin	Akin	Akin	10%
IMOP5	Akin	Hypo	Hypo	Normo	Normo	Hypo	30%
EuHeart1	Akin	Akin	Hypo	Hypo	Akin	Akin	26%
EuHeart2	Akin	Akin	Akin	Akin	Akin	Akin	24%
EuHeart3	Akin	Akin	Akin	Akin	Akin	Akin	50%
EuHeart4	Akin	Akin	Hypo	Normo	Hypo	Akin	27%
EuHeart5	Normo	Hypo	Hypo	Hypo	Normo	Normo	38%
EuHeart6	Akin	Akin	Akin	Normo	Normo	Akin	25%

(AS=AnteroSeptal, A=Anterior, L=Lateral, P=Posterior, I=Inferior, S=Septal)
(Akin=Akinetic, Hypo=Hypokinetic, Normo=Normal kinesis, EF=Ejection Fraction)

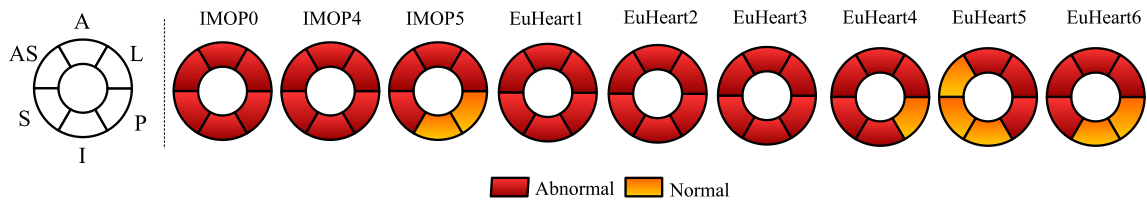


FIGURE 5.5– Ground truth for Local LV wall motion with the assessment of STE in the pathological group.

We define the following criterium to label each diametral spatio-temporal profile: if two opposite segments are normal (this is, the combination Normo-Normo), then the diametral profiles of that region are considered as profiles with LV normal motion. If one of the segment is normal and the other is akinetic or hypokinetic, then, the diametral profiles of that region are considered as profiles with LV abnormal motion (this is the combination normo-akin, normo-hypo, akin-normo or hypo-normo). Finally, if both segments of a specific region are akinetic or hypokinetic, then the diametral profiles of that region are considered as profiles with LV abnormal motion.

As observed in Table 5.4, neither combination of opposite segments is normo-normo. Then, the ground truth used for local evaluation using diametral spatio-temporal profiles corresponds for these data, to the ground truth used for global evaluation (assuming the global status of the patient as label of all the anatomical segments).

Once these different criteria of evaluation have been defined, we proceed to use the proposed spatio-temporal representations as input data and to parametrize the SVM and the dictionary learning algorithms. This is presented in next section.

TABLE 5.4– Opposite LV anatomical segments assessed by 2D-STE in the pathological group in the mid-cavity SAX plane.

Patient	Segments			EF
	AS-P	A-I	L-S	
IMOP0	Akin-Akin	Akin-Akin	Akin-Akin	8%
IMOP4	Akin-Akin	Hypo-Akin	Akin-Akin	10%
IMOP5	Akin-Normo	Hypo-Normo	Hypo-Hypo	30%
EuHeart1	Akin-Hypo	Akin-Akin	Hypo-Akin	26%
EuHeart2	Akin-Akin	Akin-Akin	Akin-Akin	24%
EuHeart3	Akin-Akin	Akin-Akin	Akin-Akin	50%
EuHeart4	Akin-Normo	Akin-Hypo	Hypo-Akin	27%
EuHeart5	Normo-Hypo	Hypo-Normo	Hypo-Normo	38%
EuHeart6	Akin-Normo	Akin-Normo	Akin-Akin	25%

(AS-P = AnteroSeptal to Posterior, A-I = Anterior to Inferior, L-S = Lateral to Septal)

5.3.2 Selection of correct number of profiles

We perform several experiments varying the number of profiles and found out that selecting diametrical profiles every 10° achieves a good trade-off between complexity and classification performance. Thus, every sample (subject) takes only 18 profiles per slice, 6 diametral spatio-temporal profiles per anatomical opposite segments at basal and mid-cavity SAX plane, and 9 diametral profiles per segment at apical SAX plane.

In the case of radial profiles, every sample takes only 36 profiles at the mid-cavity SAX plane, 6 spatio-temporal profiles per anatomical segment. Figure 5.6 shows an illustrative example of 36 points located outside the LV epicardial border spatially distributed every 10° and the orientation of two spatio-temporal profiles: a diametral profile from the anteroseptal to posterior wall and a radial profile in the lateral segment.

5.3.3 Performance measures

We evaluated the classifiers performance by computing the accuracy, specificity and sensitivity over all the datasets. Sensitivity measures the proportion of positives which are correctly identified, e.g., the percentage of the abnormal spatio-temporal profiles who are correctly identified as having abnormal LV wall motion. Specificity measures the proportion of negatives which are correctly identified as such e.g., the percentage of the normal spatio-temporal profiles who are correctly identified as having normal LV wall motion. Accuracy measures the proportion of abnormal or normal profiles those are selected correctly to the total number of profiles with abnormal or normal LV motion. These performance measures are defined as:

$$\text{Accuracy} = \frac{T_P + T_N}{P + N}, \quad \text{Sensitivity} = \frac{T_P}{P}, \quad \text{Specificity} = \frac{T_N}{N}$$

where T_P denotes true positives (number of profiles correctly classified as abnormal motion), and T_N true negatives (number of profiles correctly classified as normal motion). The total number of abnormal motion and normal motion profiles are P and N , respectively.

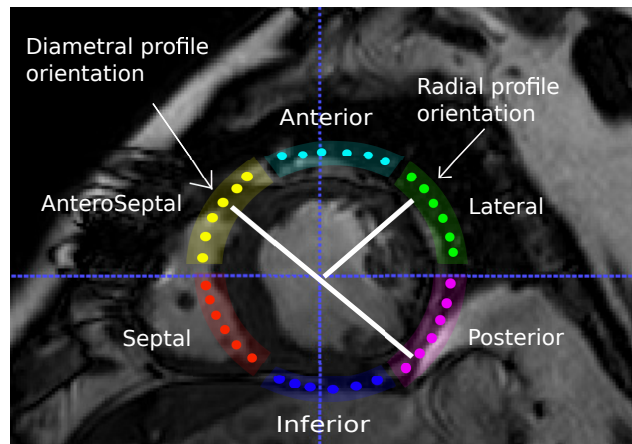


FIGURE 5.6— An illustrative example of 36 points located outside the epicardial border every 10° to construct 36 radial spatio-temporal profiles, 6 per LV anatomical segment, or to construct 18 diametral spatio-temporal profiles, 6 per opposite LV anatomical segments. An orientation of a diametral spatio-temporal profile is shown from the anteroseptal region to its opposite in the posterior segment. An orientation of radial profile is shown from the LV centroid to a point located in the lateral segment.

To evaluate the generalization capability of the machine learning techniques with respect to accuracy, sensitivity, and specificity, and for posterior comparison among them, we perform a random sub-sampling cross validation. This method randomly splits the dataset into training and validation data. For each such split, the model is fitted to the training data, and predictive accuracy is assessed using the validation data. The results are then averaged over the total of splits.

Furthermore, due to the small number of patients currently available for each class, our classifiers are evaluated using the leave-one-out (LOO) patient cross-validation performance criterium (CHAPELLE et al., 2002). In this case the training is performed with the profiles of all excepted one patient that is left out to test the classifier. The process is repeated until all patients are taken for testing the classifier. LOO-patient cross validation results are presented in parametric images known as bull-eyes.

A study of robustness of the classifiers is performed in Global non-parametric multi-slice evaluation and Local parametric/non-parametric mid-cavity evaluation with the following criteria:

- The classification accuracy of the DL algorithms is evaluated by reducing the number of atoms in the initial dictionary.
- The complexity of the classification methods is evaluated in terms of sparsity for the DL models and sparseness for the SVM models:
 1. The sparseness in SVMs is measured by the number of support vectors (SV) found by the trained model. The Support Vectors (SV), are the data points that are closest to the optimal separating hyperplane (cf. section 2.7).
 2. The FD-DL algorithm and the KSRDL algorithm are evaluated in terms of ℓ_1 -norm varying λ_1 that is the regularization parameter whose value governs the sparsity of

the solution.

3. Since LC-KSVD algorithms use a ℓ_0 -norm that counts the number of non-zero elements of \mathbf{X} , the sparsity constraint T is selected as a measure of complexity in this case.

— Computing times for training and testing are also calculated for each algorithm running on a PC with a 2.50 GHz Intel(R) Xeon(R) processor and 32 GB RAM.

5.3.4 Parameter selection of the machine learning techniques

The regularization parameters for the machine learning techniques are tuned by heuristic search, specifically:

- For the linear SVM, the regularization constant (C) was varied in $[10^{-4}, 10^{-3}, 10^{-2}, 10^{-1}, 10^0, 10^1, 10^2, 10^3, 10^4]$ and for the SVM RBF (σ) was varied in $[0.001, 0.01, 0.1, 1, 10, 100]$.
- For the LC-KSVD algorithms, according to equations (4.6) and (4.7), the weight for label constraint term (α) and the weight for classification error term (β) were tuned by heuristic search in a mesh grid from 1 to 100 with a step of 1.
- For FD-DL, according to equation (4.8), the regularization parameters (λ_1) and (λ_2) were tuned by searching in a mesh grid from 0.01 to 10 with a step of 0.01.
- Finally for KSRDL, according to equation (4.9), the regularization parameter (λ) was tuned by searching in a mesh grid from 10^{-5} to 10^0 with a step of 10^{-2} .

In the next sections, we present different experiments based on the evaluation protocol with their respective results. Firstly, for each level of evaluation we recall the specific goal, the population, input data and space domain of representation. Secondly, we present quantitative results of experiments using SVM and DL techniques. Finally a subsection of comparisons between algorithms is presented in which results are analyzed depending on the specific goal.

5.4 Global non-parametric multi-slice evaluation

The global non-parametric multi-slice evaluation was performed using the global status of the subject: Normal/Pathologic, as the label of diametral spatio-temporal profiles extracted in one slice at the apical, mid-cavity and basal short axis planes:

Specific goal: To compare results of LV wall motion classification among different short axis planes: basal, mid-cavity and apical planes, using diametral spatio-temporal profiles.

Population: The short-axis, cine MRI database used in this experiment comprises 20 studies identified in two classes: 1) abnormal LV motion samples corresponding to 14 patients with cardiac dyssynchrony (6 from the IMOP database and 8 from the euHeart database) and 2) normal LV motion samples that correspond to 6 healthy subjects from the Cardiac MR Left Ventricle Segmentation Challenge MICCAI 2009.

Input data: In summary, for each subject 18 diametral spatio-temporal profiles were extracted, thus, we have a total of 360 profiles: 252 considered as abnormal (14 patients, 18 profiles per patient) and 108 considered as normal (6 control subjects, 18 profiles per subject).

Space domain representation: Experiments were performed using the diametral spatio-temporal profiles in the original domain (Gray levels), as well as, Fourier, Wavelet and Curvelet domains.

5.4.1 Experiments with SVM

Experiments are performed independently at each short-axis slice level (basal, mid-cavity, and apical) with a SVM based classifier constructed using two kinds of kernel functions: Linear and Gaussian Radial Basis Function (RBF).

Leave-one-out LOO cross validation

In this particular case, we train with the spatio-temporal profiles of 19 subjects and test with the profiles of the single subject left out, the process is repeated until each of the subjects passed through the testing phase.

Figures 5.7 and 5.8, show the accuracy of classification in the different domains at different opposite LV anatomical segments using SVM with a linear and a RBF kernel respectively. As we can see in these graphics, accuracy results using a RBF SVM are under 95% in all the domains. In contrast some results using linear SVM are over 95%. The higher accuracy is achieved in the mid-cavity plane using linear SVM. Fourier and Curvelet domains do not show competitive results compared with Gray level and Wavelet domain that show higher results in medial planes.

The Wavelet coefficients of the spatio-temporal profiles at the Inferior-Anterior anatomical segments in the mid-cavity plane show the higher accuracy followed by the Gray level representation.

Details of the best results are presented in Table 5.5 in terms of accuracy, sensitivity and specificity using linear SVM classifier and Wavelet coefficients. As can be seen in this Table using a diametral line crossing the inferior-anterior segments at mid-cavity slice yields the best performance under the LOO criteria.

For the visualization of the different regional data that have been generated, we use parametric images known as bull's eye plots, Figure 5.9 shows the results for the subjects in our study using the linear SVM in the Wavelet domain. In these parametric images, segment colors are determined using the majority voting rule over the set of 6 diametral profiles selected per segment. Specifically, if more than one half of the 6 profiles examined in one anatomical segment is classified as normal, then, orange color is assigned to that segment. Red color is assigned to one segment if more than one half of the profiles is classified as abnormal. If exactly one half of the profiles is classified as normal and the other half as abnormal then, a decision can not be taken and black color is assigned to that region.

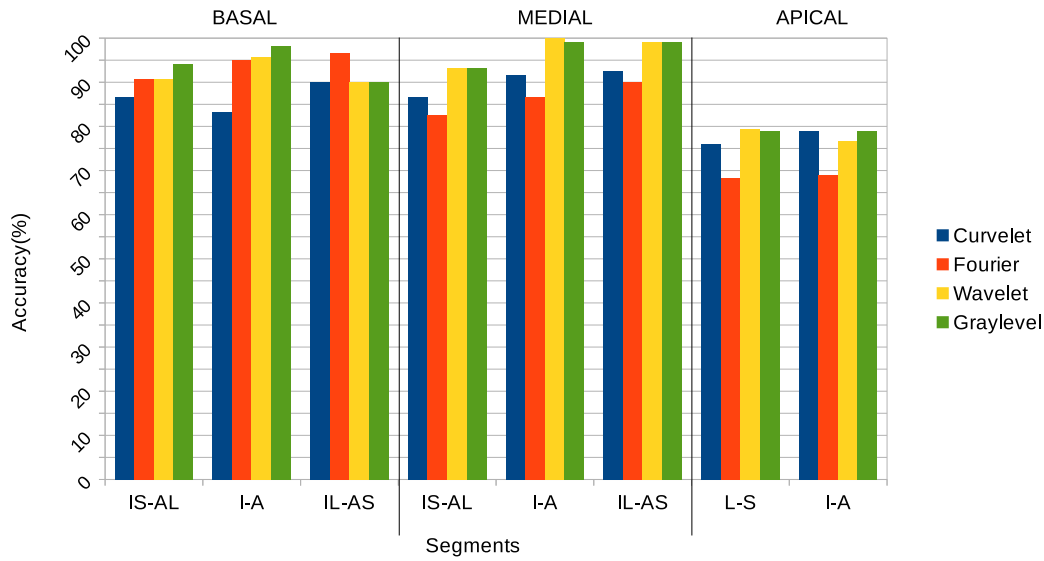


FIGURE 5.7– Comparative mean results of LOO cross validation in opposite segments using linear SVM in terms of accuracy. (IS-AL= From InfeRoSeptal to AnteroLateral, I-A= From Anterior to Inferior, IL-AS= From InfeRoLateral to AnteroSeptal, L-S= From Lateral to Septal).

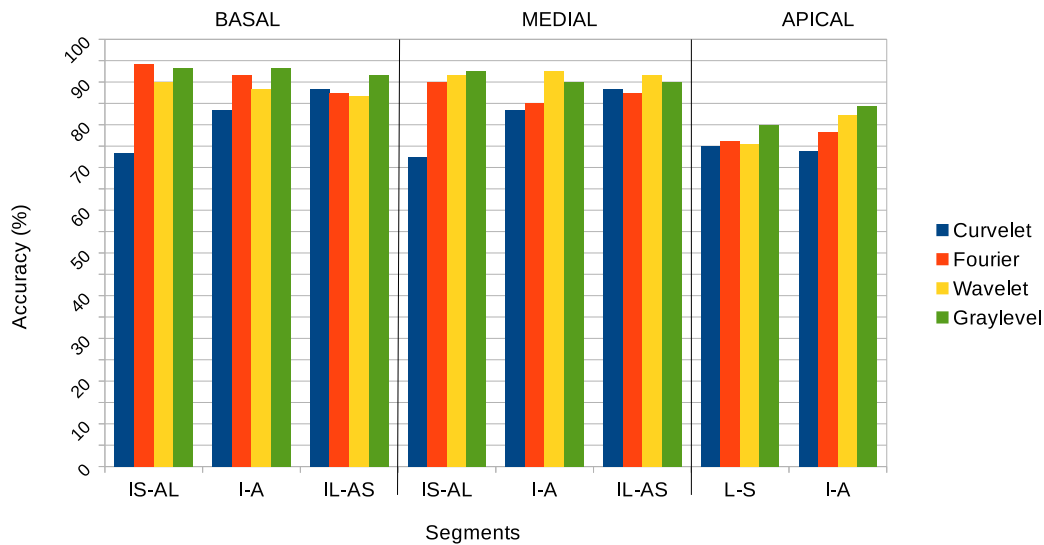


FIGURE 5.8– Comparative mean results of LOO cross validation in opposite segments using RBF SVM in terms of accuracy. (IS-AL= From InfeRoSeptal to AnteroLateral, I-A= From Anterior to Inferior, IL-AS= From InfeRoLateral to AnteroSeptal, L-S= From Lateral to Septal).

Results presented in the bull-eyes plots show that the classifier can not take a decision in some segments at the apical plane in patients: IMOP3, IMOP5, EuHeart3 (also in mid-cavity slice), EuHeart5, MICCAI1, MICCAI4 and MICCAI5. This is because one half of the profiles that

TABLE 5.5– Global multi-slice evaluation: Mean results of LOO cross validation in opposites segments with Linear SVM and Wavelets coefficients.

Plane	Segment	Accuracy	Sensitivity	Specificity
Basal	InferoLateral-AnteroSeptal	93.33%	94.05%	91.67%
	Inferior-Anterior	93.33%	95.24%	88.89%
	InferoSeptal-AnteroLateral	90.83%	100.00%	69.44%
Medial	InferoLateral-AnteroSeptal	90.83%	94.05%	83.33%
	Inferior-Anterior	100.00%	100.00%	100.00%
	InferoSeptal-AnteroLateral	99.17%	98.81%	100.00%
Apical	Lateral-Septal	78.00%	82.86%	66.67%
	Inferior-Anterior	75.00%	88.10%	44.44%

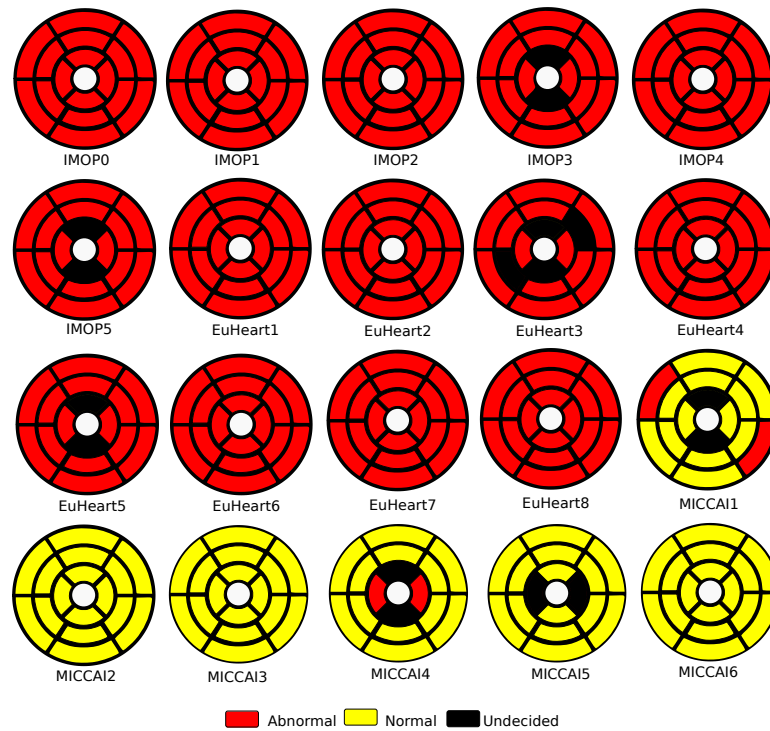


FIGURE 5.9– Bull-eyes showing accuracy of classification for the 6 patients in the IMOP database, 8 patients of euHeart database and the control group (MICCAI).

belong to those segments was classified as normal and the other half as abnormal by the SVM procedure. In the case of control subjects MICCAI1 and MICCAI4, the classifier fails when some segments were assigned to the class of abnormal profiles. These results can be quantitatively observed in Table 5.5 where specificity values are relatively small compared with sensitivity values, specially in the basal and apical plane.

Random sub-sampling cross validation

To evaluate the generalization capability of the proposed approach with respect to accuracy, sensitivity, and specificity, and for comparisons with the Dictionary Learning algorithms, several subsets of samples are constructed from the original database (14 patients and 8 control subjects) applying random sub-sampling cross validation: Each subset is composed of training and test groups. To be more precise, we use a training subset of 4 pathological patients and 4 healthy patients randomly from the database.

For each patient in the training subset, 18 spatio-temporal profiles are selected to obtain 144 profiles (8 subjects, 18 profiles per subject) where 72 present abnormal motion and the other 72 present normal wall motion. Profiles of the rest of the patients not included in the training stage (10 patients and 2 controls), are selected to test the method. Tables 5.6-5.9 show the overall average performance accuracy over 50 randomly configurations for training and testing subsets for SVM with linear and RBF kernel function in different basis (Gray level, Wavelet, Curvelet and Fourier domains) and in the three anatomical planes (Basal, medial and apical).

TABLE 5.6– Global multi-slice evaluation: Classification results using diametral profiles in Gray level domain by the SVM models.

	SVM Linear			SVM RBF		
	Acc	Sens	Spec	Acc	Sens	Spec
Basal	92.94± 4.71	93.62± 4.39	89.52±11.86	86.75± 5.89	89.81± 8.10	71.43±29.01
Medial	91.59± 5.21	91.52± 7.06	91.90± 8.00	83.73± 5.55	85.52±10.14	74.76±17.46
Apical	75.71± 6.16	74.10± 8.74	83.81±11.83	75.95± 5.05	75.71± 4.10	77.14±16.20

TABLE 5.7– Global multi-slice evaluation: Classification results using diametral profiles in Wavelet domain by the SVM models.

	SVM Linear			SVM RBF		
	Acc	Sens	Spec	Acc	Sens	Spec
Basal	93.65± 4.05	93.05± 5.35	96.67± 3.98	80.63±23.34	85.24±32.22	57.62±38.41
Medial	95.48± 1.96	97.14± 1.39	87.14±13.53	81.35±13.77	85.90±20.68	58.57±53.49
Apical	87.14± 3.35	90.10± 7.72	72.38±24.61	84.52± 2.66	97.43± 5.75	70.00±44.72

Wavelet domain turns out to be the best space where the original feature yields the highest classification rate followed, in order, by Gray level domain, Curvelet and Fourier domains. As we can see, the best classification results is achieved where Linear Kernel SVM is used in the Wavelet domain with an accuracy of 95.48%, a sensitivity of 97.14% and a specificity of 87.14% in the mid-cavity plane.

TABLE 5.8– Global multislice evaluation: Classification results using diametral profiles in Curvelet domain by the SVM models.

	SVM Linear			SVM RBF		
	Acc	Sens	Spec	Acc	Sens	Spec
Basal	90.71± 5.25	91.71± 5.41	85.71±15.79	89.05± 6.35	94.95± 7.28	59.52±38.80
Medial	90.95± 5.35	91.14± 6.72	90.00± 9.58	82.30±10.71	84.00±13.89	73.81±19.56
Apical	77.78± 5.39	78.10±11.46	76.19±40.44	75.79± 6.27	76.29± 8.19	73.33±12.53

TABLE 5.9– Global multi-slice evaluation: Classification results using diametral profiles in Fourier domain by the SVM models.

	SVM Linear			SVM RBF		
	Acc	Sens	Spec	Acc	Sens	Spec
Basal	72.38± 8.96	73.52±13.36	66.67±36.54	83.41± 5.99	86.95± 8.46	65.71±16.97
Medial	71.51± 9.92	69.71±14.29	80.48±18.85	81.27± 6.07	83.52± 6.39	70.00± 9.00
Apical	73.57± 3.44	73.14± 4.84	75.71± 5.43	65.16± 8.28	66.57±13.57	58.10±22.94

Sparseness of the SVM models

We are also interesting in finding how many profiles and which are the most relevant for classification purposes, that is, using SVM classifier which data sample are used to define the class separately hyperplane. We found that models obtained with SVM shown a sparseness of 25% in the Linear SVM using Wavelet coefficients, that means that only 25% of the feature vectors are taken as support vectors and are used as relevant vectors for classification according to Equation 2.57. 26%, 52% and 93%, are the sparseness in Gray level, Fourier and Curvelet domain, respectively. When RBF kernel is used, the sparseness of the model are 29%, 90%, 98% and 97% for Wavelet, Gray level, Curvelet and Fourier domain, respectively. Quantitative results show that sparseness of the linear SVM in the Wavelet and Gray level domains are smaller compared to those achieved in the Fourier and Curvelet domain on those achieved with RBF kernel. Upon closer examination of the segments to which belong the profiles selected as support vectors, we can determine the importance of the choice of a particular segment in the task of classification (MANTILLA et al., 2013b). Table 5.10 shows the contribution of each segment using the Linear SVM with Wavelet coefficients.

Figure 5.10 shows in green color, the regions where the linear SVM model takes into account the maximum number of profiles: for basal and mid-cavity plane: InferoLateral to AnteroSeptal segments, and for apical plane: Lateral-Septal segments. The same finding is provided for radial dyssynchrony analysis at the mid-ventricular slice level (DOHI et al., 2005; SADE et al., 2004; SUFFOLETTO et al., 2006), where septal to lateral wall mechanical activation is considered as a major feature of cardiac dyssynchrony.

TABLE 5.10– Global multi-slice evaluation: Percentage of contribution of spatio-temporal profiles in the classification task by the SVM models.

Plane	Segment	Contribution of Support Vectors
Basal	InferoLateral – AnteroSeptal	47.12%
	Inferior - Anterior	22.60%
	InferoSeptal - AnteroLateral	30.28%
Medial	InferoLateral – AnteroSeptal	41.04%
	Inferior - Anterior	22.64%
	InferoSeptal - AnteroLateral	36.32%
Apical	Lateral-Septal	71.55%
	Inferior - Anterior	28.45%

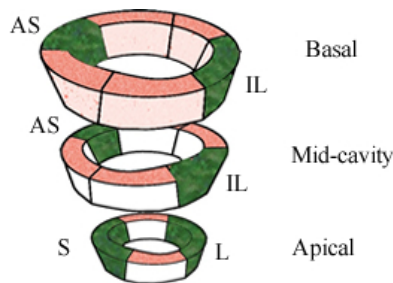


FIGURE 5.10– Relevant regions in the LV where SVM model finds optimal support vectors for classification.

5.4.2 Experiments with discriminative Dictionary Learning methods

We applied the LC-KSVD and the FD-DL classification algorithms with diametral spatio-temporal profiles in the image domain (original domain) as well as the Fourier and Wavelet domains that have been selected from the previous experiments. The DL techniques use an initial dictionary with many atoms as input spatio-temporal profiles. In this case the initial set of input atoms corresponds to the training subset composed of 4 pathological patients and 4 healthy patients randomly selected from the database.

As for the previous experiments, for each patient in the training subset, 18 spatio-temporal profiles are selected to obtain 144 profiles (8 subjects, 18 profiles per subject) where 72 present abnormal motion and the other 72 present normal wall motion. Profiles of the rest of the patients not included in the training stage (10 patients and 2 controls), are selected to test the method. The experiment is performed 50 iterations varying the configuration of training and testing subsets and the average results in terms of accuracy, sensitivity and specificity are calculated.

5.4.2.1 Results with LC-KSVD algorithms

Tables 5.11, 5.12 and 5.13 show the results for the LC-KSVD algorithms (two versions LC-KSVD1 and LC-KSVD2) at the three anatomical planes in Gray level, Wavelet and Fourier

domains respectively.

TABLE 5.11– Global multi-slice evaluation: Classification results using diametral profiles in Gray Level domain by the LC-KSVD algorithms

	LC-KSVD1			LC-KSVD2		
	Acc	Sens	Spec	Acc	Sens	Spec
Basal	87.30 ± 8.17	88.69 ± 9.94	80.33 ± 29.46	87.50 ± 8.10	88.69 ± 9.81	81.56 ± 27.05
Medial	92.43 ± 4.14	91.27 ± 4.94	98.22 ± 2.52	91.69 ± 4.30	90.42 ± 5.17	98.00 ± 2.47
Apical	74.96 ± 7.28	73.51 ± 8.31	82.22 ± 21.11	74.28 ± 6.33	72.51 ± 7.61	83.11 ± 21.52

TABLE 5.12– Global multi-slice evaluation: Classification results using diametral profiles in Wavelet domain by the LC-KSVD algorithms

	LC-KSVD1			LC-KSVD2		
	Acc	Sens	Spec	Acc	Sens	Spec
Basal	95.24 ± 4.00	95.33 ± 3.30	94.76 ± 10.28	95.40 ± 3.84	95.05 ± 3.52	97.14 ± 8.00
Medial	94.37 ± 4.00	95.62 ± 3.30	88.10 ± 10.28	94.44 ± 3.84	95.64 ± 3.52	88.57 ± 8.00
Apical	86.19 ± 4.10	89.81 ± 6.79	68.10 ± 18.90	85.24 ± 5.12	88.48 ± 7.96	69.05 ± 16.13

TABLE 5.13– Global multislice evaluation: Classification results using diametral profiles in Fourier domain by the LC-KSVD algorithms

	LC-KSVD1			LC-KSVD2		
	Acc	Sens	Spec	Acc	Sens	Spec
Basal	51.54 ± 9.45	51.89 ± 11.37	49.78 ± 16.08	88.07 ± 4.98	90.91 ± 6.24	73.89 ± 26.63
Medial	50.13 ± 8.12	49.29 ± 9.43	54.33 ± 15.30	81.17 ± 7.30	80.62 ± 9.44	83.89 ± 17.05
Apical	48.50 ± 9.71	48.84 ± 11.18	46.78 ± 17.36	69.11 ± 8.45	71.27 ± 10.17	58.33 ± 19.53

As we can see, the best performance of classification of the LC-KSVD algorithms is achieved in the Wavelet domain in the three planes. Gray level domain achieves good performance in the mid-cavity plane by the LC-KSVD1 algorithm. The best classification rate is achieved by the LC-KSVD2 algorithm with an accuracy of 95.40% in the basal plane. Fourier domain does not show competitive results of classification (MANTILLA et al., 2013a).

We have evaluated the classification accuracy of the LC-KSVD algorithms by reducing the number of atoms in the dictionary. Figure 5.11 shows the effect in accuracy varying the dictionary size for $K = 36, 72, 122, 137$ and 144 . For this experiment we have chosen the domain where the best accuracy of classification was achieved. In this case we have used the Wavelet domain in the basal plane. However, as we can see in table 5.11, the original domain also yields a good compromise in accuracy, sensitivity, and specificity in medial plane.

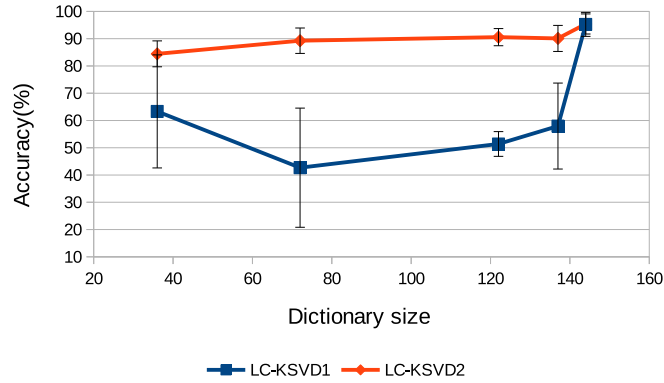


FIGURE 5.11– Accuracy of classification of LC-KSVD algorithms varying the number of dictionary atoms in the Wavelet domain at the basal plane.

Figure 5.11 shows that LC-KSVD2 maintains higher classification accuracy compared to LC-KSVD1 as the dictionary size decreases, highlighting the importance of the classification error in the objective function of DL model.

Sparsity in the LC-KSVD algorithms

Another experiment, and in order to compare the sparseness of the SVM models with the sparsity in the DL models, consists in evaluating the accuracy of classification by reducing the sparsity constraint T . In Figure 5.12 we can see the effect in accuracy varying the sparsity constraint T using spatio-temporal profiles in the Wavelet domain at basal plane, fixing the dictionary size to 144 atoms.

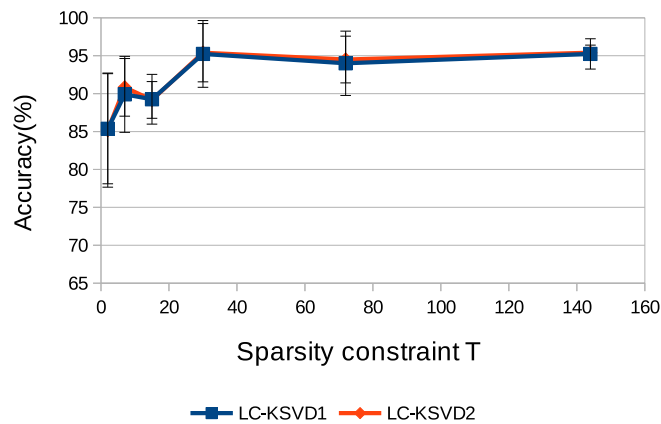


FIGURE 5.12– Accuracy of classification of LC-KSVD algorithms varying the sparsity constraint T in the Wavelet domain at the basal plane.

The Sparsity constraint T in DL models, means that each profile has a sparse representation with no more than T atoms in the Dictionary. We have evaluated the LC-KSVD algorithms using different sparsity constraint values $T = 2, 7, 15, 30, 72$ and 144 , that correspond to 1%, 5%, 10%, 25%, 50% and 100%, respectively, of the number of atoms. Figure 5.12 shows that both, LC-KSVD1 and LC-KSVD2 algorithms maintain a high classification accuracy when T is reduced almost to a value of 30 equivalent to 25% of the number of atoms. This result is similar to the sparseness obtained by the linear SVM using Wavelet coefficients where approximately 25% of the features vectors are taken as support vectors.

5.4.2.2 Results with the FD-DL algorithm

The FD-DL classification algorithm is also applied in the Gray level (image domain) as well as the Fourier and Wavelet domains. Results in terms of accuracy, sensitivity and specificity are shown in Tables 5.14-5.16 obtained with the same configuration of training and testing data employed by the LC-KSVD algorithms and the SVM with random sub-sampling cross validation.

TABLE 5.14– Global multi-slice evaluation: Classification results using diametral profiles in Gray level domain by the FD-DL algorithm

	Acc	Sens	Spec
Basal	83.61± 10.44	81.78 ± 12.24	92.78± 17.23
Medial	91.44± 4.19	89.94 ± 4.93	98.89± 2.68
Apical	71.34± 11.62	70.61 ± 15.48	75.00± 27.56

TABLE 5.15– Global multi-slice evaluation: Classification results using diametral profiles in Wavelet domain by the FD-DL algorithm

	Acc	Sens	Spec
Basal	94.21 ± 4.54	97.81 ± 5.12	76.19 ± 3.93
Medial	96.51 ± 2.59	96.48 ± 2.92	96.67 ± 2.48
Apical	74.10 ± 3.61	77.81 ± 4.80	55.24 ± 21.15

TABLE 5.16– Global multi-slice evaluation: Classification results using diametral profiles in Fourier domain by the FD-DL algorithm

	Acc	Sens	Spec
Basal	89.72 ± 3.33	95.89 ± 5.51	58.89 ± 26.38
Medial	80.60 ± 7.73	81.94 ± 13.38	73.89 ± 34.13
Apical	70.51 ± 16.41	72.61 ± 23.17	60.00 ± 22.46

Results show that, as well as the LC-KSVD algorithm, the best classification rate is achieved also in the Wavelet domain with an accuracy of 96.51%, in this case at the mid-cavity plane. We have evaluated the FD-DL algorithm using different dictionary sizes $K = 14, 22, 36, 72, 122, 137$ and 144 . Figure 5.13 shows that FD-DL algorithm is sensible to the number of atoms in the dictionary, decreasing in accuracy when the dictionary size reduces its number of atoms. However, the FD-DL algorithm yields decent results for a small dictionary.

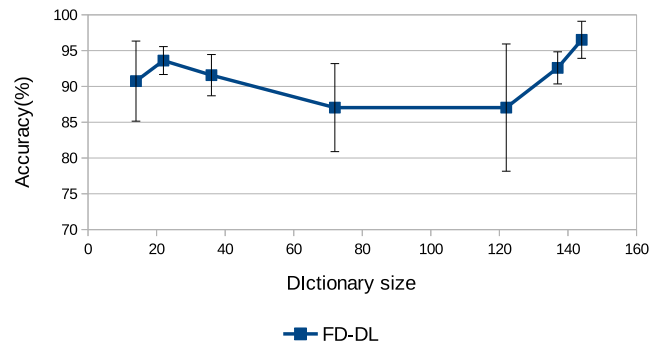


FIGURE 5.13– Accuracy of classification of the FD-DL algorithm varying the Dictionary size in the Wavelet domain at the mid-cavity plane.

Sparsity in the FD-DL algorithm

We have also evaluated the accuracy of classification by reducing the sparsity constraint λ_1 . The sparsity constraint λ_1 in the FD-DL model, is the regularization parameter whose value governs the sparsity of the solution. In Figure 5.14, we can see the effect in accuracy varying the sparsity constraint for $\lambda_1 = 0.001, 0.001, 0.01, 0.1, 1, 10$ and 100 in the Wavelet domain at the mid-cavity plane. Results show that FD-DL algorithm maintains a high classification accuracy when the sparsity constraint takes small values i.e $\lambda_1 \leq 1$, which reinforces the fact of the sparseness assumption on spatio-temporal profiles in the wavelet domain.

5.4.3 Comparison of algorithms

For comparison purposes, Figure 5.15 shows bar plots of the overall average performance of accuracy obtained at each slice level for the proposed machine learning techniques over 50 randomly configurations for training and testing subsets. All the techniques uses the same training and testing inputs.

Wavelet domain turns out to be the best space where the original feature yields the highest accuracy and sensitivity of classification in all the techniques. This can be due to the implicit denoising that is involved during the Wavelet transform that make the classification more accurate. The Gray level and Fourier representation are classified second and third respectively. In terms of specificity, Gray level domain overcomes the Wavelet domain in mid-cavity and apical planes.

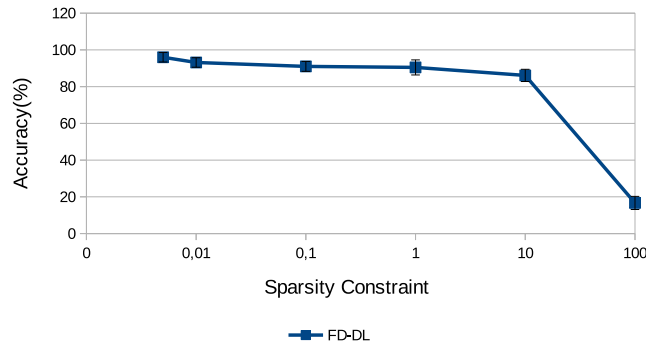


FIGURE 5.14— Accuracy of classification of the FD-DL algorithm varying the sparsity constraint λ_1 in the Wavelet domain at the mid-cavity plane.

The best performance for classification of abnormal and normal LV wall motion using diametral spatio-temporal profiles, is achieved in the Wavelet domain with a FD-DL classifier that reach 96.51% for accuracy, 96.48% for sensitivity and 96.67% for specificity, obtained at the mid-ventricular slice level. At the same level, SVM is placed as the second classifier with high classification rate: 95.48% of accuracy, followed by the LC-KSVD technique with an accuracy of 94.37%: both classifiers using the representation of diametral profiles in the wavelet domain.

These results are consistent with those found in (SUINESIAPUTRA et al., 2009) and (PUNITHAKUMAR et al., 2010) due to the fact that wall motion in the mid-ventricular level is well defined and more stable compared to basal and apical levels. LC-KSVD2 shows the highest rate of classification at basal slice, 1% over the other classification methods tested in this slice these experiments with an accuracy of 95.40%.

According to the specific goal of the Global non-parametric multi-slice evaluation, we can conclude that among the short axis planes, it is in the mid-cavity slice that the best performance of classification of LV wall motion is achieved by most of the machine learning techniques. The next evaluation stage performs the classification of LV wall motion in this short-axis plane by considering radial profiles with more control subjects. However, to allow an analysis of comparable results in the next stage of evaluation, we have chosen to select a reduced number of patients. The selected patients correspond to those with radial strain information provided by the 2D-STE study. The next experiments are performed, firstly, by not taking into account this information and secondly, by taking into account the local strain information. Experiments are performed only in Gray level (original) and Wavelet domains that are the space domains where classification is more accurate according to the previous experiments.

5.5 Global non-parametric LV mid-cavity evaluation

The global non-parametric mid-cavity evaluation was performed using the global status of the subject: Normal/Pathologic, as the label of diametral and radial spatio-temporal profiles

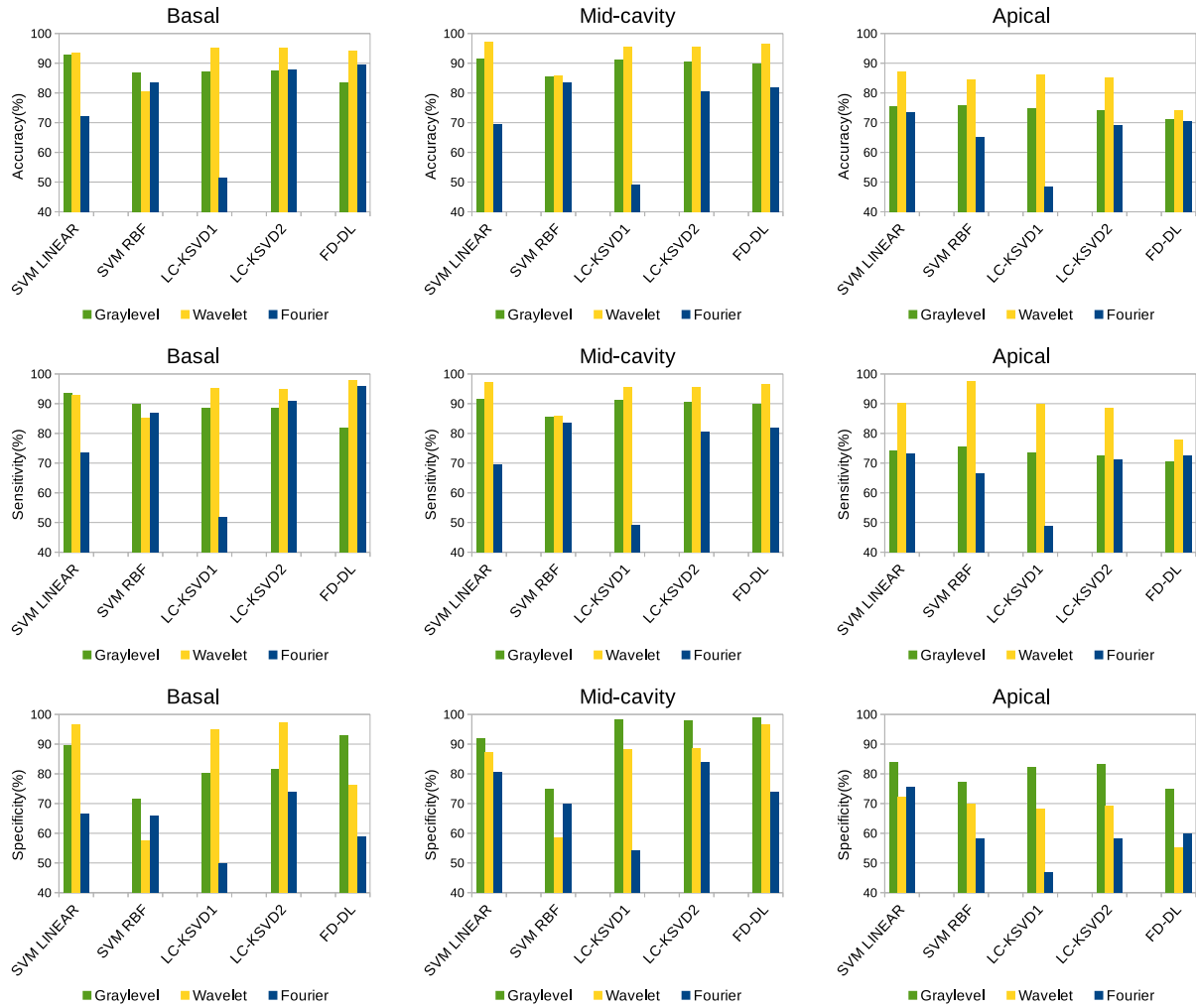


FIGURE 5.15– From top to bottom: Accuracy, Sensitivity and Specificity of the machine learning techniques using diametral profiles in Wavelet, Gray level and Fourier domains at the three LV anatomical planes. Comparisons among SVM, LC-KSVD and FD-DL approaches.

extracted in the mid-cavity short axis plane:

Specific goal: To compare performance of LV wall motion classification between diametral and radial spatio-temporal profiles at the mid-cavity short axis plane without taking into account strain information provided by the 2D-STE.

Population: The short-axis cine-MRI database used in these experiments comprises 18 cases identified in two classes: 1) patients with abnormal LV motion corresponding to 9 patients with cardiac dyssynchrony and for which we have the radial strain tracings at the mid-ventricular slice level obtained by 2D-STE and 2) patients with normal LV motion samples that correspond to 9 healthy subjects from the Cardiac Atlas Project (CAP) database.

Here, the global status of the subject is used to label the profiles. We select this population for further comparisons between taking or not the information of strain provided by the

2D-STE study. The goal is to evaluate the impact that the information of the radial strain has over the final classification of LV wall motion.

Input data: In summary, for each subject 36 radial spatio-temporal profiles and 18 diametral spatio-temporal profiles were extracted, thus, we have: i) a total of 324 diametral profiles, 162 considered as abnormal (9 patients, 18 profiles per patient) and 162 considered as normal (9 control, 18 profiles per subject), and ii) a total of 648 radial profiles, 324 considered as abnormal (9 patients, 36 profiles per patient) and 324 considered as normal (9 control, 36 profiles per subject).

Space domain representation: Experiments were performed using both the diametral and radio spatio-temporal profiles in the original domain (Gray level), as well as, the Wavelet domain.

5.5.1 Results using diametral Spatio-temporal profiles

5.5.1.1 Experiments with SVM: Leave-one-out LOO cross validation

Experiments are performed at short-axis mid-cavity slice with a SVM based classifier constructed using two kinds of kernel functions: Linear and Gaussian Radial Basis Function (RBF). Average results of LOO cross validation are shown in Table 5.17.

TABLE 5.17– Global mid-cavity evaluation: LOO results of classification using diametral profiles in Gray level and Wavelet domain by the SVM models

Classifier	Gray level			Wavelet		
	Accuracy	Sensitivity	Specificity	Accuracy	Sensitivity	Specificity
SVM linear	92.59 ± 15.82	91.97 ± 16.22	93.20 ± 16.38	93.82 ± 10.92	93.82 ± 10.91	93.82 ± 11.60
SVM RBF	92.90 ± 10.40	90.12 ± 13.25	95.67 ± 6.07	91.97 ± 12.81	90.12 ± 15.15	93.82 ± 10.55

Results show that Wavelet domain is still the space domain where classification is more accurate, more precisely, by using a linear SVM the obtained accuracy is of 93.82%. In the Gray level domain, both kernels (linear and RBF) achieves similar performance. Results of the best performance are presented in the partial bull’s eye plots (only mid-cavity plane) shown in Fig. 5.16 for the 9 pathological patients and the 9 control subjects (CAP1 to CAP9). Segment colors are determined using the majority voting rule over the set of 6 diametral profiles selected per segment.

Comparing the bull-eye’s plots with the ground truth in Table 5.4, we can see that the linear SVM classifier can not take a decision only in two opposite segments in two patients: IMOP0 and CAP2 since three profiles yielded abnormal and three yielded normal behavior. The rest of anatomical segments are accurately classified following the criterium of global status (patient status) of the subjects as the label of the diametral spatio-temporal profiles (all normal from control subjects and all abnormal form patients). However, comparing these results with the reference truth show in the bull-eyes in Figure 5.5, the use of diametral profiles is limited to

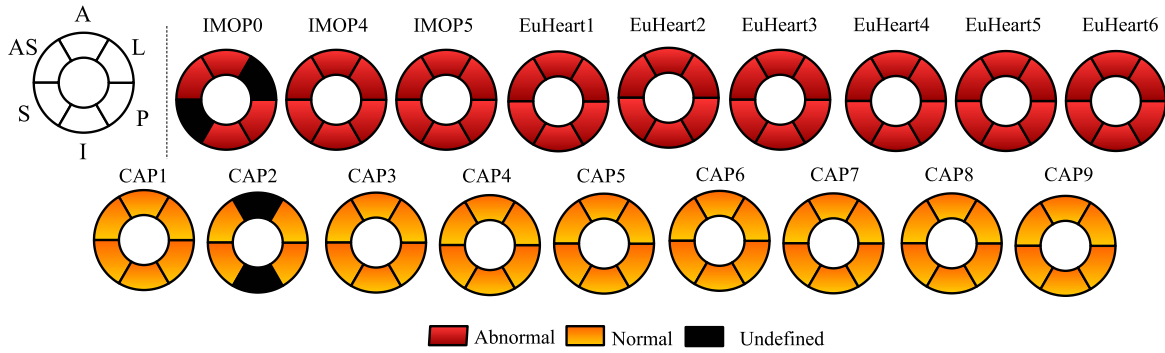


FIGURE 5.16– Global evaluation: Bull's eyes results with LOO cross validation using Linear kernel with diametral profiles in Wavelet domain

detect local regions of normal motion in patients. In fact, the SVM classifier has not well detected any of the segments with normal motion in patients.

5.5.1.2 Experiments with SVM and DL: Random sub-sampling cross validation

To evaluate the generalization capability of the proposed approach with respect to accuracy, sensitivity, and specificity, we take several subsets of samples from the original database. Each subset is composed of training and testing groups. Most specifically, we take randomly 75% of the diametral spatio-temporal profiles cataloged as abnormal to conform one half of the training group. The other half has the same number taken randomly from the group of normal profiles. In summary, the training group has 240 profiles (120 abnormal and 120 normal). The rest of profiles (84 profiles, 42 normal and 42 abnormal) that are not taken in the training stage are selected to test the methods. We repeat this procedure during 50 iterations. Then, we calculate the average of classification in terms of accuracy, sensitivity and specificity. We apply the SVM techniques and the LC-KSVD and FD-DL classification algorithms in the image domain as well as the Wavelet domain with the same input training and testing data. Results are shown in Table 5.18.

TABLE 5.18– Global evaluation: Results of classification using diametral profiles in Gray level and Wavelet domain by the SVM models and DL algorithms

Classifier	Gray level			Wavelet		
	Accuracy	Sensitivity	Specificity	Accuracy	Sensitivity	Specificity
SVM linear	91.19 ± 6.46	91.06 ± 11.81	91.33 ± 9.94	91.22 ± 6.95	90.44 ± 11.22	92.00 ± 8.36
SVM RBF	89.03 ± 5.62	88.83 ± 7.96	89.22 ± 8.77	90.28 ± 5.53	86.06 ± 9.25	94.50 ± 6.56
LC-KSVD 1	93.94 ± 4.56	93.39 ± 6.37	94.50 ± 6.10	92.14 ± 6.06	90.06 ± 8.45	94.22 ± 6.86
LC-KSVD 2	93.78 ± 4.63	92.44 ± 7.32	95.11 ± 5.23	91.22 ± 6.17	87.94 ± 9.58	94.50 ± 6.40
FD-DL	92.36 ± 5.65	91.39 ± 7.54	93.33 ± 7.21	90.58 ± 7.74	91.17 ± 11.01	90.00 ± 9.81

Results show that both versions of the LC-KSVD algorithm achieve the higher performance

in the Gray level domain, with an accuracy about 94%, approximately 2% over the performance achieved by the FD-DL algorithm. The accuracy obtained by the SVM models in the Gray level domain is always below than the one achieved by the DL techniques. In the Wavelet domain, the LC-KSVD1 algorithm achieves the highest performance, approximately 1% over the performance obtained by the other techniques.

Even when results obtained with a global evaluation are competitive, the use of diametral profiles by the classifiers is still limited to detect local regions of normal motion in patients. Next, we perform the same level of evaluation by using radial profiles.

5.5.2 Results using radial spatio-temporal profiles

5.5.2.1 Experiments with SVM: Leave-one-out LOO cross validation

As with diametral profiles, we train with the spatio-temporal profiles of 17 patients and test with the profiles of the single patient left out, the process is repeated until each patient passed through the testing phase. Experiments are performed with a SVM based classifier constructed using two kinds of kernel functions: Linear and in Radial Basis Function (RBF) with radial profiles in the image domain (original) as well as the Wavelet domain. Average results of LOO cross validation are shown in Table 5.19.

TABLE 5.19– Global mid-cavity evaluation: LOO results of classification using radial profiles in Gray level and Wavelet domain by the SVM models

Classifier	Gray level			Wavelet		
	Accuracy	Sensitivity	Specificity	Accuracy	Sensitivity	Specificity
SVM linear	80.40 ± 20.33	78.06 ± 25.13	82.71 ± 15.32	85.49 ± 12.11	82.71 ± 15.01	88.27 ± 8.30
SVM RBF	76.23 ± 16.17	70.98 ± 16.78	81.48 ± 14.56	73.91 ± 18.64	67.58 ± 21.14	80.55 ± 13.88

Like diametral profiles LOO results, the Wavelet domain remains the space domain where classification is more accurate achieving an accuracy of 85.49% with linear SVM. However, these results are low compared to previous results obtained with diametral profiles. In the Gray level domain, linear kernel overcomes RBF kernel. Results of the best performance (linear kernel with Wavelet domain) are presented in the partial bull’s eye plots (only mid-cavity plane) shown in Fig. 5.17.

As we can see in the bull-eye’s plots, the linear SVM classifier can not take a decision in 12 anatomical segments in all the population. Furthermore, 4 of the anatomical segments in the healthy population are cataloged as abnormal. The classifier failed in the identification of several anatomical segments in the pathological group. Comparing these results with the reference truth shown in the bull-eyes in Figure 5.5, we can see that the classifier has well identified only two normal anatomical segments in the patient IMOP5 and one in the patient EuHeart5. However it has failed in more segments of patients assigning a normal label when the original region is abnormal, specifically a total of six segments.

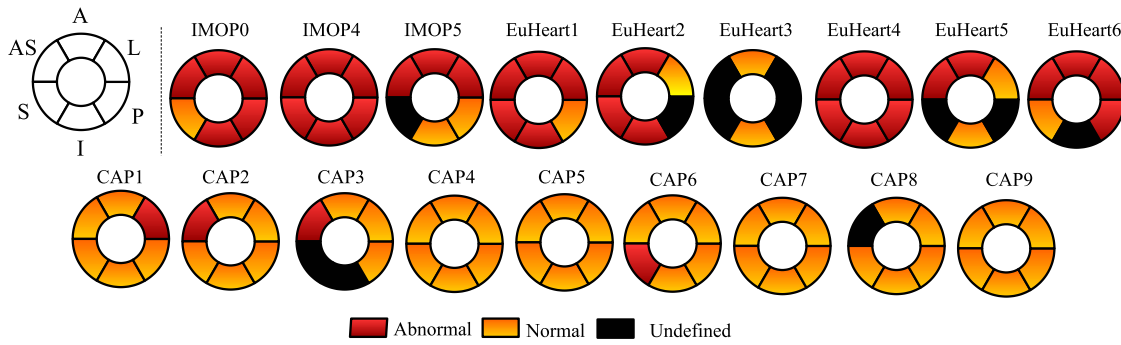


FIGURE 5.17– Global evaluation: Bull’s eyes results with LOO cross validation using Linear kernel with radial profiles in Wavelet domain

5.5.2.2 Experiments with SVM and DL: Random sub-sampling cross validation

Similar with the experiments using diametral profiles, we take randomly 75% of the radial spatio-temporal profiles cataloged as abnormal to conform one half of the training group. The other half has the same number taken randomly from the group of normal profiles. In summary, the training group has 480 profiles (240 abnormal and 240 normal). The rest of profiles (168 profiles, 84 normal and 84 abnormal) that are not taken in the training stage are selected to test the methods.

We repeat this procedure during 50 iterations. We then calculate the average of classification in terms of accuracy, sensitivity and specificity. Results are shown in table 5.20 for the linear and RBF kernels and the DL algorithms using profiles in Gray level and Wavelet domains.

TABLE 5.20– Global evaluation: Results of classification using radial profiles in Gray level and Wavelet domain by the SVM and DL models

Classifier	Gray level			Wavelet		
	Accuracy	Sensitivity	Specificity	Accuracy	Sensitivity	Specificity
linear	94.36 ± 1.56	93.25 ± 2.03	95.47 ± 2.28	96.37 ± 0.81	95.73 ± 2.28	97.01 ± 1.98
RBF	87.74 ± 11.91	75.98 ± 24.18	99.49 ± 1.08	96.45 ± 1.48	93.68 ± 2.85	99.23 ± 0.63
LC-KSVD 1	96.20 ± 0.84	95.04 ± 1.75	97.35 ± 1.82	96.24 ± 1.17	95.73 ± 2.21	96.75 ± 1.44
LC-KSVD 2	95.98 ± 0.81	94.79 ± 1.73	97.18 ± 1.89	96.32 ± 1.29	95.64 ± 2.40	97.01 ± 1.16
FD-DL	97.05 ± 1.25	95.21 ± 2.36	98.89 ± 1.07	95.77 ± 1.20	93.16 ± 2.28	98.38 ± 1.10

As we can see, the accuracy of the SVM methods and the LC-KSVD algorithms is higher than with diametral profiles using the representation of the radial profiles in the Wavelet domain with an accuracy about 96%. Results show that FD-DL algorithm improves the performance of classification compared to the other techniques in the Gray level domain. The highest accuracy achieved by the FD-DL technique is 97.05% using radial spatio-temporal profiles in the Gray level domain.

5.5.3 Comparison of algorithms

For comparison purposes, Figure 5.18 shows bar plots of the overall average performance of accuracy, sensitivity and specificity obtained at the mid-cavity short axis slice for the proposed machine learning techniques.

Results are obtained over 50 randomly configurations for training and testing subsets using diametral and radial spatio-temporal profiles with the global status of the subject as label of the spatio-temporal profiles. The same training and testing input data is taken by all the techniques according the non-parametric representation: radial or diametral.

As can be seen, in Gray level domain the higher classification accuracy is achieved with diametral profiles, i.e., by the LC-KSVD1 algorithm. In a similar way, in Gray level domain with radial profiles the best accuracy of classification is achieved by the FD-DL algorithm with 97.05% of accuracy, 95.21% of sensitivity and 98.89% of specificity.

Overall classification accuracy using radial profiles is higher than the classification accuracy obtained using diametral profiles.

According to the specific goal of the Global non-parametric mid-cavity evaluation, we can conclude that the use of radial profiles overcomes the classification performance given by diametral profiles in the mid-cavity short axis plane. Moreover, dictionary learning techniques are more homogeneous in terms of accuracy, sensitivity and specificity than the SVM models. For instance low values of sensitivity in the Gray level domain are observed with a RBF kernel.

These results have to be used with prudence, considering that a global evaluation can bias the results. They will be compared to the results obtained with a local evaluation in the next sections.

5.6 Local non-parametric LV mid-cavity evaluation

The Local non-parametric mid-cavity evaluation was performed using the information of local strain provided by the 2D-STE study, as the label of diametral and radial spatio-temporal profiles extracted in the mid-cavity short axis plane:

Specific goal: To compare results of LV wall motion classification between diametral and radial spatio-temporal profiles taking account strain information provided by the 2D-STE and to compare the previous results obtained using global evaluation.

Population: The short-axis, cine-MRI database used in these experiments comprises the same population used in in the Global non-parametric mid-cavity evaluation: 18 cases identified in two classes: 1) patients with abnormal LV motion samples corresponding to 9 patients with cardiac dyssynchrony and for which we have the radial strain tracings at the mid-ventricular slice level obtained by 2D-STE and 2) patients with normal LV motion samples that correspond to 9 healthy subjects. In the group of pathological patients in some cases, only certain segments present abnormal movement which is in accordance with the 2D-STE study.

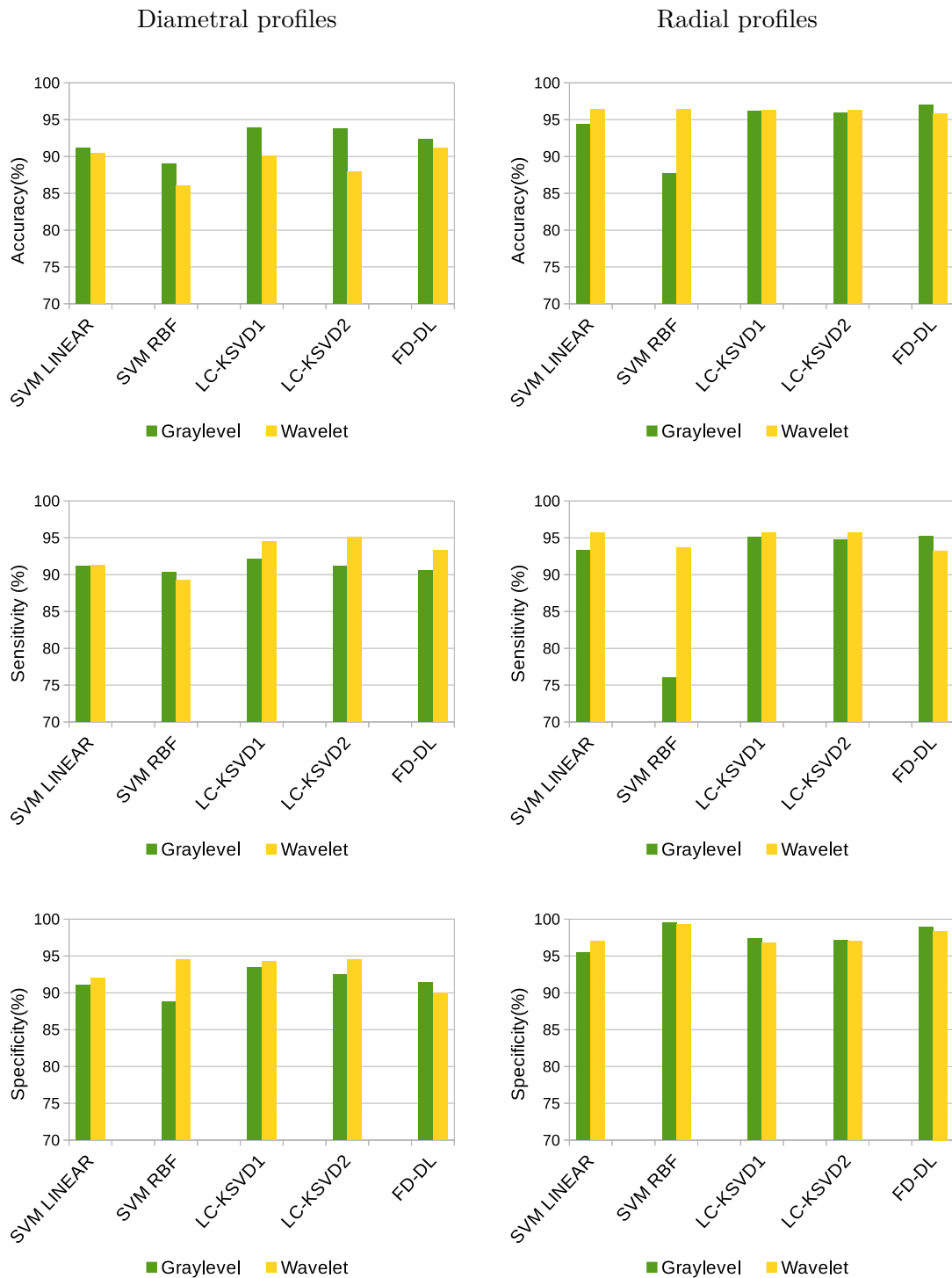


FIGURE 5.18– From top to bottom: Accuracy, Sensitivity and Specificity of the machine learning techniques (diametral profiles vs. radial profiles) in Wavelet and Gray level domains at the mid-cavity short axis plane. Comparisons between SVM, LC-KSVD and FD-DL approaches.

Input data: In summary, for each subject 36 radial spatio-temporal profiles and 18 diametral spatio-temporal profiles were extracted, thus, we have:

A total of 324 diametral profiles from the 18 subjects in study: 162 considered as abnormal (9 patients, 18 profiles per patient) and 162 considered as normal (9 control, 18 profiles per subject). We base our analysis after grouping two opposite segments and evaluate if both or them are normal to be considered as a normal diametral profile, or if almost one of them is abnormal to be considered as abnormal diametral profile.

This assessment is based on the information given in Table 5.4. This criteria shows that for this database, the local assessment given by 2D-STE over diametral profiles coincides with the global evaluation taking the global status of the subject as ground truth to label the diametral profiles.

Based on the information given in Table 5.3, a total of 648 radial profiles, 276 considered as abnormal and 372 considered as normal, are identified in the population. Table 5.21 resumes the number of radial spatio-temporal profiles assessed by 2D-STE.

TABLE 5.21– Total number of Radial Spatio-temporal profiles in the database

	Assessment by 2D-STE	
	Abnormal	Normal
Pathological patients	276	48
Control Group	0	324
Total	276	372

Space domain representation: Experiments were performed using the radial spatio-temporal profiles in the original domain (Gray levels), as well as, the Wavelet domain. As the local assessment given by 2D-STE over diametral profiles coincides with the global evaluation taking the global status of the subject as ground truth to label the diametral profiles, then, results in local evaluation using diametral profiles are the same to those obtained in the global evaluation presented in section 5.5.1 (Tables 5.17 and 5.18).

Thus, experiments in this section are based only in radial spatio-temporal profiles and will be compared to those presented in section 5.5.2. The goal is to find the technique that achieves the best compromise in accuracy, sensitivity and specificity and at the same time has low complexity and reduced computing times.

5.6.1 Experiments with SVM: Leave One Out LOO cross validation

Experiments are performed at short-axis mid-cavity slice level with a SVM based classifier constructed using two kinds of kernel functions: Linear and RBF. Similar to diametral profiles, we perform the LOO patient cross validation using radial profiles. In this particular case, we train with the profiles of 17 patients and test with the profiles of the single patient left out, the process is repeated until each of the patients passed through the testing phase. Experiments are performed with radial profiles in the image domain (original) as well as the Wavelet domain. Average results of LOO cross validation are shown in Table 5.22.

TABLE 5.22– Local mid-cavity evaluation: LOO results of classification using radial profiles in Gray level and Wavelet domain by the SVM models

Classifier	Gray level			Wavelet		
	Accuracy	Sensitivity	Specificity	Accuracy	Sensitivity	Specificity
SVM linear	67.63 ± 27.05	86.11 ± 11.19	59.78 ± 32.71	74.32 ± 20.86	71.54 ± 33.10	66.54 ± 24.70
SVM RBF	72.38 ± 25.45	88.88 ± 13.24	69.59 ± 33.78	69.52 ± 23.72	76.08 ± 27.44	68.20 ± 23.77

The Wavelet domain is the space domain where classification is more accurate i.e., using a linear SVM with an accuracy of 74.32%. In the Gray level domain, RBF kernel overcomes linear kernel in accuracy. Results of the best performance (linear kernel with Wavelet domain) are presented in the partial bull’s eye plots (only mid-cavity plane) shown in Figure 5.19.

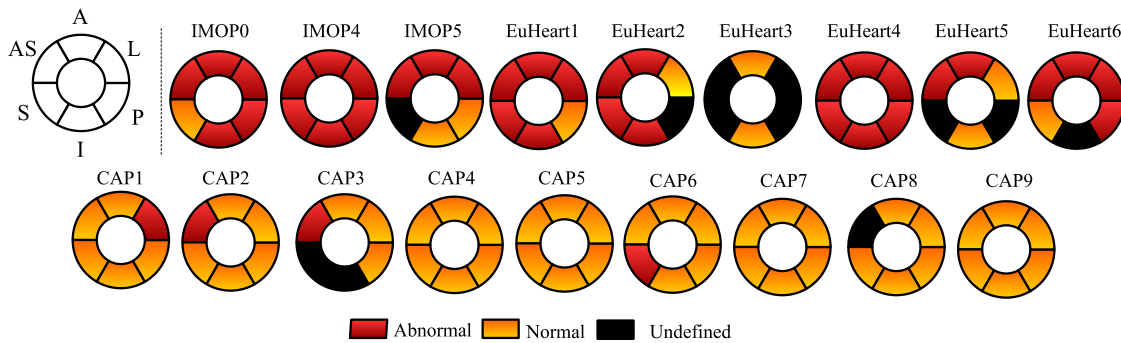


FIGURE 5.19– Local evaluation: Bull’s eyes results with LOO cross validation using Linear kernel with radial profiles in Wavelet domain

As we can see in the bull-eye’s plots, the linear SVM classifier can not take a decision in 3 anatomical segments in patients EuHeart2, EuHeart5 and EuHeart6. Comparing these results with the reference truth shown in the bull-eyes in Figure 5.5, we can see that the classifier has well identified normal segments in patients IMOP6, EuHeart 4 and EuHeart 5; partially in patient EuHeart6, but has not well identified 3 of the anatomical segments in the healthy population that were cataloged as abnormal (MANTILLA et al., 2015c).

5.6.2 Experiments with SVM and DL: Random sub-sampling cross validation

In order to evaluate the generalization capability of the classifier, we apply approximatively the same process than in 5.5.2.2: we take several subsets of samples from the original database. Each subset is composed of training and test groups, specifically we take randomly 75% of the radial spatio-temporal profiles cataloged as abnormal to conform one half of the training group. The other half has the same number taken randomly from the group of normal profiles. In summary, the training group has 414 profiles (207 abnormal and 207 normal). The rest

of profiles not taken in the training stage are selected to test the methods. We repeat this procedure during 50 iterations, after that, we calculate the average of classification in terms of accuracy, sensitivity and specificity. We apply the SVM techniques, the LC-KSVD and the FD-DL algorithms using radial spatio-temporal profiles in both the original and the Wavelet domains. Results are presented in table 5.23.

TABLE 5.23– Local mid-cavity evaluation: Results of classification using radial profiles in Gray level and Wavelet domain by the SVM and DL models

Classifier	Gray level			Wavelet		
	Accuracy	Sensitivity	Specificity	Accuracy	Sensitivity	Specificity
linear	88.46 ± 1.54	86.96 ± 5.02	89.09 ± 2.76	88.78 ± 2.27	88.62 ± 4.37	88.85 ± 3.39
RBF	91.88 ± 1.99	92.75 ± 3.01	91.52 ± 2.96	91.20 ± 1.45	92.10 ± 3.03	90.82 ± 2.31
LC-KSVD 1	90.24 ± 2.07	90.22 ± 4.84	90.24 ± 2.22	92.61 ± 2.15	93.48 ± 2.76	92.24 ± 2.58
LC-KSVD 2	91.94 ± 1.35	91.88 ± 3.74	91.97 ± 1.75	92.31 ± 1.93	93.12 ± 2.70	91.97 ± 2.45
FD-DL	92.81 ± 1.67	88.33 ± 5.10	94.68 ± 2.29	91.41 ± 2.44	83.44 ± 11.69	94.74 ± 3.31

Results show that best classification is achieved by the FD-DL algorithm in the original domain with an accuracy of 92.81%, a sensitivity of 88.33% and a specificity of 94.68%. The best classification rate by the LC-KSVD algorithm with an accuracy about 92.61% is achieved in the Wavelet domain, very close to the results obtained by the FD-DL algorithm in the original domain. Concerning SVM models, the RBF kernel achieves high rate of classification, 91.88% of accuracy in the gray level domain. The highest specificity is yielded in the Wavelet domain by the FD-DL algorithm.

We have evaluated the classification accuracy of the LC-KSVD and FD-DL algorithms by reducing the number of atoms in the dictionary. For these experiments we choose the Wavelet domain.

We have evaluated the LC-KSVD algorithms using different dictionary sizes $K = 4, 21, 42, 104, 207, 312, 373$ and 414. Figure 5.20 shows that LC-KSVD2 maintains again higher classification accuracy compared to LC-KSVD1, highlighting the importance of the classification error term ($\|\mathbf{H} - \mathbf{W}\mathbf{X}\|_2^2$) in the objective function of the discriminative DL model.

We evaluate the FD-DL algorithm using different dictionary sizes $K = 4, 21, 42, 104, 207, 312, 373$ and 414. Figure 5.21 shows that FD-DL algorithm maintains high accuracy when the number of atoms in the dictionary is decreased almost to one half of the initial dictionary size.

Sparseness in the SVM models and Sparsity in DL algorithms

Table 5.24 shows the number of support vectors (SV) founded by each model.

We have evaluated the LC-KSVD algorithms using different sparsity constraint values $T = 2, 4, 8, 15, 24, 30, 50, 105, 207,$ and 414 in the Wavelet domain. Figure 5.22 shows that both, LC-KSVD1 and LC-KSVD2 algorithms achieve a high classification accuracy when T is reduced almost to a value of 15.

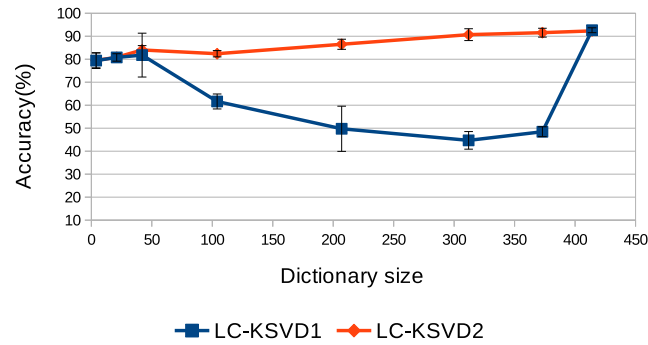


FIGURE 5.20– Accuracy of classification of LC-KSVD algorithms varying the number of dictionary atoms using radial profiles.

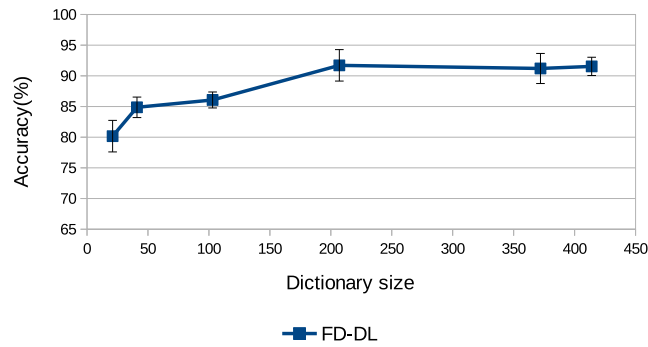


FIGURE 5.21– Accuracy of classification of FD-DL algorithm varying the number of dictionary atoms using radial profiles.

TABLE 5.24– Local mid-cavity evaluation: Number of Support vectors obtained using radial profiles in Gray level and Wavelet domain by the SVM models

Classifier	Gray level	Wavelet
Linear SVM	243	248
RBF SVM	301	286

We have evaluated the FD-DL algorithm using different sparsity constraint values $\lambda_1 = 0.001, 0.001, 0.01, 0.1, 1, 10$ and 100 in the Gray level domain. Figure 5.23 shows that this technique achieves a high classification accuracy when the sparsity constraint takes small values i.e $\lambda_1 \leq 0.05$.

Comparing the sparseness in SVM models with sparsity in DL techniques, we can conclude that the complexity is higher in SVM models since they need enough support vectors, about more than 50% of the initial input vectors to construct the hyperplane of separation between

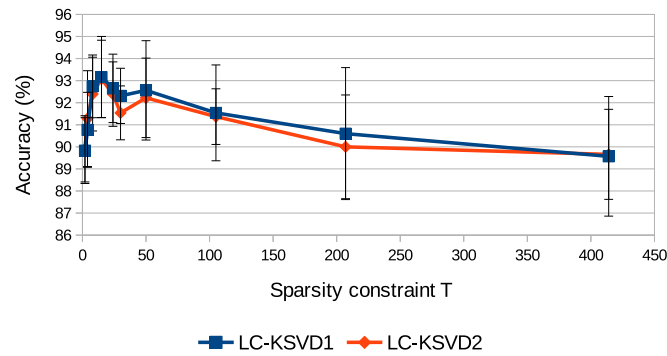


FIGURE 5.22– Accuracy of classification of LC-KSVD algorithms varying the sparsity constraint T using radial profiles.

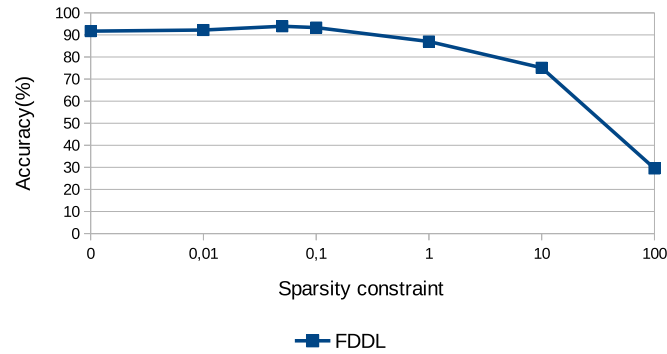


FIGURE 5.23– Accuracy of classification of the FD-DL algorithm varying the sparsity constraint λ_1 using radial profiles

normal and abnormal profiles. Opposite, the LC-KSVD algorithms employ approximately 10% of the dictionary atoms to discriminate between the two classes. This performance is maintained even when the number of atoms is reduced in the initial dictionary e.g., by the LC-KSVD2 algorithm. These results proof that sparsity in DL techniques, gives a good compromise between complexity and accuracy for LV wall motion classification.

5.6.3 Comparison of algorithms

Comparing SVM and DL techniques using radial profiles, Figure 5.24 uses bar plots to summarize the overall average performance in the original and Wavelet domains respectively, for the classification methods over 50 randomly configurations for training and testing subsets.

Results show that the best rate of classification is achieved by the FD-DL technique in the original domain (Gray level domain) with an average of 92.81% of accuracy. This technique carries out the higher specificity in both, original and Wavelet domains. Furthermore, the

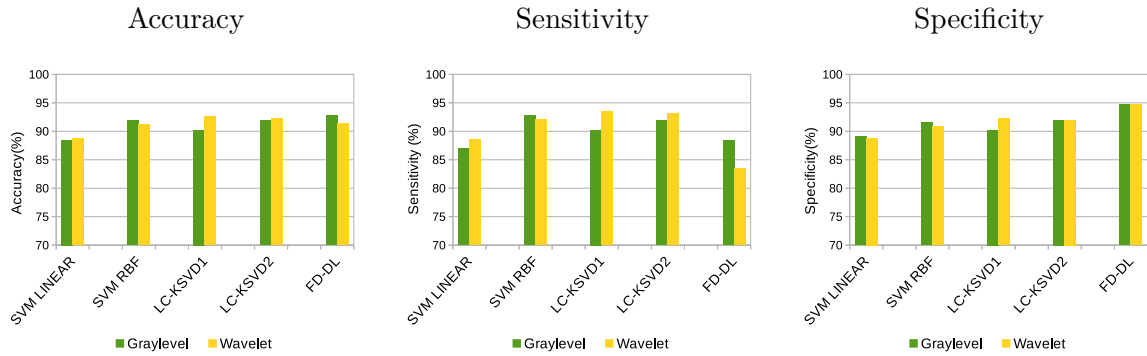


FIGURE 5.24– Local mid-cavity evaluation: Accuracy, Sensitivity and Specificity of the machine learning techniques in Wavelet and Gray level representation using radial spatio-temporal profiles.

obtained classifier in the LC-KSVD technique finds the sparse codes in the Wavelet domain more discriminant for cardiac spatio-temporal profile classification. In terms of sensitivity the higher results are the obtained with LC-KSVD in wavelet domain followed by SVM with a RBF kernel in the gray level domain.

As results, the parameters of the machine learning techniques found as the optimal ones using 5 fold cross-validation were: for Linear SVM, $C = 100$; for RBF SVM, $C = 100$ and $\sigma = 1$. For LC-KSVD1: $\alpha = 16$, for LC-KSVD2 $\alpha = 16$ and $\beta = 4$, and finally for FD-DL: $\lambda_1 = 0.05$ and $\lambda_2 = 0.5$.

To compare local results in bull eyes plots obtained by the SVM techniques using LOO cross validation, the classifier performance of the discriminative DL techniques was also evaluated with a LOO-patient cross validation. Average results of LOO cross validation are shown in Table 5.25 for the LC-KSVD algorithms in the Wavelet and Gray level domains.

TABLE 5.25– Local mid-cavity evaluation: LOO results of classification using radial profiles in Gray level and Wavelet domain by the LC-KSVD algorithms

Classifier	Gray level			Wavelet		
	Accuracy	Sensitivity	Specificity	Accuracy	Sensitivity	Specificity
LC-KSVD1	70.06 ± 16.54	65.83 ± 23.84	77.46 ± 9.25	82.53 ± 15.53	80.77 ± 23.88	87.16 ± 10.18
LC-KSVD2	69.44 ± 17.25	65.83 ± 23.84	76.54 ± 9.32	84.07 ± 15.99	80.77 ± 23.88	89.62 ± 8.21

As can be seen, the best LOO results in terms of accuracy are achieved by the LC-KSVD2 algorithm in the Wavelet domain. Bull-eyes results of LOO-patient cross validation are shown in Figure 5.25 and are the same for the three algorithms: LC-KSVD1, LC-KSVD2 and FD-DL. As we can see in Fig. 5.25, the discriminative DL algorithms are able to detect the normal regions in patients IMOP6, EuHeart4 and EuHeart6 and fail in the identification of normal/abnormal wall motion in one segment in patients IMOP5 and EuHeart5.

It should be noted that the SVM models report low values of specificity with high standard

deviation values resulting in the misclassification of several segments in normal patients. Opposite to SVM, the discriminative DL models achieve high values of specificity with relative small values of standard deviation leading to an accurate classification for all segments in the normal patients.

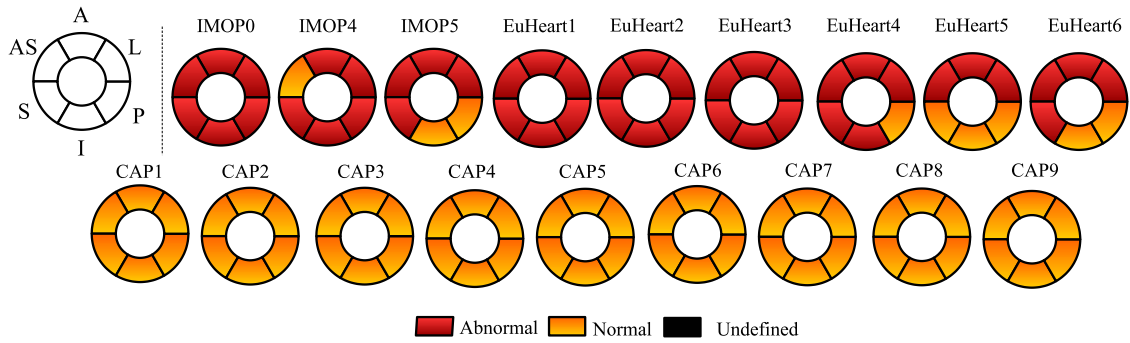


FIGURE 5.25– Local LV wall motion in the study population obtained by the three adapted discriminative DL techniques for LV wall motion classification: LC-KSVD1, LC-KSVD2 and FD-DL.

About computing times, Tables 5.26 and 5.27 shows the time in seconds (mean \pm standard deviation) employed by SVMs and the DL techniques using Gray level and Wavelet coefficients respectively at training and testing stages. Times are calculated using the optimal parameters for each algorithm. DL techniques demand more computational time in training and testing stages than SVM, particularly the FD-DL technique. Furthermore, the difference in training and testing time between SVM and the LC-KSVD techniques is very low (approximately 6 secs for training and 0.02 for testing).

TABLE 5.26– Time employed by the classification techniques in the Original domain

	Learning Time (sec)	Testing time (sec)
SVM linear	6.127 ± 0.757	0.008 ± 0.016
SVM RBF	0.542 ± 0.040	0.034 ± 0.005
LC-KSVD 1	8.355 ± 0.315	0.059 ± 0.003
LC-KSVD 2	8.275 ± 0.333	0.048 ± 0.003
FD-DL	56.034 ± 5.183	1.218 ± 0.114

TABLE 5.27– Time employed by the classification techniques in the Wavelet domain

	Learning Time (sec)	Testing time (sec)
SVM linear	1.090 ± 0.155	0.004 ± 0.001
SVM RBF	1.041 ± 0.182	0.030 ± 0.004
LC-KSVD 1	7.360 ± 0.110	0.051 ± 0.034
LC-KSVD 2	7.340 ± 0.100	0.049 ± 0.001
FD-DL	51.170 ± 2.610	1.170 ± 4.202

Discriminative DL techniques outperforms SVM slightly but with higher computational cost. The three discriminative DL techniques demand more computational time in training and testing stages than SVM, particularly the FD-DL technique. Furthermore, the difference in training and testing time between SVM and the LC-KSVD techniques is very low.

Figure 5.26, illustrates the representation coefficient matrix \mathbf{X} of a subset of the training dataset by the LC-KSVD2 and the FD-DL algorithms in the Wavelet domain. Please note that by FD-DL the coefficient matrix \mathbf{X} of the training dataset is nearly block diagonal, whereas each block is built by samples from the class corresponding to that sub-dictionary exploiting the discrimination given by the Fisher criterion that minimize the intra-class scatter of \mathbf{X} , and maximize the inter-class scatter of \mathbf{X} . In the case of LC-KSVD2 the coefficient matrix of the training dataset has many big non-block diagonal entries since the discrimination is imposed by structural constraints on the dictionary and not in the coefficients. The coefficient matrix by FD-DL is more regular than that by LC-KSVD2, validating the effectiveness of FD-DL in enhancing the discrimination of representation coefficients.

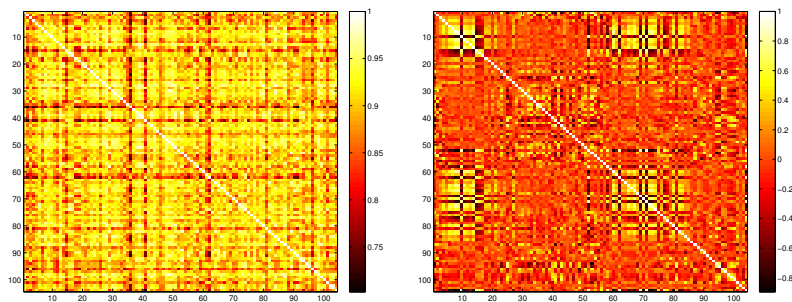


FIGURE 5.26– The representation of the coefficient matrix \mathbf{X} on the training datasets by the LC-KSVD2 (top) and by FD-DL (bottom) algorithms.

According to the specific goal of the Local non-parametric mid-cavity evaluation, we can conclude that the use of radial profiles overcomes the classification performance given by diametral profiles in the mid-cavity short axis plane. The results provide the LC-KSVD2 technique as the best compromise, both in accuracy, sensitivity, and specificity, and complexity in terms of computing time and sparsity i.e., in the Wavelet domain.

5.7 Local parametric LV mid-cavity evaluation

The Local parametric mid-cavity evaluation was performed using the descriptor parameters extracted from the radial spatio-temporal profiles assessed with the information of local strain provided by the 2D-STE study:

Specific goal: To find the parameter or combination of parameters that better contribute to LV wall motion classification.

Population: The short-axis, cine-MRI database used in these experiments comprises the same population used in in the Local non-parametric mid-cavity evaluation: 18 cases identified

in two classes: 1) patients with abnormal LV motion samples corresponding to 9 patients with cardiac dyssynchrony and for which we have the radial strain tracings at the mid-ventricular slice level obtained by 2D-STE and 2) patients with normal LV motion samples that correspond to 9 healthy subjects.

Input data: In summary, for each subject 36 radial spatio-temporal profiles were extracted, thus, we have: a total of 648 radial profiles, 276 considered as abnormal and 372 considered as normal. From these radial profiles the skewness (Sk), Clustering (Cl), Correlation (Co) and Mean transition time (Mt) parameters were extracted.

Space domain representation: Experiments were performed using different combinations of the extracted parameters: the skewness (Sk), Clustering (Cl), Correlation (Co) and Mean transition time (Mt). Specifically, the tested combinations are:

1. Skewness and Clustering: Sk - Cl.
2. Skewness, Clustering and Correlation: Sk - Cl - Co.
3. Skewness and Mean transition time: Sk - Mt.
4. Skewness, Mean transition time and Correlation: Sk - Mt - Co.
5. Skewness, Mean transition time and Clustering: Sk - Mt - Cl.
6. Clustering and Correlation: Cl - Co.
7. Clustering, Correlation and Mean transition time: Cl - Co - Mt.
8. Skewness, Mean transition time, Clustering and Correlation: Sk - Mt - Cl - Co

5.7.1 Parameter analysis

The parameter extraction procedure (cf. section 4.6.3.3) is applied over all the 648 radial profiles described in the input data. Below we present an analysis of the extracted parameters.

5.7.1.1 Average clustered curve (Cl)

Figure 5.27 shows the reference clustered signals per segment in 4 subjects. As we can see, in the case of healthy subjects CAP1 and CAP8, all the maximum peak of signals seem to focus on a single phase in time with a relative small variation, reflecting a synchronous contraction of all segments. At the other hand, for patients, maximum peak of signals appears in different phases or instants reflecting a dyssynchronous contraction among segments. For example in patient IMOP5 septal segments contract lately compared with the other segments.

The same behavior was observed in (KACHENOURA et al., 2007) where the septal wall highlighted an important delay in wall contraction in a patient with left bundle branch block (LBBB).

5.7.1.2 Mean transition time (Mt)

Mean values for the related parameter are calculated from the 108 segments of the database (18 subjects, 6 segments per subject) according the spatial location in the myocardial wall for both

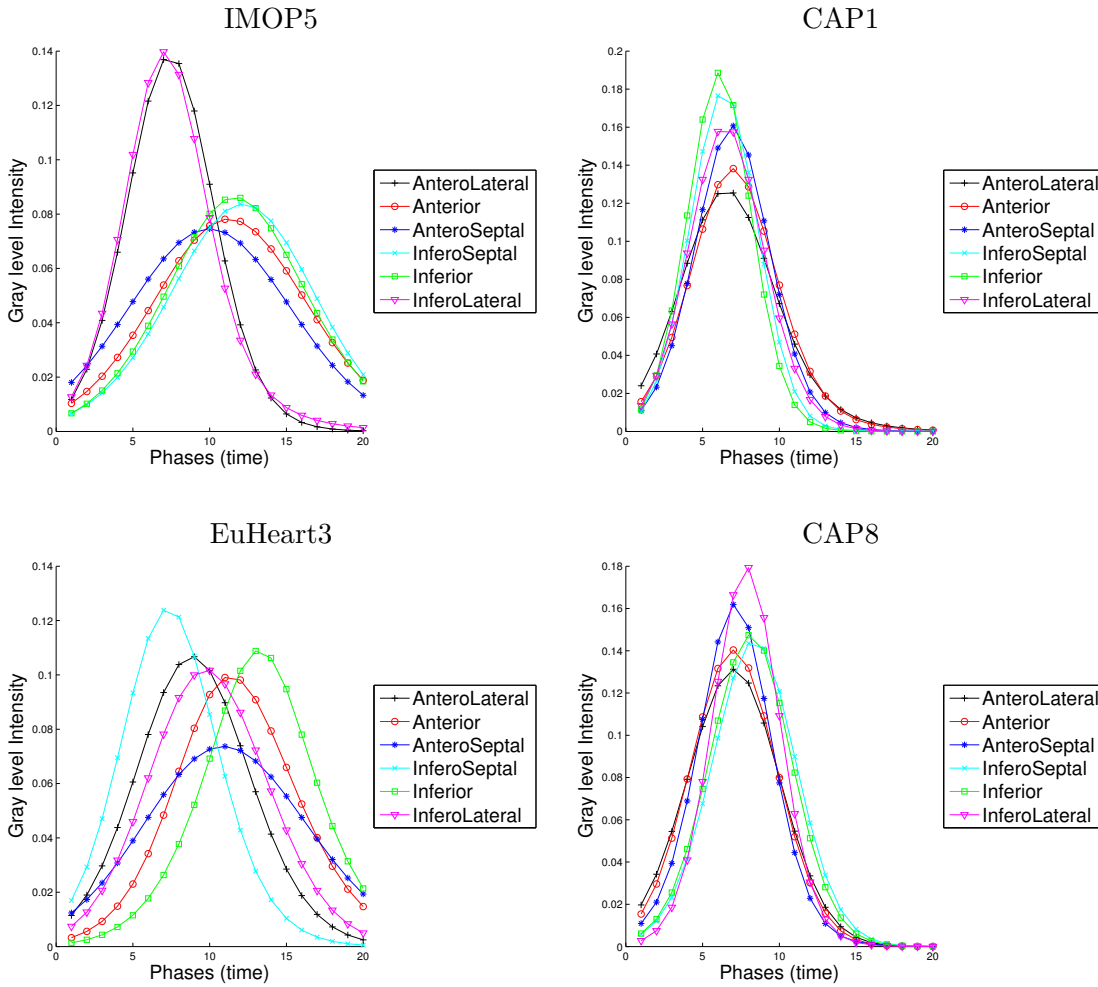


FIGURE 5.27– Clustered reference signal by segments in 4 subjects. Left: Patients IMOP6 and EuHeart3. Right: Control CAP1 and CAP8.

groups and are presented in Table 5.28. Note that the Mean transition time in the septal segments of healthy subjects take highest values, the same observation was noticed in (EL BERBARI et al., 2009). In general Mt values in the pathological group are higher than the ones obtained in the healthy population.

5.7.1.3 Skewness parameter (Sk)

Curve skewness values are shown in Figure 5.28 for both populations in different anatomical segments. Note that inferior values of skewness observed in some segments in the pathological group compared to the control group indicates that the data distribution is left-skewed reflecting late regional LV contraction. Positive skewness would indicate that the data distribution is right-skewed reflecting early and normal regional LV contraction what is observed for the healthy population. As can be seen in Fig.5.28, a noticeable difference among the values of skewness is most remarkable in the inferior anatomical segment between the two populations.

TABLE 5.28– Mean transition time (msec) obtained from TSICs

Segment	Mean transition Time	
	Pathological	Healthy
AnteroLateral	$0,548 \pm 0,014$	$0,378 \pm 0,009$
Anterior	$0,594 \pm 0,013$	$0,396 \pm 0,010$
AnteroSeptal	$0,566 \pm 0,035$	$0,454 \pm 0,011$
InferoSeptal	$0,625 \pm 0,025$	$0,465 \pm 0,014$
Inferior	$0,672 \pm 0,009$	$0,404 \pm 0,006$
InferoLateral	$0,604 \pm 0,021$	$0,398 \pm 0,011$

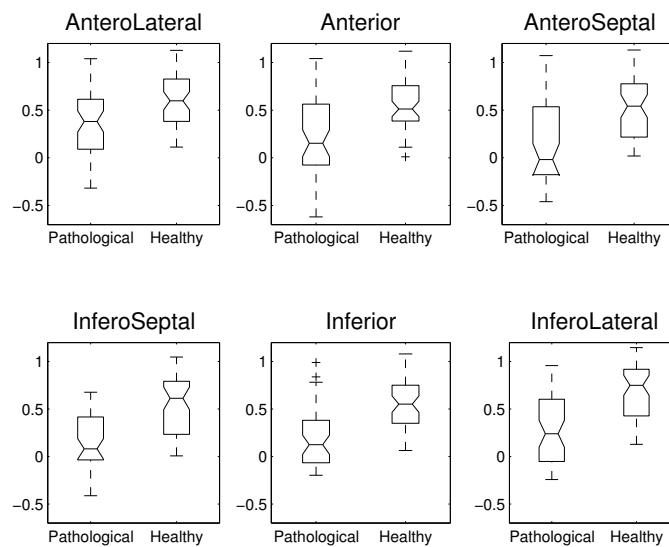


FIGURE 5.28– Average of curve Skewness for both populations in the different anatomical segments.

5.7.1.4 Cross Correlation parameter (Co)

Resulting parameters for cross correlation between each average clustered curve (CI) and the normal reference are computed and presented in Table 5.29. Average values for cross-correlation were 0.76 ± 0.11 for patients and 0.92 ± 0.02 for control subjects, reflecting a noticeable contrast between the two populations.

5.7.2 Experiments with SVM, LC-KSVD and KSRDL

Different experiments have been performed using several configurations of the proposed parameters. The different combinations of parameters are used to train the kernel-based KSRDL approach.

Significant results of these experiments are presented in Table 5.30 and are compared with classification based on SVM with a linear (SVM1) and RBF (SVM2) kernel, and also with discriminative dictionaries based on LC-KSVD2 algorithm. Experiments have also been

TABLE 5.29– Delay time based Cross Correlation obtained from the time-signal intensity curves and the patient-specific reference

Segment	Pathological	Healthy
AnteroLateral	0.827 ± 0.137	0.937 ± 0.066
Anterior	0.817 ± 0.131	0.810 ± 0.326
AnteroSeptal	0.756 ± 0.126	0.927 ± 0.071
InferoSeptal	0.758 ± 0.128	0.816 ± 0.319
Inferior	0.810 ± 0.134	0.901 ± 0.191
InferoLateral	0.827 ± 0.128	0.874 ± 0.242

performed with the FD-DL algorithm, but in this case this technique has not converged due to the small size of the input atoms.

TABLE 5.30– Accuracy obtained by different techniques

Test/Technique	SVM1	SVM2	LC-KSVD	KSRDL
Sk - Cl	72.31 ± 3.38	93.50 ± 2.35	92.22 ± 2.19	94.49 ± 1.59
Sk - Cl - Co	78.46 ± 2.11	94.34 ± 1.42	93.40 ± 1.60	94.06 ± 2.38
Sk - Mt	75.26 ± 4.60	90.50 ± 1.35	90.29 ± 2.26	94.20 ± 2.79
Sk - Mt - Cl	72.74 ± 2.56	94.25 ± 1.38	93.62 ± 1.20	93.81 ± 2.06
Cl - Co	69.06 ± 3.00	81.45 ± 3.48	58.72 ± 2.59	57.97 ± 8.39
Sk - Mt - Cl - Co	77.52 ± 2.25	94.32 ± 1.49	94.17 ± 1.46	93.99 ± 2.19

Results show that the best rate of classification is achieved using KSRDL algorithm when training vectors include the skewness (Sk) and the average curve (Cl) parameter with an accuracy of 94.49%, a sensitivity of 93.67% and a specificity of 95.13% (MANTILLA et al., 2015a,b).

Best performance for the SVM by using a RBF kernel and the LC-KSVD algorithm is achieved when all the parameters are used as input. The accuracy of the classifiers is significantly reduced when the input is constructed only with the average curve (Cl) and the Cross correlation parameter (Co), highlighting the importance of the skewness parameter in the characterization of LV wall motion.

We evaluated the classification accuracy of the KSRDL algorithm by reducing the number of atoms in the dictionary. Figure 5.29 shows the effect varying the dictionary size for $K = 2, 5, 15, 25, 35, 75$ and 135.

Results show that KRS DL maintains a high classification accuracy while the number of dictionary atoms is reduced almost to a value of 15 atoms.

About computing times, Table 5.31 shows the time in seconds (mean \pm standard deviation) employed by the classifiers that present the best results. Results show that the training time employed by the KRS DL algorithm is significantly smaller than the one of the computing time employed by the other DL techniques (MANTILLA et al., 2015d).

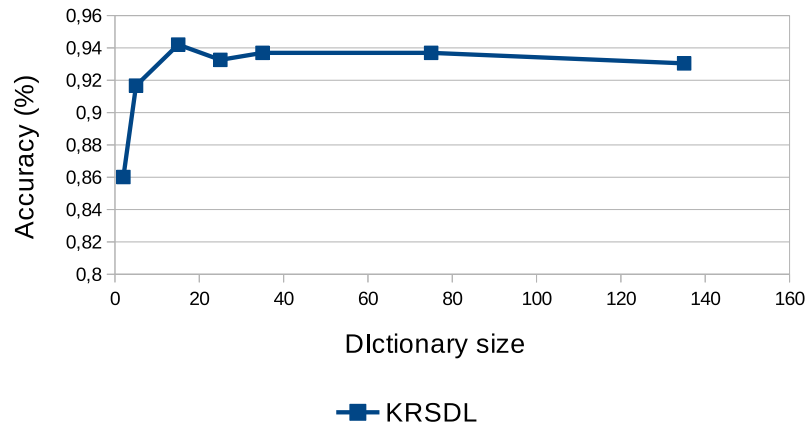


FIGURE 5.29– Accuracy of classification of KSRDL algorithm varying the number of dictionary atoms

TABLE 5.31– Computing times employed by the different techniques

Test/Technique	SVM1	SVM2	LCKSVD	KSRDL
Sk - Cl	0.887 ± 0.184 0.754e-03 ± 0.609	6.383 ± 1.307 0.004 ± 0.001	6.228 ± 0.512 0.021 ± 0.002	2.702e-04 ± 3.273e-04 0.007 ± 0.001
Sk - Cl - Co	0.808 ± 0.631e-03 6.121 ± 0.005	0.159 ± 0.696e-04 1.430 ± 0.961e-03	4.953 ± 0.347 0.020 ± 0.003	2.059e-04 ± 3.244e-04 0.015 ± 0.041
Sk - Mt	0.936 ± 0.232 0.579e-03 ± 0.961e-04	4.281 ± 1.059 0.003 ± 0.564e-03	5.593 ± 0.323 0.019 ± 0.001	3.507e-04 ± 3.781e-04 0.007 ± 0.002
Sk - Mt - Co	1.201 ± 0.421 0.721e-03 ± 0.595e-03	4.930 ± 0.804 0.003 ± 0.758e-03	0.331 ± 0.008 0.333 ± 0.002	3.010e-04 ± 1.932e-04 0.008 ± 0.001
Sk - Mt - Cl	0.971 ± 0.149 0.605e-03 ± 0.251e-03	5.808 ± 0.908 0.004 ± 0.001	0.483 ± 0.007 0.472 ± 0.003	2.809e-04 ± 7.972e-05 0.008 ± 0.002
Cl - Co - Mt	0.374 ± 0.0875 0.615e-03 ± 0.126e-03	0.823 ± 0.249 0.005 ± 0.001	0.635 ± 0.006 0.388 ± 0.003	2.047e-04 ± 7.596e-05 0.007 ± 0.002
Sk - Mt - Cl - Co	0.881 ± 0.206 0.635e-03 ± 0.131e-03	5.877 ± 0.785 0.003 ± 0.749e-03	0.317 ± 0.001 0.501 ± 0.001	2.073e-04 ± 6.683e-05 0.0079 ± 0.001

Sparsity in the KSRDL algorithm

We have also evaluated the accuracy of classification of the KSRDL algorithm varying the sparsity constraint. Figure 5.23 shows the accuracy of the KSRDL algorithm for $\lambda_1 = 0.0001, 0.001, 0.001, 0.01$ and 0.1 .

As can be seen, the KSRDL technique achieves a high classification accuracy when the sparsity constraint takes small values i.e $\lambda_1 \leq 0.01$.

According to the specific goal of the Local parametric mid-cavity evaluation, we can conclude that the best rate of classification by using the KSRDL approach is achieved when training

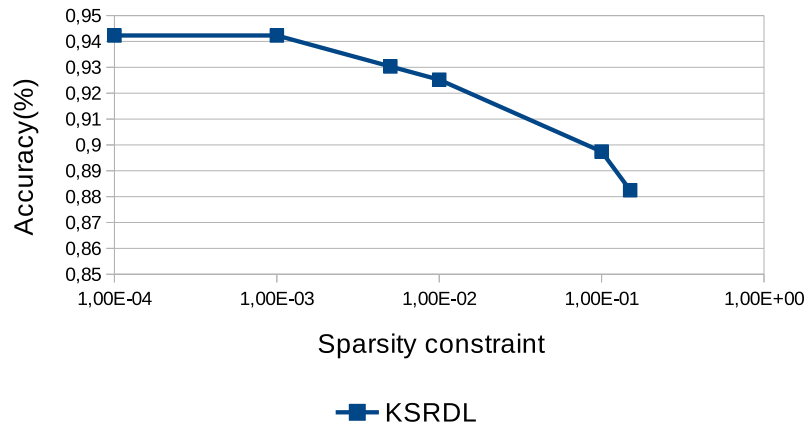


FIGURE 5.30– Accuracy of classification of the KSRDL algorithm varying the sparsity constraint λ_1

vectors include the skewness (Sk) and the average curve (Cl) parameters. However, we can observe that results obtained are close to those obtained with LC-KSVD and SVM2 approaches by using more parameters. The use of sparse classifiers based on kernel DL seems to be a promising technique for classification of LV wall motion that deserves more extensive validation.

5.8 Discussion

In section 4.5, we have presented some works in the literature related to the assessment of LV motion in cardiac MRI. Some of these works based on classification techniques are summarized in Table 5.32. All the methods analyse apical, mid-cavity and basal slices in short-axis cine MRI, excepted the method proposed in (LU et al., 2009) that shows results only for basal slices.

TABLE 5.32– Classification techniques in recent existing methods of regional LV motion classification

Method	Technique
Afshim (AFSHIN, 2012)	Linear Discriminant Analysis+ Linear Support Vector Machine
Punithakumar et.al. (PUNITHAKUMAR et al., 2010)	Shannon’s Differential Entropy (SDE) + Naive Bayes classifier
Suinesiaputra et.al. (SUINESIAPUTRA et al., 2009)	Wall thickening and Visual Wall Motion Scoring+ Independent Component Analysis (ICA)
Lu et.al. (LU et al., 2009)	Intra-segment correlation measure

In these methods, the evaluation was performed by expert visual assessment. For instance, in (LU et al., 2009) 12 of 17 patients were identified with regional abnormal wall motion for the basal slice by expert visual assessment. In (AFSHIN et al., 2014), each myocardial segment was marked following a binary score, either normal or abnormal. The local ground truth (per

segment) was built by three experienced radiologists, each of whom annotated a different portion of the data set. Among the 928 segments identified in this study, 579 segments were marked as normal and 349 as abnormal. In (PUNITHAKUMAR et al., 2010), among the 480 myocardial segments identified in the study population, 389 segments were marked as normal and 91 as abnormal by expert visual assessment. Visual wall motion scoring for the patient group in (SUINESIAPUTRA et al., 2009) was performed for each segment by an experienced cardiologist on a five-point scale: normokinetic, mid-hypokinetic, severe-hypokinetic, akinetic, and dyskinetic.

In our proposed methods, a quantitative evaluation has been performed in two levels: Global evaluation taken the global status of the patient to label each LV anatomical segment and Local evaluation taken information of local radial strain provided by 2D-Speckle tracking Echocardiography to label each LV anatomical segment.

The better results using global evaluation has been obtained with the FD-DL classifier that reached 96.51% for accuracy, 96.48% for sensitivity and 96.67% for specificity, using diametral spatio-temporal profiles in the Wavelet domain obtained at the mid-ventricular slice level. This performance was slightly improved by using radial profiles at the same anatomical plane by the same classification technique with an accuracy of 97.05%, a sensitivity of 95.21% and a specificity of 98.89%, in this case in Gray level (original domain).

It should be noted that higher values in accuracy using a global evaluation are biased. In fact there is an error introduced since the beginning of the training stage of all classifiers. Some of the anatomical segments in the pathologic population are labeled as abnormal LV motion even when some segments present normal LV motion. It is for this reason that results using local evaluation are more realistic than those obtained by using global evaluation.

Regarding local evaluation, the best performance in the mid-cavity plane was achieved by the FD-DL technique using radial profiles with the assessment of 2D-STE in the Gray level domain with an accuracy of 92.81%, a sensitivity of 88.33% and a specificity of 94.68%. This performance was improved by using the Skewness and Clustering parameters extracted from the radial profiles at the same anatomical plane by the KSRDL technique with an accuracy of 94.49%, a sensitivity of 93.67% and a specificity of 95.13%.

Table 5.33 shows the results of the proposed approaches using local evaluation compared to the reported methods in terms of accuracy at each slice level and for a specific number of patients.

As we can see in this table, the best rate of classification in methods found in the literature for the LV wall motion classification is achieved by (PUNITHAKUMAR et al., 2010) with an accuracy of 93.30%. On the one hand, this performance is better than our proposed method when the radial spatio-temporal profiles in both, gray levels (92.81% with FD-DL) and Wavelet domains (92.61% with LC-KSVD1) are used to train the respective classifiers. On the other hand, our method using the parametric features, SK and Cl, achieves the highest rate of classification (94.49% with KSRDL and 93.50% with SVM RBF). However, it has been applied in a reduced number of patients comparing to those used in (PUNITHAKUMAR et al., 2010) and these results have to be confirmed on more data patients.

TABLE 5.33– Comparisons of accuracy of the proposed methods using local evaluation with existing methods of regional LV motion classification

Method		Apical	Mid-cavity	Basal	Patients
Radial non-parametric Gray level	(FD-DL)	-	92.81	-	18
	(LC-KSVD1)	-	90.24	-	18
	(LC-KSVD2)	-	91.94	-	18
	(SVM Linear)	-	88.46	-	18
	(SVM RBF)	-	91.88	-	18
Radial non-parametric Wavelet	(FD-DL)	-	91.11	-	18
	(LC-KSVD1)	-	92.61	-	18
	(LC-KSVD2)	-	92.31	-	18
	(SVM Linear)	-	88.78	-	18
	(SVM RBF)	-	91.20	-	18
Radial parametric: Sk- Cl	(KSRDL)	-	94.49	-	18
	(LC-KSVD2)	-	92.22	-	18
	(SVM Linear)	-	72.31	-	18
	(SVM RBF)	-	93.50	-	18
(AFSHIN et al., 2014)		89.75	85.72	84.02	58
(PUNITHAKUMAR et al., 2010)		92.50	93.30	87.20	30
(SUINESIAPUTRA et al., 2009) (WT)		72.78	89.63	69.93	89
(SUINESIAPUTRA et al., 2009) (VWMS)		66.67	67.41	63.70	89
(LU et al., 2009)		-	-	86.30	17

About user interaction, in our method, 5 manual mouse clicks, are used in the first frame of the cardiac study, while other approaches seem to demand more user assistance to delineate endo and/or epicardial boundaries in all the frames. Only the methods in (AFSHIN et al., 2014) and (PUNITHAKUMAR et al., 2010) report computational times with 0.15 and 62 secs respectively. Comparative results in Table 5.33 show that the proposed method can yield a competitive performance while reducing the complexity and user interaction.

Comparing with the previous work on regional LV wall motion analysis presented in Table 5.32, our proposed method has main advantages that can be summarized as:

- The segmentation of the endocardium and epicardium is not required.
- The KSRDL and LC-KSVD methods have found an appropriate balance between accuracy, computing time, complexity and simplicity.
- The discriminative dictionary learning methods have been applied for LV motion analysis for the first time.

The results have been shown that analyzing the LV radial spatio-temporal profiles in the cardiac cine-MRI sequences at the mid-cavity short axis plane seems to be sufficient for detecting wall motion abnormalities in this patient study data set.

5.9 Limitations

In this study we have presented a novel methodology, based on DL approaches for LV wall motion classification in cardiac cine MRI. In this methodology, 5 points are located in the first frame of the cardiac study. One critical point could be the choice of the anterior intersection between LV and RV, necessary to determine the LV anatomical segments. An accurate location of this reference point in the cardiac cycle is difficult. We have assumed a stationary point of reference (anatomical landmark) located in the anterior intersection between the two ventricles at one reference frame in the end-diastole phase that is repeated on the next frames of the cardiac cycle. Therefore, this unique reference point location was used even it probably lead to slight segment location errors due to the LV twisting and ventricular torsion. Thus, we are interested in measuring the impact of the manually location of the reference point at each frame of the cardiac cycle.

Firstly, a reference anatomical landmark in the anterior intersection between RV and LV is manually positioned at the first frame of the cardiac cycle (end-diastole frame). A reference line from the LV centroid to this point is traced in order to get the angular position of the reference point. For the next frames of the cardiac cycle, a new anatomical landmark is manually located, then, the angular variation of this point is computed with respect to the reference point located in the end-diastole frame of the cardiac cycle. An illustrative example is shown in Figure 5.31. Table 5.34 shows the mean and standard deviation values of the angular variation (in degrees) that have been measured in both groups, pathological and control subjects.

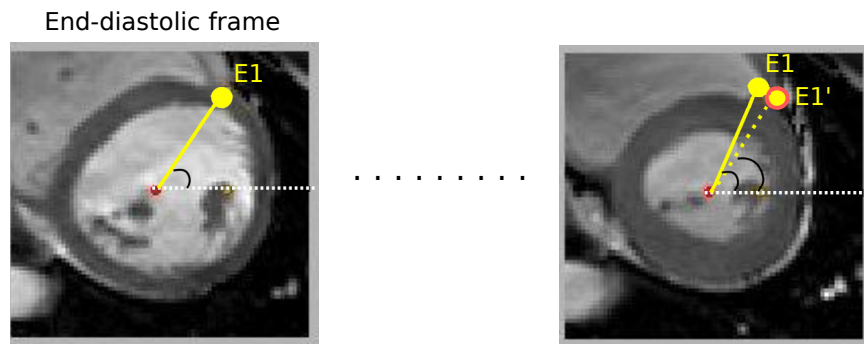


FIGURE 5.31– Angular variation of reference point E1 from end diastole to a posterior frame E1'

Average values of angular variation for the population in study, including healthy and pathologic patients, are -5.404 ± 8.329 . Results show that the higher average variation is $9.87^\circ \pm 4.07^\circ$ observed in the patient EuHeart1.

To provide a first quantification of these errors on LV wall motion classification, we are interested in evaluating our method in the two situations: 1) by fixing the anatomical landmark at the first frame of the cardiac cycle and 2) by the manual tracking of it in all the frames of the cardiac cycle. We want to determine if the angular variations observed in Table 5.34, has some impact in the classification performance of the proposed machine learning techniques.

TABLE 5.34– Angular variation in degrees of the anterior intersection point between RV and LV

Subject	Angular variation	Subject	Angular variation
IMOP0	-3.86 ± 3.20	CAP1	3.82 ± 3.77
IMOP1	-7.50 ± 4.96	CAP2	-1.79 ± 5.08
IMOP4	-1.98 ± 5.89	CAP3	2.35 ± 3.81
EuHeart1	9.87 ± 4.07	CAP4	1.98 ± 3.62
EuHeart2	-0.14 ± 3.25	CAP5	-1.17 ± 3.67
EuHeart3	2.69 ± 6.04	CAP6	-2.50 ± 7.16
EuHeart4	-9.56 ± 4.62	CAP7	-4.02 ± 4.28
EuHeart5	2.31 ± 4.19	CAP8	5.29 ± 5.51
EuHeart6	-0.59 ± 3.80	CAP9	5.15 ± 4.32

Figure 5.32 shows a comparison of the radial spatio-temporal profiles extracted every 10° in both cases. We can see that profiles in the second case present some variation in the Gray level intensity making the epicardial and endocardial borders more notorious. More homogeneity is observed in profiles for the first case.

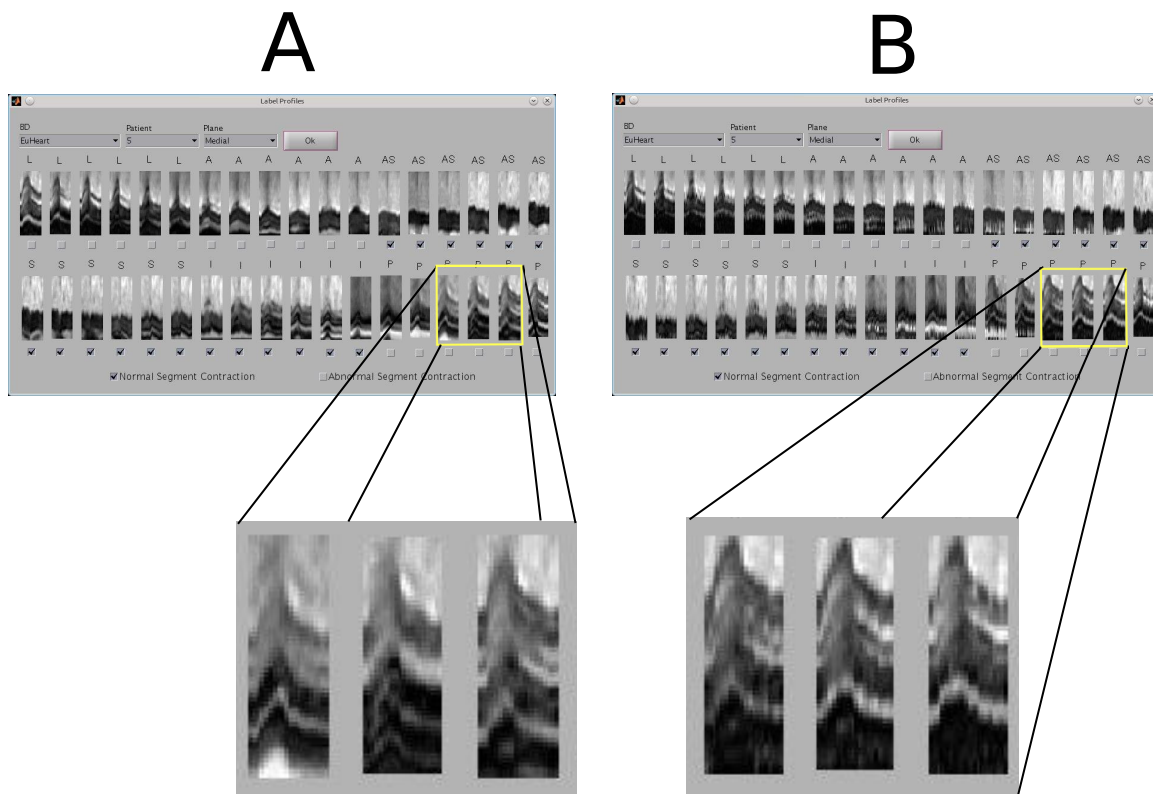


FIGURE 5.32– Radial profiles with A) simple location of the anterior intersection between RV and LV at the first frame of the cardiac cycle and B) manual location of the anterior intersection between RV and LV in all the frames of the cardiac cycle.

Once the new radial profile extraction has been performed with the manual location of the

reference point in all the frames of the cardiac cycle, we have repeated the experiments of local evaluation using radial profiles both in the Gray level domain and the Wavelet domain. The configuration of training and testing inputs are the same that those used in previous experiments with the location of the reference point only in the first frame of the cardiac cycle. Table 5.35 shows the results with the different classifiers after the average of 50 iterations by combining training and testing groups.

TABLE 5.35— Results of classification by local evaluation and by using radial profiles with the manual location of the anterior intersection between RV and LV in each frame of the cardiac cycle by the different techniques in Gray level and Wavelet domain

	Gray level			Wavelet		
	Accuracy	Sensitivity	Specificity	Accuracy	Sensitivity	Specificity
SVM linear	90.68±1.19	87.25±5.36	92.12±2.14	91.28±2.02	91.59±3.75	91.15±2.04
SVM RBF	92.39±2.15	77.39±6.53	98.67±0.79	96.23±1.74	97.68±1.94	95.63±1.98
LCKSVD 1	95.04±1.19	93.91±3.75	95.52±1.26	94.87±1.51	94.78±3.18	94.91±1.80
LCKSVD 2	94.87±1.17	93.62±3.34	95.39±1.40	95.13±1.64	95.07±2.63	95.15±1.77
FD-DL	93.59±1.86	91.79±6.54	94.34±5.30	90.28±2.22	81.52±8.23	93.94±2.47

Results show that the classification performance is generally improved using the different classifiers with the manual tracking of the anterior intersection between the two ventricles. Specifically, the best classification performance is obtained in the Wavelet domain by the SVM using a RBF kernel with an accuracy improved from 91.20% to 96.23%. The LC-KSVD2 algorithm has improved its performance from 92.31% to 95.13% also in the Wavelet domain (cf. Table 5.23).

Comparing these results with those obtained in the previous experiments shown in Table 5.23, we can conclude that the accuracy of classification is improved in almost 4% with respect to the best performance obtained by the FD-DL technique in the gray level domain: 92.81% with the anterior intersection between RV and LV fixed in all the frames.

This experiment confirmed that a manual location of the anatomical landmark between LV and RV is needed to improve the results of classification of LV wall motion. An automatic location of this point could be addressed in future works.

5.10 Conclusion

We have presented new solutions for regional LV wall motion classification using two machine learning techniques. Experiments are performed, independently, in apical, mid-cavity and basal slices using different spatio-temporal representations identified in LV anatomical segments. These spatio-temporal representations are related to diametral profiles, radial profiles and parameters extracted from radial profiles.

SVM and discriminative dictionary learning methods have been trained and validated with information from the spatio-temporal profiles.

In the case of diametral profiles, the experiments have been realized in apical, mid-cavity and basal SAX planes using 360 profiles extracted from a set of 20 subjects (14 patients and 6 controls, 18 profiles per subject) at each short axis plane.

In the case of radial profiles, the experiments have been realized on 108 anatomical segments in a set of 18 subjects (9 patients with cardiac dyssynchrony and 9 healthy subjects) from which 648 spatio-temporal profiles were extracted.

The complexity of the classification techniques has been compared in term of sparseness for the SVMs and sparsity constraint for the DL models.

Two levels of evaluation have been presented: 1) global evaluation, where the global status of the patient is used to label each LV anatomical segment; 2) local evaluation, where information of local radial strain provided by 2D-Speckle tracking Echocardiography is used to label each LV anatomical segment. This second configuration is more realistic according to the clinical practice.

In local evaluation, parametric inputs (Skewness and Clustering) have overcome the classification accuracy using non-parametric inputs (radial profiles in Wavelet or Gray level domains).

Machine learning techniques based on DL have demonstrated the best compromise between classification accuracy and complexity for the classification of radial spatio-temporal profiles. They concern the LC-KSVD algorithm with the non-parametric representation of inputs and the KSRDL algorithm with the parametric representation.

The original approach of this work is two-folds. First we have proposed an approach for classification of regional wall motion abnormalities in cardiac MRI without the need of LV boundaries segmentation. Secondly, we have introduced a first attempt to use dictionary learning based on sparse coding for classification in cardiac medical image analysis that provides competitive results compared to the literature.

References

- AFSHIN, M. (2012). “Automatic Assessment of Cardiac Left Ventricular Function Via Magnetic Resonance Images”. PhD thesis. University of Western Ontario.
- AFSHIN, M., I. BEN AYED, K. PUNITHAKUMAR, M. LAW, A. ISLAM, A. GOELA, T. PETERS, and N. SHUO LI (2014). “Regional assessment of cardiac left ventricular myocardial function via MRI statistical features”. In: *IEEE Transaction in Medical Imaging* 33.2, pp. 481–494.
- BECKER, M., E. BILKE, H. KUHL, M. KATOH, R. KRAMANN, A. FRANKE, A. BUCKER, P. HANRATH, and R. HOFFMANN (2006). “Analysis of myocardial deformation based on pixel tracking in two dimensional echocardiographic images enables quantitative assessment of regional left ventricular function”. In: *Heart* 92.8, pp. 1102–1108.
- CHAPELLE, O., V. VAPNIK, O. BOUSQUET, and S. MUKHERJEE (2002). “Choosing Multiple Parameters for Support Vector Machines”. In: *Machine Learning* 46.1-3, pp. 131–159.

- DOHI, K., M. S. SUFFOLETTO, D. SCHWARTZMAN, L. GANZ, M. R. PINSKY, and J. GORCSAN (2005). “Utility of echocardiographic radial strain imaging to quantify left ventricular dyssynchrony and predict acute response to cardiac resynchronization therapy”. In: *The American Journal of Cardiology* 96.1, pp. 112–116.
- EL BERBARI, R., N. KACHENOURA, A. REDHEUIL, A. GIRON, E. MOUSSEAUX, A. HERMENT, I. BLOCH, and F. FROUIN (2009). “Automated estimation of regional mean transition times and radial velocities from cine magnetic resonance images: evaluation in normal subjects”. In: *J Magn Reson Imaging* 30.1, pp. 236–242.
- FINE, N. M., A. A. SHAH, I.-Y. HAN, Y. YU, J.-F. HSIAO, Y. KOSHINO, H. K. SALEH, J. MILLER FLETCHER A, J. K. OH, P. A. PELLIKKA, and H. R. VILLARRAGA (2013). “Left and right ventricular strain and strain rate measurement in normal adults using velocity vector imaging: an assessment of reference values and intersystem agreement”. In: *Int J Cardiovasc Imaging* 29.3, pp. 571–580.
- JIANG, Z., Z. LIN, and L. S. DAVIS (2013). “Label Consistent K-SVD: Learning a Discriminative Dictionary for Recognition”. In: *IEEE Transactions on Pattern Analysis and Machine Intelligence* 35.11, pp. 2651–2664.
- KACHENOURA, N., A. REDHEUIL, D. BALVAY, C. RUIZ-DOMINGUEZ, A. HERMENT, E. MOUSSEAUX, and F. FROUIN (2007). “Evaluation of regional myocardial function using automated wall motion analysis of cine MR images: Contribution of parametric images, contraction times, and radial velocities.” In: *J Magn Reson Imaging* 26.4, pp. 1127–1132.
- LI, Y. and A. NGOM (2013). “Sparse representation approaches for the classification of high-dimensional biological data”. In: *BMC Systems Biology* 7.Suppl 4, S6.
- LU, Y., P. RADAU, K. CONNELLY, A. DICK, and G. WRIGHT (2009). “Pattern Recognition of Abnormal Left Ventricle Wall Motion in Cardiac MR”. In: *Proceedings of the 12th International Conference on Medical Image Computing and Computer-Assisted Intervention: Part II. MICCAI '09*. London, UK: Springer-Verlag, pp. 750–758.
- MANTILLA, J., M. GARREAU, J.-J. BELLANGER, C. LECLERCQ, and J. PAREDES (2015a). “DL-based classification of LV wall motion in cardiac MRI with a parametric approach”. In: *Recherche en Imagerie et Technologies pour la Santé (RITS)*. (in press).
- MANTILLA, J., M. GARREAU, J.-J. BELLANGER, and J. L. PAREDES (2015b). “Valoración del movimiento del ventriculo izquierdo en MRI cardiaca usando un enfoque parametrico y aprendizaje de diccionarios”. In: *V Congreso Venezolano de Bioingenieria*. (in press).
- MANTILLA, J., M. GARREAU, J.-J. BELLANGER, and J. L. PAREDES (2013a). “Automated classification of LV regional wall motion based on spatio-temporal profiles from cardiac cine magnetic resonance imaging”. In: *Proc. SPIE*. Vol. 8922, pages.
- (2013b). “Machine Learning Techniques for LV Wall Motion Classification Based on Spatio-temporal Profiles from Cardiac Cine MRI”. In: *IEEE Machine Learning and Applications (ICMLA), 2013 12th International Conference on*. Vol. 1, pp. 167–172.
- MANTILLA, J., M. GARREAU, J.-J. BELLANGER, and J. L. PAREDES (2015c). “SVM-based classification of LV wall motion in cardiac MRI with the assessment of STE”. In: *Proc.*

- SPIE 9287, 10th International Symposium on Medical Information Processing and Analysis*. Vol. 9287, pages.
- MANTILLA, J., J. PAREDES, J.-J. BELLANGER, E. DONAL, C. LECLERCQ, R. MEDINA, and M. GARREAU (2015d). “Classification of LV wall motion in cardiac MRI using kernel Dictionary Learning with a parametric approach”. In: *37th Annual International Conference of the IEEE Engineering in Medicine and Biology Society (EMBS)*. (in press), pp. 7292–7295.
- MARCHESSEAU, S., H. DELINGETTE, M. SERMESANT, R. CABRERA-LOZOYA, C. TOBON-GOMEZ, P. MOIREAU, R. M. FIGUERAS I VENTURA, K. LEKADIR, A. HERNANDEZ, M. GARREAU, E. DONAL, C. LECLERCQ, S. G. DUCKETT, K. RHODE, C. A. RINALDI, A. F. FRANGI, R. RAZAVI, D. CHAPELLE, and N. AYACHE (2013). “Personalization of a cardiac electromechanical model using reduced order unscented Kalman filtering from regional volumes”. In: *Medical Image Analysis* 17.7, pp. 816–829.
- PUNITHAKUMAR, K., I. AYED, A. ISLAM, I. ROSS, and S. LI (2010). “Regional Heart Motion Abnormality Detection via Information Measures and Unscented Kalman Filtering”. In: *Medical Image Computing and Computer-Assisted Intervention – MICCAI 2010*. Ed. by T. JIANG, N. NAVAB, J. PLUIM, and M. VIERGEVER. Vol. 6361. Lecture Notes in Computer Science. Springer Berlin Heidelberg, pp. 409–417.
- RADAU, P., Y. LU, K. CONNELLY, G. PAUL, A. DICK, and G. WRIGHT (2009). “Evaluation Framework for Algorithms Segmenting Short Axis Cardiac MRI.” In: *The MIDAS Journal - Cardiac MR Left Ventricle Segmentation Challenge*.
- SADE, L. E., H. KANZAKI, D. SEVERYN, K. DOHI, and J. GORCSAN (2004). “Quantification of radial mechanical dyssynchrony in patients with left bundle branch block and idiopathic dilated cardiomyopathy without conduction delay by tissue displacement imaging”. In: *The American Journal of Cardiology* 94.4, pp. 514–518.
- SUFFOLETTO, M. S., K. DOHI, M. CANNESON, S. SABA, and J. GORCSAN (2006). “Novel Speckle-Tracking Radial Strain From Routine Black-and-White Echocardiographic Images to Quantify Dyssynchrony and Predict Response to Cardiac Resynchronization Therapy”. In: *Circulation* 113.7, pp. 960–968.
- SUINESIAPUTRA, A., A. F. FRANGI, T. A. M. KAANDORP, H. J. LAMB, J. J. BAX, J. H. C. REIBER, and B. P. F. LELIEVELDT (2009). “Automated Detection of Regional Wall Motion Abnormalities Based on a Statistical Model Applied to Multi-Slice Short-Axis Cardiac MR Images.” In: *IEEE Transactions on Medical Imaging* 4.28, pp. 595–607.
- TAVARD, F., A. SIMON, C. LECLERCQ, E. DONAL, A. HERNÁNDEZ, and M. GARREAU (2014). “Multimodal Registration and Data Fusion for Cardiac Resynchronization Therapy Optimization”. In: *IEEE Transactions on Medical Imaging* 33.6, pp. 1363–1372.
- TOBON-GOMEZ, C., M. DE CRAENE, K. MCLEOD, L. TAUTZ, W. SHI, A. HENNEMUTH, A. PRAKOSA, H. WANG, G. CARR-WHITE, S. KAPETANAKIS, A. LUTZ, V. RASCHE, T. SCHAEFFTER, C. BUTAKOFF, O. FRIMAN, T. MANSI, M. SERMESANT, X. ZHUANG, S. OURSELIN, H.-O. PEITGEN, X. PENNEC, R. RAZAVI, D. RUECKERT, A. F. FRANGI, and

- K. S. RHODE (2013). “Benchmarking framework for myocardial tracking and deformation algorithms: An open access database”. In: *Medical Image Analysis* 17.6, pp. 632–648.
- WEESE, J., N. SMITH, R. RAZAVI, C. D. H. DELINGETTE, A. FRANGI, R. HOSE, P. HUNTER, and J. SPAAN (2013). *euHeart: Project Final Report*. Tech. rep. FP7-ICT-2007, IP Contract no: 224495.
- YANG, M., L. ZHANG, X. FENG, and D. ZHANG (2014). “Sparse Representation Based Fisher Discrimination Dictionary Learning for Image Classification”. In: *International Journal of Computer Vision* 109.3, pp. 209–232.
- YINGCHONCHAROEN, T., S. AGARWAL, Z. B. POPOVIĆ, and T. H. MARWICK (2013). “Normal Ranges of Left Ventricular Strain: A Meta-Analysis”. In: *Journal of the American Society of Echocardiography* 26.2, pp. 185–191.

Dictionary Learning-based Classification for Fibrosis detection in cardiac MRI

6.1 Introduction

In this chapter we address the problem of fibrosis detection in patients with Hypertrophic cardiomyopathy (HCM) by using a sparse-based clustering approach and Dictionary Learning. HCM, as a genetic cardiovascular disease, is characterized by the abnormal thickening of left ventricular myocardium. Myocardial fibrosis commonly presented in HCM can be detected in Late Gadolinium Enhanced (LGE) cardiac magnetic resonance imaging (MRI). In this chapter, we present the use of a Dictionary Learning (DL)-based clustering technique for the detection of fibrosis in LGE-MRI. The addressed issue in this part that concerns Hypertrophic cardiomyopathy and Fibrosis is depicted in section 6.2. Furthermore, a description of the LGE-MRI cardiac imaging modality is presented in section 6.3. A brief state-of-the-art for the assessment of myocardial fibrosis in LGE-MRI is presented in section 6.4. Next, in section 6.5, we present our proposed approach that represents a novel approach based on clustering and dictionary learning (DL) techniques for the detection of fibrosis in cardiac LGE-SAX MRI. The results of this approach are presented in section 6.6.

6.2 Hypertrophic cardiomyopathy and Fibrosis

Cardiomyopathy is a type of progressive heart muscle disease in which the heart is abnormally enlarged, thickened, and/or stiffened. As a result, the heart muscle's ability to pump blood is weakened, often causing Heart Failure (HF). The disease can also cause abnormal heart rhythms. The World Health Organization/International Society and Federation of Cardiology (WHO/ISFC) classification of 1996 associated the term cardiomyopathies to all heart muscle diseases that lead to

functional disturbances of the heart. A classification is described with 4 main phenotypes, which can be assessed by invasive and noninvasive imaging methods: dilated cardiomyopathy (DCM), hypertrophic cardiomyopathy (HCM), restrictive cardiomyopathy (RCM), and unclassified forms. The right ventricular cardiomyopathy, previously right ventricular dysplasia (ARVCM), was then added to this classification (MAISCH et al., 2012). Figure 6.1 illustrates different types of cardiomyopathies.

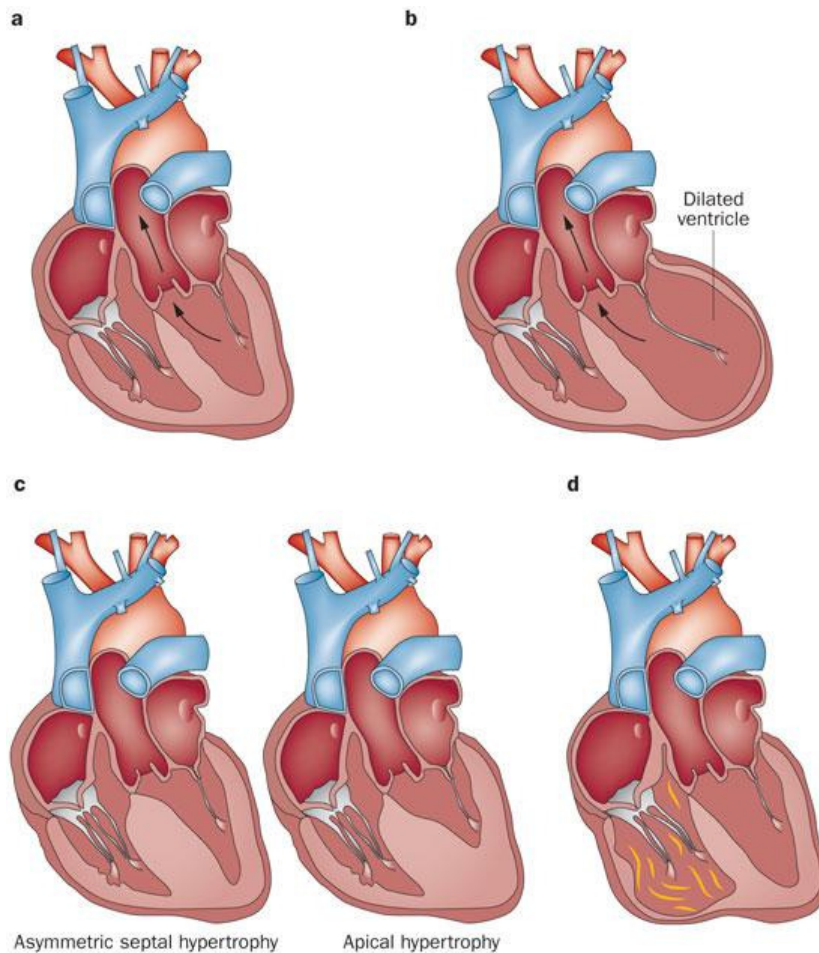


FIGURE 6.1– Different types of cardiomyopathies: a) The normal heart. b) Dilated cardiomyopathy. c) Two examples of hypertrophic cardiomyopathy: classic asymmetric septal hypertrophy, most often limited to the basal portion (not shown), and apical part. d) Arrhythmogenic right ventricular cardiomyopathy, with right-sided involvement only. From: (WILDE et al., 2013)

This work aims at characterizing the hypertrophic cardiomyopathy. HCM is the most common genetic cardiovascular disease (HOEY et al., 2014). The estimated prevalence in the general adult population with phenotypic evidence of HCM is 1 per 500 (B. MARON et al., 1995). Men are more often affected than women and black patients more so than white patients. In young adults, HCM is the most common cause of sudden cardiac death (HUGHES, 2004; MEMBERS et al., 2011).

Cardiac muscles hypertrophy in HCM is described as "concentric" or "eccentric". Concentric heart hypertrophy means increased heart muscle bulk and wall thickness, and it is best assessed on cardiac MRI by looking the heart thickness in the short axis view. Eccentric heart hypertrophy means general increase in the heart muscles with preservation of the normal cardiac wall thickness (isometric) (AL-TUBAIKH, 2010).

Sometimes, the thickened heart muscle doesn't block blood flow out of the left ventricle. This is called non-obstructive hypertrophic cardiomyopathy. The entire ventricle may thicken, or the thickening may happen only at the basal part of the heart. Hypertrophic nonobstructive cardiomyopathy may be found as an apical, a midventricular isolated septal form, or as hypertrophy of the papillary muscles (MAISCH et al., 2012; MEMBERS et al., 2011).

In both types of HCM (obstructive and non-obstructive), the thickened muscle makes the left ventricle cavity smaller, so it holds less blood. The walls of the ventricle also may stiffen. As a result, the ventricle is less able to relax and fill with blood.

HCM is a disease with an extremely variable prognosis. Some patients will die from sudden death (M. MARON et al., 2008), others will develop atrial fibrillation (Olivotto et al., 2001) with accidents due to arterial embolism, others will suffer from heart failure in most cases with a preserved left ventricular ejection fraction, and some will be life-long asymptomatic.

Some people who have HCM have no signs or symptoms. The disease doesn't affect their live. Others have severe symptoms and complications. For example, they may have shortness of breath, serious arrhythmias, or an inability to exercise (BETANCUR, 2014).

6.2.1 Myocardial Fibrosis in HCM

Myocardial fibrosis is a condition that involves the impairment of the heart's muscle cells called cardiomyocytes. When fibrosis occurs in response to injury, the term "scarring" is used. It belongs to a class of diseases collectively known as fibrosis, which denotes hardening or scarring of tissue. This is a condition that not only affects the heart, but also other organs such as the lungs and the liver. Myocardial fibrosis is also referred to by the more general term of cardiac fibrosis.

Cardiomyocytes, which come from originating cells called myoblasts, are instrumental in controlling the heart rate by producing electrical impulses (cf. 4.2.1). Each cardiomyocyte cell is organized as a collection of cylindrical filaments called myofibrils. These are the cell units that enable the heart to contract. Normally, cardiomyocytes form lines of cells in the heart (BAUM et al., 2011).

In myocardial fibrosis, cardiomyocytes are replaced by tissue that is unable to contract. This happens when fibroblasts, which produce collagen to enable wound healing, provide excessive amounts of the protein. This results in a case of abnormal scarring, or fibrosis.

Myocardial fibrosis leads to both systolic and diastolic dysfunction. On the one hand, fibrotic segments will deform less than normal ones (in systolic phases). On the other hand, fibrosis will lead to a decrease in compliance thus to difficulties to fill the left cardiac chambers (in diastolic phases). Other studies proved that the extent of regions with LGE observed in MRI

was also correlated with adverse cardiac events such as sudden cardiac death, fatal arrhythmia or worsening heart failure in patients with HCM (BETANCUR, 2014).

Fibrosis manifests in three forms, that are, reactive interstitial fibrosis, replacement fibrosis and infiltrative interstitial fibrosis (Figure 6.2). Replacement fibrosis occurs in response to an injury causing cardiomyocyte death, as in the case of myocardial infarction; a reparative response is activated in the heart, causing replacement of dead cells and formation of a collagen-based scar. In reactive interstitial fibrosis, the cardiac interstitial space expands without significant cardiomyocyte loss (KRENNING et al., 2010). Infiltrative interstitial fibrosis is a subtype of fibrosis induced by the progressive deposit of insoluble proteins (amyloidosis) or glycosphingolipids (Anderson Fabry's disease) in the cardiac interstitium.

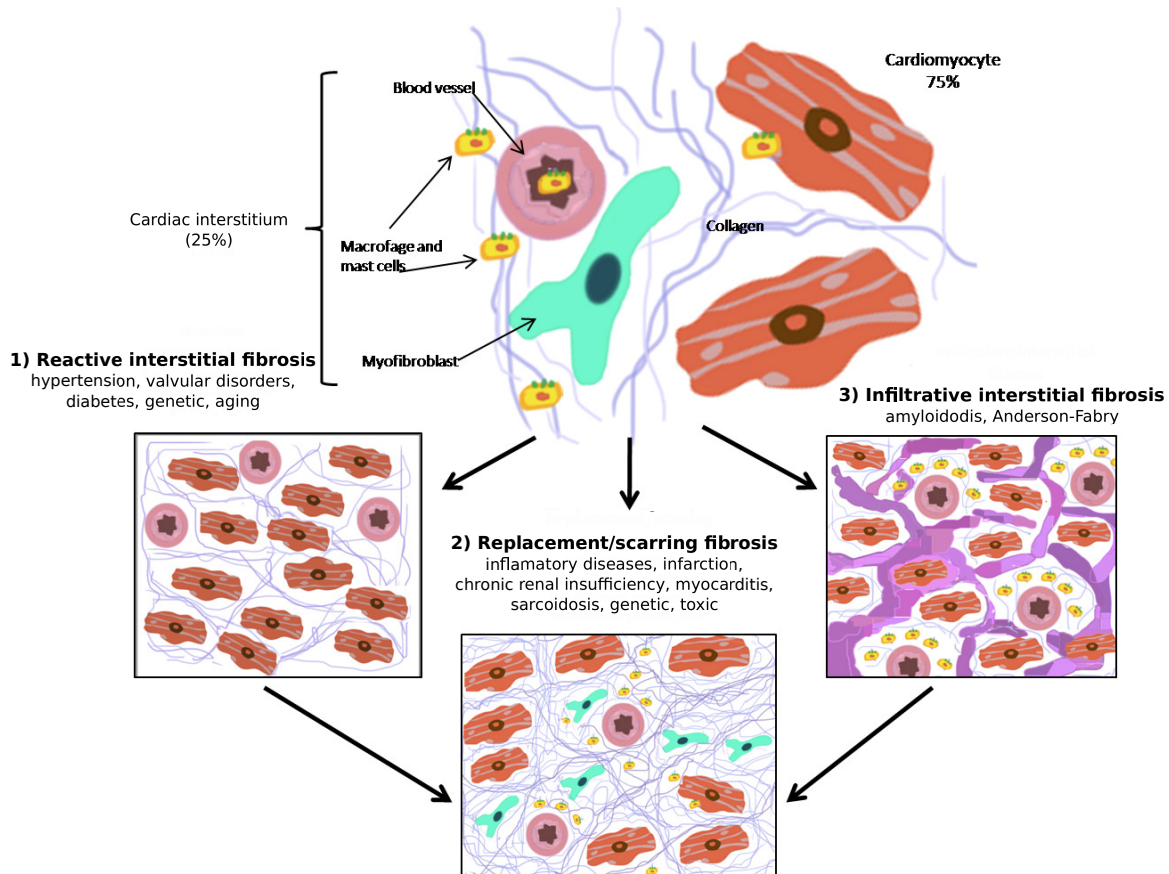


FIGURE 6.2— Different types of myocardial fibrosis according to the cardiomyopathic process. 1) reactive interstitial fibrosis, 2) replacement fibrosis and 3) infiltrative interstitial fibrosis. From: (KRENNING et al., 2010)

Being a very heterogeneous disease with variable outcome, a better characterization of HCM is needed, and especially related to the potential presence of fibrosis. In this context, cardiac imaging can provide significant information allowing to elucidate the factors explaining HCM evolution.

6.3 Cardiac magnetic resonance imaging with Late gadolinium enhancement (LGE)-MRI

The clinical diagnosis of HCM is based on the demonstration of LV hypertrophy in the absence of another disease process that can reasonably account for the magnitude of hypertrophy present. Various imaging modalities can be used to assess fibrosis and to guide treatment, screening and preclinical diagnosis. These imaging modalities include: Echocardiography, Nuclear Imaging, Cardiovascular Magnetic Resonance and Cardiac Computed Tomography. Traditionally, the diagnosis of HCM relies upon clinical assessment and transthoracic echocardiography (TTE). In recent years MRI has become established as a useful adjunct to TTE owing to its unrestricted field of view, more accurate measurement of LV wall thickness, mass, volumes and function and its ability to provide non-invasive assessment of myocardial fibrosis (HOEY et al., 2014). This work aims at characterizing myocardial fibrosis in Cardiac Magnetic Resonance Imaging (CMRI), focusing on fibrosis detection.

Cardiac magnetic resonance is the new gold standard to measure myocardial wall thickness and to diagnose HCM (MEMBERS et al., 2011). Also, it is used to characterize myocardial tissue enabling to quantify the fibrosis/scar extension (MOON et al., 2004). It is now documented that approximately half of patients with HCM have late gadolinium enhancement (LGE) suggestive of areas of fibrosis (M. MARON et al., 2008).

Assessment of myocardial viability is performed using 5- to 20-minute delayed, gadolinium-enhanced MRI which involves intravenous administration of gadolinium-based contrast agent followed by the acquisition of T1 weighted images of the myocardium using an inversion recovery (IR) technique. IR technique is commonly employed to suppress the signal from viable myocardium by modifying the contrast of the acquired image between viable and nonviable myocardium. IR uses inversion pulses typically followed by a prescribed delay to allow recovery of the prepared magnetization before a spin echo or gradient echo pulse sequence used to “read out” the MR signal. The associated delay is known as the time after inversion (TI) (BETANCUR, 2014).

Gadolinium is an extracellular contrast agent; thus, it distributes from vascular sector to the interstitial sector and never enters the cellular sector. The intensity of the gadolinium enhancement depends upon (i) tissue perfusion and (ii) the volume in which the gadolinium is distributed.

On delayed enhanced CMRI (DE-CMRI), there is a relatively decreased washout of the gadolinium contrast agent in areas of myocardium that have been replaced by fibrosis or scar. In normal viable myocardium, the gadolinium contrast agent washes out more rapidly than it does from the fibrosis or scar. Since the difference between normal and abnormal myocardium is based on washout kinetics, images after contrast injection will optimally depict the fibrosis or scar.

There are two types of DE-CMRI: early gadolinium enhanced (EGE) and late gadolinium enhanced (LGE). EGE- and LGE-CMRI are essentially the same, but the timing of the acquisition following intravenous administration of the contrast agent is a distinguishing factor, being greater than 10 min for LGE-CMRI. In a typical LGE exam, 10 to 12 breath hold slices are acquired in

short axis orientation, followed by long axis and 4-chamber views when clinically indicated.

In (MOON et al., 2004) a direct correlation between the percentage of LGE and percentage of histologic collagen in an explanted HCM heart was obtained. LGE has been reported in up to 75% of patients with HCM in whom the vast majority have patchy mid-wall-type enhancement which is typically most pronounced within the segments most severely affected by hypertrophy. LGE most often involves the interventricular septum, particularly the anteroseptal mid to basal segments and right ventricular insertion points (HOEY et al., 2014).

In this work we focus on Late gadolinium enhancement MRI. There are two types of LGE sequences: inversion recovery CMR (IR-CMR) and phase sensitive inversion recovery CMR (PSIR-CMR).

The IR sequence acquires the magnitude of the magnetization at the time of inversion (TI). This time must be carefully selected to null viable myocardium which increases the range of gray levels between viable and non-viable tissue (SIMONETTI et al., 2001).

In contrast, PSIR-CMR is less sensitive to the selection of TI because it takes account of the sign of the magnetization at the time of data acquisition; therefore, the dynamic range of IR signal intensity levels increases. Instances of IR and PSIR images revealing myocardial fibrosis in one HCM patient are showed in Figure 6.3.

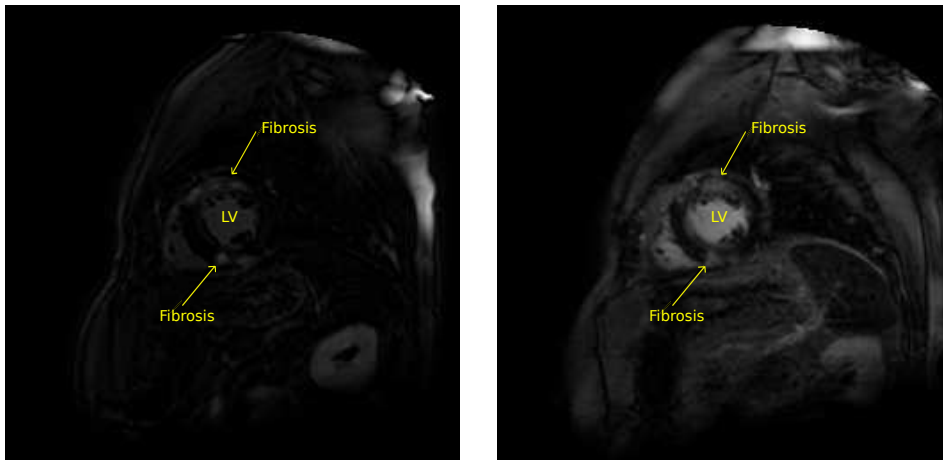


FIGURE 6.3— Example of LGE-SAX IR (left) and PSIR (right) acquisitions

6.4 The assessment of cardiac fibrosis detection in LGE-MRI: A brief state-of-the-art

Several studies have shown the relevance of Late Gadolinium Enhancement in cardiovascular magnetic resonance imaging in the location and the assessment of myocardial fibrosis (ORDOVAS et al., 2011). The accurate estimation of the transmural extent (from the endocardic to the epicardic zone) of the hyper-enhanced regions is crucial to estimate functional myocardial

recovery after reperfusion therapy that is a medical treatment after the patient has suffered from myocardial infarction, or heart attack.

Also, the degree of improvement in global wall-motion and ejection fraction is significantly related to the transmural extent of LGE. In ischemic cardiomyopathy, the transmural extent of LGE is predictive of adverse LV remodeling. At the clinical level, infarct size is an independent prognostic factor for heart failure, arrhythmic events and cardiac mortality (MEWTON et al., 2011), (ADABAG et al., 2008). Patterns of fibrosis may be also used to differentiate HCM from secondary causes of LV hypertrophy such as aortic stenosis or severe hypertension (RUDOLPH et al., 2009).

Earlier studies performed visually assessment of the transmural extent of Gadolinium enhanced and the amount of functional recovery using semiquantitative Likert scales. For example, in (KIM et al., 2000), the segmental transmural extent of the scar was graded on the conventional five-class scale: 0=no hyper-enhancement, 1=hyper-enhancement extending from 1 to 25% of LV wall thickness, 2=hyper-enhancement extending from 26% to 50% of LV wall thickness, 3=hyper-enhancement extending from 51% to 75% of LV wall thickness and 4=hyperenhancement extending from 76% to 100% of LV wall thickness.

An automated segmental scoring of infarct extent begins with the detection of the infarct on the images. Several methods based on the tuning of signal intensity thresholds with manual interaction of the user (AMADO et al., 2004; GERBER et al., 2002; KIM et al., 2000; SCHUIJF et al., 2004) or automated definition of the infarcted zones using morphological operators (HSU et al., 2006; KOLIPAKA et al., 2005) have been developed to this end.

An overview of previously published scar detection, quantification and segmentation methods in LGE-CMR is presented in (KARIM et al., 2013) where a standardised evaluation benchmarking framework for algorithms segmenting fibrosis and scar in left atrium (LA) myocardium from LGE-CMR images is also presented. Table 6.1 shows the overview reported in (KARIM et al., 2013) in terms of: a) the model or type of data evaluated (canine or human), b) the number of datasets, c) the structure of interest: LV or LA, d) the method employed and finally e) the evaluation measures used.

Most methods employed comprise: i) simple standard deviation (SD) thresholding taking as reference a base healthy tissue intensity value (KIM et al., 1999), (AMADO et al., 2004), (KOLIPAKA et al., 2005), (YAN et al., 2006), (SCHMIDT et al., 2007), (OAKES et al., 2009), ii) the full-width-at-half-maximum (FWHM) used to identify the infarct boundaries into an initial region that include all pixels with signal intensity (SI) $>50\%$ of maximum (AMADO et al., 2004), iii) expectation-maximisation (EM) fitting of a mixture model consisting in the Rayleigh distribution to represent the darker healthy myocardium, and the Gaussian distribution to represent the bright late enhanced regions (HENNEMUTH et al., 2008), iv) the Graph-cuts method which combines the intensity and boundary information to separate infarct from healthy myocardium, and v) methods based on clustering that avoid the choice of gray level thresholds (DETSKY et al., 2009; KACHENOURA et al., 2008; POSITANO et al., 2005).

The visualization of infarcted regions can be performed by using the maximum intensity

projection (MIP) of the intensities from the MR images into an anatomically derived cardiac surface (KNOWLES et al., 2010).

TABLE 6.1– Overview of previously published scar detection, quantification and segmentation methods presented in (KARIM et al., 2013)

Reference	Model	n	LV/LA	Method	Evaluation
(KIM et al., 1999)	Canine	26	LV	SD	Infarct size, ex-vivo
(AMADO et al., 2004)	Animal	13	LV	SD, FWHM	Bland altman, Infarct volume
(KOLIPAKA et al., 2005)	Human	23	LV	SD	Percentage scar, Bland-Altman
(POSITANO et al., 2005)	Human	15	LV	Clustering	Percentage scar
(YAN et al., 2006)	Human	144	LV	SD	Percentage scar
(SCHMIDT et al., 2007)	Human	47	LV	SD	Infarct size
(HENNEMUTH et al., 2008)	Human	21	LV	EM fitting	Percentage scar, Bland-Altman
(OAKES et al., 2009)	Human	81	LA	SD	Percentage scar
(DETSKY et al., 2009)	Human	15	LV	Clustering	Infarct size
(TAO et al., 2010)	Human	20	LV	Otsu thresholding	Dice
(KNOWLES et al., 2010)	Human	7	LA	MIP	Percentage scar
(LU et al., 2012)	Human	10	LV	Graph-cuts	Infarct size and Bland-Altman

(SD) = simple standard deviation thresholding, (FWHM)=full-width-at-half-maximum

(MIP)= maximum intensity projection, (EM)= expectation-maximisation.

In clustering methods, the fuzzy *c*-means is an unsupervised approach providing each voxel with a level of membership to both, LGE and non-LGE classes, describing the belongingness of the voxel to the class. The level of membership is a number between 0 and 1. This is advantageous in the case of fibrosis quantification because, excepted for highly enhanced pixels with a bright gray intensity, the enhancement between fibrotic and not fibrotic tissues remains unprecise.

The 6 standard deviations above the mean signal of the remote myocardium (the region with no contrast enhancement and normal wall thickening) method was previously shown to best correlate with visual LGE assessment and was used in several large studies analyzing the relation between fibrosis and clinical events in patients with HCM (MALEK et al., 2015; SPIEWAK et al., 2010).

In (BARON et al., 2013), a comparison of various methods for quantitative evaluation of myocardial infarct volume from LGE-CMR data is presented. The necrosis volumes were quantified using: 1) manual delineation, 2) automated fuzzy *c*-means method, and 3) +2 to 6SD thresholding approaches. The fuzzy *c*-means method proved appropriate correlations with biochemical myocardial infarct (scar) quantification as well as LV function parameters.

Segmentation of fibrosis or scar in LGE-CMR is challenging due to multiple causes including contrast variation due to inversion time, signal-to-noise ratio, motion blurring and artefacts (PETERS et al., 2007). The inversion time choice can generate the appearance of more or less scar, and change the appropriate scar threshold. Motion blurring also reduces the appearance of scar (KARIM et al., 2013). In the next section we present our proposed approach that is based on dictionary learning for the detection of fibrosis without the needs of tuning threshold parameters.

6.5 The proposed method

We follow the idea of the framework for clustering datasets that are well represented in the sparse modeling framework with a set of learned dictionaries (SPRECHMANN et al., 2010). In this framework, a set of K clusters is used to learn K dictionaries for representing the data, and then associate each signal to the dictionary for which the best sparse decomposition is obtained.

The proposed approach in LGE-MRI is applied in each LGE-SAX image (from basal to apical planes) to detect enhanced and non-enhanced regions by splitting each image in several patches. Based on the DL framework, firstly, an initial dictionary is constructed with learning samples from 2 clusters (LGE and Non-LGE regions). Secondly, the sparse coefficients of the learning data are computed and then used to train a K -Nearest Neighbor (K -NN) classifier. Finally, the label (LGE/Non-LGE) of a test patch is obtained with its respective sparse coefficients obtained over the learned dictionary and using the trained K -NN classifier. The zones of fibrosis can be finally detected in the myocardium delimited by the endo- and epicardial contours. Figure 6.4, resumes the proposed fibrosis detection procedure. The process is thus divided in 4 stages as described next (MANTILLA et al., 2015).

6.5.1 Feature extraction

The ability to compare image regions (patches) has been the basis of many approaches to core computer vision problems, including object, texture and scene categorization (SHAKHNAROVICH, 2005).

Firstly, in order to normalize the intensity differences across slices and subjects, each LGE-SAX image is normalized. For that purpose, each pixel in each LGE-SAX image is set to $(I_{i,j} - \mu) / \sigma$, where, $I_{i,j}$ is the interpolated pixel intensity value, μ and σ are, respectively, the mean and the standard deviation of the LGE-SAX image (LU et al., 2009).

Secondly, from different patients, random non-overlapping patches covering enhancing and non-enhancing regions from LGE-SAX images in the medial plane are extracted. The random extraction procedure was guided by the selection of approximately one half of the extracted patches with high gray level intensity values and the other half with low gray level intensity values. We have performed several experiments varying the number of patches and found out that selecting 1184 patches from 4 random patients achieves a good trade-off between complexity and visual detection performance. Thus the learning samples takes 296 patches from each one of the selected patients.

Figure 6.5 shows an example of the feature extraction from 4 random LGE-SAX images. The non-labeled extracted patches can belong to different regions: LV and RV cavities, fibrosis and other regularly enhancing and non-enhancing structures inside and outside the heart.

The similarity among the extracted patches is then calculated by using a Gaussian (radial basis function RBF) kernel with bandwidth σ (cf. 2.7). The RBF kernel on two samples \mathbf{x} and \mathbf{x}' , represented as feature vectors in some input space, is defined as:

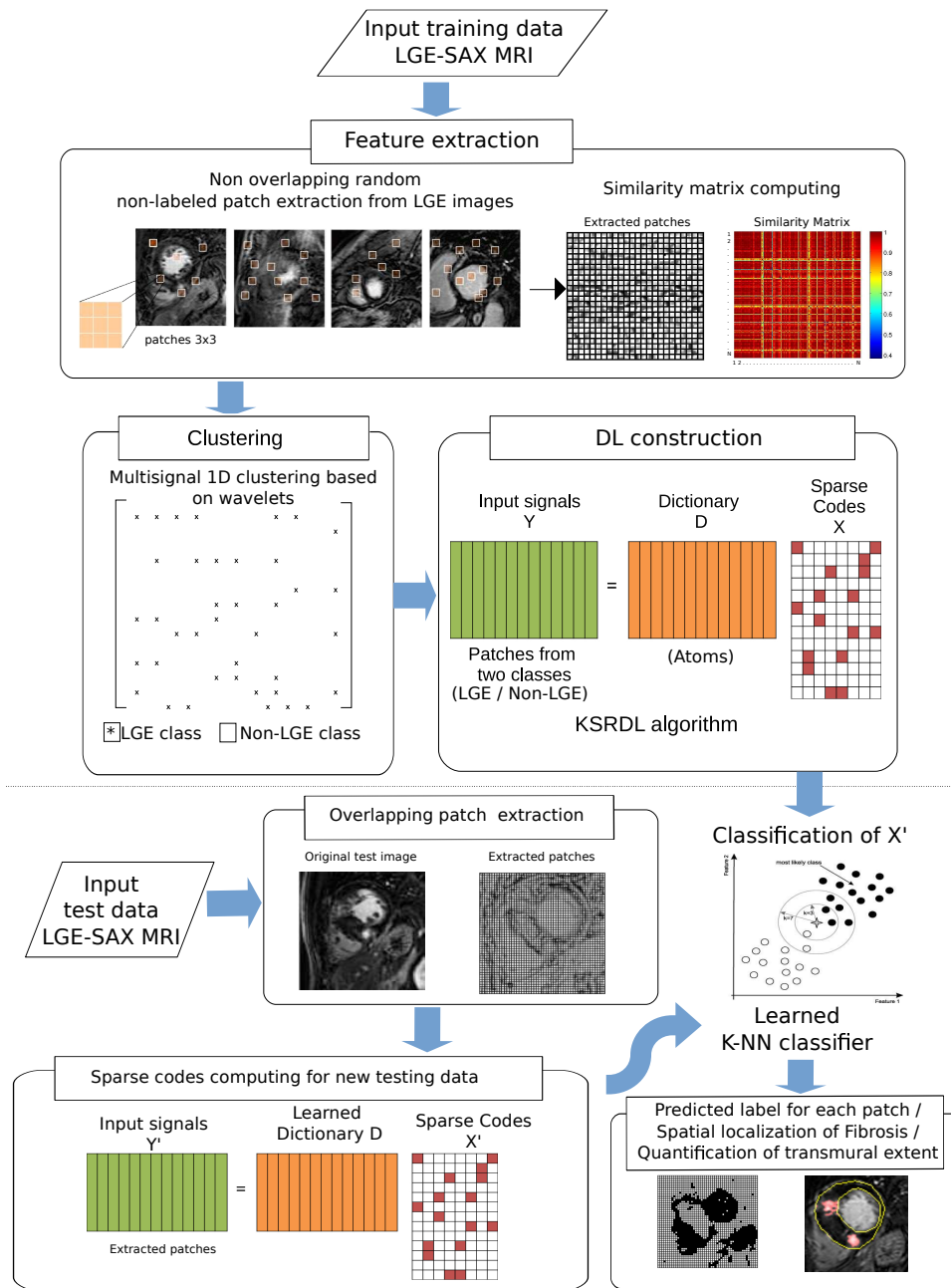


FIGURE 6.4— Overview of the proposed fibrosis detection method: in a training stage, feature extraction is performed with the extraction of non-overlapping patches from random LGE-SAX training images, then a similarity matrix among the extracted patches is computed. In a clustering step, two clusters are obtained from the similarity matrix among the training patches after performing a multisignal 1-D clustering based on wavelets: LGE/Non-LGE pixels. In a DL construction step, a dictionary is constructed with the clustered patches in two classes and a K -NN classifier is trained with the sparse codes coefficients of the training patches obtained from a DL algorithm based on kernel. In a testing stage, a new LG-SAX image is partitioned in overlapping patches and their sparse codes are computed using the learned dictionary. The label of each patch is predicted by using the trained K -NN classifier. In a post processing step the spatial localization of fibrosis and the quantification of transmural extent is performed.

$$K(\mathbf{x}, \mathbf{x}') = \exp\left(\frac{-\|\mathbf{x} - \mathbf{x}'\|_2^2}{\sigma^2}\right) \quad (6.1)$$

Since the value of the RBF kernel decreases with distance and ranges between zero (in the limit) and one (when $\mathbf{x} = \mathbf{x}'$), it has a ready interpretation as a similarity measure.

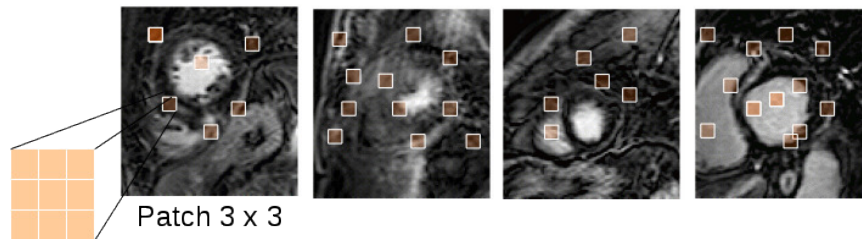


FIGURE 6.5– Feature extraction example from LGE-SAX images

In figure 6.6-left, a subset of 576 extracted patches is shown, while in figure 6.6-right, a portion of the similarity among all the extracted patches is presented where, high values of similitude between patches are represented in red and low values are represented in blue.

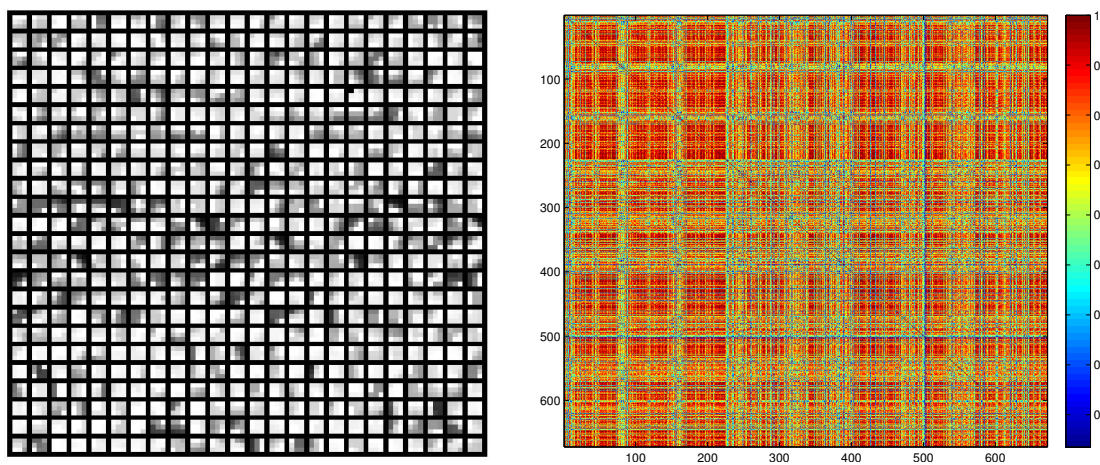


FIGURE 6.6– Extracted patches from LGE-SAX images (left) and its respective Similarity matrix (right)

6.5.2 Clustering

The initialization of the dictionary is very important for the success of the fibrosis detection process. Due to the cost associated with the procedure, repeating random initializations is practically impossible. Thus a “smart” initialization is needed. We propose the construction of an initial dictionary with two classes based on an unsupervised clustering process over the similarity measures among patches. Specifically, the aim is to split the patches in two classes, each one associated respectively with LGE and non-LGE regions.

For simplicity, we apply a clustering approach based on Wavelets (MISITI et al., 2007) which constructs clusters from a hierarchical cluster tree. This clustering approach was used in the construction of the Clustering curve parameter (Cl) in the LV wall motion classification problem presented in the previous chapter achieving good performance results. In this case, the input matrix of the clustering algorithm corresponds to the similarity matrix among patches. Each row of this matrix is decomposed using the DWT function with the Haar Wavelet. A binary hierarchical cluster tree is constructed with the first level coefficients of the decomposition. Pairs of objects that are in close proximity are linked using the euclidean distance. Data is then partitioned into two clusters.

6.5.3 DL-based classification: training stage

The detection of fibrosis is performed by adapting the Kernel Sparse Representation DL algorithm (KSRDL) (LI et al., 2013) (cf. 2.6.2) with an initial dictionary resulting from the clustering process described before where training patches are identified in two classes LGE and non-LGE patches. In the KSRDL algorithm, also applied for the assessment of LV wall motion with local parametric evaluation (cf. 5.7), sparse representation is introduced from a Bayesian viewpoint assuming Gaussian prior over the atoms of the dictionary. The KSRDL model is defined as follows:

$$\min_{\mathbf{D}, \mathbf{X}} \frac{1}{2} \|\mathbf{Y} - \mathbf{D}\mathbf{X}\|_F^2 + \frac{\alpha}{2} \text{trace}(\mathbf{D}^T \mathbf{D}) + \lambda \sum_{i=1}^N \|\mathbf{x}_i\|_1, \quad (6.2)$$

where the input signals $\mathbf{Y} \in \mathbb{R}^{n \times N}$ represent a data matrix of patches where each column is a vectorised patch (n is the signal size, N is the number of input signals or patches). $\mathbf{D} = [\mathbf{d}_1, \mathbf{d}_2, \mathbf{d}_3, \dots, \mathbf{d}_K] \in \mathbb{R}^{n \times K}$ with K atoms is the dictionary to be learned and $\mathbf{X} = [\mathbf{x}_1, \mathbf{x}_2, \dots, \mathbf{x}_N] \in \mathbb{R}^{K \times N}$ are the estimated sparse codes of input signals \mathbf{Y} . A K -NN classifier is constructed over the sparse training coefficients matrix \mathbf{X} before to perform the classification based on DL.

6.5.4 DL-based classification: testing stage

The class label of new p test instances can be predicted using the classifier obtained in the training step and the learned dictionary \mathbf{D} . As the selected classifier is trained based on the sparse coefficients of the input data, the test data need to be represented in the same space of representation (sparse coefficients) over the learned dictionary. To this end, the sparse coefficients matrix \mathbf{X} for the new test instances can be obtained by solving the Non negative Quadratic Problem (NNQP):

$$\min_{\mathbf{X}} \sum_{i=1}^p \frac{1}{2} \mathbf{x}_i^T \mathbf{H} \mathbf{x}_i + \mathbf{g}_i^T \mathbf{x}_i \quad s.t. \quad \mathbf{X} \geq 0 \quad (6.3)$$

where $\mathbf{H}_{k \times k} = \mathbf{D}^T \mathbf{D}$ and $\mathbf{g} = -\mathbf{D}^T \mathbf{Y}$. As the optimization of the above problems only require inner products between the data, the sparse coding problem is solved by replacing inner products to a radial basis function (Gaussian) kernel.

Each LGE-SAX test image is represented as input by a grid of overlapping feature patches of dimension $[3 \times 3]$. The sparse coefficients of each patch (LGE and non-LGE) are obtained as described previously with the learned dictionary and then, the label of each patch is obtained using the trained K -NN classifier. By the overlapping of patches, each pixel is categorized as LGE or non-LGE pixel. Finally, the LGE pixels corresponding to myocardium fibrosis zones are selected by adding a spatial constraint given with the endo- and epicardial borders of the myocardium.

6.6 First experiments and results

6.6.1 Study population

This study was performed in collaboration with the CIC-IT¹ 804 (BETANCUR, 2014) including 30 HCM data patients that have been acquired in the CHU Pontchaillou in Rennes. HCM was defined as recommended by recent guidelines (MEMBERS et al., 2011).

6.6.1.1 Patient selection

The inclusion and exclusion criteria were:

- Inclusion criterion: Subjects carrying a primitive non obstructive HCM with left ventricular ejection fraction (LVEF) greater than 60%, in sinus rhythm.
- Exclusion criteria: Prospective subjects with one of the following characteristics were disqualified from inclusion in this study: under legal age, contraindication to MRI (in particular, patients with an implanted cardiac stimulator/defibrillator at the moment of MRI acquisition), history of coronary artery disease, permanent atria fibrillation, left ventricular systolic dysfunction (LVEF \leq 60%).

All patients had a clinical examination, a resting arterial blood pressure measurement (Dinamap Procure Auscultatory 100), a resting 12-lead electrocardiogram, a transthoracic echocardiography (Vivid 7, General Electric Healthcare, Horten, Norway) and a cardiac MRI (Philips Achieva 3T).

6.6.1.2 Cardiac magnetic resonance imaging

CMR images were performed with a 3T Achieva® clinical imager (Philips Medical Systems, Best, The Netherlands), using cardiac SENSE Coil (multicoil). Cardiac synchronization was performed using a four-electrode vectocardiogram. Scout images were acquired initially to identify the cardiac axes. CMR acquisitions included cine-SAX, cine-LAX (4CH, 2CH), LGE-SAX and LGE-LAX (4CH, 2CH). Among the LGE-CMR acquisitions, IR and PSIR sequences were acquired, retrospective ECG-gated acquisition at mid-diastole and breath-hold volumetric SAX, 4CH and 2CH. Typical parameters for these acquisitions were:

1. Acronym from the French “Centre d’Investigation Clinique Innovation Technologique”.

- IR Acquisition: Turbo field echo (IR-TFE). TR/TE/FA=4.01 ms/1.23 ms/15°, IR prepulse delay = 280 ms,
- PSIR Acquisition: TR/TE/FA = 4.50 ms/2.19 ms/15°, IR prepulse delay = 280 ms,
- IR, PSIR resolution: 256×256 pixels (in-plane) with 16 and 12 slices for SAX and LAX, respectively. In-plane pixel size=1.25 × 1.25 mm², spacing between slices=5 mm, acquisition slice thickness=10 mm. Given that the spacing between slices is half of the slice thickness, image slices overlaps in a half of their thickness. This resulted in an output image volume with slice thickness=5 mm. All IR and PSIR acquisitions were acquired following this procedure (slice overlapping). This aimed at improving the observability of small portions with fibrosis

For this study LGE-SAX images in inversion recovery (IR) from 11 patients in the set of 30 HCM patients were retained (patients with exploitable LGE images).

6.6.2 Results

In the training stage, a set of 1184 non-overlapping patches from 4 random inter-patients LGE-SAX IR images at mid-diastole and at mid-cavity plane are extracted in order to construct the initial dictionary. The first stage of clustering process splits the patches in two clusters (LGE and non-LGE) of size 952 and 232 respectively. Then, the KSRDL algorithm (LI et al., 2013) is applied in order to obtain the sparse codes of the training data that are used in the K -NN classifier.

Several experiments were performed by reducing the number of atoms employed to represent each testing patch in the learned dictionary. The results presented here were obtained by using $K=15$ atoms from the initial dictionary to train the classifier and to represent each patch. The DL regularization parameter λ and the parameter α for the Gaussian kernel were tuned by heuristic search in a mesh from 0.01 to 10 with a step of 0.01. The final values used in this experiments were: $\lambda = 0.001$ and $\alpha=0.1$.

Several experiments has been realized varying the size of the feature patch. Figure 6.7 shows an example of a LGE-SAX image with the detection of structures varying the patch size for $[3\times 3]$, $[5\times 5]$ and $[7\times 7]$.

As it has been observed and as we can see visually in these images, a good detection of enhanced pixels is achieved by selecting patches of a dimension $[3\times 3]$. Figures 6.8 - 6.13 show LGE-SAX images at mid-cavity plane for the 11 HCM patients of the database and the Fibrosis detection using the proposed approach. In these figures, the original image for each patient is shown in the left part and the detected fibrosis is represented on the right part in colors inside the myocardium delimited by endo- and epicardial boundaries that have been manually delineated by a cardiologist.

About computing times, the proposed method employ about 59.38 seconds in the Clustering stage and for training the classifier about 83.46 seconds. For testing, the method employ about 26.35 seconds for the detection of pixels LGE per slice and per patient.

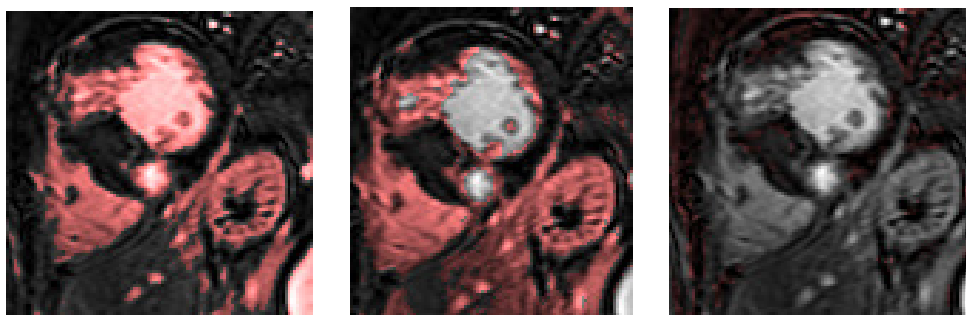


FIGURE 6.7– Examples of resulting fibrosis detection using the proposed approach with patches of size $[3 \times 3]$ (left), $[5 \times 5]$ (middle) and $[7 \times 7]$ (right)

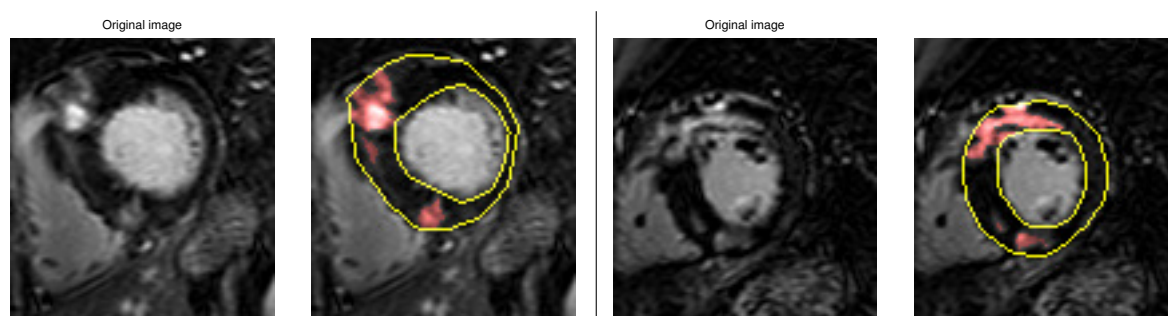


FIGURE 6.8– Examples of resulting fibrosis detection using the proposed approach: Patients 01 and 02

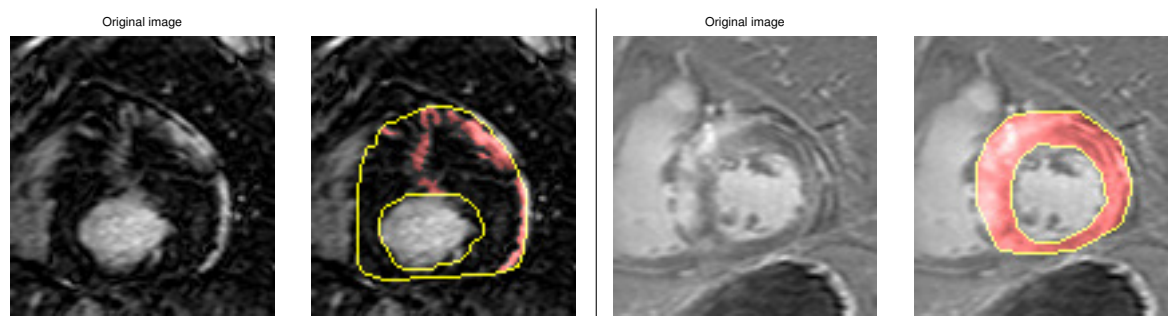


FIGURE 6.9– Examples of resulting fibrosis detection using the proposed approach: Patients 03 and 04

6.6.3 Evaluation

In a first step of evaluation, a visual analysis by a cardiologist has been performed. The proposed method is able to detect fibrosis in 9 of 11 patients. The method misclassified LGE pixels in all the slices of the patient 04, classifying 100% of the pixels as LGE pixels due to the low contrast observed between myocardium and the LV cavity. In patient 07, the method misclassified LGE pixels in apical slices.

In a second step of evaluation, our method has been compared with one method of the literature that has been proposed for the detection of fibrosis in LGE-MRI. The fuzzy *c*-means

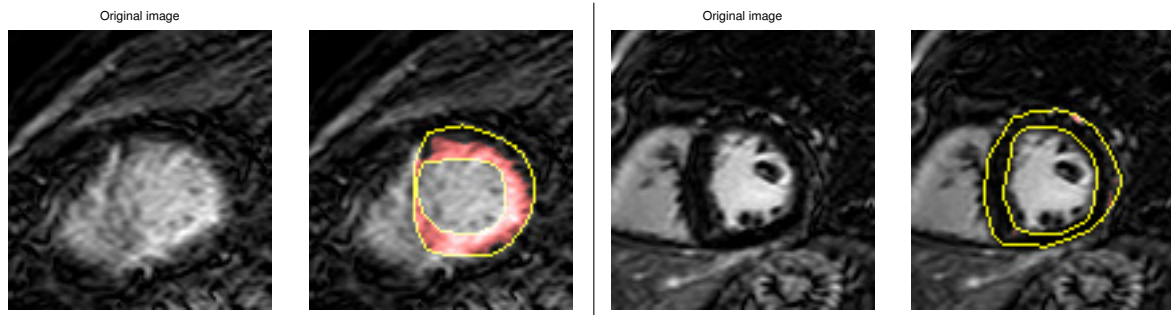


FIGURE 6.10— Examples of resulting fibrosis detection using the proposed approach: Patients 05 and 06

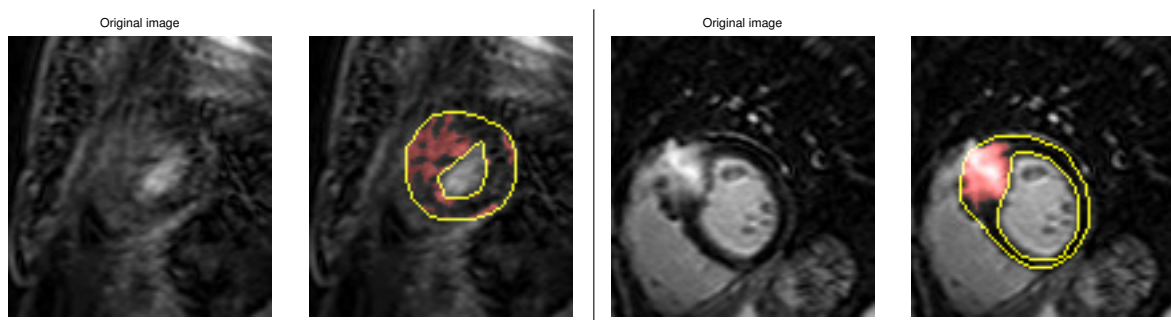


FIGURE 6.11— Examples of resulting fibrosis detection using the proposed approach: Patients 07 and 08

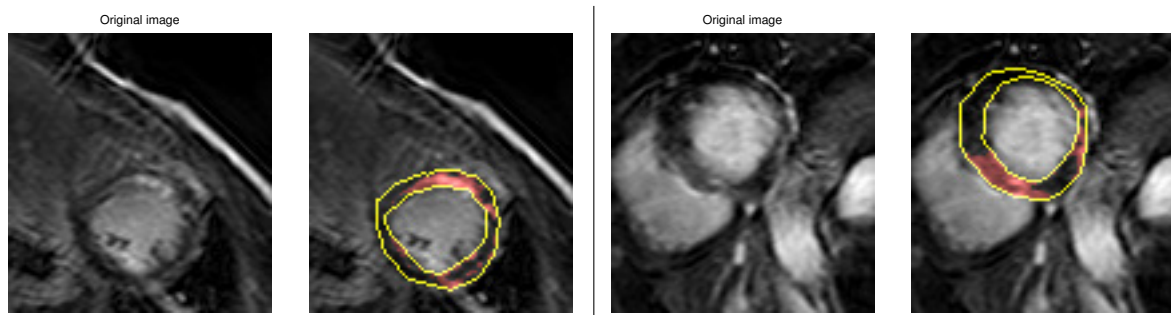


FIGURE 6.12— Examples of resulting fibrosis detection using the proposed approach: Patients 09 and 10

method proposed by (KACHENOURA et al., 2008) has been retained to compare the results.

The fuzzy *c*-means method is an unsupervised method classifying the pixels in the myocardium as belonging to one out of two possible classes: LGE pixels of non-LGE pixels. This approach provides each pixel with a level of membership to both, LGE and non-LGE classes, describing the belongingness of the pixel to the class. The level of membership is a number between 0 and 1. The approach includes a defuzzification procedure to obtain a binary description of those pixels being part or not of LGE class (fibrosis for pixels inside the myocardium). Then, for the entire myocardium, a threshold of the LGE-class membership was varied between 0.25 and 0.5, and the curve representing the number of LGE-pixels was plotted over these varying threshold. Then the threshold value providing the most stable output (the longest portion in which the

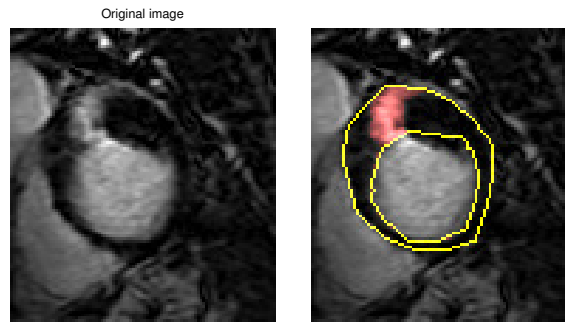


FIGURE 6.13— Examples of resulting fibrosis detection using the proposed approach: Patient 11

number of LGE-pixels remains the same), was selected as the optimal one (BARON et al., 2013). This threshold is then used to get a binary image from the output of the fuzzy c-means approach. This approach has been applied in our data and were obtained from (BETANCUR, 2014). Figure 6.14 illustrates the comparison of this approach and our method for 3 patients.

Figure 6.14-top illustrates the output of the fuzzy c-means for the LGE-pixel class for the pixels into the myocardium. Figure 6.14-middle shows the resulting detection of fibrosis for the patients on the top after the defuzzification procedure. Figure 6.14-bottom shows the resulting detection of fibrosis using our proposed approach. It can be noted that the fibrotic zones are identified in both methods, for those regions presenting a high concentration of pixels with late gadolinium enhancement, however, in general the number of pixels LGE detected by the two methods are different.

To illustrate, Table 6.2 shows the quantification of pixels LGE for the patients shown in figure 6.14 by the two methods and for each slice. The values shown in this table represent, for each slice, the percentage of pixels LGE with respect to the total number of pixel in the myocardium. In the same table, values for three patients in figure 6.14 are resalted. It can be seen that for the patient 02 both methods detect the same percentage of pixels LGE. For the other two patients, our method detect in general more LGE pixels than with the fuzzy c-method. In apical slices (1-5) both methods detect small number of pixels LGE (MANTILLA et al., 2015). These first quantitative results need to be completed by more experiments.

6.7 Qualification and Quantification of myocardial Fibrosis: A first proposal

The importance of detecting myocardial fibrosis in patients with HCM lies in the potential prognostic implication of this finding (O'HANLON et al., 2010). Previous studies have shown that the amount of myocardial fibrosis and the degree of cardiomyocyte degeneration are inversely related to both systolic and diastolic left ventricular (LV) function (HEIN et al., 2003).

For the detection and quantification of the fibrotic area, we perform a spatial localization of the myocardial fibrosis according the AHA 17 model representation.

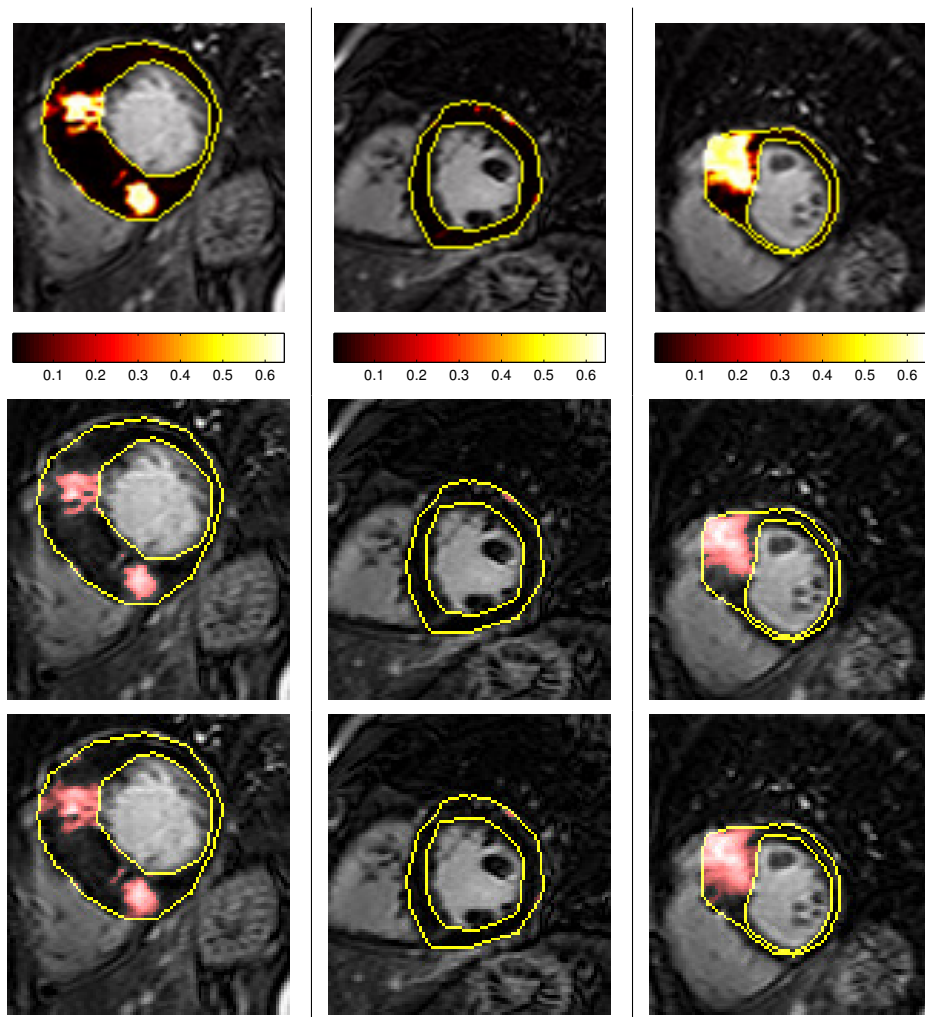


FIGURE 6.14— Comparison of results illustrated for three patients (P01 - P02 - P08): Top: the output of the fuzzy c -means with the membership map of the LGE-class. Middle: The final result with fuzzy c -mean approach. Bottom: The fibrosis detection using the proposed approach

To identify the LV anatomical segments according to the AHA model, firstly, the LV centroid is automatically calculated using the contour of the endocardium delineated by a cardiologist. Secondly, the anterior intersection between the Right and Left ventricles is manually positioned by the user. By using a radial reference line traced from the LV centroid to the anterior intersection between LV and RV, the myocardium is divided in different anatomical segments at the different level slices (basal, mid-cavity and apical): 6 segments for basal and mid-cavity slices using an angular variation of 60° and 4 segments for the apical slices using an angular variation of 90° . This procedure allows the localization of fibrosis by anatomical segments. Figure 6.15 shows an illustrative example of this procedure.

To illustrate, Figure 6.16 shows the result of the spatial localization of fibrosis LGE-SAX images at the mid-cavity plane in three patients. In Figure 6.16-left, fibrosis is localized in the anteroseptal and inferoseptal regions. For the patient in the Figure 6.16-middle, fibrosis is

TABLE 6.2– Quantification of cardiac Fibrosis per slice level in Patients 01, 02 and 08

Plane	Slice	P01	P02	P08
		fuzzy - DL	fuzzy - DL	fuzzy - DL
Apical	1	0.00 - 3.82	0.00 - 0.00	0.00 - 0.55
	2	0.06 - 5.01	0.00 - 0.00	0.00 - 0.75
	3	0.00 - 2.72	0.00 - 0.00	0.12 - 2.86
	4	1.60 - 3.26	0.79 - 0.79	2.00 - 5.36
	5	0.16 - 5.82	1.89 - 7.86	5.14 - 7.27
	6	0.15 - 5.38	3.49 - 16.98	5.00 - 7.11
Mid-cavity	7	7.59 - 10.08	12.30 - 22.10	7.78 - 13.68
	8	4.52 - 5.72	19.93 - 23.02	4.00 - 7.14
	9	1.09 - 6.56	24.32 - 19.12	4.55 - 7.97
	10	1.62 - 6.91	25.02 - 15.81	10.00 - 12.95
	11	1.44 - 8.06	11.59 - 11.91	10.29 - 13.75
	12	3.07 - 13.51	9.18 - 9.18	15.00 - 14.25
Basal	13	4.13 - 15.13	10.23 - 6.92	10.21 - 13.35
	14	5.97 - 19.81	1.84 - 6.51	24.16 - 37.77
	15	16.18 - 21.04	1.87 - 2.17	36.29 - 47.30
	16	12.57 - 21.78	0.00 - 0.50	29.72 - 37.54

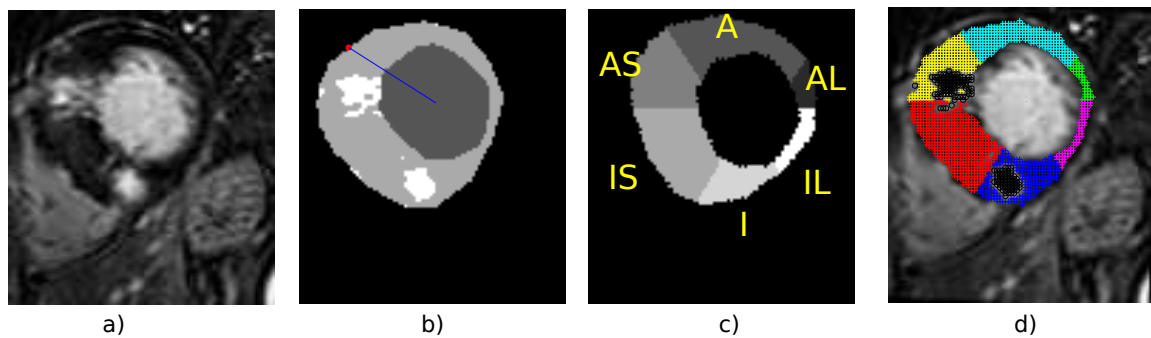


FIGURE 6.15– Framework for spatial localization of fibrosis using the proposed approach over a LGE-SAX image at mid-cavity plane: a) the original LGE-SAX image, b) a reference line from the LV centroid to the anterior intersection between RV and LV superimposed over the LV myocardium with the respective zones of fibrosis, c) the 6 anatomical segments identified in the figure at the left: AL= Antero Septal, A= Anterior, AS=Antero septal, IS=Infero Septal, I= Inferior and IL=Infero Lateral, d) the spatial localization of fibrosis according the LV anatomical segmets.

present in the anterior and anteroseptal segments and also in the inferior segment. Finally, for the patient in the Figure 6.16-right, fibrosis can be observed in the anterior and anteroseptal regions.

The quantification of fibrosis is performed by calculating the percentage of LGE pixels in one particular anatomical segment with respect to the total number of pixels in the myocardium. Table 6.3 shows the quantification of fibrosis of the patient 02 shown in the middle of Figure 6.16.

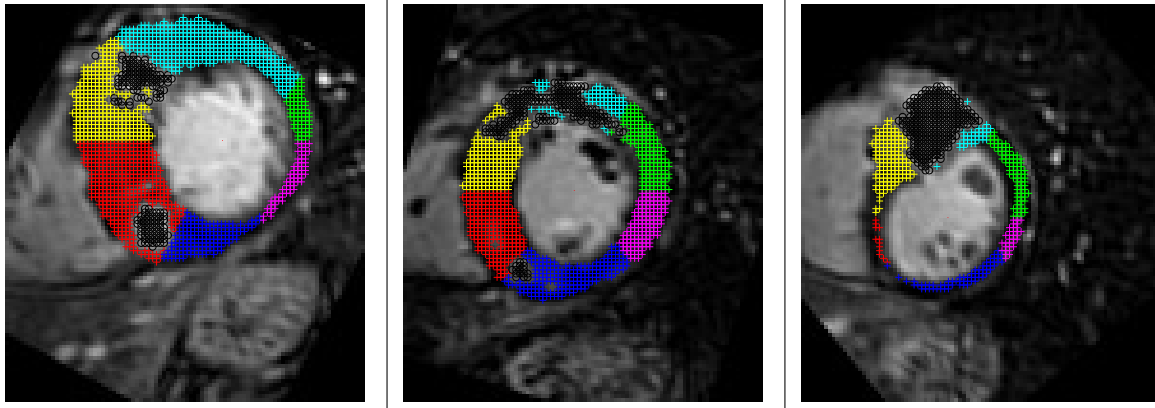


FIGURE 6.16– Spatial localization of fibrosis using the proposed approach for patients 01, 02 and 08.

TABLE 6.3– Quantification of cardiac Fibrosis per segment and slice level in Patient 02

Plane	Slice	AL	A	AS	IS	I	IL	(%) Total
Apical	1	0.00	0.00	0.00	0.00	0.00	0.00	0.00
	2	0.00	0.00	0.00	0.00	0.00	0.00	0.00
	3	0.00	0.00	0.00	0.00	0.00	0.00	0.00
	4	0.11	0.00	0.11	0.00	0.00	0.56	0.79
	5	1.88	0.00	1.44	0.00	0.00	4.54	7.86
	6	0.39	9.46	3.22	0.00	3.90	0.00	16.98
Mid-cavity	7	3.57	13.10	0.00	2.76	2.67	0.00	22.10
	8	0.96	12.38	4.36	0.00	5.32	0.00	23.02
	9	0.73	13.86	0.49	2.27	1.78	0.00	19.12
	10	0.41	11.63	2.38	1.06	0.33	0.00	15.81
	11	0.00	6.30	5.61	0.00	0.00	0.00	11.91
	12	0.00	2.69	6.49	0.00	0.00	0.00	9.18
Basal	13	0.00	1.68	5.24	0.00	0.00	0.00	6.92
	14	0.00	3.86	2.65	0.00	0.00	0.00	6.51
	15	0.00	1.79	0.38	0.00	0.00	0.00	2.17
	16	0.00	0.25	0.25	0.00	0.00	0.00	0.50

AL= Antero Septal, A= Anterior, AS=Antero septal
IS=Infero Septal, I= Inferior and IL=Infero Lateral

As we can see, the highest concentration of LGE pixels is quantified in the medial plane, with 23.02% of fibrosis presented in slice 8. In this slice, broader areas of fibrosis are observed in the anterior and antero-septal segments with 12.38% and 4.36% respectively.

Table 6.4 shows the quantification of fibrosis in each anatomical segment, calculating the percentage of LGE pixels in one particular anatomical segment with respect to the total number of pixels in that anatomical segment.

As we can see, the highest concentration of LGE pixels is quantified in the medial plane (slice 8), in which the Antero Septal segment presents 54.25% of fibrosis, the Anterior segment presents 51.89% and the Inferior segment presents 30.79% of fibrosis. Results are consistent

TABLE 6.4– Quantification of cardiac Fibrosis per segment and slice level in Patient 02

Plane	Slice	AL	A	AS	IS	I	IL
Apical	1	0.43	1.47	0.00	8.20	2.30	2.67
	2	0.40	0.46	0.00	0.00	0.00	1.81
	3	0.00	0.00	0.00	2.78	0.00	0.00
	4	1.20	9.05	3.83	0.00	3.28	0.00
	5	0.51	26.14	21.15	0.00	13.92	0.00
	6	0.00	33.95	41.42	0.92	23.43	0.00
Mid-cavity	7	0.52	42.09	50.39	0.00	29.52	0.67
	8	0.94	51.89	54.25	0.00	30.79	0.00
	9	0.00	51.55	44.44	2.00	23.76	0.00
	10	0.00	45.08	43.23	0.66	9.15	0.00
	11	0.51	34.39	37.85	0.38	0.37	0.00
	12	0.00	18.69	37.55	0.00	0.83	0.00
Basal	13	0.00	10.42	31.85	0.00	0.00	0.00
	14	0.00	12.23	34.83	0.00	0.60	0.00
	15	0.00	8.15	15.03	0.00	0.00	0.70
	16	1.11	1.78	12.90	2.56	2.30	2.14

AL= Antero Septal, A= Anterior, AS=Antero septal
IS=Infero Septal, I= Inferior and IL=Infero Lateral

with the observations in (HOEY et al., 2014; NOURELDIN et al., 2012) in which LGE most often involves the interventricular septum, particularly the anteroseptal mid to basal segments and right ventricular insertion points.

6.8 Conclusion

We have presented a method for the detection of Fibrosis in LGE-SAX images using a Dictionary learning-based clustering approach. The detection approach has been applied on a set of 11 patients with HCM from which LGE-SAX images at 16 different slices were processed. The proposed method allows the detection of fibrosis inside the myocardium using the endo- and epicardial boundaries manually delineated by a cardiologist. The method has been evaluated by a visual evaluation and by comparing with the results of one method of the literature. The method has been able to successfully detect fibrosis in 9 of the 11 patients. By using the boundaries and a manual localization of the anterior intersection between the right and left ventricles, the region of fibrosis can be localized in different anatomical segments according to the AHA representation. The method could also be applied without the endo- and epicardial contours resulting in a segmentation approach of different structures in the MRI image that has to be analyzed. The proposed method based on DL has resulted in a promising technique for the detection of fibrosis in LGE-MRI that deserves more extensive validation. The method should be evaluated in a quantitative way on a set of more HCM patients with the fibrotic zones delineated by an expert. It must be deepened with broader experiments in the clustering and DL stages, for example,

varying the number of patches for the initialization of the dictionary and performing a manual selection of LGE/Non LGE pixels. An analysis of the retained atoms used to represent each testing patch is also required.

References

- ADABAG, A. S., B. J. MARON, E. APPELBAUM, C. J. HARRIGAN, J. L. BUROS, C. M. GIBSON, J. R. LESSER, C. A. HANNA, J. E. UDELSON, W. J. MANNING, and M. S. MARON (2008). “Occurrence and frequency of arrhythmias in hypertrophic cardiomyopathy in relation to delayed enhancement on cardiovascular magnetic resonance”. In: *Journal of the American College of Cardiology* 51.14, pp. 1369–1374.
- AMADO, L. C., B. L. GERBER, S. N. GUPTA, D. W. RETTMANN, G. SZARF, R. SCHOCK, K. NASIR, D. L. KRAITCHMAN, and J. A. C. LIMA (2004). “Accurate and objective infarct sizing by contrast-enhanced magnetic resonance imaging in a canine myocardial infarction model”. In: *Journal of the American College of Cardiology* 44.12, pp. 2383–2389.
- BARON, N., N. KACHENOURA, P. CLUZEL, F. FROUIN, A. HERMENT, P. GRENIER, G. MONTALESCOT, and F. BEYGUI (2013). “Comparison of various methods for quantitative evaluation of myocardial infarct volume from magnetic resonance delayed enhancement data”. In: *International Journal of Cardiology* 167.3, pp. 739–744.
- BAUM, J. and H. S. DUFFY (2011). “Fibroblasts and Myofibroblasts: What are we talking about?” In: *Journal of cardiovascular pharmacology* 57.4, pp. 376–379.
- BETANCUR, J. (2014). “Multimodal image registration for the characterization of the hypertrophic cardiomyopathy and the cardiac asynchronism”. PhD thesis. Université Rennes 1.
- DETSKY, J. S., G. PAUL, A. J. DICK, and G. A. WRIGHT (2009). “Reproducible classification of infarct heterogeneity using fuzzy clustering on multicontrast delayed enhancement magnetic resonance images”. In: *IEEE transactions on medical imaging* 28.10, pp. 1606–1614.
- GERBER, B. L., J. GAROT, D. A. BLUEMKE, K. C. WU, and J. A. C. LIMA (2002). “Accuracy of Contrast-Enhanced Magnetic Resonance Imaging in Predicting Improvement of Regional Myocardial Function in Patients After Acute Myocardial Infarction”. In: *Circulation* 106.9, pp. 1083–1089.
- HEIN, S., E. ARNON, S. KOSTIN, M. SCHÖNBURG, A. ELSÄSSER, V. POLYAKOVA, E. P. BAUER, W.-P. KLÖVEKORN, and J. SCHAPER (2003). “Progression from compensated hypertrophy to failure in the pressure-overloaded human heart: structural deterioration and compensatory mechanisms”. In: *Circulation* 107.7, pp. 984–991.
- HENNEMUTH, A., A. SEEGER, O. FRIMAN, S. MILLER, B. KLUMPP, S. OELTZE, and H.-O. PEITGEN (2008). “A comprehensive approach to the analysis of contrast enhanced cardiac MR images”. In: *IEEE transactions on medical imaging* 27.11, pp. 1592–1610.
- HOEY, E. T., M. ELASSALY, A. GANESHAN, R. W. WATKIN, and H. SIMPSON (2014). “The role of magnetic resonance imaging in hypertrophic cardiomyopathy”. In: *Quantitative Imaging in Medicine and Surgery* 4.5, pp. 397–406.

- HSU, L.-Y., A. NATANZON, P. KELLMAN, G. A. HIRSCH, A. H. ALETRAS, and A. E. ARAI (2006). “Quantitative myocardial infarction on delayed enhancement MRI. Part I: Animal validation of an automated feature analysis and combined thresholding infarct sizing algorithm”. In: *Journal of magnetic resonance imaging: JMRI* 23.3, pp. 298–308.
- HUGHES, S. E. (2004). “The pathology of hypertrophic cardiomyopathy”. In: *Histopathology* 44.5, pp. 412–427.
- KACHENOURA, N., A. REDHEUIL, A. HERMENT, E. MOUSSEAU, and F. FROUIN (2008). “Robust assessment of the transmural extent of myocardial infarction in late gadolinium-enhanced MRI studies using appropriate angular and circumferential subdivision of the myocardium”. In: *European Radiology* 18.10, pp. 2140–2147.
- KARIM, R., R. J. HOUSDEN, M. BALASUBRAMANIAM, Z. CHEN, D. PERRY, A. UDDIN, Y. AL-BEYATTI, E. PALKHI, P. ACHEAMPONG, S. OBOM, A. HENNEMUTH, Y. LU, W. BAI, W. SHI, Y. GAO, H.-O. PEITGEN, P. RADAU, R. RAZAVI, A. TANNENBAUM, D. RUECKERT, J. CATES, T. SCHAEFFTER, D. PETERS, R. MACLEOD, and K. RHODE (2013). “Evaluation of current algorithms for segmentation of scar tissue from late Gadolinium enhancement cardiovascular magnetic resonance of the left atrium: an open-access grand challenge”. In: *Journal of Cardiovascular Magnetic Resonance* 15.1, p. 105.
- KIM, R., D. FIENO, T. PARRISH, K. HARRIS, E. CHEN, O. SIMONETTI, J. BUNDY, J. FINN, F. KLOCKE, and R. JUDD (1999). “Relationship of MRI delayed contrast enhancement to irreversible injury, infarct age, and contractile function”. In: *Circulation* 100.19, pp. 1992–2002.
- KIM, R., E. WU, A. RAFAEL, E. CHEN, M. PARKER, O. SIMONETTI, F. KLOCKE, R. BONOW, and R. JUDD (2000). “The Use of Contrast-Enhanced Magnetic Resonance Imaging to Identify Reversible Myocardial Dysfunction”. In: *New England Journal of Medicine* 343.20, pp. 1445–1453.
- KNOWLES, B. R., D. CAULFIELD, M. COOKLIN, C. A. RINALDI, J. GILL, J. BOSTOCK, R. RAZAVI, T. SCHAEFFTER, and K. S. RHODE (2010). “3-D visualization of acute RF ablation lesions using MRI for the simultaneous determination of the patterns of necrosis and edema”. In: *IEEE transactions on bio-medical engineering* 57.6, pp. 1467–1475.
- KOLIPAKA, A., G. P. CHATZIMAVROUDIS, R. D. WHITE, T. P. O’DONNELL, and R. M. SETSER (2005). “Segmentation of non-viable myocardium in delayed enhancement magnetic resonance images”. In: *The International Journal of Cardiovascular Imaging* 21.2-3, pp. 303–311.
- KRENNING, G., E. M. ZEISBERG, and R. KALLURI (2010). “The Origin of Fibroblasts and Mechanism of Cardiac Fibrosis”. In: *Journal of cellular physiology* 225.3, pp. 631–637.
- LI, Y. and A. NGOM (2013). “Sparse representation approaches for the classification of high-dimensional biological data”. In: *BMC Systems Biology* 7.Suppl 4, S6.
- LU, Y., P. RADAU, K. CONNELLY, A. DICK, and G. WRIGHT (2009). “Pattern Recognition of Abnormal Left Ventricle Wall Motion in Cardiac MR”. In: *Proceedings of the 12th International Conference on Medical Image Computing and Computer-Assisted Intervention: Part II. MICCAI ’09*. London, UK: Springer-Verlag, pp. 750–758.

- LU, Y., Y. YANG, K. A. CONNELLY, G. A. WRIGHT, and P. E. RADAU (2012). “Automated quantification of myocardial infarction using graph cuts on contrast delayed enhanced magnetic resonance images”. In: *Quantitative Imaging in Medicine and Surgery* 2.2, pp. 81–86.
- MAISCH, B., M. NOUTSIAS, V. RUPPERT, A. RICHTER, and S. PANKUWEIT (2012). “Cardiomyopathies: Classification, Diagnosis, and Treatment”. In: *Heart Failure Clinics* 8.1, pp. 53–78.
- MAŁEK, Ł. A., K. WERYS, M. KŁOPOTOWSKI, M. ŚPIEWAK, B. MIŁOSZ-WIECZOREK, Ł. MAZURKIEWICZ, J. PETRYKA-MAZURKIEWICZ, M. MARCZAK, and A. WITKOWSKI (2015). “Native T1-mapping for non-contrast assessment of myocardial fibrosis in patients with hypertrophic cardiomyopathy — comparison with late enhancement quantification”. In: *Magnetic Resonance Imaging* 33.6, pp. 718–724.
- MANTILLA, J., J. L. PAREDES, J.-J. BELLANGER, J. BETANCUR, F. SCHNELL, C. LECLERCQ, and M. GARREAU (2015). “Detection of fibrosis in LGE-cardiac MRI using Kernel DL-based clustering”. In: *Computing in Cardiology*. (in press).
- MARON, B., J. GARDIN, J. FLACK, S. GIDDING, T. KUROSAKI, and D. BILD (1995). “Prevalence of hypertrophic cardiomyopathy in a general population of young adults. Echocardiographic analysis of 4111 subjects in the CARDIA Study. Coronary Artery Risk Development in (Young) Adults”. In: *Circulation* 92.4, pp. 785–789.
- MARON, M., E. APPELBAUM, C. HARRIGAN, J. BUROS, C. GIBSON, C. HANNA, J. LESSER, J. UDELSON, W. MANNING, and B. MARON (2008). “Clinical profile and significance of delayed enhancement in hypertrophic cardiomyopathy”. In: *Circulation. Heart Failure* 1.3, pp. 184–191.
- MEMBERS, W. C., B. J. GERSH, B. MARON, R. O. BONOW, J. A. DEARANI, M. A. FIFER, M. S. LINK, S. S. NAIDU, R. A. NISHIMURA, S. R. OMMEN, H. RAKOWSKI, C. E. SEIDMAN, J. A. TOWBIN, J. E. UDELSON, and C. W. YANCY (2011). “2011 ACCF/AHA Guideline for the Diagnosis and Treatment of Hypertrophic Cardiomyopathy A Report of the American College of Cardiology Foundation/American Heart Association Task Force on Practice Guidelines”. In: *Circulation* 124.24, e783–e831.
- MEWTON, N., C. Y. LIU, P. CROISILLE, D. BLUEMKE, and J. A. C. LIMA (2011). “Assessment of myocardial fibrosis with cardiovascular magnetic resonance”. In: *Journal of the American College of Cardiology* 57.8, pp. 891–903.
- MISITI, M., Y. MISITI, G. OPPENHEIM, and J.-M. POGGI (2007). “Clustering Signals Using Wavelets”. In: *Computational and Ambient Intelligence*. Ed. by F. SANDOVAL, A. PRIETO, J. CABESTANY, and M. GRAÑA. Lecture Notes in Computer Science 4507. Springer Berlin Heidelberg, pp. 514–521.
- MOON, J. C. C., E. REED, M. N. SHEPPARD, A. G. ELKINGTON, S. Y. HO, M. BURKE, M. PETROU, and D. J. PENNELL (2004). “The histologic basis of late gadolinium enhancement cardiovascular magnetic resonance in hypertrophic cardiomyopathy”. In: *Journal of the American College of Cardiology* 43.12, pp. 2260–2264.

- NOURELDIN, R. A., S. LIU, M. S. NACIF, D. P. JUDGE, M. K. HALUSHKA, T. P. ABRAHAM, C. HO, and D. A. BLUEMKE (2012). “The diagnosis of hypertrophic cardiomyopathy by cardiovascular magnetic resonance”. In: *Journal of Cardiovascular Magnetic Resonance* 14.1, p. 17.
- OAKES, R. S., T. J. BADGER, E. G. KHOLMOVSKI, N. AKOUM, N. S. BURGON, E. N. FISH, J. J. E. BLAUER, S. N. RAO, E. V. R. DiBELLA, N. M. SEGERSON, M. DACCARETT, J. WINDFELDER, C. J. MCGANN, D. PARKER, R. S. MACLEOD, and N. F. MARROUCHE (2009). “Detection and Quantification of Left Atrial Structural Remodeling With Delayed-Enhancement Magnetic Resonance Imaging in Patients With Atrial Fibrillation”. In: *Circulation* 119.13, pp. 1758–1767.
- O’HANLON, R., A. GRASSO, M. ROUGHTON, J. C. MOON, S. CLARK, R. WAGE, J. WEBB, M. KULKARNI, D. DAWSON, L. SULAIBEEKH, B. CHANDRASEKARAN, C. BUCCIARELLI-DUCCI, F. PASQUALE, M. R. COWIE, W. J. MCKENNA, M. N. SHEPPARD, P. M. ELLIOTT, D. J. PENNELL, and S. K. PRASAD (2010). “Prognostic significance of myocardial fibrosis in hypertrophic cardiomyopathy”. eng. In: *Journal of the American College of Cardiology* 56.11, pp. 867–874.
- ORDOVAS, K. G. and C. B. HIGGINS (2011). “Delayed Contrast Enhancement on MR Images of Myocardium: Past, Present, Future”. In: *Radiology* 261.2, pp. 358–374.
- PETERS, D. C., J. V. WYLIE, T. H. HAUSER, K. V. KISSINGER, R. M. BOTNAR, V. ESSEBAG, M. E. JOSEPHSON, and W. J. MANNING (2007). “Detection of Pulmonary Vein and Left Atrial Scar after Catheter Ablation with Three-dimensional Navigator-gated Delayed Enhancement MR Imaging: Initial Experience¹”. In: *Radiology* 243.3, pp. 690–695.
- POSITANO, V., A. PINGITORE, A. GIORGETTI, B. FAVILLI, M. F. SANTARELLI, L. LANDINI, P. MARZULLO, and M. LOMBARDI (2005). “A fast and effective method to assess myocardial necrosis by means of contrast magnetic resonance imaging”. In: *Journal of Cardiovascular Magnetic Resonance: Official Journal of the Society for Cardiovascular Magnetic Resonance* 7.2, pp. 487–494.
- RUDOLPH, A., H. ABDEL-ATY, S. BOHL, P. BOYÉ, A. ZAGROSEK, R. DIETZ, and J. SCHULZ-MENGER (2009). “Noninvasive detection of fibrosis applying contrast-enhanced cardiac magnetic resonance in different forms of left ventricular hypertrophy relation to remodeling”. eng. In: *Journal of the American College of Cardiology* 53.3, pp. 284–291.
- SCHMIDT, A., C. F. AZEVEDO, A. CHENG, S. N. GUPTA, D. A. BLUEMKE, T. K. FOO, G. GERSTENBLITH, R. G. WEISS, E. MARBÁN, G. F. TOMASELLI, J. A. C. LIMA, and K. C. WU (2007). “Infarct tissue heterogeneity by magnetic resonance imaging identifies enhanced cardiac arrhythmia susceptibility in patients with left ventricular dysfunction”. In: *Circulation* 115.15, pp. 2006–2014.
- SCHUIJF, J. D., T. A. M. KAANDORP, H. J. LAMB, R. J. v. D. GEEST, E. P. VIERGEVER, E. E. v. D. WALL, A. DE ROOS, and J. J. BAX (2004). “Quantification of myocardial infarct size and transmuralty by contrast-enhanced magnetic resonance imaging in men”. In: *The American Journal of Cardiology* 94.3, pp. 284–288.

- SHAKHNAROVICH, G. (2005). “Learning task-specific similarity”. Thesis. Massachusetts Institute of Technology.
- SIMONETTI, O. P., R. J. KIM, D. S. FIENO, H. B. HILLENBRAND, E. WU, J. M. BUNDY, J. P. FINN, and R. M. JUDD (2001). “An improved MR imaging technique for the visualization of myocardial infarction”. In: *Radiology* 218.1, pp. 215–223.
- SPIEWAK, M., L. A. MALEK, J. MISKO, L. CHOJNOWSKA, B. MILOSZ, M. KLOPOTOWSKI, J. PETRYKA, M. DABROWSKI, C. KEPKA, and W. RUZYLLLO (2010). “Comparison of different quantification methods of late gadolinium enhancement in patients with hypertrophic cardiomyopathy”. In: *European Journal of Radiology* 74.3, e149–153.
- SPRECHMANN, P. and G. SAPIRO (2010). “Dictionary learning and sparse coding for unsupervised clustering”. In: *2010 IEEE International Conference on Acoustics Speech and Signal Processing (ICASSP)*, pp. 2042–2045.
- TAO, Q., J. MILLES, K. ZEPPENFELD, H. J. LAMB, J. J. BAX, J. H. C. REIBER, and R. J. VAN DER GEEST (2010). “Automated segmentation of myocardial scar in late enhancement MRI using combined intensity and spatial information”. In: *Magnetic Resonance in Medicine: Official Journal of the Society of Magnetic Resonance in Medicine / Society of Magnetic Resonance in Medicine* 64.2, pp. 586–594.
- AL-TUBAIKH, J. A. (2010). *Internal Medicine: An Illustrated Radiological Guide*. Springer Science & Business Media.
- WILDE, A. A. M. and E. R. BEHR (2013). “Genetic testing for inherited cardiac disease”. In: *Nature Reviews Cardiology* 10.10, pp. 571–583.
- YAN, A. T., A. J. SHAYNE, K. A. BROWN, S. N. GUPTA, C. W. CHAN, T. M. LUU, M. F. DI CARLI, H. G. REYNOLDS, W. G. STEVENSON, and R. Y. KWONG (2006). “Characterization of the peri-infarct zone by contrast-enhanced cardiac magnetic resonance imaging is a powerful predictor of post-myocardial infarction mortality”. In: *Circulation* 114.1, pp. 32–39.

Conclusion and Perspectives

In this thesis, we have proposed new methods i) for the assessment of LV wall motion in the context of patients with Heart Failure and ii) for the detection of cardiac fibrosis in the context of patients with Hypertrophic Cardiomyopathy (HCM).

In the context of Heart Failure, we aimed at developing new methods for the assessment of LV wall motion in cardiac cine-MRI that is currently used in medical imaging for the assessment of LV function. In clinical practice, this assessment relies mainly on manual segmentations as well as visual analysis and interpretations of wall motion. Assessment of the LV includes two main steps: i) global assessment, that is routinely performed based on measurements of LV volumes, ejection fraction and mass, and ii) regional assessment, that is mostly based on visual and semi quantitative analysis of dynamic cine images of the left ventricle in several planes.

The interpretation of regional wall motion relies on integrating spatial and temporal information, which is subjective and requires extensive training and clinical experience. Another type of cardiac image modality is Echocardiography that is considered as the reference for cardiac mechanical analysis. Currently methods for analysis of regional LV function integrate deformation measures extracted from two dimensional (2D) echocardiographic images, in particular with 2D speckle tracking echocardiography (2D-STE).

In the literature, works for the automatic assessment of LV wall motion in cardiac MRI are grouped in three categories: i) Methods based on shape statistics, that provide a statistical shape modeling of cardiac contraction, ii) Methods based on image features extraction, with the hypothesis that motion patterns of normal LV segments should be deviated away from motion patterns of the abnormal LV segments and, iii) Methods based on parametric imaging-based quantification, that relies on the reader's ability to integrate spatial and temporal information on LV wall motion by creating parametric images from which motion abnormalities can be easily identified.

Most of these methods are sensitive to the quality of the myocardial contours, as they have the myocardial contours as input. Furthermore, some of them base their analysis only on two phases (ES and ED) while others exploit all the cardiac sequence. In these methods, the discrimination

of LV wall motion abnormality is performed by the application of pattern recognition techniques. Different techniques have been employed: Linear Discriminant Analysis (LDA), linear SVM, Naive Bayes classifier or specific classifiers based on correlation measures and the quantification of regional indicators of LV wall motion. In most of these methods, the evaluation is performed by expert visual assessment.

We have developed an approach for the assessment of LV function using a classification method based on sparse representations and dictionary learning (DL) to classify normal or abnormal regional LV motion.

Sparse representation and DL methods used in medical imaging are mostly based on applications such as denoising that involves the use of dictionaries trained with known basis as DCT or dictionaries learned using K-SVD algorithm. In the case of supervised sparse representation for segmentation and classification most of the methods are based on the framework of the SRC algorithm. In cardiac medical images works are focused on segmentation on epicardial and endocardial contours of LV in echocardiography images.

In this study, we have searched the benefits of using dictionaries, directly learned from a set of training medical images, that better capture the distribution of the data and then, used in specific tasks such as classification and detection.

Our method differs from those methods reported in the literature in three points: firstly, it differs in the feature extraction procedure which exploits all the information contained in the cardiac cycle without the need of segmentation of the epicardial and endocardial boundaries. Secondly, it differs by the use of DL techniques for classification of LV wall motion in cardiac MRI. Finally, it differs by the evaluation that incorporates for some points of the work, reference measures provided by local strain information measured in 2D-Speckle tracking Echocardiography.

Firstly, cardiac cine-MRI sequences in short axis view have been collected from two populations: pathologic and control subjects. Secondly, the subsequent process has been divided in three main stages: pre-processing, feature extraction and Dictionary Learning-based classification.

In the pre-processing stage, a region of interest (ROI) has been defined at the first frame of each sequence in order to keep only the LV cavity. Then, the ROI has been spatially normalized according to the AHA representation to identify different anatomical segments.

In the feature extraction stage, a set of features have been proposed: i) diametral spatio-temporal profiles, ii) radial spatio-temporal profiles, and iii) time signal intensity curve parameters extracted from the radial profiles. These kind of representations have not been previously reported for the classification of LV wall motion in cardiac MRI.

The first proposed feature used in this work correspond to diametral spatio-temporal profiles that show the temporal evolution of epicardium and endocardium at the same time in opposite LV anatomical segments, exploiting thus, the relation exhibited by radial motion profiles at the same orientation.

The second proposed feature is based on the construction of radial spatio-temporal profiles where motion of LV's walls is observed for each segment of the LV cavity. Furthermore, the assessment of these profiles has been performed with the analysis of radial strain curves obtained

from the 2D-STE studies, where a profile is classified as normal or abnormal (akinetic or hypokinetic cases).

The third feature for LV wall motion classification is based on the idea that information of contraction is given by specific information extracted from the radial spatio-temporal profiles that can be described as quantitative parameters. Specifically, 4 parameters have been extracted: 1) an average curve based on a clustering process, 2) curve skewness over the clustered curves 3) cross correlation values between each average clustered curve and a patient-specific reference and 4) mean transition time parameter. These parameters have been defined from time signals intensity curves that reflect dynamic information of the LV contraction.

In each case, the proposed representations have been taken as input atoms for the training of DL approaches to provide a classification of local LV wall motion.

In the Dictionary Learning-based classification stage, firstly, two discriminative DL algorithms have been adapted for LV wall motion classification: the first one, where the discrimination of the learned dictionary is enforced by imposing structural constraints on the dictionary: the Label Consistent K-SVD algorithm (LC-KSVD) (JIANG et al., 2013), and a second one, where the discrimination is enforced by imposing a discrimination term on the sparse decomposition vectors: the Fisher discriminant DL algorithm (YANG et al., 2014). These two algorithms have taken, as input atoms, the diametral or the radial spatio temporal profiles. Secondly, another type of DL algorithm based on kernels: the Kernel Sparse Representation DL (KSRDL) (LI et al., 2013), has been adapted for LV wall motion classification using parameters extracted from the radial spatio-temporal profiles. LC-KSVD has been also used with the parametric inputs. Classical classification based on Support Vector Machines (SVMs) with two different kernels has been also performed for comparisons purposes.

In the case of diametral profiles, the experiments have been realized in apical, mid-cavity and basal SAX planes using 360 profiles extracted from a set of 20 subjects (14 patients and 6 controls, 18 profiles per subject) at each short axis plane.

In the case of radial profiles and parameters extracted from radial spatio-temporal profiles, the experiments have been realized on 108 anatomical segments in a set of 18 subjects (9 patients with cardiac dyssynchrony and 9 healthy subjects) from which 648 spatio-temporal profiles have been extracted.

Two levels of evaluation have been elaborated: global evaluation, where the global status of the patient was used to label each LV anatomical segment and local evaluation, where information of local radial strain provided by 2D-Speckle tracking Echocardiography was used to label each LV anatomical segment.

In global evaluation a systematic error has been introduced since the beginning of the training stage were some anatomical segments in patients that present normal wall motion were assumed as segments with abnormal LV wall motion regarding the global status of the patient.

We aimed to compare global vs. local evaluation to analyze the impact that the systematic error has in the classifiers comparing to the more realistic local evaluation.

The complexity of the classification techniques has been compared in term of sparseness

for the SVMs and sparsity constraint for the DL models. Local results have been presented in parametric images known as bull-eyes in anatomical segments of the LV according to the AHA 17 myocardial segments.

The best results using global evaluation have been obtained by the FD-DL classifier that reached 96.51%, using diametral spatio-temporal profiles in the Wavelet domain obtained at the mid-ventricular slice level. This performance has been slightly improved by using radial profiles at the same anatomical plane by the same classification technique with an accuracy of 97.05% in this case in gray level (original domain).

Regarding local evaluation, the best performance in the mid-cavity plane has been achieved by the FD-DL technique using radial profiles with the assessment of 2D-STE in the gray level domain with an accuracy of 92.81%. This performance has been improved by using the Skewness and Clustering parameters extracted from the radial profiles at the same anatomical plane by the KSRDL technique with an accuracy of 94.49%.

Even through this study has been limited to the number of patients and the availability of the strain information, our results obtained with local validation can be analyzed taking as reference results obtained by methods in the literature. The proposed method has two main characteristics that can be summarized as: i) by performing the evaluation using strain information and complete information from all phases and segments we were able to determine a wall motion estimation comparable to the standard manual wall motion scores performed by cardiologists, and ii) the analysis of the LV radial spatio-temporal profiles in the cardiac cine-MRI sequences at the mid-cavity short axis plane has been shown to be sufficient for detecting wall motion abnormalities in this patient study data set.

From the methodological point of view, the adaptation of DL methods to the task of classification has resulted in a promising technique for LV motion analysis, achieving an appropriate balance between complexity and simplicity.

In the context of Hypertrophic Cardiomyopathy (HCM), we aimed at developing new methods for the detection of fibrosis in LGE-MRI that is the most accessible and accurate noninvasive imaging tool to assess myocardial fibrosis in a routine clinical practice even if new T1-mapping sequences seem to be promising and have to be analyzed.

In the literature, methods for the detection of fibrosis in LGE-MRI include: i) methods based on the tuning of thresholds with manual interaction of the user, ii) methods based on the automated detection of the infarcted zones using morphological operators and, iii) methods based on clustering that avoid the choice of gray level thresholds.

We developed an approach that combines a feature extraction method based on clustering with a classification method based on sparse representations and DL for the detection of fibrosis in LGE-SAX images. The process has been divided in 4 stages: feature extraction, clustering and DL training and testing.

In a feature extraction step, the extraction of non-overlapping patches from random LGE-SAX training images has been performed, then a similarity matrix among the extracted patches has

been computed.

In a clustering step, two clusters, LGE/Non-LGE pixels, have been obtained from the similarity matrix among the training patches after performing a multisignal 1-D hierarchical clustering algorithm based on Wavelet representation of similarities.

In a DL training step, a dictionary has been constructed with the clustered patches in two classes and a K -NN classifier has been trained with the sparse codes coefficients of the training patches obtained from a DL algorithm based on kernel: the KSRDL algorithm (Li et al., 2013).

In a DL testing stage, a new LG-SAX image is partitioned in overlapping patches and their sparse codes are computed using the learned dictionary. The label of each patch is predicted by using the trained K -NN classifier. In a post processing step the spatial localization of fibrosis is quantified inside the myocardium.

The detection approach has been applied in a set of 11 patients with cardiac hypertrophy from which 16 images from 16 slices covering apical, mid-cavity and basal planes have been processed for each patient.

The proposed method allowed the detection of fibrosis (LGE regions), localized inside the myocardium using the endo- and epicardial boundaries manually delineated by a cardiologist. The method has been evaluated by a visual evaluation and by comparing with the results of one method of the literature. The method has been able to successfully detect fibrosis in 9 out of the 11 patients.

By using the boundaries and a manual localization of the anterior intersection between right and left ventricles, the region of fibrosis is localized and visualized in different anatomical segments according the AHA representation.

The method has been focused on the fibrosis detection problem, but it can also be applied without the use of endo- and epicardial contours resulting in a segmentation approach of different structures in the MRI image.

The perspectives of this study include the following aspects:

Performance of classification of LV wall motion could potentially be improved by an automatic location of the anatomical landmark between the LV and the RV. In fact, results have shown that the classification performance has been generally improved using the different classifiers with the manual tracking of the anterior intersection between the two ventricles. Furthermore, the accuracy in the detection of fibrosis associated to LV anatomical segments could be improved, since it depends on the AHA decomposition and thus on the location of the anterior intersection between the LV and the RV.

We have performed a binary classification between normal/abnormal LV motion based on the spatio-temporal representations extracted in anatomical segments. This classification could be extended to a multiclass classification into one of four classes: normal, hypokinetic, akinetic and dyskinetic LV wall motion.

This work that is focused on LV wall motion characterization could be extended for characterization of cardiac dyssynchrony by considering additional parameters that could be also

incorporated as input atoms in the DL-based classification methods. These parameters could include information from global functional indexes (like time-volume curves, ejection fraction, stroke volume) as well as regional anatomical and functional parameters (like thickening, velocities, strain and mechanical delays).

The method could be improved with an extensively validation by using more patients. Furthermore, it could be extended for a new precise classification according to subgroups in HF pathologies, such as, the classification of responders or non-responders patients in the context of CRT. Furthermore, it could be applied for the characterization of different cardiac pathologies and in other cardiac imaging modalities.

References

- JIANG, Z., Z. LIN, and L. S. DAVIS (2013). “Label Consistent K-SVD: Learning a Discriminative Dictionary for Recognition”. In: *IEEE Transactions on Pattern Analysis and Machine Intelligence* 35.11, pp. 2651–2664.
- LI, Y. and A. NGOM (2013). “Sparse representation approaches for the classification of high-dimensional biological data”. In: *BMC Systems Biology* 7.Suppl 4, S6.
- YANG, M., L. ZHANG, X. FENG, and D. ZHANG (2014). “Sparse Representation Based Fisher Discrimination Dictionary Learning for Image Classification”. In: *International Journal of Computer Vision* 109.3, pp. 209–232.

List of associated publications

A.1 International journals

- **Juan Mantilla**, José Paredes, Jean-Jacques Bellanger, Erwan Donal, Christophe Leclercq, Rubén Medina and Mireille Garreau. Local LV wall motion classification via discriminative dictionary learning in cardiac MRI. *In preparation*.
- **Juan Mantilla**, Mireille Garreau, Jean-Jacques Bellanger, Erwan Donal, Christophe Leclercq and José Luis Paredes. Signal parameter extraction for LV wall motion classification in cardiac MRI using DL. *In preparation*
- **Juan Mantilla**, José Luis Paredes, Jean-Jacques Bellanger, Julian Betancur, Frédéric Schnell, Christophe Leclercq and Mireille Garreau. Quantification of fibrosis in LGE-cardiac MRI using Kernel DL-based clustering. *In preparation*.

A.2 International conferences

- **Juan Mantilla**, José Paredes, Jean-J. Bellanger¹, Erwan Donal, Christophe Leclercq, Rubén Medina and Mireille Garreau. Classification of LV wall motion in cardiac MRI using kernel Dictionary Learning with a parametric approach. *In proceedings of: 37th Annual International Conference of the IEEE Engineering in Medicine and Biology Society (EMBS) 978-1-4244-9270-1/15*, pp. 7292-7295.
- **Juan Mantilla**, José Luis Paredes, Jean-Jacques Bellanger, Julian Betancur, Frédéric Schnell, Christophe Leclercq and Mireille Garreau. Detection of fibrosis in LGE-cardiac MRI using Kernel DL-based clustering. *Accepted for publication in: Computing in Cardiology*.
- **Juan Mantilla**, Mireille Garreau, Jean-Jacques Bellanger and José Luis Paredes. “Machine learning techniques for LV wall motion classification based on spatio-temporal profiles from cardiac cine MRI”. Proc. IEEE 12th International Conference on Machine Learning and Applications, Pages: 167-172, DOI 10.1109/ICMLA.2013.36.(Dec, 2013)

- **Juan Mantilla**, Mireille Garreau, Jean-Jacques Bellanger and José Luis Paredes. “SVM-based classification of LV wall motion in cardiac MRI with the assessment of STE”. Proc. SPIE 9287, X International Seminar on Medical Information Processing and Analysis 2015, pp. 92 870N-92 870N-6.
- **Juan Mantilla**, Mireille Garreau, Jean-Jacques Bellanger and José Luis Paredes. “Automated classification of LV regional wall motion based on spatio-temporal profiles from cardiac cine magnetic resonance imaging”. Proc. SPIE 8922, IX International Seminar on Medical Information Processing and Analysis, 892204; doi:10.1117/12.2035517. (Nov, 2013)

A.3 National conferences

- **Juan Mantilla**, Mireille Garreau, Jean-Jacques Bellanger, Christophe Leclercq and José Paredes. "DL-based classification of LV wall motion in cardiac MRI with a parametric approach". Recherche en Imagerie et Technologies pour la Santé (RITS) Dourdan, France du 25 au 27 mars 2015.
- **Juan Mantilla**, Mireille Garreau, Jean-Jacques Bellanger, and José Luis Paredes. "Valoración del movimiento del ventriculo izquierdo en MRI cardiaca usando aprendizaje de diccionarios". V Congreso Venezolano de Bioingeniería. Mérida Venezuela du 20 au 22 May 2015.

List of Figures

2.1	Example of a sparse signal represented by a linear combination of atoms of an orthogonal dictionary	8
2.2	Wavelet Haar atoms in an overcomplete dictionary	18
2.3	Image lena and its orthogonal Wavelet transform at six scales	18
2.4	An illustration of the DL process.	20
2.5	Applications of Sparse representation in image processing	25
2.6	Separating hyperplanes in a SVM classification problem with two classes	38
4.1	A schematic illustration of the heart	60
4.2	Left ventricular long axis, apex and illustration of the long-axis (LAX) and the short-axis (SAX)	61
4.3	Electrical function of the heart.	62
4.4	Detailed phases in the cardiac cycle	64
4.5	AHA 17 segment representation	65
4.6	Components to describe LV wall motion	66
4.7	Cardiac Imaging planes in MRI	72
4.8	ECG synchronization of imaging pulse sequences.	73
4.9	Different spatial acquisitions in short axis view	73
4.10	Transthoracic echocardiographic (TTE-US) images at end-diastole.	74
4.11	Speckle tracking echocardiography from a pathologic patient in the short axis view .	76
4.12	Overall scheme of the adaptation of discriminative DL approaches for LV wall motion classification based on radial spatio-temporal profiles extracted in cardiac cine-MRI	83
4.13	Region of interest for normal/abnormal wall motion classification	86
4.14	Spatial normalization according to AHA model	87
4.15	Rotation of the diametrical line for the extraction of diametral spatio-temporal profiles	87
4.16	Example of the construction of diametral spatio-temporal profile	88
4.17	Spatio-temporal image profiles examples	89
4.18	Graphical User Interface (GUI) for profiles extraction in CMR databases	90
4.19	Spatio-Temporal profile and its respective representation on other bases	91
4.20	Example of construction of Radial spatio-temporal profile	92
4.21	Radial Spatio-Temporal profile and its respective representation on the Wavelet domain	93

4.22	Four patterns of time-signal intensity curves TSIC	94
4.23	Example of construction of Radial spatio-temporal profile	94
4.24	A Gaussian p.d.f. function fitted to a a selected TSIC.	95
4.25	Example of an angular subregion in the LV anterolateral segment.	97
4.26	Histogram of maximum peak time in time-signal intensity curves from abnormal profiles and normal profiles	98
4.27	Illustrative scheme for DL based framework	99
4.28	An illustrative example of the “discriminative” sparse codes matrix \mathbf{Q} in the LC-KSVD algorithm.	101
5.1	Overview of the proposed evaluation protocol at two levels	113
5.2	Radial strain tracings for one cardiac cycle obtained from the short axis view in the EuHeart5 patient	117
5.3	Radial strain tracings for the EuHeart5 patient, for the six anatomical segments. Superimposition of the range of normal, hypokinesis and akinesis zones.	117
5.4	GUI for Radial spatio-temporal profiles labelling	118
5.5	Ground truth for Local LV wall motion with the assessment of STE in the pathological group.	119
5.6	An illustrative example of 36 points located outside the epicardial border every 10° to construct 36 radial spatio-temporal profiles	121
5.7	Comparative mean results of LOO cross validation in opposite segments with linear SVM	124
5.8	Comparative mean results of LOO cross validation in opposite segments with RBF SVM	124
5.9	Bull-eyes showing accuracy of classification	125
5.10	Relevant regions in the LV where SVM model finds optimal support vectors for classification	128
5.11	Accuracy of classification of LC-KSVD algorithms varying the number of dictionary atoms	130
5.12	Accuracy of classification of LC-KSVD algorithms varying the sparsity constraint T	130
5.13	Accuracy of classification of the FD-DL algorithm varying the Dictionary size	132
5.14	Accuracy of classification of the FD-DL algorithm varying the sparsity constraint λ_1 in the Wavelet domain at the mid-cavity plane	133
5.15	Accuracy, Sensitivity and Specificity of the machine learning techniques (diametral profiles)	134
5.16	Global evaluation: Bull’s eyes results with LOO cross validation using Linear kernel with diametral profiles in Wavelet domain	136
5.17	Global evaluation: Bull’s eyes results with LOO cross validation using Linear kernel with radial profiles in Wavelet domain	138

5.18	Accuracy, Sensitivity and Specificity of the machine learning techniques (diametral profiles vs. radial profiles)	140
5.19	Local evaluation: Bull's eyes results with LOO cross validation using Linear kernel with radial profiles in Wavelet domain	142
5.20	Local mid-cavity evaluation: Accuracy of classification of LC-KSVD algorithms varying the number of dictionary atoms (radial profiles)	144
5.21	Accuracy of classification of FD-DL algorithm varying the number of dictionary atoms (radial profiles)	144
5.22	Local mid-cavity evaluation: Accuracy of classification of LC-KSVD algorithms varying the sparsity constraint T (radial profiles).	145
5.23	Local mid-cavity evaluation: Accuracy of classification of the FD-DL algorithm varying the sparsity constraint λ_1 (radial profiles)	145
5.24	Local mid-cavity evaluation: Accuracy, Sensitivity and Specificity of the machine learning techniques in Wavelet and Gray level representation using radial spatio-temporal profiles	146
5.25	Local LV wall motion in the study population obtained by the three adapted discriminative DL techniques for LV wall motion classification	147
5.26	The representation of the coefficient matrix \mathbf{X} on the training datasets	148
5.27	Clustered reference signal by segments in 4 subjects	150
5.28	Average of curve Skewness for both populations in the different anatomical segments.	151
5.29	Accuracy of classification of KSRDL algorithm varying the number of dictionary atoms	153
5.30	Accuracy of classification of the KSRDL algorithm varying the sparsity constraint λ_1	154
5.31	Angular variation of reference point E1 from end diastole to a posterior frame E1'	157
5.32	Radial profiles with A) simple location of the anterior intersection between RV and LV at the first frame of the cardiac cycle and B) manual location of the anterior intersection between RV and LV in all the frames of the cardiac cycle.	158
6.1	Different types of cardiomyopathies.	166
6.2	Different types of myocardial fibrosis according to the cardiomyopathic process.	168
6.3	Example of LGE-SAX IR (left) and PSIR (right) acquisitions	170
6.4	Overview of the proposed fibrosis detection method	174
6.5	Feature extraction example from LGE-SAX images	175
6.6	Extracted patches from LGE-SAX images and its respective Similarity matrix	175
6.7	Examples of resulting fibrosis detection using the proposed approach with different patch size	179
6.8	Examples of resulting fibrosis detection using the proposed approach: Patients 01 and 02	179
6.9	Examples of resulting fibrosis detection using the proposed approach: Patients 03 and 04	179

6.10	Examples of resulting fibrosis detection using the proposed approach: Patients 05 and 06	180
6.11	Examples of resulting fibrosis detection using the proposed approach: Patients 07 and 08	180
6.12	Examples of resulting fibrosis detection using the proposed approach: Patients 09 and 10	180
6.13	Examples of resulting fibrosis detection using the proposed approach: Patient 11 . .	181
6.14	Examples of resulting fibrosis detection using the fuzzy c-means approach in three patients	182
6.15	Framework for Spatial localization of fibrosis	183
6.16	Spatial localization of fibrosis using the proposed approach for patients 01, 02 and 08	184

List of Tables

2.1	Sparse Representation Classification SRC algorithm	29
4.1	Comparison of ACCF/AHA Stages of HF and NYHA Functional Classifications. . .	68
5.1	Reference normal mean segmental peak systolic LV radial strain values	115
5.2	Reference radial strain related to regional LV function defined by cardiac magnetic resonance imaging	116
5.3	LV anatomical segments assessed by 2D-STE in the pathological group in the mid-cavity SAX plane.	119
5.4	Opposite LV anatomical segments assessed by 2D-STE in the pathological group in the mid-cavity SAX plane.	120
5.5	Global multi-slice evaluation: Mean results of LOO cross validation in opposites segments with Linear SVM and Wavelets coefficients.	125
5.6	Global multi-slice evaluation: Classification results using diametral profiles in Gray level domain by the SVM models.	126
5.7	Global multi-slice evaluation: Classification results using diametral profiles in Wavelet domain by the SVM models.	126
5.8	Global multislice evaluation: Classification results using diametral profiles in Curvelet domain by the SVM models.	127
5.9	Global multi-slice evaluation: Classification results using diametral profiles in Fourier domain by the SVM models.	127
5.10	Global multi-slice evaluation: Percentage of contribution of spatio-temporal profiles in the classification task by the SVM models.	128
5.11	Global multi-slice evaluation: Classification results using diametral profiles in Gray Level domain by the LC-KSVD algorithms	129
5.12	Global multi-slice evaluation: Classification results using diametral profiles in Wavelet domain by the LC-KSVD algorithms	129
5.13	Global multislice evaluation: Classification results using diametral profiles in Fourier domain by the LC-KSVD algorithms	129
5.14	Global multi-slice evaluation: Classification results using diametral profiles in Gray level domain by the FD-DL algorithm	131

5.15	Global multi-slice evaluation: Classification results using diametral profiles in Wavelet domain by the FD-DL algorithm	131
5.16	Global multi-slice evaluation: Classification results using diametral profiles in Fourier domain by the FD-DL algorithm	131
5.17	Global mid-cavity evaluation: LOO results of classification using diametral profiles in Gray level and Wavelet domain by the SVM models	135
5.18	Global evaluation: Results of classification using diametral profiles in Gray level and Wavelet domain by the SVM models and DL algorithms	136
5.19	Global mid-cavity evaluation: LOO results of classification using radial profiles in Gray level and Wavelet domain by the SVM models	137
5.20	Global evaluation: Results of classification using radial profiles in Gray level and Wavelet domain by the SVM and DL models	138
5.21	Total number of Radial Spatio-temporal profiles in the database	141
5.22	Local mid-cavity evaluation: LOO results of classification using radial profiles in Gray level and Wavelet domain by the SVM models	142
5.23	Local mid-cavity evaluation: Results of classification using radial profiles in Gray level and Wavelet domain by the SVM and DL models	143
5.24	Local mid-cavity evaluation: Number of Support vectors obtained using radial profiles in Gray level and Wavelet domain by the SVM models	144
5.25	Local mid-cavity evaluation: LOO results of classification using radial profiles in Gray level and Wavelet domain by the LC-KSVD algorithms	146
5.26	Time employed by the classification techniques in the Original domain	147
5.27	Time employed by the classification techniques in the Wavelet domain	147
5.28	Mean transition time (msec) obtained from TSICs	151
5.29	Delay time based Cross Correlation obtained from the time-signal intensity curves and the patient-specific reference	152
5.30	Accuracy obtained by different techniques	152
5.31	Computing times employed by the different techniques	153
5.32	Classification techniques in recent existing methods of regional LV motion classification	154
5.33	Comparisons of accuracy of the proposed methods using local evaluation with existing methods of regional LV motion classification	156
5.34	Angular variation in degrees of the anterior intersection point between RV and LV .	158
5.35	Results of classification by local evaluation and by using radial profiles with the manual location of the anterior intersection between RV and LV in each frame of the cardiac cycle by the different techniques in Gray level and Wavelet domain	159
6.1	Overview of previously published scar detection, quantification and segmentation methods	172
6.2	Quantification of cardiac Fibrosis per slice level in Patients 01, 02 and 08	183
6.3	Quantification of cardiac Fibrosis per segment and slice level in Patient 02	184

6.4	Quantification of cardiac Fibrosis per segment and slice level in Patient 02	185
-----	--	-----

VU:

VU:

Le Directeur de Thèse

PRENOM NOM

Le Responsable de l'école

doctorale

VU pour autorisation de soutenance
Rennes, le

Le Président de l'Université de
Rennes 1

Guy CATHELINÉAU

VU après soutenance pour autorisation de publication:

Le Président de Jury